SURFACE-ENHANCED RAMAN SPECTROSCOPY FOR ENVIRONMENTAL ANALYSIS – OPTIMIZATION AND QUANTITATION

Haoran Wei

Dissertation Submitted to the faculty of the Virginia Polytechnic Institute and State University in partial fulfillment of the requirements for the degree of

Doctor of Philosophy in Civil Engineering

Peter J. Vikesland, Chair

Linsey C. Marr

Wei Zhou

Zhen (Jason) He

Jan. 19th, 2018

Blacksburg, VA

Keywords: Surface-enhanced Raman spectroscopy, quantitation, Rayleigh scattering, internal standard, surface coating, aerosol droplet, pH.

Surface-Enhanced Raman Spectroscopy for Environmental Analysis: Optimization and Quantitation

Haoran Wei

Abstract (academic)

Fast, sensitive, quantitative, and low-cost analysis of environmental pollutants is highly valuable for environmental monitoring. Due to its single-molecule sensitivity and fingerprint specificity, surface-enhanced Raman spectroscopy (SERS) has been widely employed for heavy metal, organic compound, and pathogen detection. However, SERS quantitation is challenging because 1) analytes do not stay in the strongest enhancing region ("hot spots") and 2) SERS reproducibility is poor. In this dissertation, gold nanoparticle/bacterial cellulose (AuNP/BC) substrates were developed to improve SERS sensitivity by increasing hot spot density within the laser excitation volume. Environmentally relevant organic amines were fixed at "hot spots" by lowering solution pH below the analyte pK_a and thus enabling SERS quantitation. In addition, a new SERS internal standard was developed based upon the electromagnetic enhancement mechanism that relates Rayleigh (elastic) and Raman (in-elastic) scattering. Rayleigh scattering arising from the amplified spontaneous emission of the excitation laser was employed as a normalization factor to minimize the inherent SERS signal variation caused by the heterogeneous distribution of "hot spots" across a SERS substrate. This highly novel technique, hot spot-normalized SERS (HSNSERS), was subsequently applied to evaluate the efficiency of SERS substrates, provide *in situ* monitoring of ligand exchange kinetics on the AuNP surface, and to reveal the relationship between the pK_a of aromatic amines and their affinity to citrate-coated AuNPs (cit-AuNPs). Finally, colloidally stable stable pH nanoprobes were synthesized using co-solvent mediated AuNP aggregation and

subsequent coating of poly(ethylene) glycol (PEG). These nanoprobes were applied for pH detection in cancer cells and in phosphate buffered aerosol droplets. The latter experiments suggest that stable pH gradients exist in aerosol droplets.

Surface-Enhanced Raman Spectroscopy for Environmental Analysis: Optimization and Quantitation

Haoran Wei

Abstract (general audience)

Traditional analytical methods, such as gas chromatography/mass spectroscopy, liquid chromatography/mass spectroscopy, etc., cannot meet the demand for rapid screening of target environmental pollutants in drinking water. This issue arises due to the requirements for time-consuming sample pre-treatment, well-trained experts, complex instrumental parameter optimization, and scale challenges that limit onsite measurement. Surface-enhanced Raman spectroscopy is a promising approach to overcome these limitations. To improve SERS quantitation, surface-enhanced elastic scattering was developed as a novel internal standard to account for the SERS signal variation caused by substrate heterogeneity ("hot spot" normalization). Compared with traditional SERS internal standards, using scattered light as an internal standard reduces cost, time, interference, and experimental complexity for SERS detection. With this novel approach, the kinetics of adsorption/desorption of guest ligands/citrate onto/from the AuNP surface were quantified *in situ* and in real time. In addition, the SERS intensities of organic amines acquired at different solution pH values were differentiated using "hot spot" normalization, which revealed the relationship between aromatic amine pK_a and their affinity to the AuNP surface. Finally, the chemistry in confined aqueous environments, such as aerosol droplets, membrane channels, and cells, is challenging to probe using conventional analytical tools due to their inaccessible small volumes. To address this problem, SERS pH nanoprobes were synthesized and used to detect the pH inside cancer cells and micrometer-sized aerosol droplets.

Acknowledgements

First I would like to thank my advisor – Dr. Peter J. Vikesland for his great help in my Ph.D. study. Dr. Vikesland is both an excellent scientist and excellent advisor. He created a free environment for me to explore the science and always gave me valuable suggestions when I needed. His intellectual contributions are key factors for me to complete this dissertation. I feel lucky and honored to be one of the members in Dr. Vikesland's group. His good taste to science and mentoring philosophy will influence mine throughout my career.

I would like to thank all my committee members, Dr. Marr, Dr. He, and Dr. Zhou for their valuable contributions to this dissertation. Their insightful suggestions, encouragement, and guidance are important for me to make it here.

I would like to thank all my group mates, especially Dr. Weinan Leng for his help in instrumentation and nanoparticle synthesis and Marjorie R. Willner for her help in data processing.

I would like thank all my collaborators, Dr. Eric Vejerano, Dr. Scott Renneckar, Dr. Katia Rodriguez, and Junyeob Song. Thank you all for your help.

Finally, I would like to thank my family, especially my wife Mohan Qin. She is the most precious treasure of my life. Her support is the fundamental motivation for me to move forward. Her enthusiasm and love towards life and everybody around has made and will make huge positive effect on my life.

Table of Contents

Tables

Figures

Chapter 1 Introduction

Water shortage is identified as one of the major environmental challenges in 21st century due to the increasing frequency of droughts due to climate change and the growing water demand resulting from the rapid increasing world population.[1-3] To make matters worse, hazardous organic compounds present in domestic, industrial wastewater, and agricultural runoffs may end up in rivers, lakes, and groundwater and make them unsafe drinking water sources.[4-6] In addition, drinking water in distribution systems is vulnerable to heavy metal contamination due to the corrosion of water supply pipelines (e.g., Flint Incident).[7, 8] Rapid and cost-efficient sensors for water monitoring are highly desired to protect drinking water safety.

Currently, commonly adopted methods for organic compound analysis include gas chromatography/mass spectrometry, liquid chromatography/mass spectrometry, and high performance liquid chromatography/tandem mass spectrometry.[9, 10] Although powerful, these methods require extensive sample pretreatment, tedious instrumental parameter optimization, and well-trained personnel to conduct the analyses. Therefore, the high cost and long time required for these methods prevent them from application for rapid water pollutant screening. In addition, the water samples to be analyzed need to be transported to specialized labs, which further increases analysis time and uncertainty. For onsite analytical purposes, such as water quality monitoring for point-of-use devices, it remains challenging to timely and cost-efficiently quantify many organic pollutants.

Optical approaches, such as fluorescence spectroscopy, Fourier-transformation infrared spectroscopy, second-harmonic generation spectroscopy, Raman spectroscopy etc., are promising candidates to overcome the disadvantages of traditional analytical tools.[11-15] First, optical detectors

collect light signals generated directly/indirectly from the target analytes. For this reason, the detector does not contact with the water sample, thus making several sample pretreatment steps (e.g., filtration, dilution, pH adjustment etc.) unnecessary. Second, optical spectrometers are easier to operate than chromatography/mass spectrometers. Finally, miniaturized and portable optical spectrometers are available, which can be brought to the water sampling site for onsite measurement. These advantages collectively suggest optical approaches can be competitive for rapid, cost-efficient, and on site water monitoring.

Among all the optical analytical methods, Raman spectroscopy is arguably the most promising for water monitoring due to its low water band interference, high photostability, abundant vibrational bond information, and capability for multiplex detection.[11, 16, 17] However, Raman scattering reflects only 1 in 10^8 among total scattered photons, making it challenging to be applied for trace chemical detection.[18] In 1974 the enhanced Raman scattering cross section of pyridine adsorbed on a roughened silver electrode surface was observed and was later described as surface-enhanced Raman spectroscopy (SERS).[19, 20] SERS originates from the collective oscillation of conductive electrons on a plasmonic nanoparticle surface and enhances the Raman scattering efficiency of organic chemicals by several orders of magnitude.[21, 22] Since the first reports of single molecule detection by SERS in 1997, its potential as an ultrasensitive analytical tool has been extensively examined.[23-25]

Although SERS exhibits great potential, its real-world applications have rarely been reported mostly due to its poor reproducibility. The enhancing capabilities of SERS "hot spots" depend on the shape, size, and alignment pattern of plasmonic nanostructures.[26-28] The variation of these factors may overwhelm the signal variation induced by the changing analyte concentration, making SERS quantitation challenging. In addition, the low affinity between many organic pollutants and

the plasmonic nanoparticle surface can also limit SERS applications.[29-31] From the materials side, one approach to improve SERS quantitation is to make SERS substrates uniform(i.e., to reduce the heterogeneity of "hot spot" distribution across the substrate).[32-34] Such approaches rely on expensive nanofabrication methods and are challenging for large-scale production. Another viable approach for improving SERS quantitation is to introduce a chemical as an internal standard.[35-37] Because the internal standard undergoes the same enhancement as the target analyte, normalizing the analyte Raman signal with the internal standard Raman signal can significantly reduce the influence of "hot spot" heterogeneity. However, this approach also has several disadvantages such as generating interferent Raman bands, occupying "hot spot" volume, increasing cost, and lacking universal applicability.

The overarching aim of this dissertation was to improve the quantitative performance of SERS for environmental analysis. Sensitivity, reproducibility, and affinity are three aspects that determine SERS quantitation performance. To improve sensitivity, we developed gold nanoparticle/bacterial cellulose (AuNP/BC) SERS substrates, which contained an extremely high "hot spot" density. To improve reproducibility, we developed "hot spot"-normalized SERS (HSNSERS) that employed surface-enhanced Rayleigh scatterings as SERS internal standards. To improve affinity, we developed a pH-triggered approach to enhance the electrostatic attraction between organic amines and a citrate-coated AuNP (cit-AuNP) surface. HSNSERS was applied to evaluate SERS substrate efficiency, *in situ* monitoring ligand exchange kinetics on cit-AuNP surface, and to reveal the relationship between aromatic amine pK_a and affinity to a cit-AuNP surface. pH-triggered SERS was applied to reproducibly detect environmental pollutants – atrazine and carbamazepine. Another direction that was explored in this dissertation was to apply SERS pH nanoprobes to detect the pH in a confined water environment, such as human prostate cancer

cells and aerosol droplets. High spatial resolution detection was enabled by the combination of SERS nanoprobes and the confocal microscope. We developed a co-solvent induced aggregation approach to control nanoprobe size and optimize their SERS signal. These suspended pH nanoprobes suggest the existence of stable pH gradients inside aerosol droplets.

There are 11 chapters in this dissertation. Following this Introduction (**Chapter 1**), we reviewed the recent progress in applying plasmonic nanosensors for environmental analysis (**Chapter 2**). **Chapter 3** discusses the preparation and evaluation of AuNP/BC SERS substrates. **Chapter 4** introduces the HSNSERS approach and **Chapters 5-7** describe three environmental applications of HSNSERS. **Chapter 8** introduces pH-triggered detection of environmental pollutants. And **Chapters 9 & 10** discuss pH nanoprobe synthesis and application in aerosol droplet pH detection, respectively. The dissertation concludes with **Chapter 11** that summarizes the work conducted and its potential future directions.

Attribution

Haoran Wei, Department of Civil and Environmental Engineering, Virginia Tech

Primary author of this dissertation

Peter J. Vikesland, Ph.D. Professor of Civil and Environmental Engineering, Virginia Tech

Principal Investigator and coauthor of chapters 2-10

Linsey C. Marr, Ph.D. Professor of Civil and Environmental Engineering, Virginia Tech

Coauthor of chapters 9&10

Weinan Leng, Ph.D. Department of Civil and Environmental Engineering, Virginia Tech

Coauthor of chapters 3-7

Wei Zhou, Ph.D. Professor of Electrical and Computer Engineering, Virginia Tech

Coauthor of chapters 4-6

Junyeob Song, Department of Electrical and Computer Engineering, Virginia Tech

Coauthor of chapters 4-6

Eric Vejerano, Ph.D. Professor of Public Health, University of South Carolina

Coauthor of chapter 10

Scott Renneckar, Ph.D. Professor of Wood Science, The University of British Columbia

Coauthor of chapter 3

Katia Rodriguez, Ph.D. Department of Sustainable Biomaterials, Virginia Tech

Coauthor of chapter 3

Marjorie R. Willner, Department of Civil and Environmental Engineering, Virginia Tech

Coauthor of chapter 4-7, 9&10

Qishen Huang, Department of Civil and Environmental Engineering, Virginia Tech

Coauthor of chapters 6&7

Chang Liu, Department of Civil and Environmental Engineering, Virginia Tech

Coauthor of chapters 6

Seyyed M. Hossein, Abtahi, Department of Civil and Environmental Engineering, Virginia Tech

Coauthor of chapter 2

Alexis McCarthy, Department of Chemistry, Virginia Tech

Coauthor of chapter 5

Chapter 2 Plasmonic Colorimetric and SERS Sensors for Environmental Analysis

Haoran Wei,[1,2,3] Seyyed M. Hossein Abtahi,[1,2,3] and Peter J. Vikesland[1,2,3*]

[1]Department of Civil and Environmental Engineering, Virginia Tech, Blacksburg, Virginia

[2]Virginia Tech Institute of Critical Technology and Applied Science (ICTAS) Sustainable Nanotechnology Center (VTSuN), Blacksburg, Virginia

[3]Center for the Environmental Implications of Nanotechnology (CEINT), Duke University, Durham, North Carolina

*Corresponding author. Phone: (540) 231-3568, Email: pvikes@vt.edu

(This chapter has been published in ***Environmental Science: Nano***.[26] – Reproduced by permission of the Royal Society of Chemistry. The publisher - the Royal Society of Chemistry does not require formal reproduction permission when the article is used in the dissertation of the authors.)

Abstract

The potential for water pollution outbreaks requires the development of rapid, yet simple detection methods for water quality monitoring. Plasmonic nanostructures such as gold (AuNPs) and silver (AgNPs) nanoparticles are compelling candidates for the development of highly sensitive biosensors due to their unique localized surface plasmon resonances (LSPRs). The LSPR of AuNPs and AgNPs lies in the visible and infrared light range and is sensitive to the size, shape, and aggregation state of these NPs. This plasmonic behavior provides the basis for fabrication of colorimetric sensors for environmental analyses. Furthermore, the LSPR also enhances the electromagnetic field near the NP surface, which provides the basis for surface-enhanced Raman spectroscopy (SERS) based detection. Organic or inorganic pollutants and pathogens can be detected and differentiated based upon the finger-print spectra that arise when they enter SERS-active hot spots. In this tutorial review, we summarize progress made towards environmental analysis based on LSPR-based colorimetric and SERS detection. The problems and challenges that have hindered the development of LSPR-based nanosensors for real-world environmental pollutant monitoring are extensively discussed.

2.1 Introduction

One notorious side effect of global development is the ever-increasing number of gaseous and aqueous pollutants that pose ecosystem and human-health risks. Rapid pollutant recognition is vitally important in some emergent situations. For example, in the 2014 Elk River, WV incident in excess of 7500 gallons of 4-methylcyclohexanemathanol (4-MCHM) rapidly leaked into the Elk River such that the drinking water distribution system for the greater Charleston, WV area was heavily contaminated.[38] Similarly, in the summer of 2014 a massive algal bloom led to closure of

the Toledo, OH drinking water treatment plant due to the contamination of the water by microcystin toxins.[39] In addition to outbreaks caused by chemicals, outbreaks of waterborne pathogens are also problematic. For example, the 1993 Milwaukee *Cryptosporidiosis* outbreak in drinking water caused 104 deaths in only two weeks.[40] In November 2010, *Cryptosporidiosis* infected ≈27000 people in Östersund, Sweden via contaminated drinking water, and in December 2012 an outbreak of waterborne Norovirus caused acute gastrointestinal illness in a district containing 368 families in Denmark.[41, 42] In addition to waterborne contaminants, airborne contaminants, such as dioxins from garbage incineration plants or pandemic bird flu, also threaten people's health.[43, 44]

To prevent contaminants from causing environmental catastrophes it would be ideal to detect such contamination events as quickly as possible in order to rapidly initiate remedial strategies. Unfortunately, many traditional detection methods for water and airborne contaminants require either laborious sample preparation procedures or onerous analysis methods and are thus very time-consuming. Plasmonic nanostructures such as gold and silver nanoparticles (AuNPs and AgNPs) provide a promising avenue for the development of rapid and highly sensitive sensor platforms.[45] Many of the sensing capabilities enabled by AuNPs and AgNPs rely upon localized surface plasmon resonance (LSPR). When excited by light of a specific wavelength, the conduction electrons on the nanoparticle surface collectively oscillate and generate a significantly enhanced electromagnetic field or LSPR.[45-47] LSPR is an extremely sensitive optical transducer, which is dependent on the type, size, shape and aggregation state of plasmonic nanoparticles as well as the refractive index of the surrounding environment.[48-50] Changes in the LSPR result in color changes of the colloid suspension. Based on this phenomenon, LSPR-based colorimetric sensors have been developed.[51-53]

When the incident light wavelength is coupled with the LSPR of plasmonic NPs the electromagnetic field near the NP surface is significantly enhanced.[54, 55] When analytes closely associate with the NP surface, their Raman scattering cross-section increases substantially and this phenomenon is the basis for surface-enhanced Raman scattering (SERS).[55] SERS is an ultrasensitive sensing technique, which has been shown to enable the detection of single molecules.[24, 25, 56, 57] Compared with fluorescent techniques, SERS has greater potential for multiplex analysis due to the narrower peak widths in the collected Raman spectra. Because SERS is a vibrational spectroscopy method it provides chemical bonding information that facilitates differentiation of highly similar molecules and different molecular orientations.[58, 59] Unlike other environmental analysis techniques such as inductively coupled plasmon atomic emission spectroscopy (ICP-AES) and gas chromatography-mass spectroscopy (GC-MS), SERS does not require complex sample pretreatment, sophisticated analytical method optimization, or advanced analyst training. During the last decade, the rapid development of nanotechnology has created a number of novel nanostructures that have the potential for ultrasensitive SERS detection of environmental contaminants.[33, 60, 61]

Ultrasensitive chemical analysis via SERS was reviewed in the late 1990s, with the focus on the mechanisms responsible for "single molecule detection".[17, 62] Subsequently, many review papers have appeared that describe the fundamental theories, material fabrication methods, and applications of SERS.[21, 54, 55, 57, 63-68] Reviews on colorimetric sensors that monitor the LSPR band location have also been produced.[69-71] However, relatively few of these reviews focus explicitly on environmental applications of LSPR based sensing. A number of recent reviews discuss nanomaterial-based sensors for environmental monitoring.[72-77] However, these reviews covered either a broad suite of nanoparticles and sensing techniques or focused exclusively on SERS-based

sensors. Herein we focus on the application of AuNPs and AgNPs for environmental sensing via either colorimetric or SERS approaches because these two related methods dominate much of the current literature. Readers interested in SPR sensors based on refractive index sensing are referred elsewhere.[78-80] This review is organized into five parts (including this introduction). The second part briefly introduces the photonic behavior responsible for LSPR-based colorimetric and SERS sensors. The third and fourth parts summarize recent progress in environmental analysis with colorimetric and SERS sensors, respectively. In the SERS portion of the review, we focus on organic pollutants, biomolecules, and pathogen detection. For inorganic SERS detection the reader is referred elsewhere.[81] The concluding part of this tutorial review discusses the extant challenges associated with ultimate application of these sensors in environmental samples.

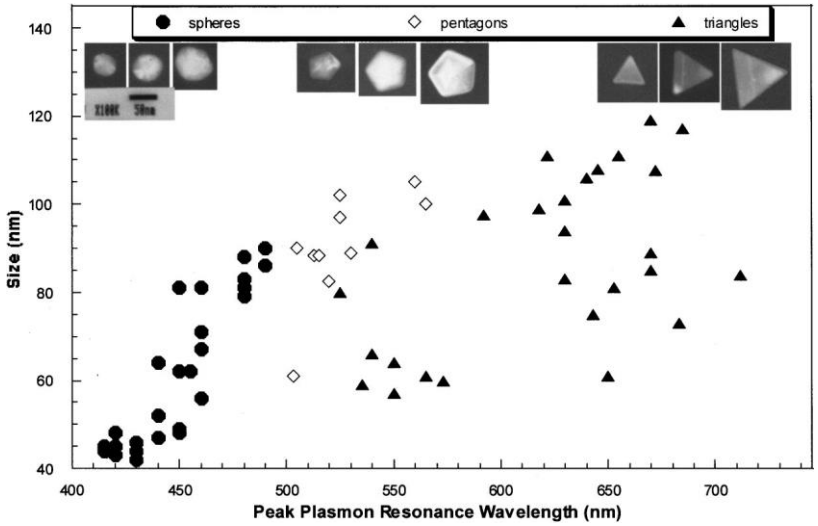

Figure 2.1 TEM images of silver spheres, pentagons, and triangles with different size (above) and their size-dependent peak LSPR wavelength. The size of a silver triangle is its edge length; the size of a silver pentagon is the distance between its opposite corners; the size of a silver sphere is its diameter. Reprinted with permission from J. Mock, M. Barbic, D. Smith, D. Schultz and S. Schultz, *J. Chem. Phys.*, 2002, 116, 6755-6759. Copyright 2014 American Institute of Physics.

2.2 Background on Photonics

Colloidal gold and silver nanoparticles exhibit intense colors due to a phenomenon known as surface plasmon resonance.[49, 82-84] This phenomenon occurs when conduction band electrons undergo coherent oscillations following excitation by an electromagnetic field. The interaction between the electric field of the incoming light and NPs with dimension smaller than the incident wavelength causes polarization of the electrons in the nanoparticle relative to its heavier ionic core.[85] This net charge difference is confined to the nanoparticle surface and acts as a restoring force that causes the collective oscillation of the surface electrons (i.e., a surface plasmon).[85] The frequency at which these surface plasmons oscillate is known as the LSPR.

The LSPR bands for gold and silver are within the visible portion of the electromagnetic spectrum. For example, the LSPR of spherical 50 nm gold nanoparticles is at ≈530 nm, which falls into the green light range (495-570 nm). Accordingly, green light is absorbed and red light is transmitted thus causing suspensions of this size AuNP to exhibit red colors under visible light excitation. Similarly, the LSPR of spherical 50 nm silver nanoparticles is at ≈430 nm, which falls in the violet light range, leading suspensions of this size AgNP to exhibit green colors.[49, 84] The exact location of the LSPR band is highly dependent on the identity, size, shape, and aggregation state of the noble metal nanoparticle, and the suspension medium.[49, 82] Increases in size result in red-shifts (an absorption peak shift to a longer wavelength), while changes in shape result in more complicated effects. For example, the peak LSPR wavelength of 100 nm edge-length silver triangles is approximately 100 nm larger than that for 100 nm silver pentagons (pentagon length is defined as the distance between opposite corners), which is in turn 100 nm greater than that of 50 nm diameter silver spheres (Figure 2.1).[49] Asymmetric gold nanorods exhibit two LSPR bands

– one that corresponds to the longitudinal direction and the other the transverse direction of the rods.[86, 87]

In addition to shape mediated effects, changes in aggregation result in quantifiable red-shifts or blue-shifts.[88, 89] The potential development of secondary LSPR bands at longer wavelengths has been observed in end-to-end assembly of gold nanorods and at shorter wavelengths in side-by-side assembly of gold nanorods.[88] Although the physics are quite complex, in simplistic terms the new LSPR band is the result of dipole alignment between adjacent particles.[90] A tunable LSPR is crucial for sensing applications. The overlap between laser wavelength and the LSPR peak results in high SERS enhancement factors, which will be discussed later.[54] Changes in the LSPR band location can also elicit quantifiable color changes. Using 50 nm AuNPs as an example, aggregation results in the development of a new red-shifted peak at about 700 nm that falls in the red light range. Therefore, red light will be absorbed, while blue light will be scattered and the suspension color changes to blue. Because this color change is distinct and can be easily measured, it has been found to be highly useful for analyte detection.[51, 70, 91] A broad range of analytes have been detected solely on the basis of this color change.[52, 91-93]

Surface-enhanced Raman scattering (SERS) is another phenomenon that arises due to LSPR. A schematic illustrating the basic working principle of SERS is shown in Figure 2.2. Raman scattering is the inelastic scattering of photons by the vibrational chemical bonds of a molecule. The Raman spectrum is unique for each molecule due to the different vibrational modes present within it. Unfortunately, the Raman scattering signal is only 10^{-7} of the total scattering, which makes it challenging to use Raman to detect low concentration analytes. When a molecule is adsorbed on AuNPs or AgNPs, its Raman cross section can be enhanced by several orders of magnitude due to SERS. Two primary mechanisms are responsible for SERS: electromagnetic and

chemical. The former refers to the enhanced electromagnetic field near the nanoparticle surface, which is a long-range mechanism.[94] Long-range enhancements occur at greater distances away from the nanoparticle surface whose edge is schematically shown by the green circle in Figure 2.2. As shown in Figure 2.2, analyte molecules located within the green circle (position 2 and 3) exhibit clear Raman spectra, while analytes located outside the green circle (position 1) exhibit no detectable Raman signal. For example, the SERS signal of the CH_3 group of an alkanethiol molecule decreased by a factor of 2 when its distance from a SERS enhancing silver substrate increased from 0.8 nm to 2.5 nm.[95] The latter reflects charge transfer between the guest molecule and nanoparticle, which is a short-range mechanism.[94] Shorter-range enhancements only occur when an analyte is absorbed to a nanoparticle surface.

Studies to understand the SERS effect have shown that the largest SERS enhancements are produced by strongly interacting metal nanoparticles.[54, 96] Clusters of two or more nanoparticles give rise to an extinction spectrum consisting of multiple peaks and facilitate single-molecule SERS.[25] This effect can be attributed to the coupling of the intense localized electromagnetic fields on each nanoparticle produced by incident light excitation of the appropriate wavelength and polarization. The long range coupling of the electromagnetic fields, although it decays exponentially with particle distance, can extend to a distance of 2.5× the nanoparticle diameter.[96, 97] It is generally thought that significant Raman enhancements primarily occur within gaps smaller than 10 nm although the exact distance is still a subject of debate.[98-100] These localized areas are often referred to as 'hotspots' (Figure 2.2).[101] As shown in Figure 2.2, analyte molecules located within the hot spot (position 3) show a much stronger Raman signals than those located on an AuNP monomer surface (position 2). In addition to the gap between two adjacent nanoparticles, the sharp corners and tips of anisotropic plasmonic nanoparticles such as nanorods, nanoprisms,

and nanostars produce another type of SERS "hot spot".[102, 103] A recent study demonstrated that isolated single gold nanorods can generate strong SERS signals that approach those obtained in the gap between spherical particles.[104] Because of the importance of hot spots for SERS application, a substantial body of research has focused on the creation and maximization of the number and location of SERS hot spots.[105-108]

Other than SERS hot spots, several factors also show a significant influence on the SERS effect, such as nanoparticle type, shape, size, solution pH and so on.[109-115] AgNPs can generate stronger SERS intensities than AuNPs because the extinction coefficient of AgNPs can be 4× larger than AuNPs of the same size and shape.[116, 117] Anisotropic plasmonic nanoparticles show multiple LSPR modes and are suitable for use under different laser lines.[118-120] For example, gold nanostars (40 nm) show a second LSPR peak at 730 nm, while gold nanospheres (40 nm) show only one peak at 530 nm. Therefore, when excited by a 785 nm laser, the SERS intensity of gold nanostars is 2-3 orders of magnitude higher than that of gold nanospheres.[121] Nanoparticle size affects its LSPR, which determines its SERS intensity as well. A recent study shows even under random aggregation conditions, nanoparticle size still plays an important role in the Raman signal. With 785 nm laser excitation, AuNPs with size between 46-74 nm showed the strongest Raman signal. It has been shown that for elongated shape gold nanoparticles such as rods that the aspect ratio (length/diameter) is an important factor. Results suggest that enhancement can be two orders of magnitude greater when the plasmon band of the gold nanorod overlaps with the excitation wavelength.[122] These results indicate that it is necessary to carefully choose nanoparticle size according to the excitation laser wavelength.[123] Solution pH influences analyte adsorption to the NP surface and can subsequently influence its SERS signal.[109] For example, diclofenac sodium only exhibited a clear SERS spectrum under acidic and neutral pH conditions and not under

alkaline pH conditions due to electrostatic repulsion between its carboxylic group and the citrate-coated AgNP surface.[124]

Organic chemical detection is comparatively easy to achieve because small molecules can readily enter SERS hot spots. Pathogens, however, such as bacteria and viruses, are too large to enter SERS hot spots thus resulting in several orders of magnitude lower Raman enhancement factors. To circumvent this problem, a SERS tag is often employed.[64, 125] A SERS tag includes a recognition element, Raman reporter, and a signal transducer.[77] AuNPs and AgNPs are most commonly used signal transducers, while dyes with large Raman cross-sections are used as Raman reporters. Specific antibodies or aptamers against the target pathogens are used as recognition elements. Generally, a protection layer is needed for the Raman reporter modified nanoparticle to prevent the leakage of Raman reporter and improve the stability of the nanoparticle.

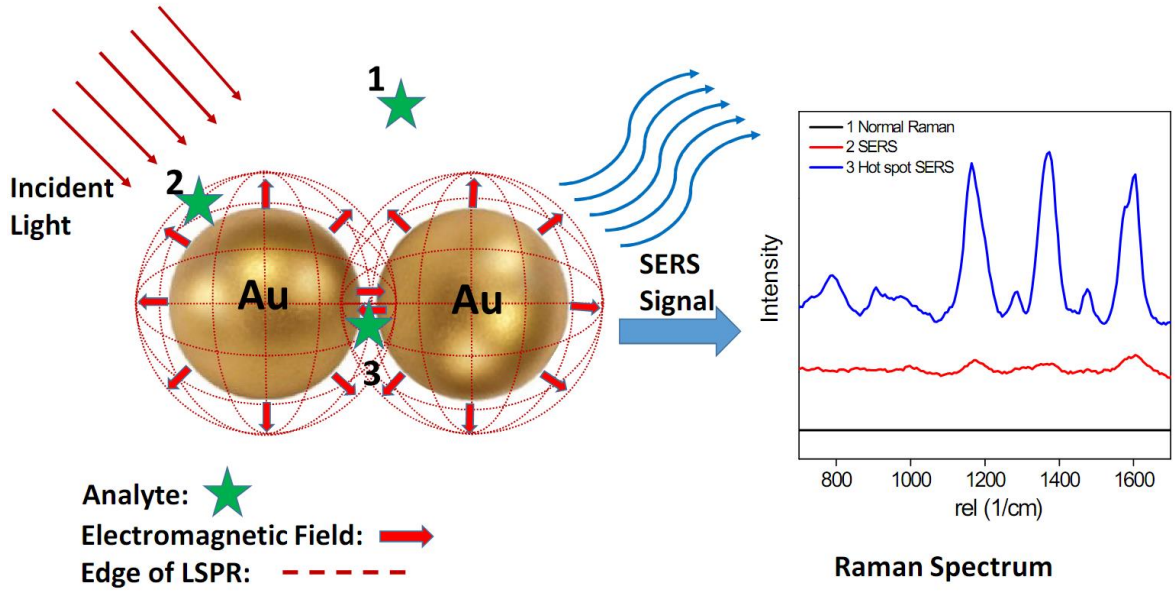

Figure 2.2 Schematic of SERS phenomenon for an organic analyte on AuNPs.

2.3 Colorimetric Detection

Perhaps the most convenient mechanism for a rapid, field-deployable contaminant detection assay would be to observe color changes with our naked eye. Because the LSPR of gold and silver colloids fall within the visible spectrum, color changes that occur due to changes in aggregation state have been exploited for colorimetric sensor fabrication. Colorimetric sensing of DNA using functionalized AuNPs was pioneered by Mirkin et al.[126] In that study, two batches of 13 nm AuNPs were functionalized with two non-complementary oligonucleotides and were then combined. After the addition of a target DNA duplex with two "sticky ends" (complementary to the oligonucleotides on each type of AuNP), the suspension color changed from red to purple due to DNA hybridization induced AuNP aggregation.[126] Both the oligonucleotide modification position and the AuNP size greatly influenced probe sensitivity. When the two batches of AuNPs were modified with 5'-oligonucleotide and 3'-oligonucleotide, respectively, single base imperfections could be detected.[91] Importantly, larger AuNPs (50 nm, 100 nm) were found to be more sensitive than smaller AuNPs (13 nm) because of their larger extinction coefficients.[127] In addition to oligonucleotide-gold nanoparticle (OGN) conjugates, oligonucleotide-silver nanoparticle (OSN) conjugates were also used as DNA probes. Because of the larger extinction coefficients of AgNPs compared with AuNPs, the detection limit for target DNA by the OSNs was 50× lower than with the OGNs.[128]

Aggregation induced by oligonucleotide hybridization is one example of a cross-linked colorimetric sensor. Similar sensor designs have been applied for detection of a range of biomolecules, heavy metal ions, and pathogens.[129] When the target directly binds to a recognition element on the nanoparticle surface, it induces aggregation and, in the case of AuNPs, a red to blue color change. Alternatively, the target can induce dissociation of nanoparticle aggregates by

competitively binding to the linker between nanoparticles. Under these conditions a blue to red color change is expected. For example, an aptamer-linked gold nanoparticle aggregate was developed for adenosine detection. Aptamers are single oligonucleotide strands of DNA or RNA that can bind pathogens, molecules, or even ions with high affinity and specificity.[130] Adenosine addition resulted in dissociation of the aptamer-linked aggregates due to its competitive binding to the aptamer linker between the two AuNPs. Following addition of adenosine, the suspension color changed from purple to red indicating the transformation from AuNP aggregates to monomers. This result was further indicated by the blue shift of the LSPR band in the UV-VIS spectrum from 700 to 522 nm.[131] A similar protocol was successfully applied for the fabrication of a cocaine sensor with a detection limit of 50-500 μM.[93] Recently this protocol was extended to development of a "smart hydrogel" sensor, where dissociation of the cross-linked hydrogel following addition of target resulted in the release of AuNPs to the solution and a change in color.[132]

In a non cross-linked detection protocol there is no hybridization between different gold/silver nanoparticles. In this case, aggregation/dissociation of the nanoparticles is achieved by decreasing/increasing the concentration of stabilizer on the nanoparticle surface. For example, an ultrasensitive colorimetric DNA probe (1 pM detection limit by eye) was developed by using a polyelectrolyte that forms conjugates with single stranded DNA. Following polyelectrolyte addition, AuNPs stabilized with single stranded DNA aggregated due to preferential binding between the aptamer and the polyelectrolyte, while AuNPs stabilized with target double stranded DNA remained stable.[52]

The detection protocols described above have been used for heavy metal detection due to their capacity to form strong complexes with chelators and other recognition agents. In this manner, a sensitive and selective probe for Hg^{2+} was fabricated by modifying the 13 nm AuNP surface with

mercaptopropionic acid (MPA). Hg^{2+} forms complexes with the carboxylate groups of MPA and induces AuNP aggregation. After addition of 2,6-pyridinedicarboxylic acid (PDCA) into the probe suspension, the selectivity for Hg^{2+} relative to other heavy metals was significantly improved. This result was attributed to the 100× higher complexation coefficient of PDCA for Hg^{2+} than for other heavy metals. The combined method enabled quantitative detection of Hg^{2+} over a concentration range of 250-500 nM with a limit of detection of 100 nM.[92] In addition to using toxic organic compounds as recognition elements, urine can also be used for Hg^{2+} sensing. The uric acid and creatinine in urine can synergistically bind to AuNPs as well as selectively adsorb Hg^{2+}. In addition to the low cost sensor fabrication, a low detection limit of 50 nM was achieved in this manner.[53] It has been shown that Zn^{2+} and Cu^{2+} can be detected using agglomeration and the resulting suspension color change of 20 nm chitosan-capped gold nanoparticles.[133] Chitosan is a well-known chelating agent for heavy metals and the presence of Zn^{2+} and Cu^{2+} can cause colloidal instability and loose aggregation (agglomeration) of gold nanoparticles. This phenomenon causes a rapid color change that is directly related to the heavy metals conentration. Pb^{2+} with a tunable detection limit of 100 nM to 200 µM has been detected following an aggregation-dissociation protocol. The DNAzyme-directed assembly of gold nanoparticles cleaves in the presence of Pb^{2+} and results in a blue to red color change (Figure 2.3A).[134]

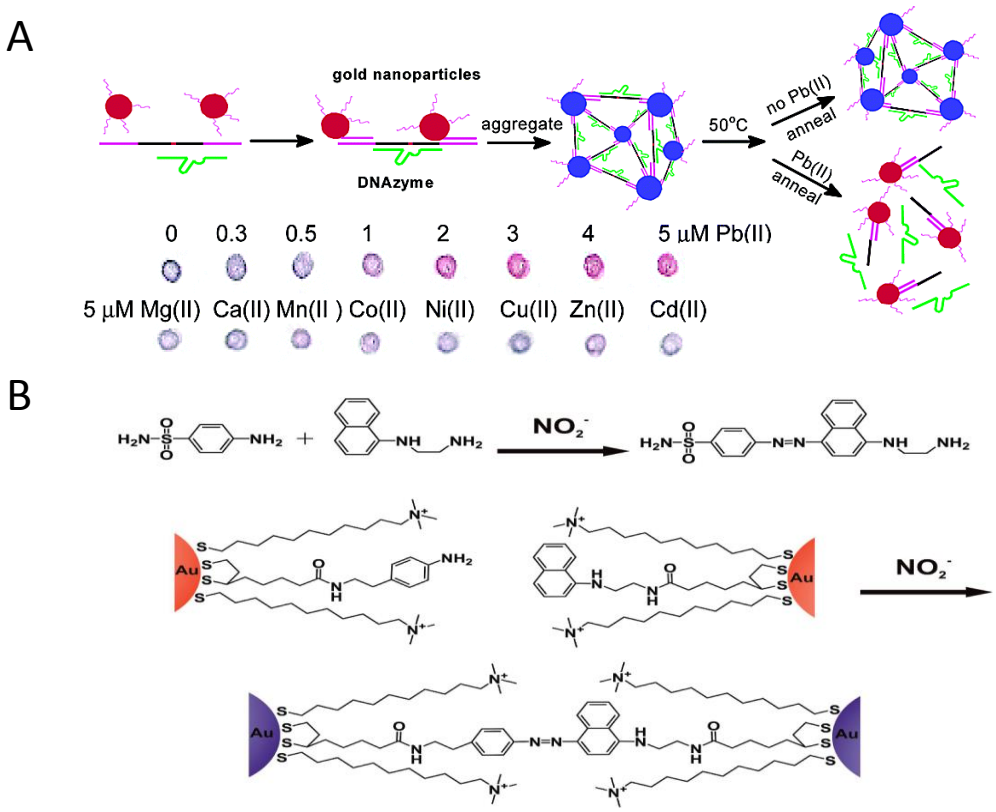

Figure 2.3 A) DNAzyme-directed assembly formation and cleavage mechanism of gold nanoparticles in a Pb^{+} colorimetric sensor; Reprinted with permission from J. Liu and Y. Lu, *J. Am. Chem. Soc.*, 2003, 125, 6642-6643. Copyright 2014 American Chemical Society. B) Schematic of the Griess reaction and Griess reaction induced aggregation of AuNPs. Reprinted with permission from W. L. Daniel, M. S. Han, J. S. Lee and C. A. Mirkin, *J. Am. Chem. Soc.*, 2009, 131, 6362-6363. Copyright 2014 American Chemical Society.

Nitrate and nitrite ions are two regulated contaminants in drinking water. A simple colorimetric method was developed for their detection based upon the Griess reaction (Figure 2.3B).[51] As shown in Figure 2.3B, two batches of AuNPs were functionalized with 5-[1,2]dithiolan-3-yl-pentazoic acid [2-(4-amino-phenyl)ethyl]amide (DPAA) and 5-[1,2]dithiolan-3-yl-pentazoic acid [2-(naphthalene-1-ylamino)ethyl]amide, respectively. Following nitrite ion addition, the amino group and naphthalene group were linked via an azide linkage, which then resulted in AuNP aggregation and the fading of the suspension color. The color change threshold could be controlled by adjusting the incubation time and temperature to meet the EPA standard (1 ppm for nitrite ion).

The same procedure was applied for nitrate detection after the nitrate ions were reduced to nitrite by nitrate reductase. The specificity of this probe is high enough that it is not affected by the presence of other inorganic ions (F^-, SO_4^{2-}, HCO_3^-, etc.) even when their concentrations are two orders of magnitude larger than that of nitrite.[51]

A majority of the plasmonic nanoparticle based colorimetric detection methods are based on crosslinking. However, non-crosslinking methods are also sometimes employed. A homogeneous method for the selective detection of Hg^{2+} and Ag^+ using Tween 20-modified AuNPs has been developed. Citrate-capped AuNPs were modified with Tween 20. In the presence of silver and mercury ions, citrate ions reduce Hg^{2+} and Ag^+ to form Hg^0 and Ag^0 on the surface of the AuNPs. This phenomenon was followed by Tween 20 removal from the NP surface and aggregation of AuNPs. The detection limit can be as low as 0.1 μM in the presence of NaCl and EDTA.[135] In another study, a sensor for quantitative detection and differentiation of two nitroamine explosives - hexahydro-1,3,5-trinitro-1,3,5-triazine (RDX) and octahydro-1,3,5,7-tetranitro-1,3,5,7-tetrazocine (HMX) was developed.[136] In this sensor, nitrite hydrolyzed from RDX and HMX reacted with 4-aminothiolphenol on AuNPs to form an azo dye with naphthylene diamine. Dye formation changed the LSPR of the AuNPs because of a charge-transfer interaction on the AuNP surface. The absence of a second LSPR peak indicated the color change was not due to AuNP aggregation, but instead due to dye formation. AuNPs improved the sensitivity of the probe but the mechanism responsible for this behavior was not clearly elucidated.

Some special detection protocols have also been used for heavy metal ion detection. Cr^{6+} can selectively etch the tips of gold nanorods (AuNRs) due to its strong oxidation state. Shortening of the nanorod induces a blue shift in its longitudinal LSPR band and a corresponding color change. Using this approach a detection limit of 90 nM was obtained.[137] This method does not require

aggregation or dissociation of nanoparticles and as such has been described as a non-aggregation method. Cu^{2+} could also etch tips of AuNRs in the presence of HBr. The Au^0 was oxidized to Au^+ and Cu^{2+} was reduced to Cu^+, which was subsequently oxidized to Cu^{2+} by dissolved oxygen (Figure 2.4A).[138] The presence of cetyltrimethylammonium bromide (CTAB) was the key for this redox reaction because it reduced the redox potential of Au^+/Au^0 from 0.93 V to less than 0.2 V. The decrease in aspect ratio due to etching resulted in a blue shift of the LSPR band and a color change from blue to red (Figure 2.4A). With this method, 50 nM Cu^{2+} was detected by the naked eye and 0.5 nM Cu^{2+} was detectable by UV-VIS.[138] The same type of protocol was applied for Hg^{2+} detection. In the presence of ascorbic acid, Hg^{2+} was reduced to Hg^0 and deposited on AuNR, which induced a color change from purple to blue green. The detection limit of Hg^{2+} was 800 pM. The Hg^0-AuNR can subsequently be used as a S^{2-} sensor because S^{2-} can exfoliate Hg^0 from the AuNR surface.[139]

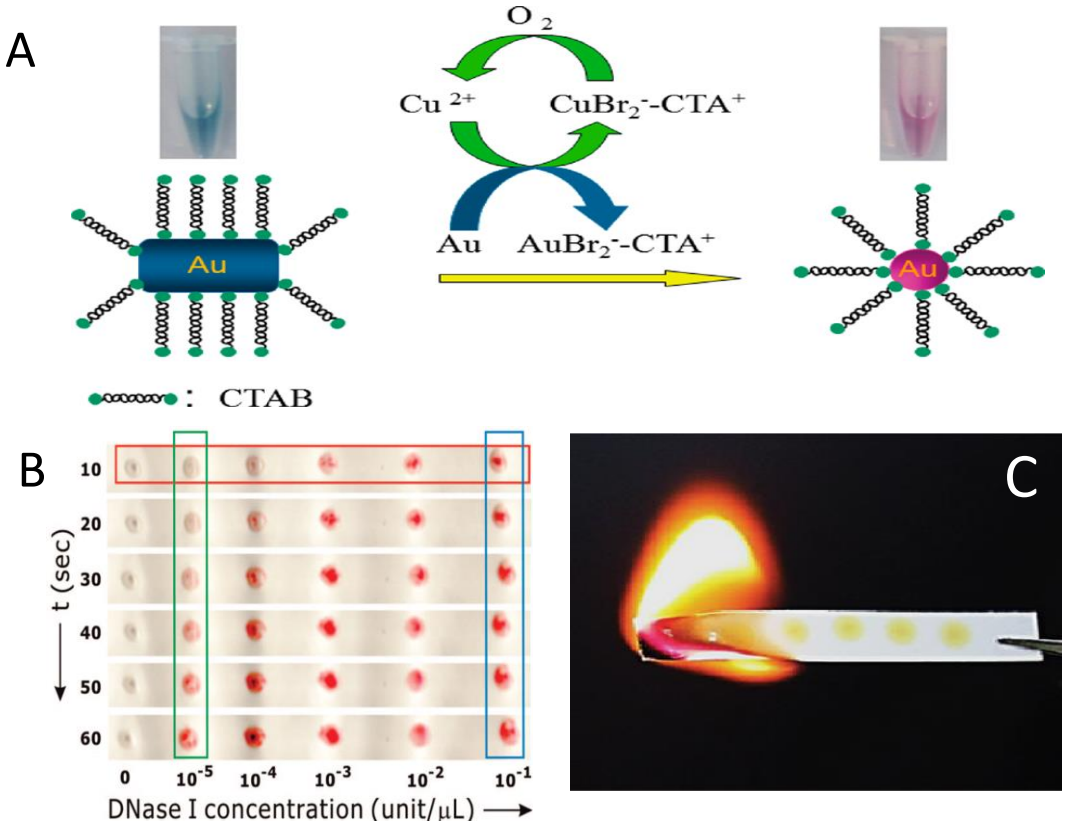

Figure 2.4 A) Schematic of colorimetric detection of Cu^{2+} by etching AuNR tips by Cu^{2+} in the presence of CTAB and HBr. Reprinted with permission from Z. Zhang, Z. Chen, C. Qu and L. Chen, *Langmuir*, 2014, 30, 3625-3630. Copyright 2014 American Chemical Society. B) DNA-hybridized AuNP aggregates on a hydrophobic paper after exposure to DNase I droplets. Reprinted with permission from W. Zhao, M. M. Ali, S. D. Aguirre, M. A. Brook and Y. Li, *Anal. Chem.*, 2008, 80, 8431-8437. Copyright 2014 American Chemical Society. C) Spent paper substrates are burnt to minimize hazardous chemical handling. Reprinted with permission from S. C. Tseng, C. C. Yu, D. Wan, H. L. Chen, L. A. Wang, M. C. Wu, W. F. Su, H. C. Han and L. C. Chen, *Anal. Chem.*, 2012, 84, 5140-5145. Copyright 2014 American Chemical Society.

For practical field applications, paper-based colorimetric sensors may be better than suspension-based ones due to their smaller volume, longer-term stability, and convenient handling and processing. Recently it has been reported that the protocols for suspension-based colorimetric detection can also be applied on a paper substrate.[140, 141] For example, DNA-hybridized AuNP aggregates that were spotted on paper can be redispersed into a droplet that contains endonuclease (DNase I), which could cleave hybridized DNA. Following endonuclease addition, the blue or

black spot on paper rapidly changed color to red and this color change could be discerned by the naked eye even at low nM endonuclease concentrations (Figure 2.4B).[141] It is notable that the paper used in these assays should be hydrophobic paper or surfactant-treated hydrophilic paper to avoid the rapid spread and drying of the droplet applied on the surface. In addition to drop-coated AuNP suspensions on paper, paper/AuNP composites can also be synthesized by a laser-induced thermal method. When 15 nm thin gold films coated on paper were exposed to KrF excimer laser irradiation, AuNPs (46 nm) formed on the paper surface with a high density of 318/μm^2. Following immersion into cysteine solution the color of the paper changed from light yellow to dark yellow. The paper could be burnt after use, which is a simple mechanism for hazardous waste disposal (Figure 2.4C).[142] Another paper-based analytical protocol has been reported for colorimetric sensing of Cu^{2+} by AgNPs functionalized with homocysteine and dithiothreitol. The LSPR peak intensity of AgNPs at 404 nm decreased while a new red-shifted band at 502 nm appeared as Cu^{2+} is added. Consequently, the color of the paper coated with AgNPs changed from yellow to orange or green-brown. A linear response was observed for the color intensity change as a function of Cu^{2+} concentration in the range of 7.8–62.8 μM.[143] Based on these results, we are confident that paper-based colorimetric LSPR sensors should have applicability for detection of a broad range of environmental pollutants.

2.4 SERS Detection

The SERS phenomenon was first observed in 1974 when the Raman signal of pyridine adsorbed on a roughened silver electrode was substantially enhanced.[144] SERS was subsequently proposed as an analytical technique for many organic compounds using substrates such as roughed Ag electrodes or Ag films on nanospheres (AgFON).[145, 146] However, the detection limits achieved

with these methods are high (above 1 μM), which limits their application. In 1997, however, single molecule detection was achieved for resonant dye molecules, such as rhodamine 6G (R6G) and crystal violet (CV) using AgNP colloids as SERS substrates.[24, 25] It was subsequently realized that aggregates in the colloid are responsible for the substantially enhanced Raman signal and the concept of the aforementioned SERS "hot spot", the gap between the aggregates, was proposed.

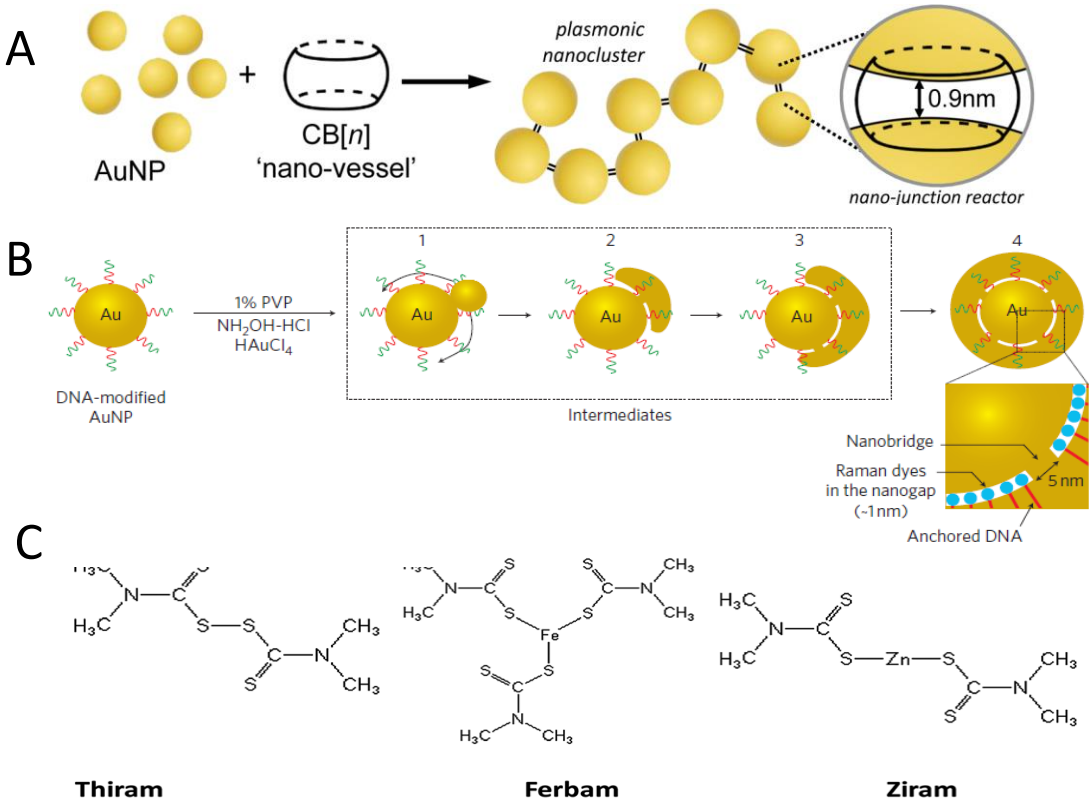

Figure 2.5 A) CN[n] induced AuNP aggregation with a fixed sub nanometer gap; Reprinted with permission from R. W. Taylor, R. J. Coulston, F. Biedermann, S. Mahajan, J. J. Baumberg and O. A. Scherman, *Nano Lett.*, 2013, 13, 5985-5990. Copyright 2014 American Chemical Society. B) Formation of 1 nm gap between AuNP core and shell linked with a Au nanobridge. Reprinted with permission from D. K. Lim, K. S. Jeon, J. H. Hwang, H. Kim, S. Kwon, Y. D. Suh and J. M. Nam, *Nat. Nanotechnol.*, 2011, 6, 452-460. Copyright 2014 Nature Publishing Group. C) Chemical structures of three dithiolcarbamate pesticides. Reproduced from B. Saute, R. Premasiri, L. Ziegler and R. Narayanan, *Analyst*, 2012, 137, 5082-5087. With permission from The Royal Society of Chemistry. Copyright 2014 The Royal Society of Chemistry.

In the past decade, numerous research efforts have been devoted to create and maximize the number of "hot spots" within SERS substrates.[147-149] Adding salts or organic electrolytes to gold or silver colloid suspensions can induce aggregation and generate SERS "hot spots".[150] However, the aggregation process is random and thus hard to replicate. Recently, methods to generate highly reproducible and controllable SERS hot spots in suspension have been reported.[147, 151-153] For example, the supermolecule cucurbit[n]uril (CB[n]) can link AuNPs with a fixed gap of 0.9 nm and this molecule can also specifically capture target analytes within the hot spot (Figure 2.5A).[151] DNA-mediated gold nanogap particles have been synthesized, which contain a 20 nm gold core and 11 nm gold shell linked by a gold nanobridge (Figure 2.5B).[147] Dyes located in the 1 nm gap were quantitatively detected over an ultra low concentration range of 10 fM - 1 pM. Raman mapping results demonstrate that 90% of these nanoparticles show SERS enhancement factors between 10^8 and 10^9 – a range that is sufficient for single molecule detection.[147] Despite its excellent homogeneity, this nanoparticle is more appropriate for use as a SERS tag rather than as a SERS substrate due to the difficulty associated with getting analyte chemicals to diffuse into the nanogap.

For real applications, solid SERS substrates are often considered superior to suspension-based SERS due to the long term stability and transport and handling convenience that the solid substrates provide. Extensive research efforts have been devoted to making homogeneous solid SERS substrates using approaches such as electron lithography, focused ion beam lithography, and nanosphere lithography.[50, 56, 66, 114, 154-156] These top-down methods make highly ordered plasmonic nanostructures with tunable shape, size, and gap and have very high SERS enhancement factors.[157] However, these methods, especially electron lithography, can be quite expensive and are difficult to scale up. Recently reported nanoporous gold and gold/silver nanoporous films are

easy to make at large scale. After thermal treatment, the films wrinkled and created quasi-periodic nanogaps and nanotips, which act as SERS "hot spots". With these wrinkled films, single molecule detection of R6G was achieved.[56, 154] Recent studies find that covering Au nano-pyramid arrays with graphene can improve the SERS signal 10× due to the enhanced charge transfer.[158]

In contrast to the aforementioned rigid SERS substrates, flexible substrates such as paper-based SERS substrates are cheaper, easier to make, and can be applied for curvy surfaces.[159-165] A paper-based SERS swab was fabricated by simply dipping a filter paper in AuNR suspension. AuNRs were adsorbed efficiently onto the surface of filter paper due to the electrostatic attraction between the negatively charged cellulose and the positively charged CTAB-coated AuNRs. The biggest advantage of this SERS substrate is its ease of use for the collection of trace samples from a solid surface. By swabbing a glass surface contaminated with a 140 pg 1,4-benzenedithiol (1,4-BDT) residue, the chemicals were readily adsorbed on the paper surface and their Raman spectrum was easily obtained (Figure 2.6A).[160] Similarly, a star-shape μPAD whose fingers were coated with polyelectrolyte was fabricated (Figure 2.6B).[164] This μPAD showed the capability to separate chemicals based upon their charge and to concentrate the chemicals into the small volume of the tips (Figure 2.6B). For example, positively charged R6G readily moved to the finger tip coated with positively charged poly(allylamine hydrochloride), while it was retained at the entrance of the finger coated with negatively charged poly(sodium 4-styrenesulfonate). This μPAD exhibited a preconcentration factor of 10^9 for R6G and thus a super low detection limit of 100 aM was detected.[164] In addition to paper, electrospun nanofiber mats have also been used as the SERS substrate scaffold.[165, 166] For example, a AgNP/PVA (poly(vinyl alcohol)) membrane was fabricated by electrospinning AgNPs and PVA mixture. The bulk material and nanofibers coated

with AgNPs are shown in Figure 2.6C and D, respectively. 4-mercaptobenzoic acid (4-MBA) at a concentration of 10^{-6} M was detected using this SERS substrate.[166]

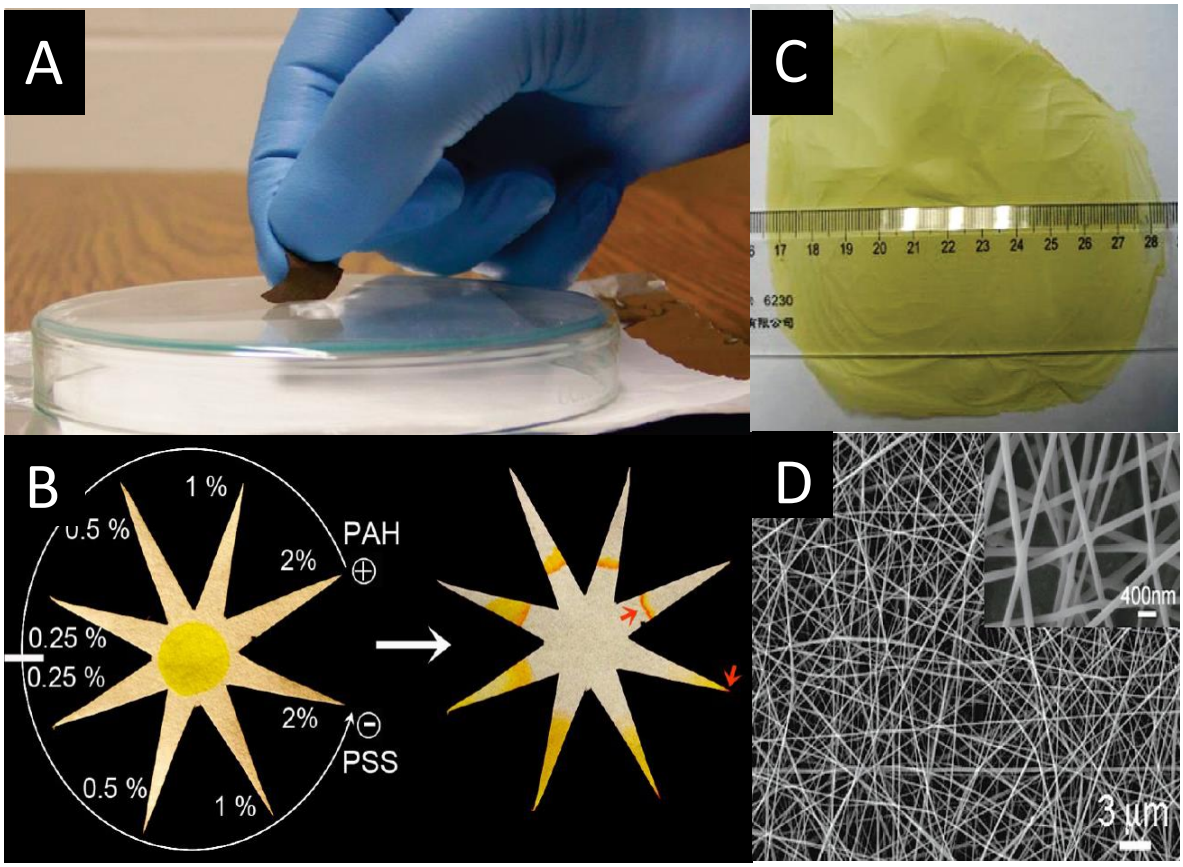

Figure 2.6 A) A glass with 1,4-BDT residue is swabbed by the paper-based SERS substrate; Reprinted with permission from C. H. Lee, L. Tian and S. Singamaneni, *ACS Appl. Mater. Interfaces*, 2010, 2, 3429-3435. Copyright 2014 American Chemical Society. B) A star-shape paper with eight fingers were coated by polyelectrolyte, which could separate and preconcentrate chemicals efficiently; Reprinted with permission from A. Abbas, A. Brimer, J. M. Slocik, L. Tian, R. R. Naik and S. Singamaneni, *Anal. Chem.*, 2013, 85, 3977-3983. Copyright 2014 American Chemical Society. C) The photo and D) SEM image of AgNP/PVA membrane fabricated by electrospinning. Reprinted with permission from D. He, B. Hu, Q. F. Yao, K. Wang and S. H. Yu, *ACS Nano*, 2009, 3, 3993-4002. Copyright 2014 American Chemical Society.

Although significantly improved average enhancement factors (EF) have been achieved (generally greater than 10^9) for Raman active dyes and other test materials, the application of such SERS substrates for ultrasensitive detection of organic pollutants are few.[167-172] The reason for this is that many organic pollutants are non-resonant under the laser excitation wavelengths (> 514 nm)

typically used for Raman spectroscopy. Accordingly, their Raman cross-sections are generally several orders of magnitude lower than those for the resonant dyes most commonly used for SERS substrate development.

SERS detection of pesticides with high affinity to AuNPs has been reported.[169, 172] Dithiolcarbamate pesticides - thiram, ferbam, and ziram were detected and differentiated by SERS using a gold nanorod suspension as the SERS substrate. The chemical structures of these three pesticides with similar chemical structures are shown in Figure 2.5C. They all contain sulfur groups that can form covalent Au-S bonds with the AuNP surface. To obtain high SERS intensity, gold nanorods whose longitudinal LSPR was well coupled with the laser wavelength were used as the SERS substrate. The detection limits of these three pesticides are 34 nM, 26 nM, and 13 nM, respectively, well below the EPA standards (17 μM, 10 μM, 23 μM).[172] These results indicate that for organic pollutants showing high affinity with gold or silver nanoparticles, SERS detection is feasible if the LSPR of the SERS substrate matches the excitation laser wavelength. An organophosphorus pesticide - paraoxon at a concentration of 10 nM was detected using a self-assembled gold nanoparticle film. The film is made by casting methoxy-mercapto-poly(ethylene glycol) (mPEG-SH) functionalized AuNP suspension onto a solid substrate. The AuNPs were closely packed on the substrate with 5 nm gaps. Self-assembly induced by mPEG-SH modification significantly improved the SERS intensity and homogeneity of the film.[169] This is a simple and cost-efficient method for SERS substrate fabrication. However, the author did not explain how the mPEG-SH-AuNP suspension and the analyte solution overcame the "coffee ring effect" when cast on a solid substrate.

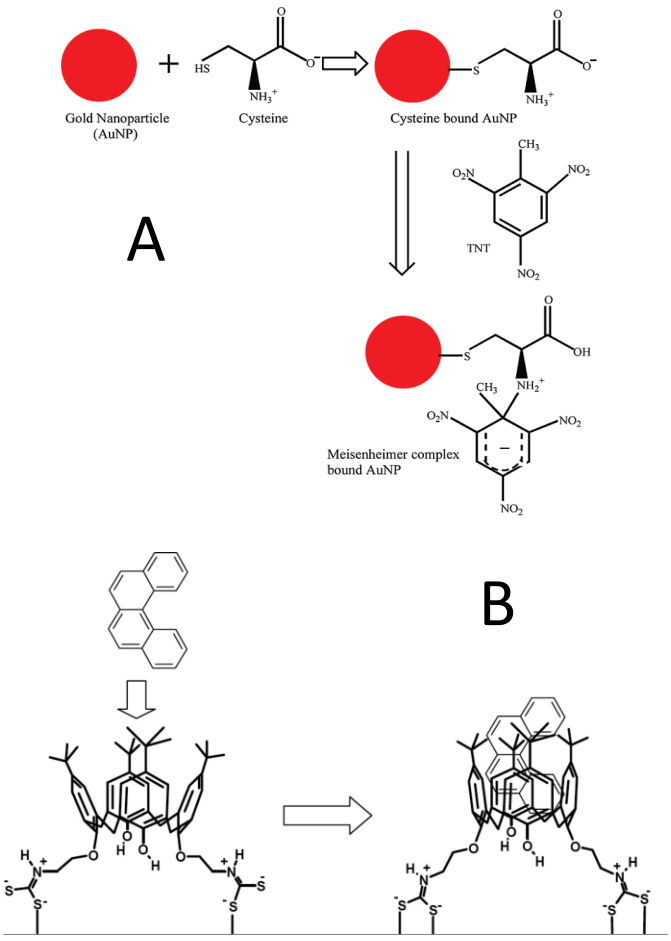

Figure 2.7 A) Trinitrotoluene (TNT) is captured by cysteine-functionalized AuNPs by form Meisenheimer complex; Reprinted with permission from S. S. Dasary, A. K. Singh, D. Senapati, H. Yu and P. C. Ray, *J. Am. Chem. Soc.*, 2009, 131, 13806-13812. Copyright 2014 American Chemical Society. and B) calix[4]arene links PAHs and AgNPs. L. Guerrini, J. V. Garcia-Ramos, C. Domingo and S. Sanchez-Cortes, *Anal. Chem.*, 2009, 81, 953-960. Copyright 2014 American Chemical Society.

A significant challenge that has limited SERS detection of organic pollutants is not only their generally small Raman cross sections, but also their low affinity to the NP surface. Therefore, methods to increase the affinity between pollutants and the gold/silver NP surface have been pursued to solve this problem.[173-178] One way to achieve this goal is through addition of a molecular trap on the gold/silver nanoparticle surface to specifically capture organic molecules. A thermal sensitive polymer poly-(N-isopropylacrylamide) (pNIPAM) was recently used as the trap for 1-naphthol (1-NOH). At a temperature of 277 K, pNIPAM exists in a swollen state, so the 1-NOH

trapped in it is far away from AuNPs, which then results in weak SERS signal. While at temperature of 333 K, pNIPAM shrinks to half of its swollen volume, thus bringing 1-NOH closer to the AuNP surface resulting in a substantial increase in the SERS signal.[174] This method enabled acquisition of the SERS spectrum of 1-NOH for the first time. However, the limit of detection for 1-NOH is high (10 μM). TNT was trapped on cysteine-functionalized AuNP surface by forming a Meisenheimer complex with cysteine (Figure 2.7A).[173] Electrostatic attraction between Meisenheimer complex-bound AuNPs and cysteine-bound AuNPs subsequently resulted in AuNP aggregation and the generation of a number of SERS hot spots. With this method, 2 pM TNT was detected in aqueous solution.[173] Dithiolcarbamate calix[4]arene was also used as a linker between AgNPs and polycyclic aromatic hydrocarbons (PAHs). The cup shape calix[4]arene is able to host hydrophobic PAHs and the dithiolcarbamate on the linker increases the affinity between the linker and the nanoparticle (Figure 2.7B).[176] This novel SERS substrate can achieve a limit of detections for four PAHs (pyrene, benzo[c]phenanthrene, triphenylene, and coronene) in the range between 10 nM to 100 pM.[176] Calixarene-functionalized AgNP embedded in silica film was applied in a flow cell designed for in situ monitoring of PAHs in seawater.[179-181] Limits of detection of 100 pM and 310 pM for pyrene and anthracene were achieved when artificial sea water spiked with PAHs traveled through the flow cell.[179] A field study using this SERS substrate was conducted in the Gulf of Gdańsk (Baltic Sea). The limit of detection for 12 different PAHs was 150 ng/L, which is comparable to the results obtained via GC/MS, thus indicating the SERS technique has potential for monitoring pollution events *in situ*.[181] Viologens have also been used as a PAH linker. Because of their high affinity to both AgNPs and guest PAHs, viologens could induce the aggregation of AgNPs and thus further increase the SERS intensity. With this method, 80 pyrene molecules were

detected, which is the lowest limit of detection ever reported.[175] The drawback of this method is the high background signal from the linker, which makes spectrum analysis challenging.

The SERS spectrum of the dioxin 2-benzoyldibenzo-*p*-dioxin (BDPD), a highly toxic compound, was first reported in 2009 using AgNPs loaded in poly(diallyldimethylammonium chloride) (PDDA) and poly-(acrylic acid) (PAA) film. This film was fabricated using a layer-by-layer method and subsequently impregnated with AgNPs. After drying in air, this SERS substrate showed a 5× higher Raman signal for 1-naphthalenethiol (1-NAT) than an AgNP suspension due to hot spot formation in this 3D structure. More importantly, the SERS dioxin spectrum at 10 nM was observed on this substrate although the signal was very weak.[171] This substrate works for dioxin partly because the PDDA-PAA can trap dioxin in the film thus creating the opportunity for dioxin contact with the AgNP surface. Recently, a detection limit down to three molecules was reported for atrazine detection via SERS.[182] This detection limit was achieved by directly adding a specific volume of 100 μM atrazine into AgNP colloid. This result demonstrates that SERS achieved similar detection limit (ppt) to sophisticated liquid chromatography-tandem mass spectroscopy (LC-MS/MS) and outperformed it due to its facile operation and fast measurement. However, this paper did not report a detailed characterization of the SERS substrate, the Raman measurement conditions, or the reproducibility of the data. The reason why the authors were able to achieve such a low detection limit is probably the addition of high concentrations of atrazine (100 μM) that induced AgNP aggregation. More research efforts are required in this field to discuss if SERS can be used for single or few molecule detection of organic pollutants in environmentally relevant samples.

To facilitate on site pollutant detection, a portable Raman instrument integrating a SERS sensor is highly desired.[183, 184] Recently such an instrument containing a silver dendrite SERS substrate

was developed for pesticide detection. The large laser spot of 2 mm minimizes SERS intensity variation among parallel samples. A pesticide - ferbam with concentrations of 0 ppm, 4 ppm, 7 ppm, and 14 ppm was used as references indicating no risk, low risk, risk, and high risk, respectively. The self checking tests for the four references all passed, indicating this instrument shows potential for on site pesticide detection.[183] Combining microfluidic chips and SERS substrates in the portable Raman instrument is promising for real-time on site pollutant detection. With a micropillar array PDMS chip integrated in the instrument, complete mixing of the two confluents - AgNPs and pollutants (dipicolinic acid and malachite green) is achieved. Dipicolinic acid and malachite green were quantitatively detected with limits of detection of 200 ppb and 500 ppb, respectively.[184]

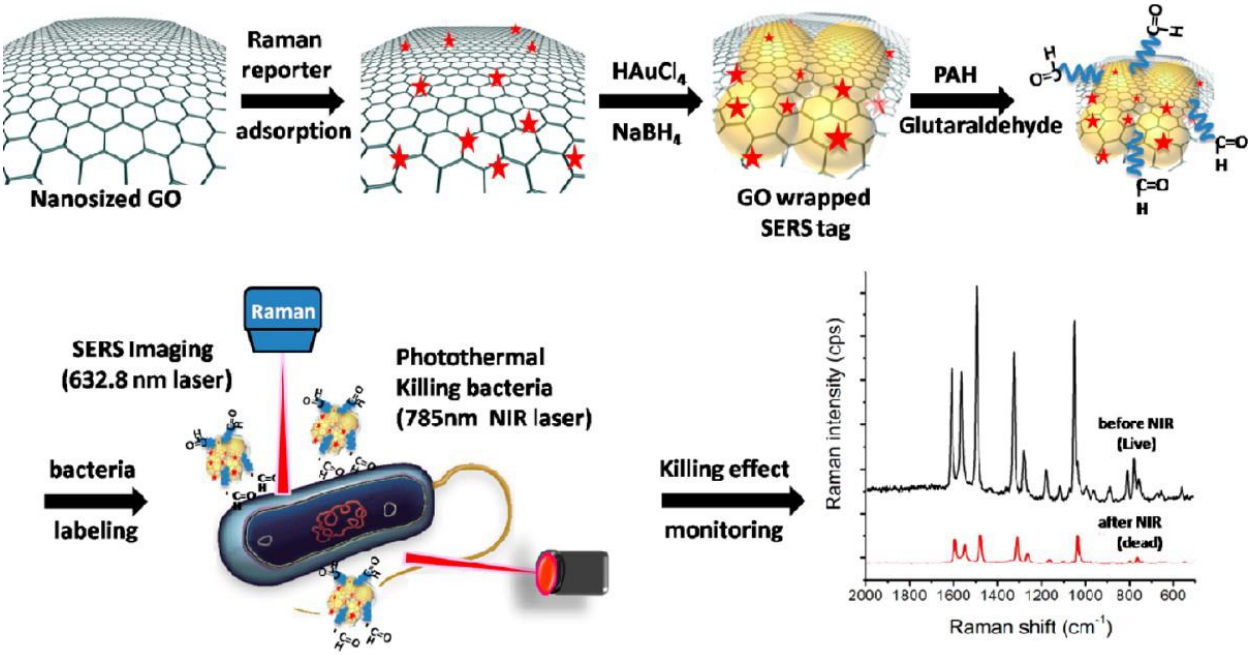

Figure 2.8 Schematic for AuNP/GO/Rubpy/GA SERS tag synthesis and its application for monitoring the photothermal ablation of bacteria. Reprinted with permission from D. Lin, T. Qin, Y. Wang, X. Sun and L. Chen, ACS Appl. Mater. Interfaces, 2014, 6, 1320-1329. Copyright 2014 American Chemical Society.

For larger targets, such as biomolecules, viruses, cancer cells, bacteria and protozoa, it is very difficult to directly acquire their SERS spectra by adding them to SERS substrates because they

are too big to fit into the hot spots due to their large size.[185, 186] Instead, a SERS tag is used to specifically bind the targets and the SERS spectrum of a Raman reporter functionalized on the SERS tag is then monitored.[125, 187] Raman reporter is usually a dye having a large Raman cross section. Ideal SERS tags are able to generate strong enough signals for single target detection. Interested readers are referred to a very good review for additional details on SERS tags.[64] Yang et al. fabricated a nanopillar-based SERS substrate to detect the macromolecule vasopressin, which was labeled by a Raman reporter 5-carboxytetramethylrhodamine. The nanopillar is made by depositing gold vapor onto etched silicon wafer. The coated gold film on the tip of silicon wire formed a pillar, which was functionalized with a vasopressin-specific aptamer. After exposure to vasopressin and subsequent drying, the intensified SERS signal of TAMRA was acquired due to the capillary force-driven aggregation of the nanopillars. The detection limit of vasopressin was reported to be 1 pM.[149] Recently, graphene oxide (GO) was used for SERS tag fabrication because of its capacity to significantly enhance the SERS signal.[188, 189] The schematic of this SERS tag synthesis is shown in Figure 2.8.[189] Different from the traditional SERS tag fabrication, Raman reporter - tris(2,2'-bipyridyl)ruthenium(Ⅱ) chloride (Rubpy) was first adsorbed on GO and subsequently AuNPs formed by *in situ* reduction of $HAuCl_4$ on GO/Rubpy. GO was able to not only enhance the SERS signal by two fold but also improve the colloid stability by wrapping around the small nanoparticle aggregates. AuNP/GO/Rubpy was subsequently functionalized with positively charged poly(allylamine hydrochloride) (PAH), which provided amine groups to link with the recognition element glutaraldehyde (GA). GA can bind to both gram-positive and gram-negative bacteria by crosslinking with the peptidoglycan layer on their surfaces. In addition to its single cell identification capability, this SERS tag can also be used for photothermal ablation of

bacteria when exposed to a 400 mW 785 nm laser. The decrease in the SERS signal can be used to monitor the bacterial ablation process (Figure 2.8).[189]

Although detecting large targets using SERS tags can achieve very high sensitivity, it is complex and costly to fabricate these tags. Most recently, the SERS spectrum of virus on SERS substrates without a SERS tag has been reported. This is called label-free SERS detection of virus.[34] Progress made in this promising area of research was recently summarized elsewhere.[34] Briefly, a highly sensitive and reproducible SERS substrate was fabricated by oblique angle deposition. The obtained SERS substrate contains tilted silver nanowire arrays. Virus was directly added to the SERS substrate and its SERS spectrum was readily acquired. Using this technique, three viruses - adenovirus, rhinovirus, and HIV were distinguished and even different strains of respiratory syncytial virus (RSV) could be differentiated. This approach was also applied to measure the SERS spectrum of RSV in its infected cell lysate although the background interference is strong. These results indicate that label-free detection of virus is feasible if SERS substrates are well designed. However, the weak signal, strong background disturbance, and subtle change of spectrum between different viruses make the data analysis challenging. Principle component analysis (PCA) and other chemometic approaches are often required to differentiate the viruses from the background and from one another.

2.5 Challenges

Although the rapid development of nanotechnology has facilitated substantial progress towards improved colorimetric and SERS detection, the high costs of sensor fabrication still impede their practical environmental applications. Development of low-cost and scalable detection platforms remains a big challenge. It is thus desirable to incorporate detection components within paper or

other sustainable materials without using costly lithography techniques. Paper-based colorimetric sensors can be used at home to monitor drinking water quality by simply dipping test strips into water. However, the sensitivity and resistance of these test strips to potential interferents such as drinking water disinfectants should be improved to make such a sensor truly useful. SERS sensors have the capacity to replace the complex lab assays currently used in water and wastewater treatment plants because of their simple sample preparation and rapid detection process. Suspension-based sensors may not be appropriate for use in real water samples since the colloids may not be stable in complex water chemistries and the challenges associated with long-term storage. As noted, paper-based SERS substrates have potential application. However, their SERS hot spot densities and affinities for specific organic pollutants currently do not meet real world application requirements. It is a considerable challenge to develop universal SERS substrates that have broad applicability to all of the organic chemicals of interest because the size, polarity, and isoelectric point of the chemicals determine their capacity to enter the hot spots on the SERS substrate. For on-site detection, portable SERS instrumentation is required and those systems currently rely only on near infrared lasers because of their ease of miniaturization. Accordingly, the SERS substrate must be optimized for application with near infrared lasers. Unfortunately, most organic pollutants are non-resonant at this laser wavelength, which makes their detection more challenging. Moreover, if we want to achieve real-time detection, the laser integration time must be very short, which further increases the difficulty. In addition to organic pollutant detection, SERS sensors also show potential for label-free pathogen detection. Since pathogens are generally too large to readily enter hot spots, the SERS substrate must have extremely high enhancement factor to make the pathogen spectrum visible. The reproducibility of SERS pathogen detection is also challenged because the contact between pathogens and Au or AgNPs may vary with time. The

steps required for development of low-cost and efficient SERS substrates for pathogen detection are an ongoing area of research focus.

Chapter 3 Preparation of Nanocellulose-Gold Nanoparticle Nanocomposites for SERS Applications

Haoran Wei,[1,2,3] Katia Rodriguez,[2,4] Scott Renneckar,[2,4] Weinan Leng,[1,2,3] and Peter J. Vikesland[1,2,3*]

[1]Department of Civil and Environmental Engineering, Virginia Tech, Blacksburg, Virginia

[2]Virginia Tech Institute of Critical Technology and Applied Science (ICTAS) Sustainable Nanotechnology Center (VTSuN), Blacksburg, Virginia

[3]Center for the Environmental Implications of Nanotechnology (CEINT), Duke University, Durham, North Carolina

[4]Department of Sustainable Biomaterials, Virginia Tech, Blacksburg, Virginia

*Corresponding author. Phone: (540) 231-3568, Email: pvikes@vt.edu

(This chapter has been published in ***Analyst***.[190] – Reproduced by permission of the Royal Society of Chemistry. The publisher - the Royal Society of Chemistry does not require formal reproduction permission when the article is used in the dissertation of the authors.)

Abstract

Nanocellulose is of research interest due to its extraordinary optical, thermal, and mechanical properties. The incorporation of guest nanoparticles into nanocellulose substrates enables production of novel nanocomposites with a broad range of applications. In this study, gold nanoparticle/bacterial cellulose (AuNP/BC) nanocomposites were prepared and evaluated for their applicability as surface-enhanced Raman scattering (SERS) substrates. The nanocomposites were prepared by citrate mediated *in situ* reduction of Au^{3+} in the presence of a BC hydrogel at 303 K. Both the size and morphology of the AuNPs were functions of the $HAuCl_4$ and citrate concentrations. At high $HAuCl_4$ concentrations, Au nanoplates form within the nanocomposites and are responsible for high SERS enhancements. At lower $HAuCl_4$ concentrations, uniform nanospheres form and the SERS enhancement is dependent on the nanosphere size. The time-resolved increase in the SERS signal was probed as a function of drying time with SERS 'hot-spots' primarily forming in the final minutes of nanocomposite drying. The application of the AuNP/BC nanocomposites for detection of the SERS active dyes MGITC and R6G as well as the environmental contaminant atrazine is illustrated. The results indicate the broad applicability of this nanocomposite for analyte detection.

3.1 Introduction

Nanocellulose consists of a bundle of *β-1,4*-glucan chains with a nanoscale radial diameter. In recent years, nanocellulose has attracted increasing attention due to its extraordinary mechanical, thermal, and optical properties.[191-193] Bacterial celluloses (BC) are a class of extracellular hydrogel

characterized by uniformly spaced nanocellulose layers that are produced by specific bacteria such as *Achromobacter*, *Alcaligenes*, and *Gluconacetobacter xylinus* in liquid culture medium.[194] Due to their reported ease of production as well as their biocompatibility and biodegradability, BCs are being increasingly tested for use as artificial blood vessels and for tissue engineering.[195, 196]

BC is an excellent host substrate for guest nanoparticles due to its large surface area, highly porous structure, and the abundant number of active hydroxyl groups on its surface.[197-200] BC-based nanocomposites combine the advantages of the nanocellulose and the guest nanoparticles and show excellent potential for many applications. For example, silver nanoparticle (AgNP)/BC nanocomposites exhibit superior antimicrobial properties relative to AgNPs alone and are being tested for wound dressing.[198, 201] Furthermore, platinum or palladium BC nanocomposites containing small, dispersed NPs are excellent catalysts for organic compound degradation.[197, 200] Recently, hydrothermally prepared gold nanoparticle (AuNP)/BC nanocomposites have been proposed for use as surface enhanced Raman spectroscopy (SERS) substrates for the detection of organic compounds.[202]

SERS is a term used to reflect the enhanced Raman scattering that occurs in the vicinity of AuNPs or AgNPs that is induced by the localized surface plasmon resonance (LSPR) of the particles.[62] SERS has been recently suggested as a tool for analyte detection due to its reported low detection limits (< ng/L) and relatively straightforward application.[146, 203] Although high signal enhancements have been achieved using delicate nanostructures fabricated by lithography, oblique angle deposition, Langmuir-Blodgett methods, and the recent glass capillary method, the development of cost-effective and scalable SERS substrates is highly desirable to make this technique feasible for practical applications.[114, 155, 204, 205] Accordingly, there is growing interest in the development of flexible SERS substrates that incorporate plasmonic nanoparticles.[163]

Compared with traditional rigid SERS substrates, such as silicon or glass, flexible SERS substrates that can change their shape should improve analyte collection from solid surfaces.[160]

Paper-based substrates are the most commonly used flexible SERS substrates.[160, 206] In most of these substrates pre-synthesized plasmonic NPs are adsorbed, printed, or written onto cellulose based-filter paper and then paper-based microfluidics are used to separate and concentrate analytes within a defined detection zone.[164, 207, 208] Compared with the cellulose in filter paper, however, nanocelluloses have much smaller diameters that are comparable with those of the guest NPs. For this reason, nanofiber-based papers or films can be expected to support higher NP loadings as well as improved homogeneity. Recently, electrospun polymer nanofibers have been used to fabricate high-performance SERS substrates.[166, 209-211] Compared with synthetic nanofibers, however, nanocelluloses are more sustainable due to their abundant natural sources. However, to the best of our knowledge, only two studies to date have explored the possible use of nanocellulose for SERS substrate fabrication.[202, 212] Unfortunately neither of the extant studies has reported satisfactory detection limits.

Herein we propose a method for the low-temperature synthesis of AuNP/BC nanocomposites by the *in situ* reduction of $HAuCl_4$ by sodium citrate in the presence of BC. AuNPs were selected for study due to their long-term stability relative to AgNPs. The performance of these nanocomposites as SERS substrates was primarily evaluated using malachite green isothiocyanate (MGITC) as a model analyte due to its capacity to form covalent bonds with the AuNPs through its isothiocyanate group.[213] Additional proof of concept experiments were also conducted with Rhodamine 6G as well as the herbicide atrazine.

3.2 Experimental Section

3.2.1 Chemicals and Materials

Gold chloride trihydrate ($HAuCl_4 \bullet 3H_2O$, reagent grade) was purchased from MP Biomedicals (Solon, OH). Sodium citrate tribasic dihydrate ($Na_3Cit \bullet 2H_2O$, ≥99.0%, ACS) and Rhodamine 6G (R6G, ≥99.0%) were purchased from Sigma-Aldrich. MGITC was acquired from Invitrogen Corp. (Grand Island, NY). Atrazine (purity 98.9%) was purchased from Chem. Service Inc. (West Chester, PA). All DI water used was ultrapure with resistance >18 MΩ-cm.

3.2.2 Preparation of AuNP/BC Nanocomposites

BC was prepared by incubating *Gluconacetobacter xylinus* in ATCC medium 459. This medium was prepared by sequentially adding 40 g fructose, 4 g yeast extract, and 10 g $CaCO_3$ to 800 mL DI water. After autoclave sterilization and cool down, the medium was inoculated with *Gluconacetobacter xylinus* rich medium (80:1 volume ratio) and incubated at 303 K for three days. The BC prepared via this approach was purified with 0.1 M NaOH under continuous stirring at room temperature for 5 days and it was then extensively washed with DI water until a stable pH value of 7 was attained.

Six AuNP/BC nanocomposites were prepared using different $HAuCl_4$ concentrations and $Na_3Cit/HAuCl_4$ ratios. We differentiate these nanocomposites using the following nomenclature: AuNP/BC-X-Y, where X represents the $Na_3Cit/HAuCl_4$ molar ratio and Y represents the applied $HAuCl_4$ concentration (in mM). In brief, pieces of BC hydrogel (2.5 cm × 2.5 cm) were placed onto bibulous paper for 20 s to wick away excess water and were then immersed in 5 mL of $HAuCl_4$ solution with final concentrations ranging from 1-15 mM. Subsequently, aliquots with volumes of 33-495 μL of 30 mM Na_3Cit solution were added. In each case, except for one sample with a

$Na_3Cit/HAuCl_4$ molar ratio of 3:1, the $Na_3Cit/HAuCl_4$ molar ratio was fixed at 1:1. The samples were then heated to 303 K for a given reaction time. For AuNP/BC-3-1, AuNP/BC-1-1, and AuNP/BC-1-2, the reaction time was fixed at 72 h. For AuNP/BC-1-5, AuNP/BC-1-10 and AuNP/BC-1-15, the reaction time was fixed at 2 h. These reaction times were chosen based upon visual observation that the suspension color did not change for longer reaction periods. The as produced AuNP/BC nanocomposites were extensively washed and kept in DI water. The samples were stable for ≈6 months with no discernible change in color or morphology.

3.2.3 Analyte Preconcentration/Adsorption

Generally, a piece of wet AuNP/BC nanocomposite (about 0.5 cm × 0.5 cm) was immersed in 5 mL MGITC, R6G, and atrazine solution for 48 h and then washed to remove unbound analytes. For a comparison, a piece of dry AuNP/BC film was also used for analyte preconcentration. The AuNP/BC nanocomposite was put on a glass coverslip and mounted on the sample stage for Raman test. Procedures for investigating adsorption capacity of BC for pre-formed AuNPs are: Pre-synthesized AuNPs (AuNP-ps) with a uniform size of 50 nm were synthesized using the seed-mediated growth method.[214, 215] A piece of BC hydrogel (2 cm^2) was immersed in 15 mL of AuNP-ps suspension (5.35×10^{10} NPs/ml) and shaken for 24 h. The UV-Vis spectra of the AuNP-ps suspension before and after adsorption were measured to quantify the adsorption capacity of BC for AuNP-ps. If all AuNP-ps were adsorbed by BC (no LSPR band in the UV-vis spectrum), the hydrogel was immersed in a second 15 mL of AuNP-ps suspension. This process was repeated for four cycles until a detectable AuNP LSPR band appeared in the UV-vis spectrum, thus indicating the adsorption process had reached saturation. The concentration of AuNPs remaining in suspension was calculated by dividing the LSPR band height of the AuNP-ps suspension prior to the sorption experiment by that after sorption.

3.2.4 Instrumentation

Raman measurements were collected with a WITec alpha500R Raman spectrometer using a 633 nm excitation laser. The signal was dispersed using a 300 groove/mm grating and collected with a Peltier cooled charge coupled device (CCD). A 10× objective and 1.43 mW laser intensity at the sample were used for all Raman measurements, unless otherwise noted. All the spectra were the average from 400 spectra in a Raman map except for those in section 3.3 "Influence of sample drying time", in which the spectra were obtained in one spot because it is challenging to scan an area without "losing focus" while a hydrogel is drying. For the study of the time-resolved Raman signal change, a single spectrum was acquired every 15 min until the sample was completely dry. Single spectrum was collected using an integration time of 0.5 s. The final condition is established to be the point when SERS intensity of MGITC stops significantly increasing. Under these conditions the nominal laser spot size at the sample was ≈10 μm. For the study of the influence of $HAuCl_4$ concentration on the Raman signal, three image scans were acquired and averaged for each sample. Each image scan covers a 100 μm × 100 μm area with 20 lines and 20 points per line. The integration time for each point was 0.01 s to reduce scan time and avoid overheating by laser in this area. Similarly, to illustrate the homogeneity of the AuNP/BC SERS substrates, five 100 μm × 100 μm image scans were acquired and averaged for each sample.

Extinction spectra of four AuNP/BC nanocomposites (AuNP/BC-3-1, AuNP/BC-1-1, AuNP/BC-1-2, AuNP/BC-1-10) were measured using a UV-Vis-NIR spectrophotometer (Cary 5000, Agilent). Prior to each measurement, the AuNP/BC nanocomposite was adhered to the inner wall of a cuvette and dried in air. This approach took advantage of the transparency of the AuNP/BC film and its capability to adhere to solid surfaces. The morphologies of the AuNPs within the dry films were characterized by field-emission scanning electron microscopy (FESEM,

LEO (Zeiss) 1550). Both secondary (InLens detector) and backscattered (RBSD detector) electrons were detected. The InLens mode provides contrast for both nanocellulose and AuNPs, while the RBSD mode provides sharp contrast between individual AuNPs. The average size of the AuNPs in a given AuNP/BC sample was determined using ImageJ software.

3.2.5 Measurement of AuNP/BC Thickness and Density

The thickness of the AuNP/BC-1-10 nanocomposite and dry film were measured using the optical microscope of the Raman instrument. For this purpose, visible light was focused on the nanocomposite surface using a 10× objective and then re-focused on the surface once the nanocomposite was completely dry. The objective travel distance was recorded as H_1. The 100× objective was focused on the edge of the dried AuNP/BC film and then on the glass coverslip. The distance the 100× objective moved was recorded as H_2, which corresponds to the thickness of the dried AuNP/BC film. The AuNP/BC nanocomposite thickness is H_1+H_2. The BC density (ρ_{BC}, mg/cm^2) was measured using the following procedure: a large BC film (64 cm^2) was weighed using an analytical balance (detection limit of 0.1 mg) and the mass (m) was recorded. The density was calculated by dividing m by the surficial BC area. AuNP densities within the AuNP/BC nanocomposites ($\rho_{Au,}$ mg/cm^2) were estimated by assuming 100% conversion of $AuCl_4^-$ into AuNPs and no loss of AuNPs during washing.

3.3 Results and Discussion

3.3.1 AuNP/BC Nanocomposite Synthesis and Characterization

The AuNP/BC nanocomposites were synthesized by *in situ* reduction of $HAuCl_4$ by Na_3Cit in the presence of BC at 303 K. Past studies have suggested that the hydroxyl groups within nanocellulose can reduce metal salts to metal NPs at 373 K.[202, 216] However, we found that this

reaction is quite slow at 303 K. To accelerate AuNP formation, Na_3Cit was added as an external reductant. Na_3Cit is widely used for AuNP production at both room and elevated temperature.[214, 217, 218] Within 4 h, the mixture of $HAuCl_4$+Na_3Cit+BC changed color from yellow to dark purple, while the mixture of $HAuCl_4$+BC remained yellow after seven days (Figure 3.1A). This result indicates that the AuNPs primarily form by Na_3Cit mediated reduction of gold salt and not by the action of the BC surface hydroxyl groups. AuNP/BC prepared with Na_3Cit reduction at room temperature contains much higher AuNP density than that prepared with BC surface hydroxyl group reduction at 373 K, indicating the much higher reducing efficiency of Na_3Cit than the BC surface hydroxyl groups (Figure 3.2A&B).

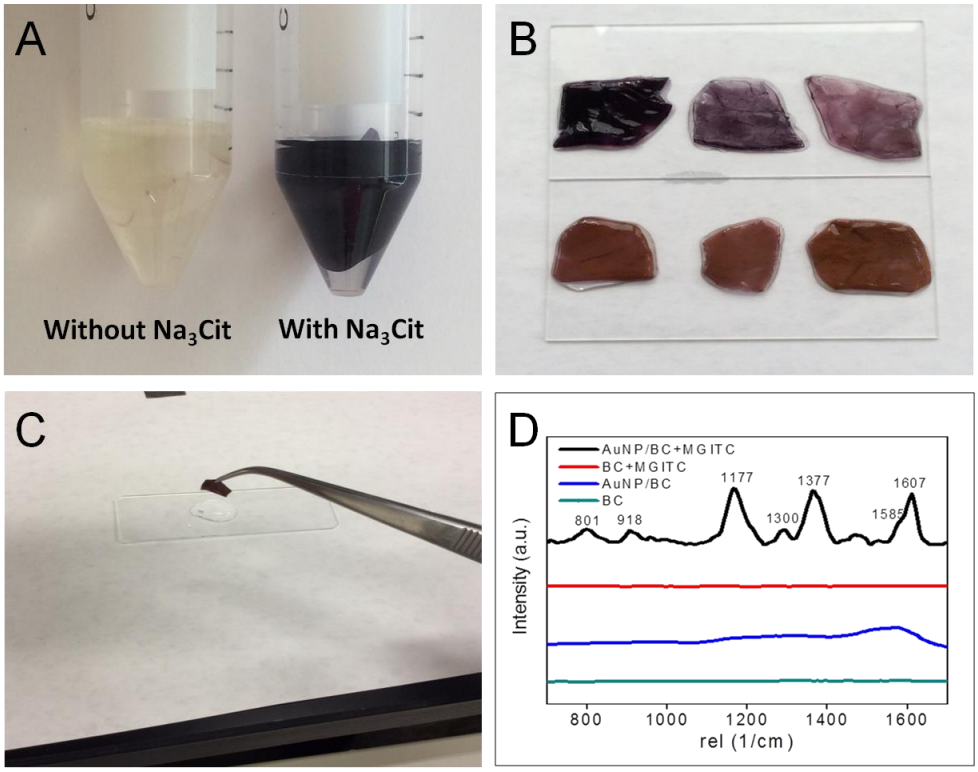

Figure 3.1 A) BC immersed in 1 mM $HAuCl_4$ with (right) and without (left) Na_3Cit for one week. B) AuNP/BC nanocomposites: top row from left to right: AuNP/BC-3-1, AuNP/BC-1-1, AuNP/BC-1-2; bottom row from left to right: AuNP/BC-1-5, AuNP/BC-1-10, AuNP/BC-1-15. C) AuNP/BC film readily adheres to glass coverslip, yet can be easily peeled off when water is added. D) Raman spectra of BC, AuNP/BC, BC+MGITC, and AuNP/BC+MGITC (MGITC concentration: 1 µM) following background subtraction.

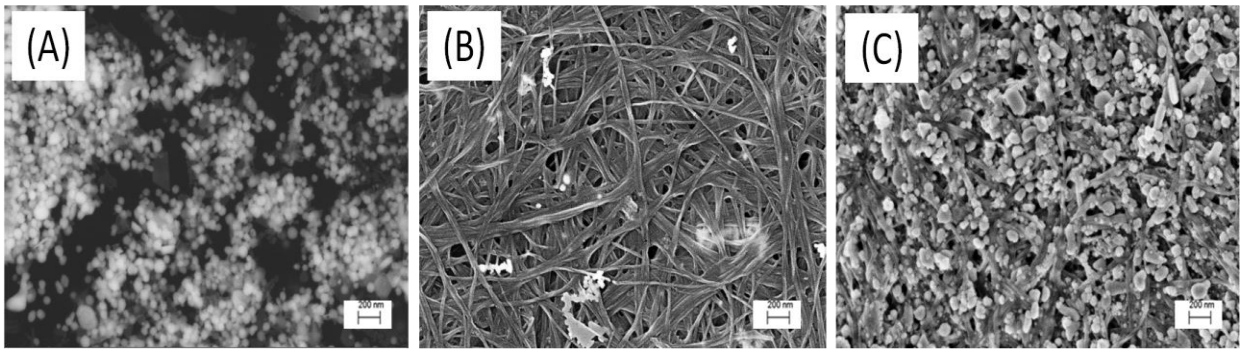

Figure 3.2 SEM images of AuNP/BC prepared with A) Na_3Cit reduction at room temperature, B) BC surface hydroxyl group reduction at 373 K, and C) Na_3Cit reduction at 373 K.

The AuNP/BC nanocomposites were prepared using different $Na_3Cit/HAuCl_4$ ratios and $HAuCl_4$ concentrations. The nanocomposites could be divided into two categories: 1) brown colored samples prepared with high $HAuCl_4$ concentrations (≥ 5 mM; bottom row in Figure 3.1B); and 2) samples prepared with lower $HAuCl_4$ concentrations (< 5 mM; upper row in Figure 3.1B) that are dark purple, blue, or red. Sample AuNP/BC-1-10 is exemplary of the first category. The AuNP/BC-1-10 suspension color changed from yellow to dark purple after 15 min indicating that AuNP formation was rapid. After 2 h, the suspension color faded while the nanocomposite became brown. The brown color indicates that high $HAuCl_4$ concentrations result in rapid nucleation, growth, and agglomeration of the AuNPs within the BC matrix. Sample AuNP/BC-3-1 is exemplary of the second category. Prior to Na_3Cit addition the $HAuCl_4$ solution containing BC had a yellow tint, while four hours after Na_3Cit addition the suspension color was black thus indicating AuNP formation. After 48 h, the suspension was pink and the BC had transitioned from colorless to dark purple, by 72 h the suspension was almost completely clear (Figure 3.3). Synthesis time of AuNP/BC can be reduced to 1 h by raising reaction temperature to 373 K. The AuNP/BC prepared at elevated temperature showed higher size and shape heterogeneity than that

prepared at room temperature (Figure 3.2A&C), so we focus on the room temperature synthesis procedure in this paper.

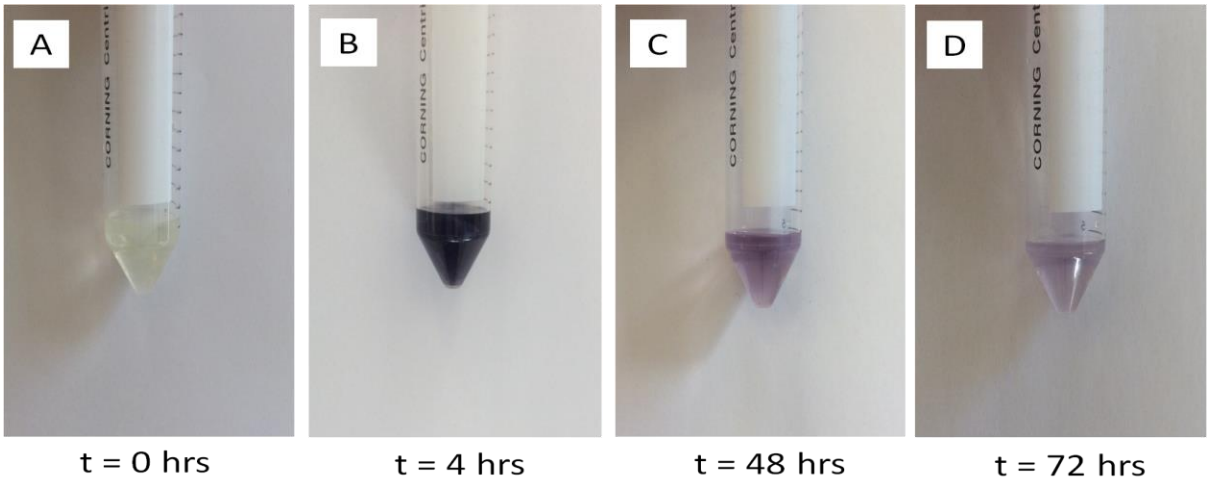

Figure 3.3 Residual AuNPs following immersion of BC in $HAuCl_4$ (1 mM) and Na_3citrate (3 mM) solution for A) 0 h, B) 4 h, C) 48 h, and D) 72 h. (In each case the BC hydrogel was removed from the tube prior to taking the picture.)

The time series experiments indicate that AuNPs that precipitate outside of the BC matrix are readily sorbed by BC over time. Similarly, pre-formed AuNPs can also be readily sorbed by the BC matrix (Figure 3.4A&B). As shown in Figure 3.4A&B, the UV-Vis spectrum of AuNP suspensions before and after sorption by the BC exhibited a single peak at 533 nm, which corresponds to the LSPR band of the 50 nm AuNPs. Following the first and second sorption cycles the UV-Vis spectra are straight lines, thus indicating complete removal of AuNP-ps by the BC (Figure 3.4B). After the third sorption cycle, 1.5% of the AuNP-ps remained in suspension. After the fourth sorption cycle, a prominent peak appeared at 533 nm (8.6% AuNP-ps remained), indicating complete surface saturation. Based upon this experiment the sorption capacity of BC for the AuNPs was calculated to be 5.82 (g AuNP/g BC). A SEM image of the final nanocomposite illustrates the incorporation of AuNP-ps within the BC matrix. Importantly, however, the AuNPs are not homogeneously distributed within the matrix and thus it was concluded that

nanocomposites made by this approach would not exhibit reproducible SERS responses. Nonetheless, this result demonstrates that BC has a very large sorption capacity for AuNPs (about 6× its own weight) and by extension this is probably true for other nanostructures.

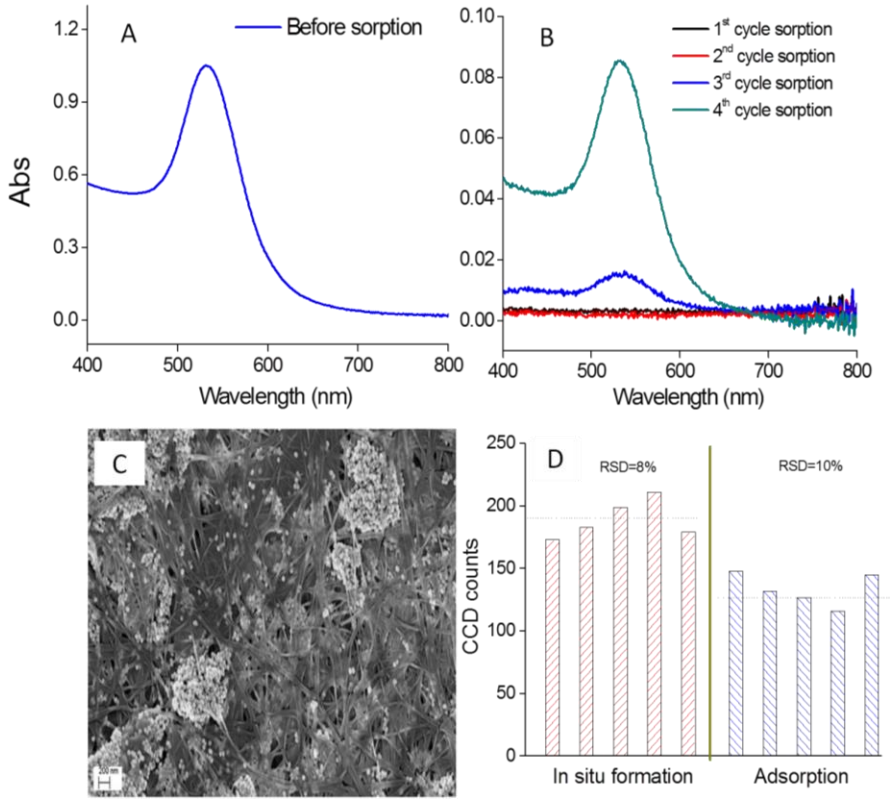

Figure 3.4 Experimental evidence for AuNP-ps uptake by BC. A) Initial extinction spectrum of 50 nm AuNPs in suspension. B) Extinction spectra of AuNPs in suspension following exposure to BC. After three exposure cycles there is a measurable LSPR band thus indicating the BC is reaching its sorption capacity. C) SEM image illustrated the entrainment of AuNPs within the BC matrix. Note that the AuNPs are not homogeneously distributed within the matrix. D) SERS intensity of MGITC average spectra in five randomly selected areas of in situ synthesized AuNP/BC and AuNP/BC prepared by sorption of pre-formed AuNPs. (Dotted line is the average Raman intensity of the five average spectra.)

Neat BC has a reported isoelectric point at pH 3.7[219] and our citrate-stabilized AuNPs exhibit a ζ-potential of -36±1 mV at neutral pH, a value consistent with the literature.[220] Because both BC and citrate-stabilized AuNPs are negatively charged it would not be expected for there to be an electrostatic attraction between them. Similarly, because we did not observe evidence of a redox reaction between surface hydroxyls on the BC and $HAuCl_4$ at our reaction temperature it seems

unlikely that AuNPs would be stabilized by the BC hydroxyl groups. The hydrogen bonding between carboxyl groups of AuNP surface coating and the hydroxyl groups of BC probably plays a key role in the adsorption of AuNPs on BC. Recently, however, it was observed that AuNPs readily sorb to unmodified cellulose filter paper.[162] In that effort, the large volume fraction of pores into which AuNPs can diffuse was determined to be the driving force for AuNP incorporation into the filter paper.[162] Considering the much smaller diameter of nanocellulose than the cellulose fibers in filter paper, BC should provide a much larger volume fraction of pores and therefore should house more AuNPs.

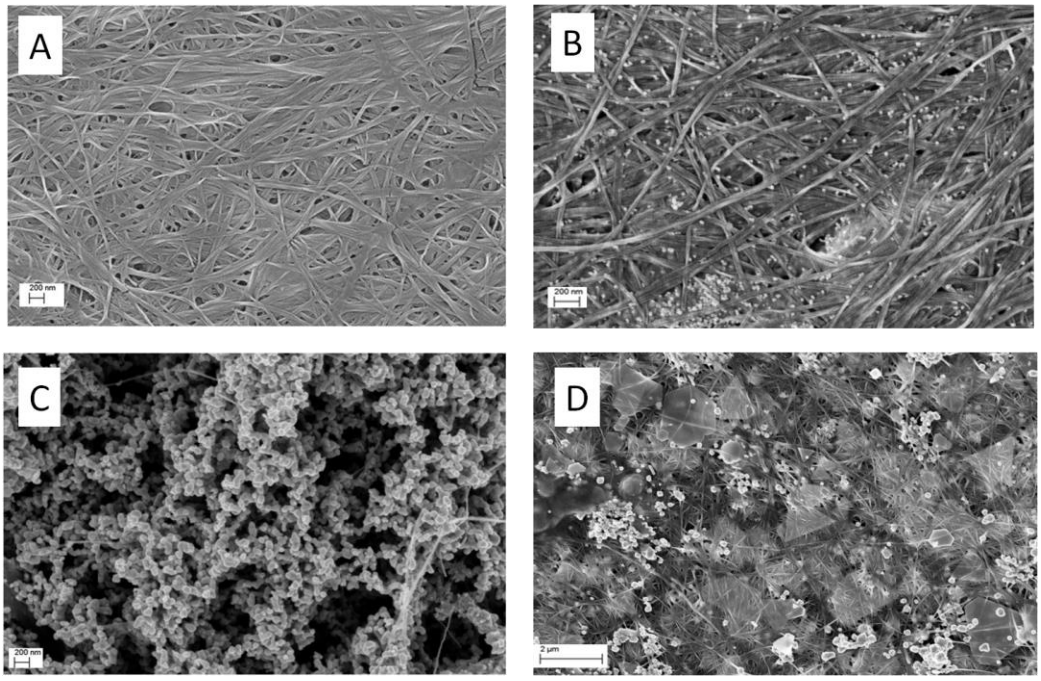

Figure 3.5 Secondary electron images of A) BC alone, B) AuNP/BC-3-1, C) AuNP/BC-3-5, D) AuNP/BC-1-10.

The morphologies of the AuNPs within the AuNP/BC films were characterized using SEM. Secondary electron imaging provides contrast for both the AuNPs and BC on the surface (Figure 3.5), while backscattered electron imaging provides contrast between individual AuNPs and facilitates imaging to depths of 500 nm. Initial characterization was done using secondary electron

imaging. As shown in Figure 3.5A, neat BC dry film consists of a network of interwoven nanocellulose fibers with approximate diameters of 50 nm. For AuNP/BC-3-1, gold nanospheres with a uniform size of 20.5±2.2 nm (n = 50) are well distributed within the BC matrix (Figure 3.5B). An increase in the initial $HAuCl_4$ concentration to 5 mM led to increased numbers of highly dispersed AuNP of size 71.8±14.3 nm (n = 50 Figure 3.5C), while a further increase in concentration to 10 mM (and a simultaneous decrease in the $Na_3Cit/HAuCl_4$ ratio to 1:1) resulted in nanoplate formation (Figure 3.5D). It is important to note that in general the nanocomposites produced via *in situ* reduction of $HAuCl_4$ were slightly more homogeneous and SERS-active than those produced via addition of preformed AuNPs (Figure 3.4 & Figure 3.5). This property suggests that *in situ* preparation could produce more SERS-efficient and reproducible SERS substrates.

Considering that AuNP size and morphology dictate the SERS signal intensity, we also utilized backscattered electron imaging to characterize our samples. As shown in Figure 3.6A, when the $Na_3Cit/HAuCl_4$ ratio was set at 1:1 the average nanoparticle size in the AuNP/BC samples was 47.3±10.8 nm (n = 50). This value was significantly larger than that for the higher $Na_3Cit/HAuCl_4$ ratio of 3:1. We also found that the initial $HAuCl_4$ concentration influenced the AuNP size. When the $HAuCl_4$ concentration was increased from 1 to 2 mM, the average nanoparticle size increased to 51.3±9.0 nm (n=50; Figure 3.6B) and the total number of AuNPs increased. A SEM image with higher magnification showed the relatively even distribution of AuNPs in BC matrix (Figure 3.2A). For $HAuCl_4$ concentrations higher than 5 mM the AuNP size distribution broadened and spherical particles with sizes in excess of 200 nm were found (data not shown). For excitation with either a 633 or a 785 nm laser these large particles are typically not as efficient as smaller AuNPs for SERS. It is noteworthy, however, that large triangular and hexagonal Au nanoplates also form under these reaction conditions (Figure 3.6C&D). Energy-dispersive X-ray spectroscopy (EDS)

results indicate the nanoplates are AuNPs (inset of Figure 3.6D). It has previously been reported that strong SERS enhancements occur at the vertices of gold (or silver) nanoplates.[221, 222]

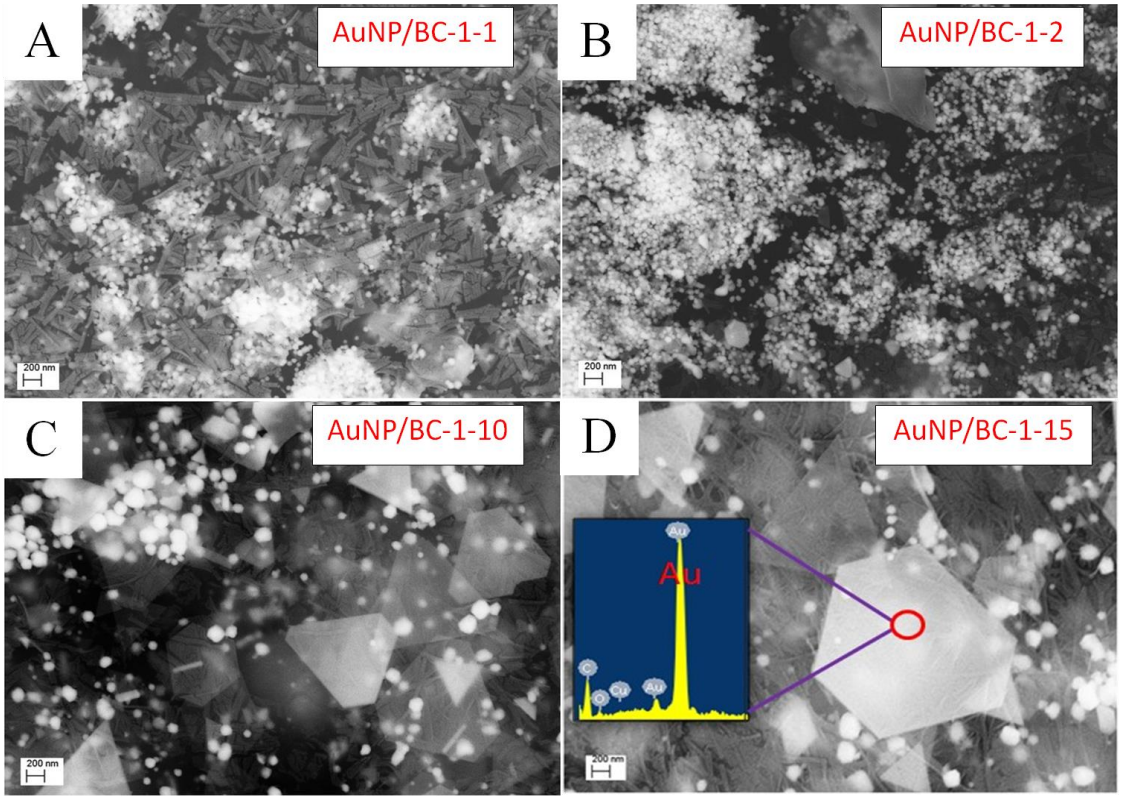

Figure 3.6 Backscattered electron images of AuNP/BC nanocomposites prepared with initial $HAuCl_4$ concentrations of 1-15 mM and a fixed $Na_3Cit/HAuCl_4$ molar ratio of 1:1. Inset of figure 2D is the energy dispersive spectroscopy (EDS) of the Au nanoplate.

The nanoplates formed in these samples are very thin (< 30 nm) and are transparent under the electron beam of the SEM. Hexagonal or triangular gold nanoplates are generally synthesized in the presence of shape-directing agents that selectively adsorb to the (111) crystal face and hinder crystal growth along that face.[223-226] In our syntheses, higher initial $HAuCl_4$ concentrations (Figure 3.6C&D) facilitate gold nanoplate formation, while lower $Na_3Cit/HAuCl_4$ ratios and lower initial $HAuCl_4$ concentrations facilitate gold nanosphere formation. These results are consistent with prior reports in the literature.[223, 225, 227] As illustrated in Figure 3.5D, the majority of the Au

nanoplates appear to be located between the nanocellulose layers. We therefore speculate that the nanoplates form within the confined space between adjacent nanosheets.

The plasmonic properties of the nanocomposites were probed via UV-Vis spectroscopy (Figure 3.7). As shown, BC does not absorb light across the wavelength range of 400-800 nm. In contrast, AuNP/BC-3-1, AuNP/BC-1-1, and AuNP/BC-1-2 all exhibit a narrow extinction band in the wavelength range of 533-549 nm that redshifts across these samples. The relatively narrow LSPR band is indicative of the general monodispersity of the AuNPs (as previously determined via SEM) and the red shift indicates that the AuNPs grow larger as the $Na_3Cit/HAuCl_4$ ratio decreases from 3:1 to 1:1 (i.e., AuNP/BC-3-1 to AuNP/BC-1-1). When the $HAuCl_4$ concentration was increased to 10 mM (AuNP/BC-1-10), the LSPR broadened substantially. We attribute this latter observation to a broader AuNP size distribution, the presence of gold nanoplates, as well as enhanced interparticle coupling.

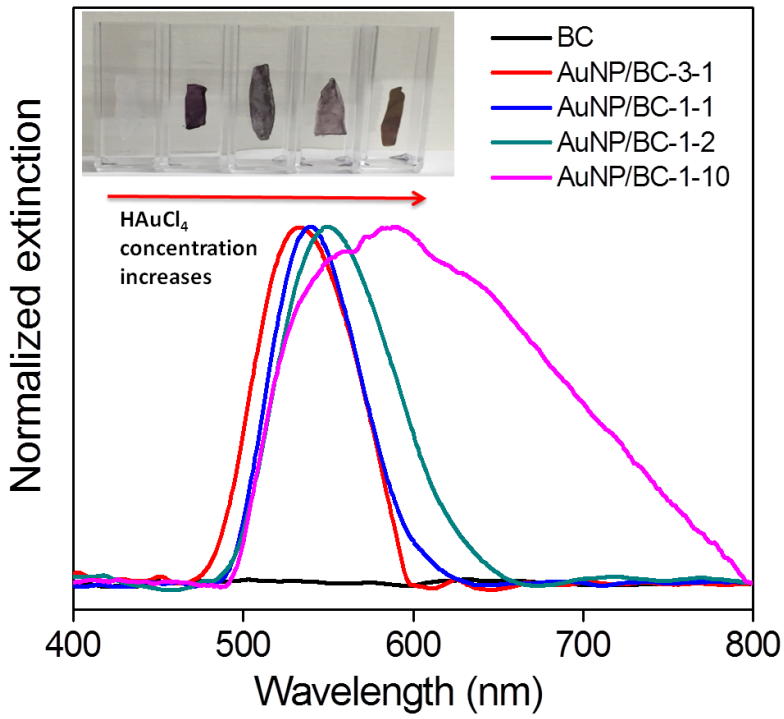

Figure 3.7 Extinction spectra of BC, AuNP/BC-3-1, AuNP/BC-1-1, AuNP/BC1-2, and AuNP/BC-1-10. The inset is a photograph of the five samples adhered to the inner walls of separate cuvettes.

The AuNP/BC nanocomposites obtained by this approach exhibit interesting physical properties. Initially they exist in the form of a hydrogel with a saturated thickness of 1.6±0.1 mm. When dried, the nanocomposite shrinks to produce a 6±1 μm thin film that is tightly bound to the underlying solid surface (Figure 3.8). When the film is wetted it can be easily peeled from the substrate (Figure 3.1C). To test their chemical resistance the AuNP/BC films were subjected to 20 min ultrasonic treatment. Over this period the films were stable and the AuNPs remained firmly attached to the BC substrate. The strong interaction forces between AuNPs and BC were attributed to the dipole-dipole interaction such as hydrogen bonding between the carboxyl groups of AuNP surface coating and hydroxyl groups of BC. When the $HAuCl_4$ concentration was below 2 mM, the nanocomposite film was semitransparent due to the minimal light scattering of nanocellulose.[192] The AuNP and BC densities (mg/cm^2) in the AuNP/BC-1-10 nanocomposite

were calculated using the methods described in the Materials and Methods section. The measured BC and AuNP/BC densities were 0.26 mg/cm^2 and 1.58 mg/cm^2. These data demonstrate that the nanocomposites produced by this approach are very light. For comparison, the weight of this BC substrate is roughly 1/60 of that of normal printer paper of the same area. AuNP suspension suffered from uncontrollable aggregation and flocculation at extreme pH while the AuNP/BC nanocomposites were expected to exhibit higher resistance to both acidic and alkaline solutions since AuNPs were restrained in BC matrix (Figure 3.9A). The strong SERS intensity of MGITC spectra acquired at different pH indicates that AuNP/BC can be used in both extremely acidic and alkaline conditions (Figure 3.9B).

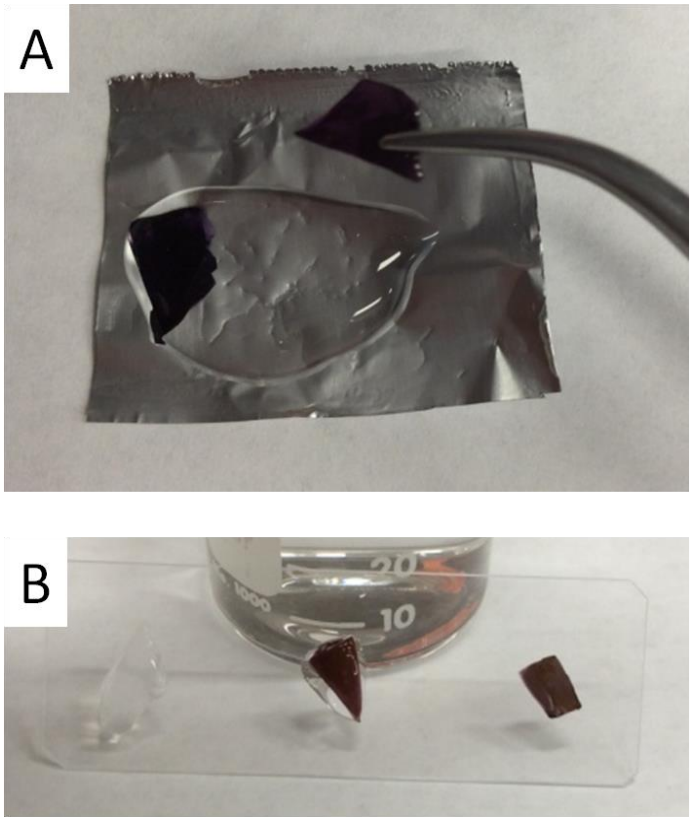

Figure 3.8 A) AuNP/BC-3-8 bound to aluminum foil and peeled off when wetted. B) *left*: BC hydrogel, *middle*: AuNP/BC-1-10 hydrogel, and *right*: AuNP/BC-1-10 film.

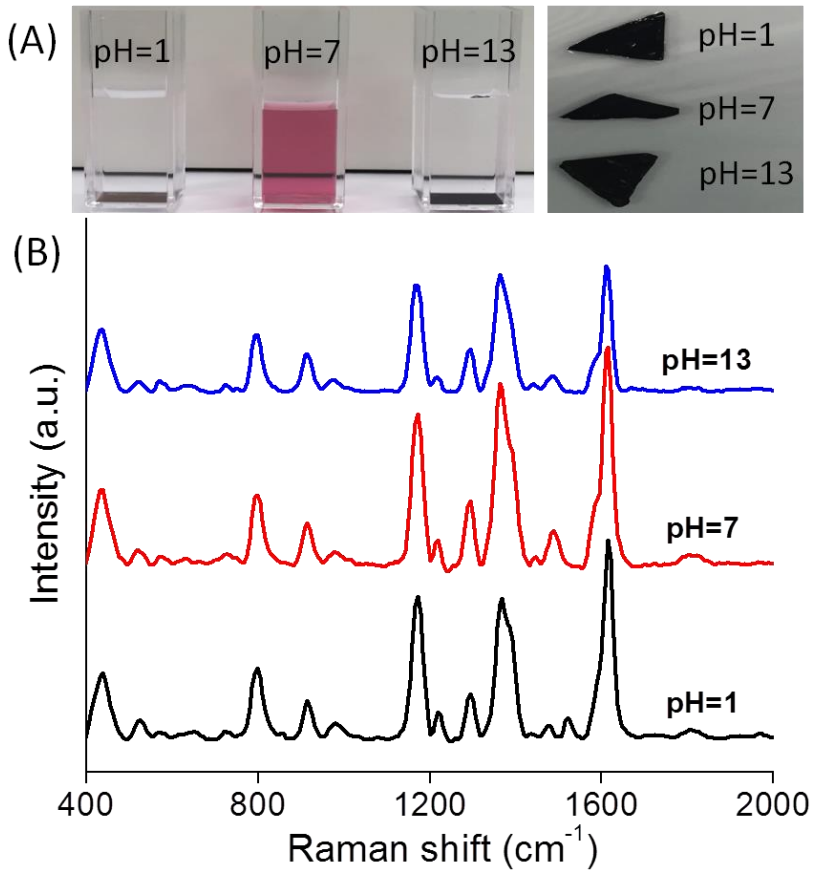

Figure 3.9 A) AuNP suspension at different pH after settling for 6 h (left) and AuNP/BC nanocomposites taken out of MGITC solutions with different pH (right). B) Influence of solution pH on MGITC SERS spectra obtained with AuNP/BC as the SERS subtrates.

3.3.2 AuNP/BC Nanocomposite SERS Evaluation

To illustrate the capabilities of the AuNP/BC films as SERS substrates we exposed the AuNP/BC-1-10 nanocomposite to 5 mL of 1 μM MGITC solution for 48 h. As a control, pure BC was also immersed in 5 mL of 1 μM MGITC solution for 48 h. Raman spectra of BC, AuNP/BC, BC+MGITC, and AuNP/BC+MGITC are shown in Figure 3.1D. No discernible Raman bands were observed for pure BC and BC+MGITC under 633 nm excitation. For AuNP/BC-1-10, however, there is a broad Raman band between 1000-1600 cm^{-1}. Furthermore, more detailed analysis of this spectrum indicates prominent peaks at 257, 734, 1016, 1326, 1591, and 2927 cm^{-1}. The Raman band at 257 cm^{-1} is attributed to covalent interactions between the AuNPs and Cl^-,

while the other prominent Raman bands are attributed to nanocellulose itself (1090 $cm^{-1;}$ υ(COC) glycosidic)[228, 229] or residual citrate/citrate oxidation products on the AuNP surface. Of the peaks attributed to citrate or citrate oxidation products the band at 2927 cm^{-1} is the most prominent. In Figure 3.10 we compare the spatial variation in the 2927 cm^{-1} signal to that of the 257 cm^{-1} band. As illustrated in this figure, the Raman signals from the citrate/citrate residuals and the AuNPs are highly correlated, thus indicating that the Raman signal of the citrate/citrate residuals is surface enhanced.

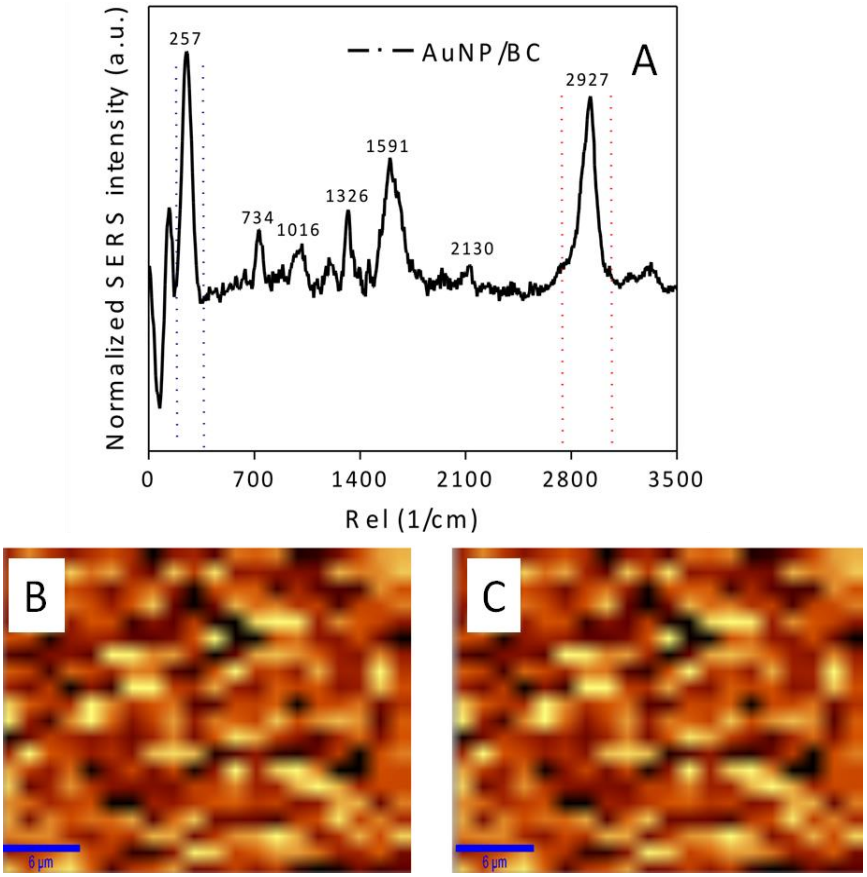

Figure 3.10 A) Average Raman spectrum of AuNP/BC-1-10 (no added MGITC); Raman maps of B) nanocellulose and C) AuNPs. Each map covers a 32 µm × 16 µm area with 20 lines and 20 points per line. The integration time for each point was 0.5 s. A 10× objective and 0.26 mW laser intensity were used. The maps were obtained by tracking the intensity of the peak at 2927 cm^{-1} (B) or the peak at 257 cm^{-1} (C).

Under our test conditions any residual citrate/citrate oxidation products adhered to the AuNP surface should not impede analyte detection for the following reasons: 1) the affinity between citrate and the AuNP surface is expected to be low, so citrate molecules will be relatively easily displaced by guest analytes; 2) the SERS signal of citrate/citrate oxidation products is weak (below 10 CCD counts); 3) Even if an analyte is separated from the AuNP surface by residual citrate/citrate oxidation products, its Raman signal can still be enhanced by the long range electromagnetic mechanism; 4) The fixed peak positions of residual citrate/citrate oxidation products make it easy to distinguish the analyte spectrum from the background. In support of these assertions we note that the SERS intensity of the synthesis residuals is minimal relative to the strong characteristic peaks of MGITC (1177 cm^{-1}, 1377 cm^{-1}, and 1607 cm^{-1}) for AuNP/BC exposed to MGITC (Figure 3.1D). At a laser wavelength of 633 nm, MGITC exhibits a resonance enhancement that facilitates higher SERS enhancements than non-resonant citrate/citrate residuals. Based upon these experiments it is reasonable to conclude that the peaks shown in Figure 3.1D reflect the SERS of MGITC.

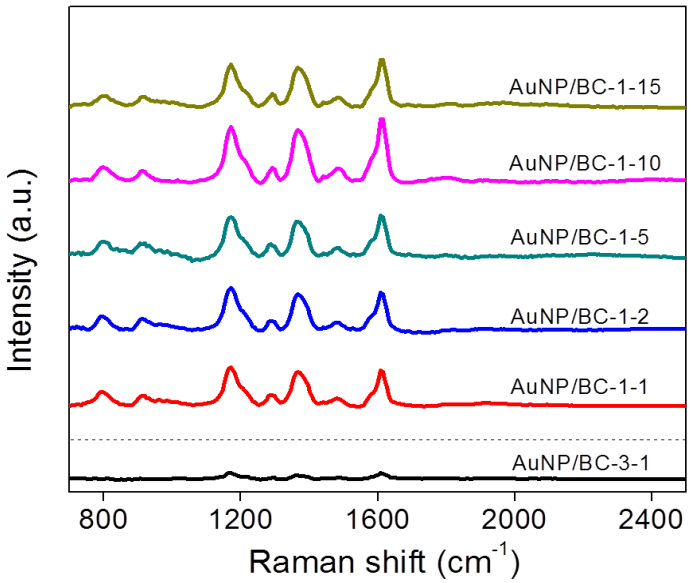

Figure 3.11 Raman spectra of MGITC (100 nM) on AuNP/BC film prepared with different concentrations of $HAuCl_4$ and different $Na_3Cit/HAuCl_4$ ratios (each spectrum is the average of three 100 μm × 100 μm image scans with each image scan the average of 400 spectra).

The $Na_3Cit/HAuCl_4$ ratio and the initial $HAuCl_4$ concentration are expected to have a significant influence on the capabilities of the nanocomposites as SERS substrates. Average SERS spectra obtained from 100 × 100 μm^2 image scans for AuNP/BC nanocomposites prepared under different conditions are shown in Figure **3.11**. A strong MGITC signal was distributed uniformly everywhere across the Raman map and average spectra from five randomly selected areas are almost the same (relative standard deviation (RSD) = 8%) thus illustrating the reproducibility of the SERS substrates (Figure 3.12). The small variation of SERS spectra (RSD=12%) obtained by three batches of independently prepared AuNP/BC samples indicated that the synthesis method is also reproducible (inset of Figure 3.12). For all samples prepared at a $Na_3Cit/HAuCl_4$ molar ratio of 1:1 the MGITC signal is readily observed. However, for the sample prepared at a $Na_3Cit/HAuCl_4$ molar ratio of 3:1, the MGITC spectrum, although discernible, is much weaker. When the initial $HAuCl_4$ concentration was increased from 1 to 15 mM the average SERS signal exhibits only minor fluctuations in intensity (as shown quantitatively in a plot of the height of the

peak at 1177 cm^{-1}; Figure 3.13). It is well known that SERS enhancements of gold nanospheres are a function of their diameter and size distribution (and thus the location and width of their LSPR) and that ≈55 nm is optimal for SERS under 633 nm excitation.[230] Given this knowledge, we might have expected that the nanocomposites with AuNPs primarily of this size would give the greatest signal enhancements; however, that expectation was not met. Instead, with the exception of the AuNP/BC-3-1 substrate containing 20.5±2.2 nm nanospheres that exhibited relatively little enhancement, all of the other substrates performed similarly. We attribute the similar performance of the different substrates to the production of large quantities of highly SERS active nanoplates as well as our use of areal scans that produce average spectra for a large sampling area. However, because AuNP/BC-1-10 exhibited the strongest SERS signal, it was selected for further study.

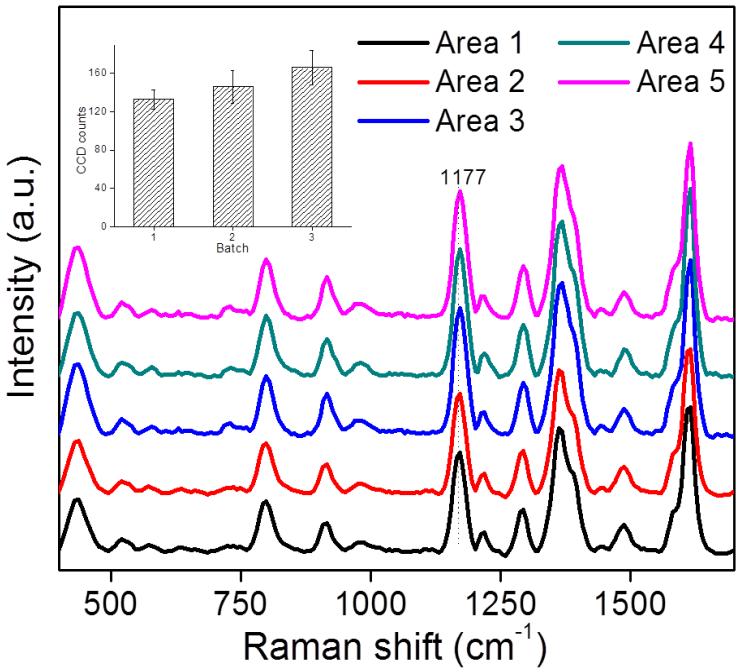

Figure 3.12 Average SERS spectra of MGITC (1 μM) on five randomly selected areas on AuNP/BC-1-10. Inset is the intensity of Raman band at 1170 cm^{-1} of SERS spectra obtained by three batches of independently prepared AuNP/BC samples.

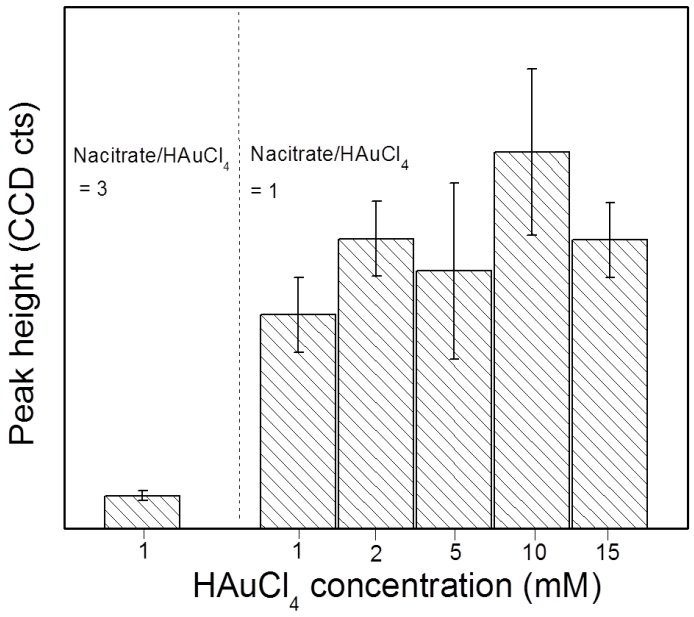

Figure 3.13 Raman signal intensity (denoted as the height of peak at 1170 cm^{-1}) of MGITC on AuNP/BC films prepared with different conditions of $HAuCl_4$ (each value is the average of three 100 µm × 100 µm image scans, each image scan is the average of 400 spectra, the error bars represent the standard deviation of replicate measurements).

3.3.3 Influence of Sample Drying Time

SERS "hot spots" are generally indicative either of small spatial gaps between adjacent AuNPs in which the electromagnetic fields of the individual nanoparticles couple and produce extremely large Raman enhancements or of large electromagnetic fields at the ends or vertices of isotropic nanostructures (i.e., nanoplates).[231] As noted previously, the AuNP/BC nanocomposites have a layered 3D structure. When these nanocomposites dry the interstitial water is eliminated and the distance between AuNPs in each layer decreases and the increased proximity of the AuNPs is expected to produce hot spots.[202]

We monitored the SERS signal of our AuNP/BC-1-10 nanocomposite as a function of drying time to obtain information about the kinetics of "hot spot" formation induced by nanocomposite deformation. For this purpose, the nanocomposite was exposed to 5000 nM MGITC for 48 h. After rinsing away unbound MGITC, the sample was mounted on the Raman stage and SERS spectra

were recorded every 15 min. As shown in Figure 3.14A, the SERS intensity increased slowly from 0 min to 45 min. During this period, the thickness of the AuNP/BC nanocomposite decreased by ≈91%. Further drying between 45-60 min., during which time the nanocomposite became completely dry, led to a 300% increase in the SERS intensity. Similar drying mediated trends in signal were observed when AuNP/BC-1-10 was exposed to MGITC concentrations between 4-1000 nM. As shown in Figure 3.14B, the drying induced signal enhancement (DISE; defined as the ratio of SERS intensity of the dry AuNP/BC relative to the SERS intensity when wet) generally increased slowly (0-15 min) and then increased more rapidly. Under our sampling conditions, the time between 15 and 60 min is when the AuNP/BC nanocomposite changes from nearly dry to completely dry. We note that the rate of drying of these samples was not completely consistent because the humidity of the environment was not controlled. Control of the humidity during drying can be expected to increase the sample-to-sample consistency and reduce drying time.

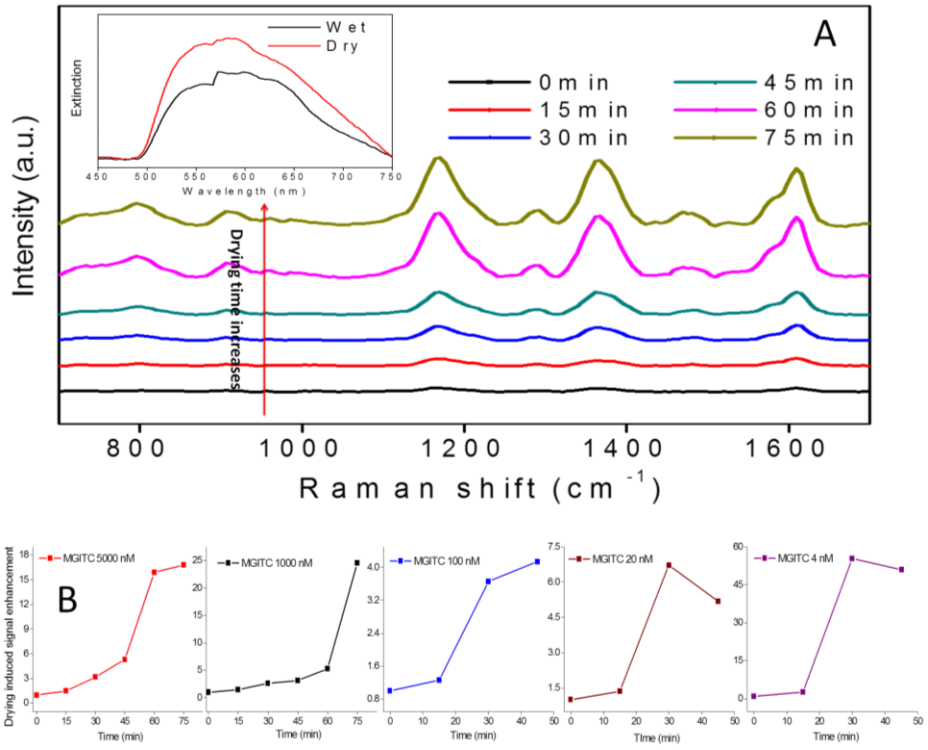

Figure 3.14 A) SERS intensity of AuNP/BC-1-10 exposed to 5000 nM MGITC (inset is UV-Vis absorption spectra of AuNP/BC-1-10 under wet and dry conditions). B) Drying induced signal enhancement as a function of drying time for 4 – 5000 nM MGITC.

In the lowest concentration samples we observed that extended laser illumination could result in a slight decrease in SERS intensity. This result is consistent with laser induced damage either to MGITC or the nanocomposite. A control experiment supports the latter hypothesis. When a fully dry AuNP/BC sample was illuminated by the 633 nm laser for 1 min, its SERS intensity decreased by 44% (Figure 3.15).

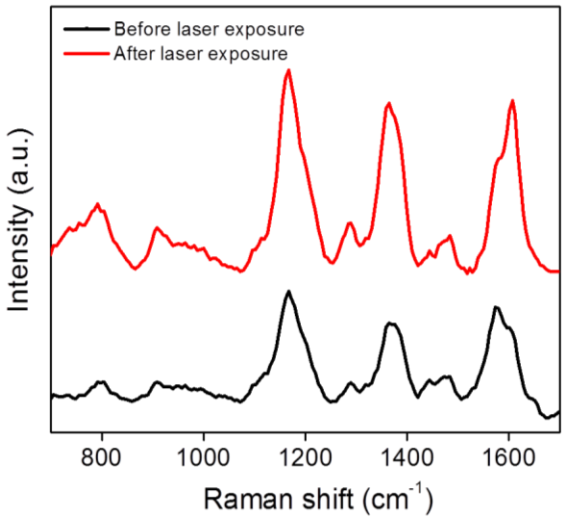

Figure 3.15 Raman spectrum of MGITC on AuNP/BC-1-10 before and after laser exposure for 1 min.

The measured increase in SERS intensity as a result of nanocomposite drying suggests that large numbers of hot spots form as a result of drying and that the majority of these hot spots form during the period when the AuNP/BC changes from being nearly dry to completely dry. Apparently only under completely dry conditions are large numbers of AuNPs in adjacent layers close enough to one another to produce strong SERS intensities. One alternative explanation for the observed increase in the Raman signal due to drying is the anisotropic shrinking of BC as it dries on the glass substrate.[232] When BC is dry, uniplanar orientation of the (101) crystallographic planes will take place. Therefore, the (101) planes where hydroxyl groups as well as AuNPs dominate are not twisted around the nanofibers, but rather positioned in the same direction and thus enhance the Raman signal.[232] We were able to exclude this latter hypothesis based upon comparison of UV-Vis spectra of the AuNP/BC-1-10 nanocomposite under wet and dry conditions (inset of Figure 3.14A). Under both conditions each sample exhibited a broad absorption in the range 500-700 nm that was centered at 589 nm – a wavelength that is well coupled with the laser wavelength (633 nm). Upon drying the signal intensity increased substantially, but did not red-shift, thus suggesting

a greater density of AuNPs and not drying induced alignment. This result demonstrates that the drying-induced Raman intensity enhancement can be attributed to the formation of SERS hot spots.

3.3.4 SERS Dynamic Range

To test the dynamic range of the AuNP/BC nanocomposite we examined its response towards MGITC at concentrations of 400 pM and 400 fM. As shown in Figure 3.16, the characteristic peaks of MGITC are easily observed for the dried 400 pM AuNP/BC sample, while no MGITC peaks could be identified when the sample was wet. We note that the MGITC spectrum in Figure 3.16A was obtained at randomly selected spots across the substrate. To further test the dynamic range we decreased the MGITC concentration to 400 fM and scanned a 100 μm × 100 μm area. For this sample the three most prominent peaks of MGITC were readily detected at discrete locations (Figure 3.17). Assuming the homogeneous distribution of MGITC across the nanocomposite, we estimate that only 24 molecules should be within the probe volume (≈10 μm^3), thus indicating the excellent SERS enhancement of our material.

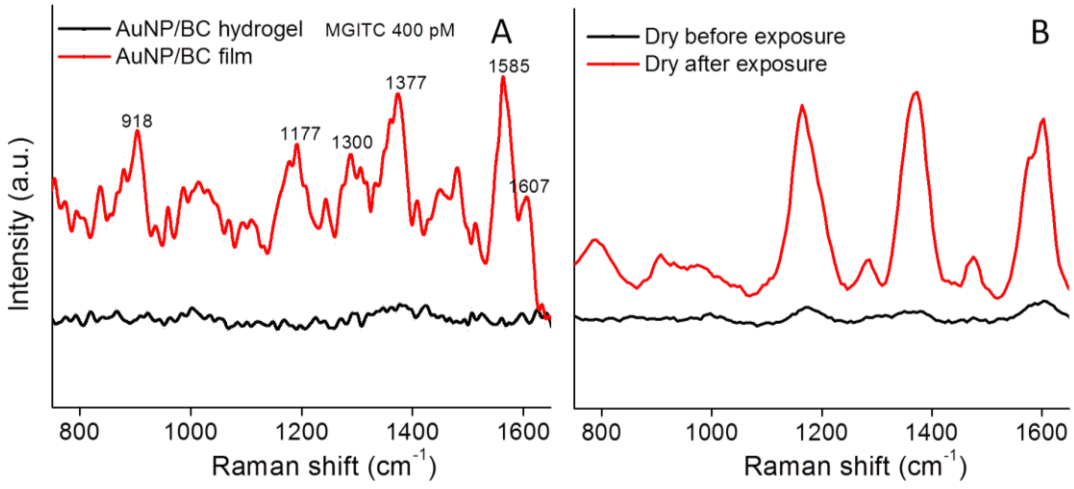

Figure 3.16 A) SERS of MGITC (400 pM) AuNP/BC-1-10 before and after drying and B) SERS of MGITC (20 nM) adsorbed on AuNP/BC before and after it was dried.

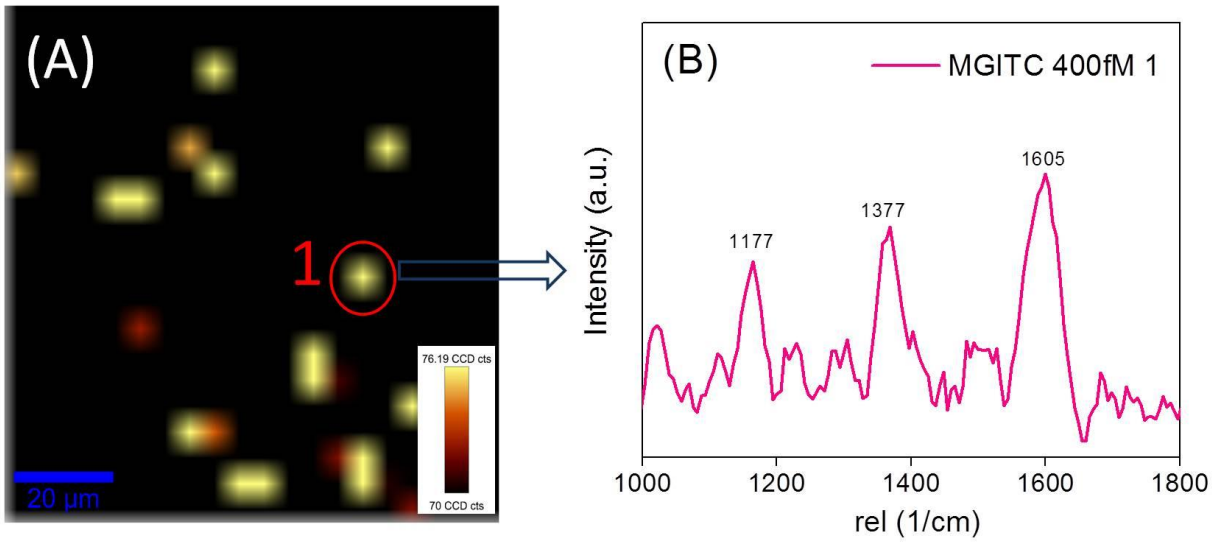

Figure 3.17 A) Raman map of MGITC (400 fM) (The maps were obtained by tracking the intensity of peak at 1177 cm^{-1}) ; B) Raman spectrum at spot 1 labeled in the Raman map.

3.3.5 Accumulation of Analytes

The AuNP/BC nanocomposite not only can act as a detection substrate, but also can accumulate MGITC from solution. Such an accumulation process can be significantly accelerated by sample agitation. The SERS intensity of the sample exposed to MGITC solution with agitation was 4× higher than that without agitation (Figure 3.18). To ensure MGITC not only adsorbed to the surface of AuNP/BC nanocomposite, we also exposed the dry AuNP/BC film to MGITC solution and measured its SERS intensity. As shown in Figure 3.16B, the SERS intensity of AuNP/BC exposed to MGITC as a nanocomposite was 6.7× higher than that exposed to MGITC as dry film. This result demonstrated that MGITC sorbs not only to the AuNP/BC nanocomposite top surface, but also into its bulk. The accumulation of chemicals and drying-induced formation of SERS "hot spots" makes this material very promising for trace pollutant detection in water.

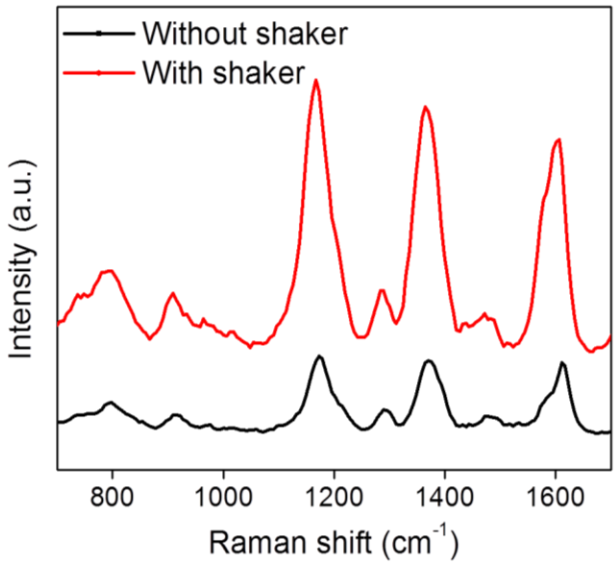

Figure 3.18 SERS of MGITC (1 μM) on AuNP/BC-1-10 exposed to MGITC solution with or without a shaker.

3.3.6 Additional Analytes

In addition to MGITC, which can form covalent bonds with the AuNP surface due to its isothiocyanate group, we also tested R6G, a positively charged dye that can adsorb to the AuNP surface via electrostatic attraction, to further test the performance of the AuNP/BC nanocomposites. The SERS intensity (indicated by the peak at 1188 cm^{-1}) generally increased with an increase in drying time (Figure 3.19A) thus indicating that drying induced signal enhancement also occurs for molecules with relatively low AuNP surface affinity. To illustrate this effect, we randomly scanned a 100 μm × 100 μm area exposed to a low R6G concentration (78 nM) and consistently observed a detectable R6G Raman signal (Figure 3.19B). This result demonstrated that there are numerous "hot spots" within the sample area. Even after excluding the highest intensity "hot spots" in the image, the average spectrum of R6G exhibited excellent signal to noise (Figure 3.19C).

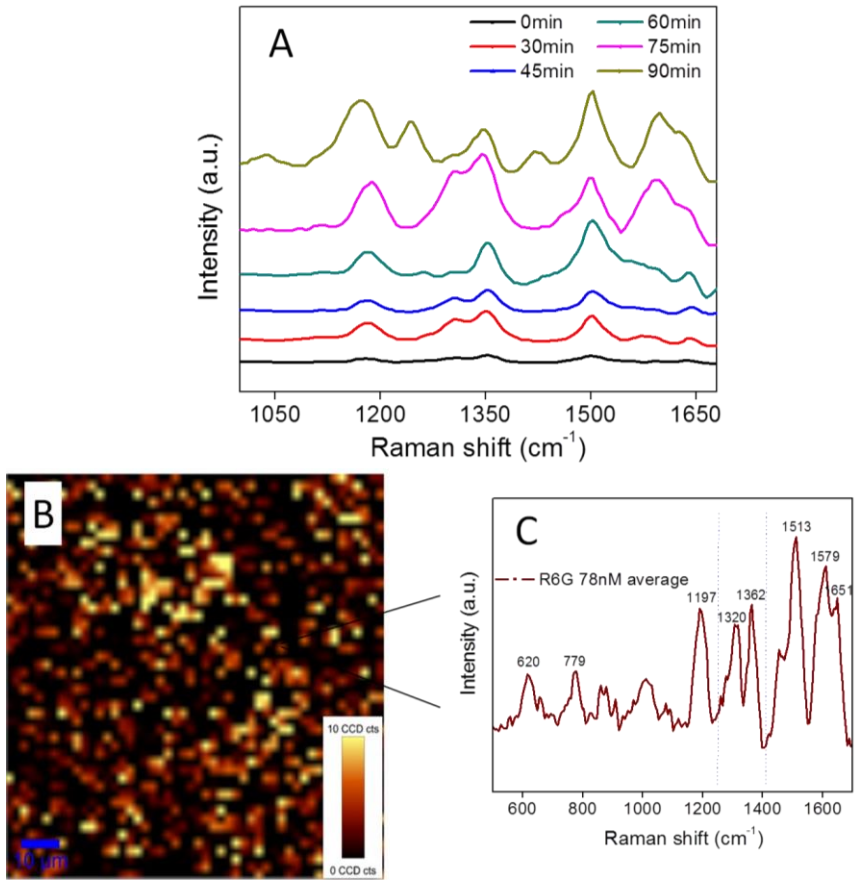

Figure 3.19 A) SERS of R6G (7.8 μM) on AuNP/BC-1-10 as a function of drying time, B) image scan of R6G (78 nM) on AuNP/BC-1-10, and C) the average spectrum of R6G on AuNP/BC-1-10 in image scan. Image scan was acquired by tracking the area between 1250-1410 cm^{-1} (between the two dash lines).

To further demonstrate the general applicability of the AuNP/BC SERS substrates, atrazine - a hydrophobic and neutral organic pollutant - was used as the analyte. A clear SERS spectrum of atrazine (10 μM) was readily observed on AuNP/BC-1-10 (Figure 3.20). In general the measured peak positions match very well (< 5-10 nm shift in wavelength) with those in the normal Raman spectrum of atrazine. The enhancement factor (EF) for atrazine was calculated to be as high as 2 × 10^8 based upon the expression:

$$EF = \frac{I_{SERS}}{I_{NR}} \times \frac{N_{NR}}{N_{SERS}} \qquad \text{Equation 3.1}$$

where I_{SERS} and I_{NR} are the SERS and normal Raman signal intensities of the atrazine peak at 961 cm^{-1}, N_{SERS} and N_{NR} are estimates of the numbers of atrazine molecules in the laser probe volume for SERS and normal Raman. Quantitative analysis of atrazine was performed at a solution pH of 1.3. As shown in Figure 3.21, atrazine signal (band at 961 cm^{-1}) to citrate background (band at 734 cm^{-1}) increased linearly as the atrazine concentration (in logarithm) increased from 250 nM - 250 μM, indicating the applicability of AuNP/BC nanocomposites for quantitative analysis of atrazine. These results collectively show that the AuNP/BC SERS substrates have general applicability for a broad range of organic pollutants.

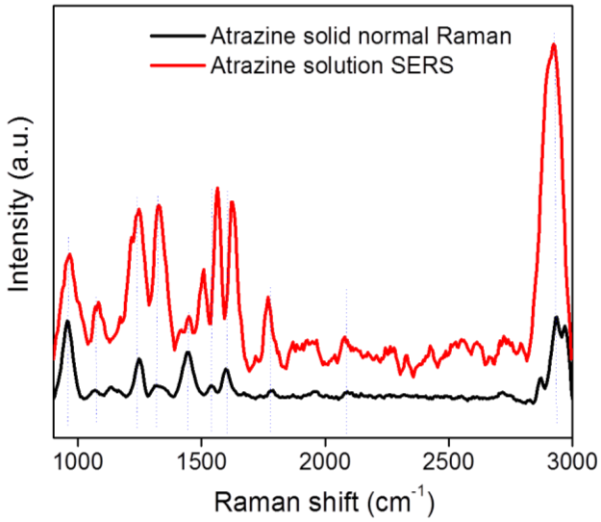

Figure 3.20 SERS spectrum of atrazine (10 μM) on AuNP/BC-1-10 and normal Raman spectrum of atrazine solid.

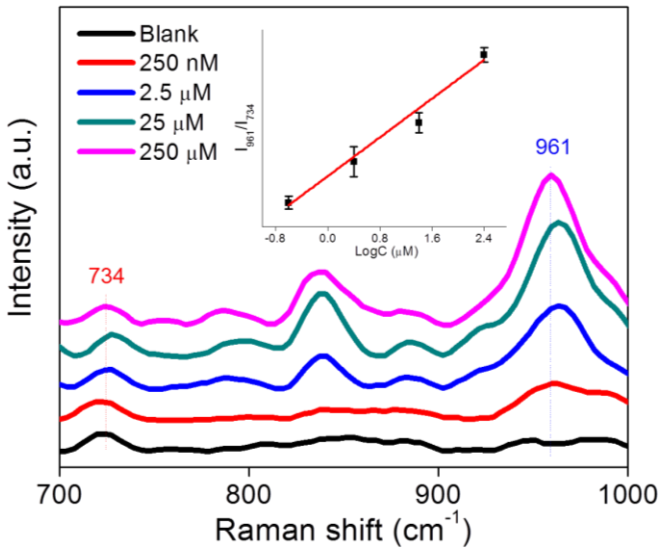

Figure 3.21 Quantitative analysis of atrazine at solution pH of 1.3. (Raman band at 734 cm^{-1} is from Na_3Cit coating and the Raman band at 961 cm^{-1} is from atrazine. Their intensity ratio I_{961}/I_{734} was used for the quantitative analysis of atrazine.)

3.4 Conclusions

AuNP/BC nanocomposites were prepared by *in situ* reduction of $HAuCl_4$ in the presence of BC and the feasibility of these nanocomposites as SERS substrates was evaluated. The AuNP size and morphology in the nanocomposites could be adjusted by $HAuCl_4$ concentration. At high $HAuCl_4$ concentration, Au nanoplates were synthesized and were thought to be responsible for the high SERS intensity. Following the drying of the AuNP/BC nanocomposite, the distance between its layers is reduced and hot spots form in the vertical direction. Most of the hot spots formed during the period when the AuNP/BC changed from being nearly dry to completely dry corresponding to the significant increase of SERS intensity in this period. The drying-induced enhancement factor increased with a decrease in MGITC concentration, which enabled an ultra low detection limit of ~24 molecules of MGITC. The AuNP/BC nanocomposites reported here show the potential to detect trace contaminants in water. Compared with paper-based SERS substrates, these nanocomposite films are lighter and more flexible in terms of their potential applications. This nanocomposite can be expected to be more resistant to water, acidic and alkaline solutions and it

thus has potential to serve as a passive sampler for ultimate field deployment. The large adsorption capacity of BC for AuNPs indicates the potential for all kinds of SERS-active nanostructures to be easily integrated into the BC structure. The cost of these SERS substrates is very low. Taking AuNP/BC-1-2 as an example, the price of gold contained in a 0.5 cm × 0.5 cm sample (more than enough for a single analysis) is only $0.003 based upon the August 2014 international price for gold. Considering the facile synthesis procedure and sustainable nature of nanocellulose, these super light and flexible nanocomposites show great potential for mass production.

Chapter 4 Improved Quantitative SERS Enabled by Surface-Enhanced Elastic Light Scattering

Haoran Wei,[†‡§] Weinan Leng,[†‡§] Junyeob Song,[‖] Marjorie R. Willner,[†‡§]

Linsey C. Marr,[†‡§] Wei Zhou,[‖] Peter J. Vikesland[†‡§*]

[†]Department of Civil and Environmental Engineering, Virginia Tech, Blacksburg, Virginia

[‡]Virginia Tech Institute of Critical Technology and Applied Science (ICTAS) Sustainable Nanotechnology Center (VTSuN), Blacksburg, Virginia

[§]Center for the Environmental Implications of Nanotechnology (CEINT), Duke University, Durham, North Carolina

[‖]Department of Electrical and Computer Engineering, Virginia Tech, Blacksburg, Virginia

*Corresponding author. Phone: (540) 231-3568, Email: pvikes@vt.edu

(This chapter has been published in ***Analytical Chemistry***. Adapted with permission from Haoran Wei et al., *Analytical Chemistry*, 2018[233]. Copy right (2018) American Chemical Society.)

Abstract

The application of surface-enhanced Raman spectroscopy (SERS) for everyday quantitative analysis is hindered by the point-to-point variability of SERS substrates that arises due to the heterogeneous distribution of localized electromagnetic fields across a suite of plasmonic nanostructures. Herein, for the first time, we adopt surface-enhanced elastic (i.e., Rayleigh) scattering as a SERS internal standard. Both elastic and inelastic (i.e., Raman) scattering are simultaneously enhanced by a given "hot spot" and thus the surface-enhanced elastic scattering signal provides a localized intrinsic internal standard that scales across all of the plasmon-enhanced electromagnetic fields within a substrate. The elastic scattered light used as normalization factor originates from the amplified spontaneous emission of laser that forms a pseudo band in low wavenumber range where edge filters cut on. A theoretical model is established to illustrate the mechanism of this normalization approach. The normalized Raman signals are independent of incident laser intensities and "hot spot" densities in SERS substrates. Following "hot-spot" (HS) normalization, the coefficient of variation of SERS substrates significantly decrease from 10%-60% to 2%-7%. The batch-to-batch and substrate-to-substrate variations decrease from 55% and 94% to 5% and 9%, respectiviely. This approach significantly improves the SERS quantitation performance for four chloroanilines and its reproducibility for monitoring analyte adsorption to AuNP in both static and dynamic systems. Overall, this approach provides an easy and cheap way to improve SERS reproducibility without the need to use additional chemicals as internal standards.

4.1 Introduction

Surface-enhanced Raman spectroscopy (SERS) has long been proposed as an ultrasensitive analysis method with single molecule sensitivity, minimal need for sample pretreatment, rapid detection time, and potential for on-site deployment.[21, 24, 25, 68, 234] However, in spite of the volume of research conducted to develop SERS substrates and optimize the technique, the poor reproducibility of the SERS signal makes it a challenge to achieve reliable quantitative analysis. SERS largely remains a laboratory curiosity, but with great potential for multiple real-world applications.[26, 235-237] One means to improve SERS reproducibility is to develop uniform SERS substrates through "top-down" nanofabrication.[60, 98, 147, 157, 238, 239] However, it is challenging to create such substrates at scale and at reasonable cost. Especially for environmental monitoring, it is highly desired to achieve pollutant quantitation using comparatively cheap and easy-to-make SERS substrates.

An alternative approach to reduce SERS irreproducibility is to incorporate internal standards (IS) into the substrate.[37, 240-242] The IS undergoes the same enhancement as target analytes, thus reducing point-to-point fluctuations in the signal caused by substrate heterogeneity, laser intensity fluctuations, or temperature variation. Although SERS quantitation was achieved using IS, it adds to the cost and complexity of substrate preparation, lacks universal applicability, generate interferent Raman bands, and the reference probe molecules may occupy SERS "hot spots". In addition, it is nontrivial to find an appropriate IS for the target analyte. Isotope-edited internal standards (IEIS) are ideal candidates for IS because the two isotope analogues share the same Raman cross-section and affinity to plasmonic nanoparticle (NP) surface.[37, 243] While analyte concentrations can be determined based on the ratios of the Raman band intensities of the two isotope analogues, their adsorption kinetics cannot be acquired. In addition, IEIS for a large

number of chemicals of analytical interest are not readily available. Importantly, none of the aforementioned approaches is applicable for SERS sensing under dynamic conditions wherein "hot spot" densities change over time. Such conditions are prevalent in SERS assays for biomedical and environmental detection.[18, 244-247]

The SERS effect is inherently surface enabled with the highest signal enhancements observed at locations where the electromagnetic field is highest (i.e., either at edges or between two nanoparticles).[26, 248] Regions with the highest enhancement factors are typically referred to as SERS "hot spots". Variation of SERS signals induced by the heterogeneous distribution of "hot spots" oftentimes surpasses that induced by the change of analyte concentrations on NP surfaces. Therefore, normalizing "hot spot" distribution across a single substrate or among different substrates is vitally important for improving the performance of SERS quantitation. It was recently reported that the elastic scattering undergoes the same electromagnetic enhancement as the inelastic scattering coming from the same SERS "hot spot".[249] Based on this study and considering the intrinsic drawbacks of the reported IS, it is possible and preferable to introduce a light instead of a chemical as SERS IS.

In this effort, we demonstrate an easy and cheap approach for improving SERS reproducibility that exploits surface plasmon enhanced Rayleigh scattering signals as internal standards for SERS signal normalization. Both theory and experiments show that the intensity of the surface plasmon enhanced elastic scattering signal of a low-wavenumber pseudo-band (ν_e) scales linearly with the integrated "hot-spot" signal strength. This pseudo-band can be used to calibrate "hot spot" variations and minimize the signal heterogeneity of a SERS substrate, substrates prepared in different batches, and different types of SERS substrates. We first discuss the fundamental theory supporting our approach, provide supporting experimental results, and conclude by demonstrating

"hot spot" normalization for 1) quantitative pH-triggered SERS detection of chloroanilines; and 2) differentiation of analyte adsorption and "hot spot" formation in a dynamic colloidal system.

4.2 Results and Discussion

4.2.1 Theoretical Basis for "Hot Spot" Normalization

Using a scalar phenomenological theory,[250, 251] we developed an analytical expression that predicts that the intensity of the surface enhanced elastic Rayleigh scattering signal is proportional to the SERS signal from the ensemble of analyte and background molecules in the vicinity of plasmonic nanostructures. We propose that the surface enhanced Rayleigh scattering signal can serve as an intrinsic internal standard for quantitative SERS under carefully controlled conditions.

As depicted in Figure 4.1a, a molecule is located at position r_0 close to a plasmonic metal nanostructure (at r') that supports localized surface plasmon resonances (LSPRs) and converts the incident fields $E_0(r_0, \omega_0)$ into local scattered fields $E_R(r_0, \omega_0) \sim f(r_0, \omega_0)E_0(r_0, \omega_0)$, where $f(r_0, \omega_0)$ is the field enhancement factor. Laser illumination gives rise not only to the stimulated emission fields $E_0(r_0, \omega_0)$ at the lasing frequency ω_0, but also amplified spontaneous emission (ASE) fields $E_0(r_0, \omega_1)$ over broad frequencies ω_1 that have weaker amplitudes than the lasing emission. An analyte molecule at r_0 experiences the total local fields $E_0 + E_s \sim (1+ f(r_0, \omega))*E_0(r_0, \omega)$ at lasing frequency ω_0 and ASE frequencies ω_1, respectively. The interaction of the molecule with the enhanced total local fields at ω_0 gives rise to the dipole moment associated with inelastic Raman scattering according to $p(\omega_0 \pm \omega_{vib}, \omega_0) = \alpha(\omega_0 \pm \omega_{vib}, \omega_0)[1 + f(r_0, \omega_0)]E_0(r_0, \omega_0)$, where ω_{vib} is a vibrationally shifted frequency and $\alpha(\omega_0 \pm \omega_{vib}, \omega_0)$ is the polarizability for the frequency mixing Stokes ($\omega_0 - \omega_{vib}$) or anti-Stokes ($\omega_0 + \omega_{vib}$) Raman scattering process. Similarly, the dipole moment associated with elastic Rayleigh scattering at frequency ω_1 can be induced according to $p(\omega_1) = \alpha(\omega_1)[1 + f(r_0, \omega_1)]E_0(r_0, \omega_1)$, where $\alpha(\omega_1)$ is the polarizability of the Rayleigh

scattering process. In the presence of plasmonic nanostructures, the Green function $G(r_\infty, r_0, \omega)$ of the combined molecule-nanostructure system is represented as $(1+f(r_0, \omega))\, G_0(r_\infty, r_0, \omega)$, where G_0 is the free-space Green function in the absence of plasmonic nanostructures and f is the field enhancement factor at the radiation frequency. The electric field intensity I_{Raman} of the radiation from the induced Raman scattering dipole $p(\omega_0 \pm \omega_{vib}, \omega_0)$ depends on the incident field intensity I_0 and can be expressed as:

$$I_{Raman}(r_\infty, \omega_0 \pm \omega_{vib}) = |E(r_\infty, \omega_0 \pm \omega_{vib})|^2$$

$$= \left|\frac{(\omega_0 \pm \omega_{vib})^2}{\varepsilon c^2}[G(r_\infty, r_0, \omega_0 \pm \omega_{vib})]p(\omega_0 \pm \omega_{vib}, \omega_0)\right|^2$$

$$\approx \frac{(\omega_0 \pm \omega_{vib})^4}{\varepsilon^2 c^4}\left|[1 + f(r_0, \omega_0 \pm \omega_{vib})]G_0(r_\infty, r_0, \omega_0 \pm \omega_{vib})\alpha(\omega_0 \pm \omega_{vib}, \omega_0)[1 + f(r_0, \omega_0)]\right|^2 I_0(r_0, \omega_0). \quad \text{(Equation 4.1)}$$

Similarly, the radiation intensity $I_{Rayleigh}$ from the induced Rayleigh scattering dipole $p(\omega_1)$ is

$$I_{Rayleigh}(r_\infty, \omega_1) = |E(r_\infty, \omega_1)|^2 = \left|\frac{{\omega_1}^2}{\varepsilon c^2}[G_0(\overrightarrow{r_\infty}, \overrightarrow{r_0}, \omega_1) + G_R(\overrightarrow{r_\infty}, \overrightarrow{r_0}, \omega_1)]p(\omega_1)\right|^2$$

$$\approx \frac{{\omega_1}^4}{\varepsilon^2 c^4}\left|[1 + f(r_0, \omega_1)]G_0(r_\infty, r_0, \omega_1)\alpha(\omega_1)[1 + f(r_0, \omega_1)]\right|^2 I_0(r_0, \omega_1). \quad \text{(Equation 4.2)}$$

For most quantitative SERS applications, we want to quantify analyte molecule concentrations by measuring Raman signals from an ensemble of analyte molecules in a dielectric environment (e.g., various liquids). Under laser illumination both the inelastic Raman scattering and the elastic Rayleigh scattering signals come from an ensemble of analyte and background molecules. According to Eq. 4.1 and Eq. 4.2, the ratio of signal intensities between Raman scattering at $\omega_0 \pm \omega_{vib}$ and Rayleigh scattering at ω_1 can be expressed as

$$\frac{I_{Raman}(\mathrm{r}_\infty,\omega_0\pm\omega_{vib})}{I_{Rayleigh}(\mathrm{r}_\infty,\omega_1)} = \frac{\sum_{i=1}^{N_AV} I^i_{Raman}(\mathrm{r}_\infty,\mathrm{r}^i_0,\omega_0\pm\omega_{vib})}{\sum_{i=1}^{N_AV} I^i_{Rayleigh}(\mathrm{r}_\infty,\mathrm{r}^i_0,\omega_1)+\sum_{j=1}^{N_BV} I^j_{Rayleigh}(\mathrm{r}_\infty,\mathrm{r}^j_0,\omega_1)} \approx \frac{\sum_{i=1}^{N_AV} I^i_{Raman}(\mathrm{r}_\infty,\mathrm{r}^i_0,\omega_0\pm\omega_{vib})}{\sum_{j=1}^{N_BV} I^j_{Rayleigh}(\mathrm{r}_\infty,\mathrm{r}^j_0,\omega_1)}$$

$$= \frac{\sum_{i=1}^{N_AV}\left|G_0(\mathrm{r}_\infty,\mathrm{r}^i_0,\omega_0\pm\omega_{vib})\alpha_A(\omega_0\pm\omega_{vib},\omega_0)f(\mathrm{r}^i_0,\omega_0\pm\omega_{vib})f(\mathrm{r}^i_0,\omega_0)\right|^2 I_0(\mathrm{r}^i_0,\omega_0)}{\sum_{j=1}^{N_BV}\left|G_0\left(\mathrm{r}_\infty,\mathrm{r}^j_0,\omega_1\right)\alpha_B(\omega_1)\left[f\left(\mathrm{r}^j_0,\omega_1\right)\right]^2\right|^2 I_0(\mathrm{r}^j_0,\omega_1)}.$$

(Equation 4.3)

where N_A, N_B are the molar concentrations of the analyte and the background solvent molecules ($N_B \gg N_A$) present within the sampling volume V, $\alpha_A(\omega_0 \pm \omega_{vib}, \omega_0)$ is the Raman scattering polarizability of the analyte molecules, $\alpha_B(\omega_1)$ is the Rayleigh scattering polarizability of the background molecules, and r^i_0, r^j_0 are the positions of analyte molecule *i* and background molecule *j*.

If we constrain the optical sampling volume within a tightly focused spot that contains plasmonic nanostructures (e.g., by use of a confocal configuration), both the surface enhanced elastic scattering and the inelastic scattering signals will be dominated by the analyte and background molecules located in close proximity to "hot spots" that induce the maximum intensities of both elastic and inelastic scattering proportional to $|f_{max}|^4$, where f_{max} is the maximum field enhancement factor in the hot spot region at the excitation frequency ω_0.[249] Since $\omega_0 \cong \omega_1 \gg \omega_{vib}$, we assume $f_{max}(\mathrm{r}_0, \omega_0) \cong f_{max}(\mathrm{r}_0, \omega_1) \cong f_{max}(\mathrm{r}_0, \omega_0 \pm \omega_{vib}) \equiv f_{max} \gg 1$, and $G_0(\mathrm{r}_\infty, \mathrm{r}_0, \omega_1) \cong G_0(\mathrm{r}_\infty, \mathrm{r}_0, \omega_0 \pm \omega_{vib})$. In this case, the ratio of Raman and Rayleigh signal intensities can be approximated as

$$\frac{I_{Raman}(\mathrm{r}_\infty,\omega_0\pm\omega_{vib})}{I_{Rayleigh}(\mathrm{r}_\infty,\omega_1)} \approx \frac{N_A\left|G_0(\mathrm{r}_\infty,\mathrm{r}_0,\omega_0\pm\omega_{vib})\alpha_A(\omega_0\pm\omega_{vib},\omega_0)[f_{max}]^2\right|^2 I_0(\mathrm{r}_0,\omega_0)}{N_B|G_0(\mathrm{r}_\infty,\mathrm{r}_0,\omega_1)\alpha_B(\omega_1)[f_{max}]^2|^2 I_0(\mathrm{r}_0,\omega_1)}$$

$$\approx \frac{N_A|\alpha_A(\omega_0\pm\omega_{vib},\omega_0)|^2 I_0(\mathrm{r}_0,\omega_0)}{N_B|\alpha_B(\omega_1)|^2 I_0(\mathrm{r}_0,\omega_1)} \qquad \text{(Equation 4.4)}$$

During a SERS measurement, all factors (e.g., N_B, α_A, α_B, and $I_0(r_0, \omega_0)/I_0(r_0, \omega_1)$) except N_A in Eq. 4.4 are constant. By normalizing the SERS signals with the surface enhanced Rayleigh

scattering signals of the background molecules in the "hot spots", the new ratiometric signal, $\frac{I_{Raman}(\mathrm{r}_\infty,\omega_0\pm\omega_{vib})}{I_{Rayleigh}(\mathrm{r}_\infty,\omega_1)}$, provides quantitation of the molar concentration of analyte molecules N_A without being affected by the many experimental factors that give rise to uncontrollable spatial and temporal perturbations (e.g., local refractive index environments, local field enhancement factors, and local laser illumination fluxes).

We emphasize that the Rayleigh scattering polarizability $\alpha_B(\omega_1)$ is many orders larger than the Raman scattering polarizability $\alpha_A(\omega_0 \pm \omega_{vib}, \omega_0)$ and that N_B is generally orders of magnitude higher than N_A. Consequently, to maintain a large signal-to-noise for quantitative SERS applications, we must ensure that $I_0(r_0, \omega_0)$ (=excitation field intensity for Raman scattering) >> $I_0(r_0, \omega_1)$ (=excitation field intensity for Rayleigh scattering) in Eq. 4.4. This condition can be satisfied by using intense lasing light and weak ASE light in the laser emission.

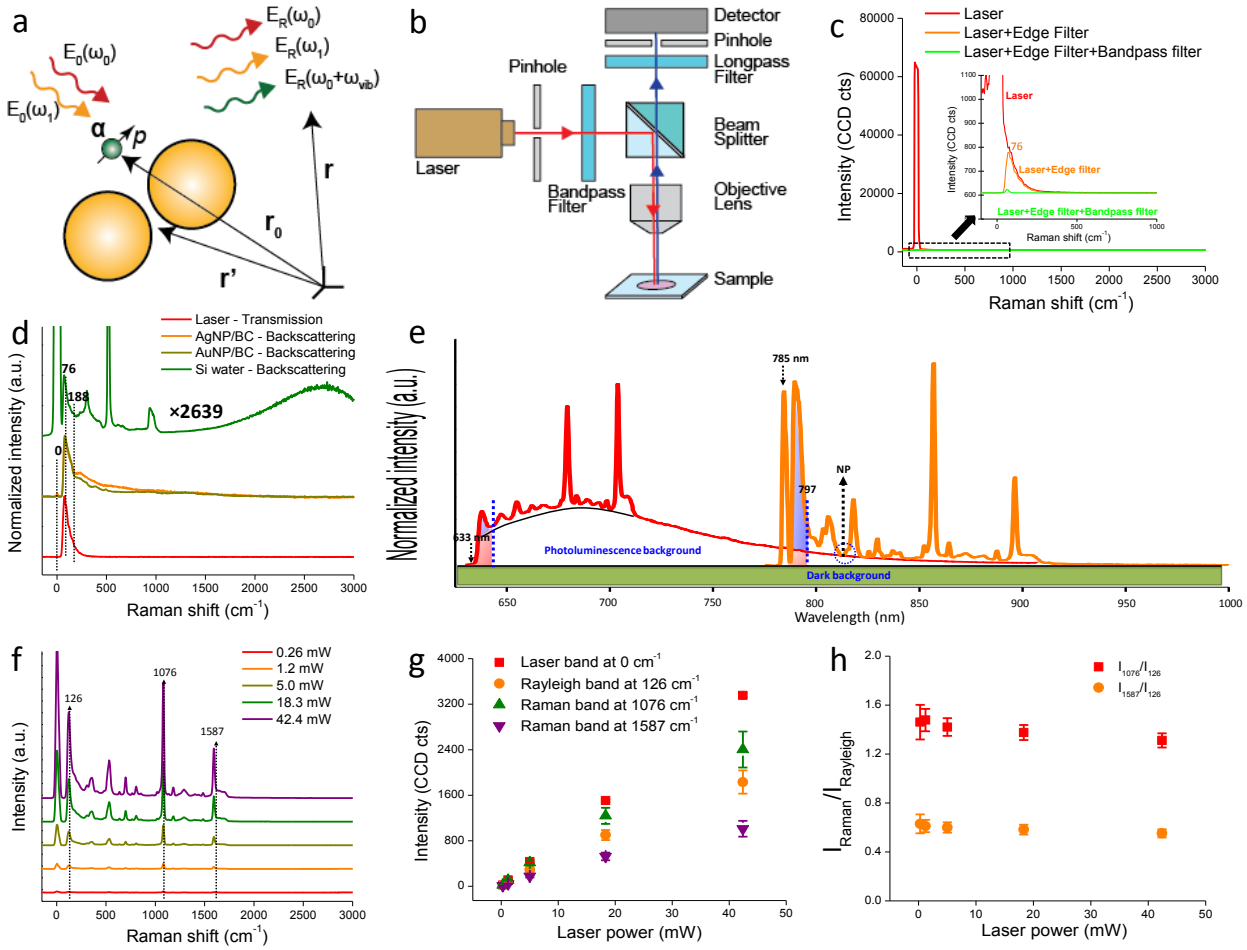

Figure 4.1 a) Schematic illustration of the relation between the incident field (E_0) and scattered (E_R) Rayleigh and Raman fields passing through a "hot spot". b) The system employed for backscattering confocal Raman micro-spectroscopy/imaging. c) Laser emission spectra in transmission mode with or without an edge or bandpass filter. d) Raman spectra of two SERS substrates and Si wafer collected using backscattering Raman mode compared to transmission mode laser emission spectra. e) Raman spectra of AuNP/BC exposed to 4-MBA excited by 633 nm and 785 nm lasers. The spectra are normalized to the intensity at 813 nm (= normalization point (NP)). Blue and red shaded areas represent contribution of Rayleigh scattering and photoluminescence (PL), respectively, to ν_e. f) Raman spectra of 4-mercaptobenzoic acid (4-MBA) under various laser powers. g) Variation of band intensities of the laser peak, ν_e at 126 cm^{-1}, and the principal 4-MBA bands at 1076 and 1587 cm^{-1} as a function of laser power. h) Variation of the intensity ratio between the 4-MBA bands at 1076 cm^{-1} and 1587 cm^{-1} and the ν_e pseudo-peak (at 126 cm^{-1}) as a function of laser power.

4.2.2 Origin of ν_e

As a proof of concept, we used a confocal Raman micro-spectroscopy/imaging setup (Figure 4.1b) to simultaneously collect and compare inelastic Raman and elastic Rayleigh scattering signals

from a tightly focused spot on a nanostructured plasmonic substrate. As shown in Figure 4.1c, the measured diode laser (785 nm) emission spectrum (red curve) consists of a narrow laser line at 0 cm^{-1} along with a broad ASE background that extends beyond 200 cm^{-1}. After blocking the laser emission with a longpass (edge) filter, we observe an asymmetric peak (ν_e) at 76 cm^{-1} that is an artificial/pseudo spectral feature due to the convolution of the spectral profile of the ASE and the transmittance of the filter (cut-on wavenumber: 68 cm^{-1}). By choosing longpass filters with different cut-on wavenumbers and cut-off slopes, we can control the spectral position, shape, and amplitude of ν_e (Figure 4.2). For instance, when we insert a bandpass filter in addition to the longpass filter, the pseudo peak (ν_e) at 76 cm^{-1} (green curve) is significantly attenuated showing that ν_e originates from the laser ASE.

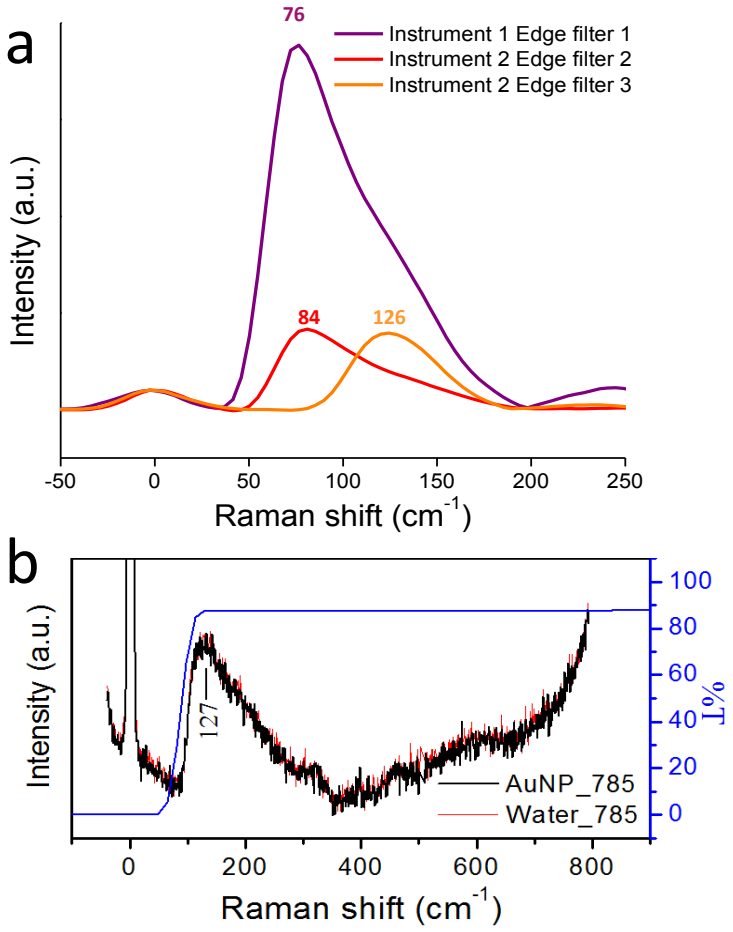

Figure 4.2 a) SERS spectra of AuNP/BC nanocomposite collected by Raman instruments equipped with longpass (edge) filters with different cut-on wavenumbers. (The spectra were collected in backscattering mode using two separate Raman instruments and normalized to the laser band at 0 cm^{-1}). b) Transmission spectrum of the longpass filter (shown as instrument 2 filter 3 in Fig. S1a) collected with a UV-VIS spectrometer (Cary 5000, Agilent). The transmission reached its maximum at 127 cm^{-1}, indicating this longpass filter should cut on at this wavenumber. This is consistent with the position of the ν_e band in Fig. S1a. The Raman spectra of deionized water and AuNP monomer suspension are shown in Fig. S1b, which exhibit bands at the same position where the longpass filter cuts.

Because ν_e is weak, it has been typically overlooked based on the assumption that Rayleigh scattering will be fully blocked by the longpass filter.[252, 253] This assumption deviates from the reality of many SERS studies. We speculated that the weak ν_e interacts with SERS "hot spots", is elastically scattered by the molecules within them, and experiences the same electromagnetic enhancement as Raman scattering.[249] To test this hypothesis, backscattered Raman spectra of a Si

wafer and a SERS substrate – gold nanoparticle/bacterial cellulose (AuNP/BC) – were collected. As shown in Figure 4.1d, an asymmetric peak at 76 cm^{-1} appears in the Raman spectra for both Si and the SERS substrate that reflects the line shape of the laser ASE (red curve). Notably, the ν_e of AuNP/BC was 2600× larger than that of the Si wafer, thus supporting the hypothesis that ν_e is significantly enhanced by SERS "hot spots" (Figure 4.1d).

As shown in Figure 4.3, additional experiments using a second Raman instrument equipped with an edge filter (cut-on wavenumber: 126 cm^{-1}) to probe AuNP/BC, a commercial SERS substrate, and aggregated AuNP colloids corroborate this result. In the absence of plasmonic nanostructures (e.g., in DI water) the intensity of ν_e at 126 cm^{-1} is very weak, but the signal intensity is significantly enhanced by substrates such as AuNP/BC or a commercial SERS substrate. The presence of a strong ν_e for AuNP/BC and the commercial substrate suggests that this band is enhanced when SERS "hot spots" are highly concentrated. This assertion was further supported by the observation that ν_e was weak for 50 nm AuNP colloid when no "hot spots" were present, but it developed following electrolyte addition and concomitant colloid aggregation. This finding suggests there is a correlation between the plasmon enhanced elastic scattering signal and the strength of plasmonic "hot spots" for local field enhancement. Across all experiments, ν_e is characteristically weak in the absence of large numbers of SERS hotspots.

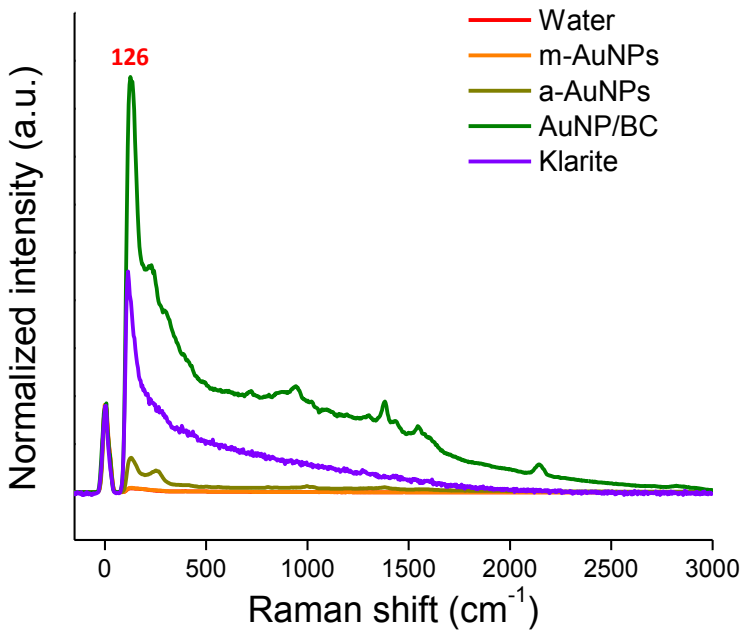

Figure 4.3 Raman spectra collected from DI water, AuNP monomer suspension (m-AuNPs), AuNP aggregate suspension (a-AuNPs), AuNP/BC nanocomposite, and a commercial SERS substrate – Klarite using backscattering Raman mode. a-AuNPs were prepared by adding 0.5 mL phosphate buffer (100 mM) into 0.5 mL AuNP monomer suspension and vortex mixing for 30 s.

We emphasize that ν_e occurs in addition to the SERS background continuum that originates from the combination of the photoluminescence (PL) of the plasmonic nanostructures and the fluorescence emitted by fluorophores near the surface under laser excitation.[254-257] Fluorophores in resonance with the excitation laser are subject to surface-enhanced fluorescence (SEF) that contributes to the background continuum.[256, 258, 259] To minimize this possibility, we primarily used a non-resonant molecule, 4-MBA, and thoroughly washed our substrates such that residual fluorophores were removed. PL originates from the radiative recombination of sp band electrons and excited d band holes in noble metals and can be significantly enhanced by the surface plasmon resonance of nanostructures.[253, 257, 260] PL is an inherent characteristic of the SERS spectrum and is typically the primary contributor to the SERS continuum. Many SERS studies report spectra in a range far away from the excitation wavelength (> 200 cm^{-1})[258, 261, 262] where the PL signal can

dominate the SERS continuum. It should be noted, however, that for any given SERS substrate the contribution of PL to the SERS continuum will be a function of the laser excitation wavelength.[253, 261] To illustrate, the AuNP/BC substrate was probed using both 633 and 785 nm excitation. As shown in Figure 4.1e, the PL background of the SERS spectrum obtained with the 633 nm laser perfectly predicts the PL background of the SERS spectrum collected under 785 nm excitation. The contribution of PL to the pseudo-peak at 84 cm^{-1} (the red-shaded areas) is a function of the laser excitation, with a larger contribution under 633 nm excitation (~50.1%) than at 785 nm (~6.5%). Figure 4.1e illustrates the additive contribution of surface enhanced Rayleigh scattering to ν_e relative to the broad, smooth PL background.[257] The influence of PL on the intensity of ν_e is readily accounted for by baseline correction using published Matlab scripts (Figure 4.4).[263]

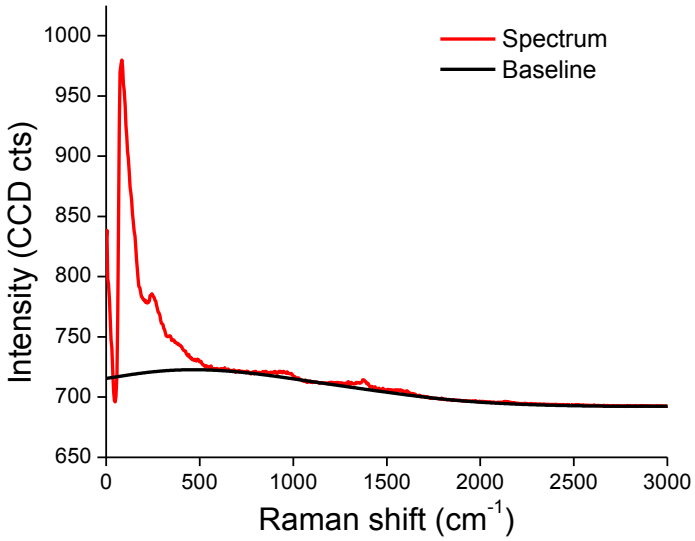

Figure 4.4 Baseline (black) that is subtracted from the SERS spectrum (red) collected from the AuNP/BC substrate.

The strong correlation between PL and the dark-field scattering spectra of individual plasmonic nanoparticles/clusters demonstrates that the PL spectrum is dependent on the localized surface plasmon resonance (LSPR) of the nanostructures.[253, 255, 257, 264, 265] This LSPR dependence was experimentally demonstrated by the dissimilar SERS backgrounds of two SERS substrates,

AgNP/BC and AuNP/BC, for wavenumbers >188 cm^{-1} where the laser ASE is quite weak (Figure 4.1d & Figure 4.5). The ν_e line shapes for these substrates overlap and resemble the line shape of the laser ASE <188 cm^{-1} (Figure 4.1d), further indicating that ν_e originates from ASE and not PL.

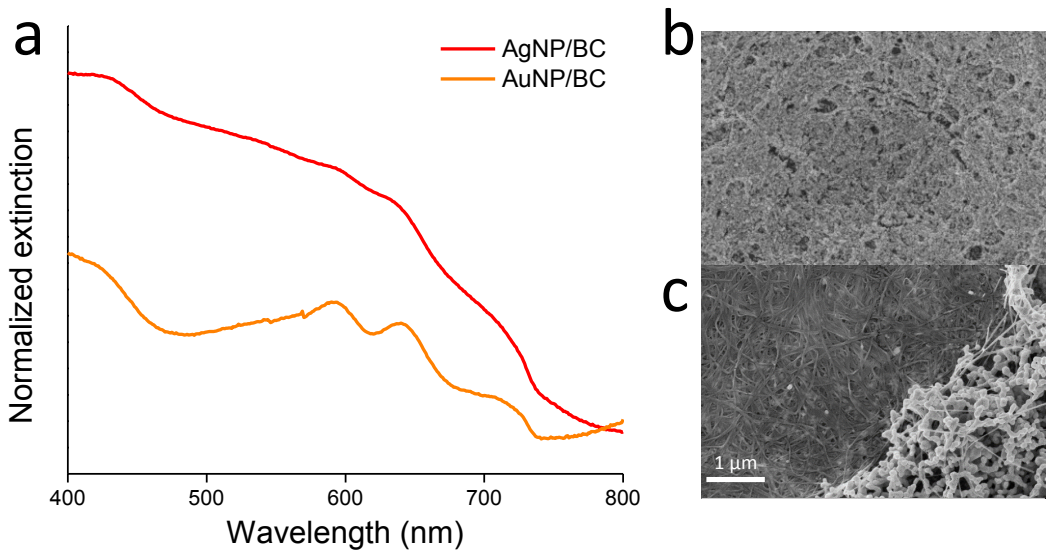

Figure 4.5 a) The normalized extinction spectra of AgNP/BC and AuNP/BC; SEM images of b) AuNP/BC and c) AgNP/BC.

Figure 4.1f shows the Raman spectra of 4-mercaptobenzoic acid (4-MBA) functionalized AuNP clusters under various laser powers. The intensities of the laser band (0 cm^{-1}), the elastic pseudo peak (126 cm^{-1}), and the most intense Raman bands (1076 and 1587 cm^{-1}) are plotted in Figure 4.1g. Each of these bands increase linearly with an increase in laser power. As expected based on our theoretical analysis, the intensity trend for the pseudo elastic scattering peak is similar to that of the Raman bands. The intensity of ν_e at 126 cm^{-1} is of comparable magnitude to the Raman scatting intensity, which makes it a potentially suitable internal standard for calibration of the SERS signals. To validate this hypothesis the intensity ratios of the pseudo peak (126 cm^{-1}) and two Raman bands (1076 and 1587 cm^{-1}) are plotted in Figure 4.1h. These ratios are independent of laser intensity, a finding in agreement with Eq. 4.4.

4.2.3 Reducing SERS Substrate Heterogeneity by HS Normalization

All other parameters being fixed, the ratio defined by Eq. 4.4 will be constant no matter how "hot spot" density changes. To illustrate, we exploited an AuNP/BC hydrogel[236] that exhibits temporally variable "hot spot" densities as a function of drying time (Figure 4.6a). Over a 1 h drying period, both the 4-MBA Raman band at 1076 cm^{-1} and ν_e increase in intensity due to the drying mediated increase in "hot spot" density (Figure 4.6b&c). Despite these temporal changes, however, the ratio between the Raman band and ν_e remained constant (Figure 4.6d), as expected.

We suggest that the intensity of ν_e provides an indication of the integrated strength of SERS efficiency from all "hot spots" within the microscope collection volume. One hundred spectra were randomly selected from a 400 pixel SERS map of 4-MBA on AuNP/BC. Across this map, as shown in Figure 4.6e, the intensity of the 4-MBA Raman band at 1076 cm^{-1} increased linearly with the intensity of ν_e (R^2=0.99). This linearity shows that ν_e quantitatively reflects the integrated SERS efficiency of the excited "hot spots". We note that the intensity of the 4-MBA Raman band correlates poorly with the intensity of the PL background (Figure 4.6f), thus indicating that ν_e can serve as a SERS internal standard while the SERS continuum cannot.

The measured SERS intensity of any analyte reflects the combined effects of laser intensity, the electromagnetic field within SERS "hot spots", "hot spot" density, and the number of analyte molecules within the probe volume.[266] As discussed previously, the fluctuations of the first three factors are significantly reduced by ν_e normalization, leaving the number of analyte molecules as the remaining variable dictating signal intensity. Normalization by ν_e ($=I_{Raman}/I_{Rayleigh}$) decreases the variability of the SERS signal by minimizing point-to-point variations in SERS "hot spot" densities. We refer to this approach as "hot spot" (HS) normalization.

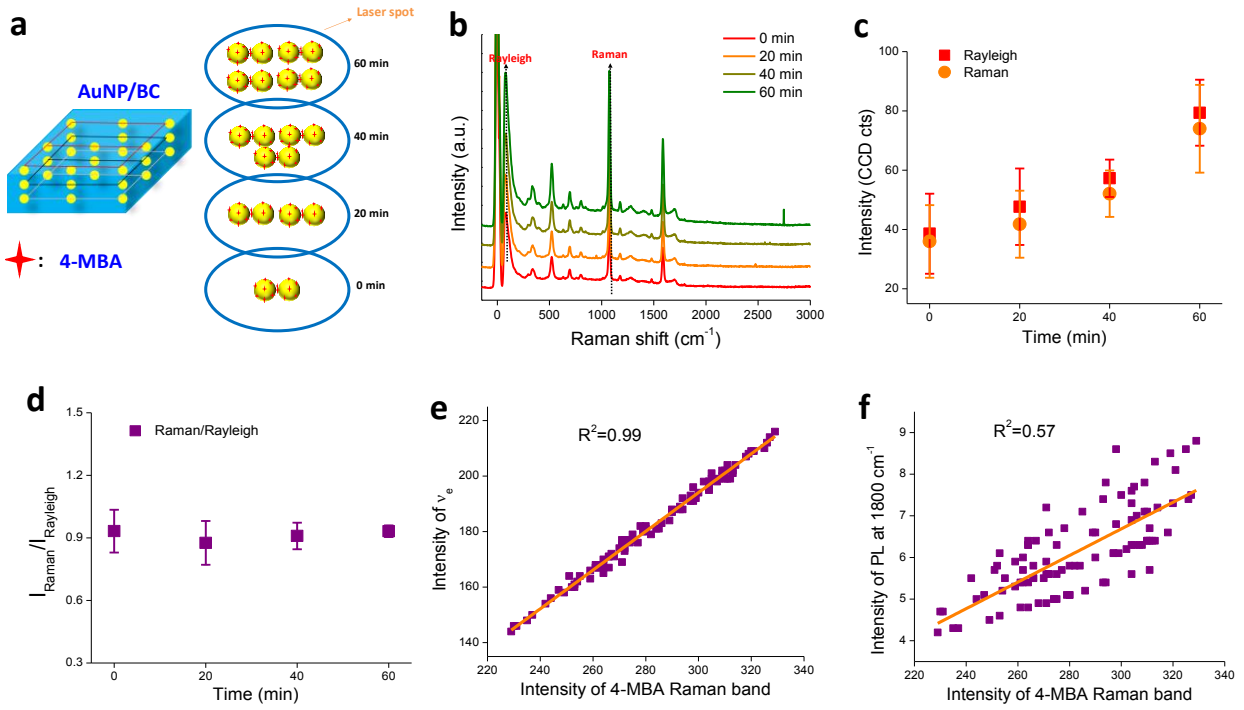

Figure 4.6 a) Schematic of the increase in SERS "hot spot" density within the laser excitation volume that occurs due to AuNP/BC hydrogel drying; b) The Raman spectra of 4-MBA on AuNP/BC platform at different drying times; The intensity of the Raman band at 1076 cm^{-1} of 4-MBA as the AuNP/BC hydrogel was drying c) before and d) after HS normalization; Variation of the SERS intensity of the 4-MBA Raman band at 1076 cm^{-1} as a function of the intensity of the e) elastic band at 84 cm^{-1} and f) photoluminescence (PL) background at 1800 cm^{-1} across a SERS map acquired on the AuNP/BC platform (100 points were randomly selected from a SERS map containing 400 pixels).

HS normalization significantly reduces the point-to-point heterogeneity of SERS substrates. Using the AuNP/BC substrate and 4-MBA as our test analyte, Raman maps (100×100 μm^2; 400 pixels) were constructed by separately tracking the Raman band at 1076 cm^{-1}, ν_e at 84 cm^{-1}, and background PL at 1820 cm^{-1} (Figure 4.7a-j). The maps tracking the Raman band and ν_e exhibit highly similar "hot spot" distributions illustrating that Raman scattering and Rayleigh scattering are similarly enhanced. The measured coefficients of variation (CV), or the ratio of the standard deviation to the mean, were 9.3 and 18.8% for the 10× and 100× objectives, respectively. However, following HS normalization the CVs declined to 2.3 and 7.9%, respectively. After HS normalization, all the "hot spots" and "cold spots" (i.e., spots with below average signal intensity)

disappear, graphically illustrating the concept of HS normalization. Maps normalized using background PL exhibit little improvement in CV. The differential performance of PL vs. ν_e as a SERS internal standard is attributed to their different enhancement mechanisms. PL reflects the enhancement of a radiating dipole comprising d-bands and s-electrons in the presence of a LSPR.[267] In contrast, ν_e is enhanced by the same electromagnetic mechanism responsible for SERS.[249] The concept of HS normalization is extendable to other 4-MBA Raman bands as well as AuNP suspension-based SERS (Figure 4.8, Figure 4.9, & Figure 4.10). HS normalization is possible with ν_e pseudo-peaks set using a range of longpass filters (Figure 4.10) and variable sampling areas (Figure 4.11).

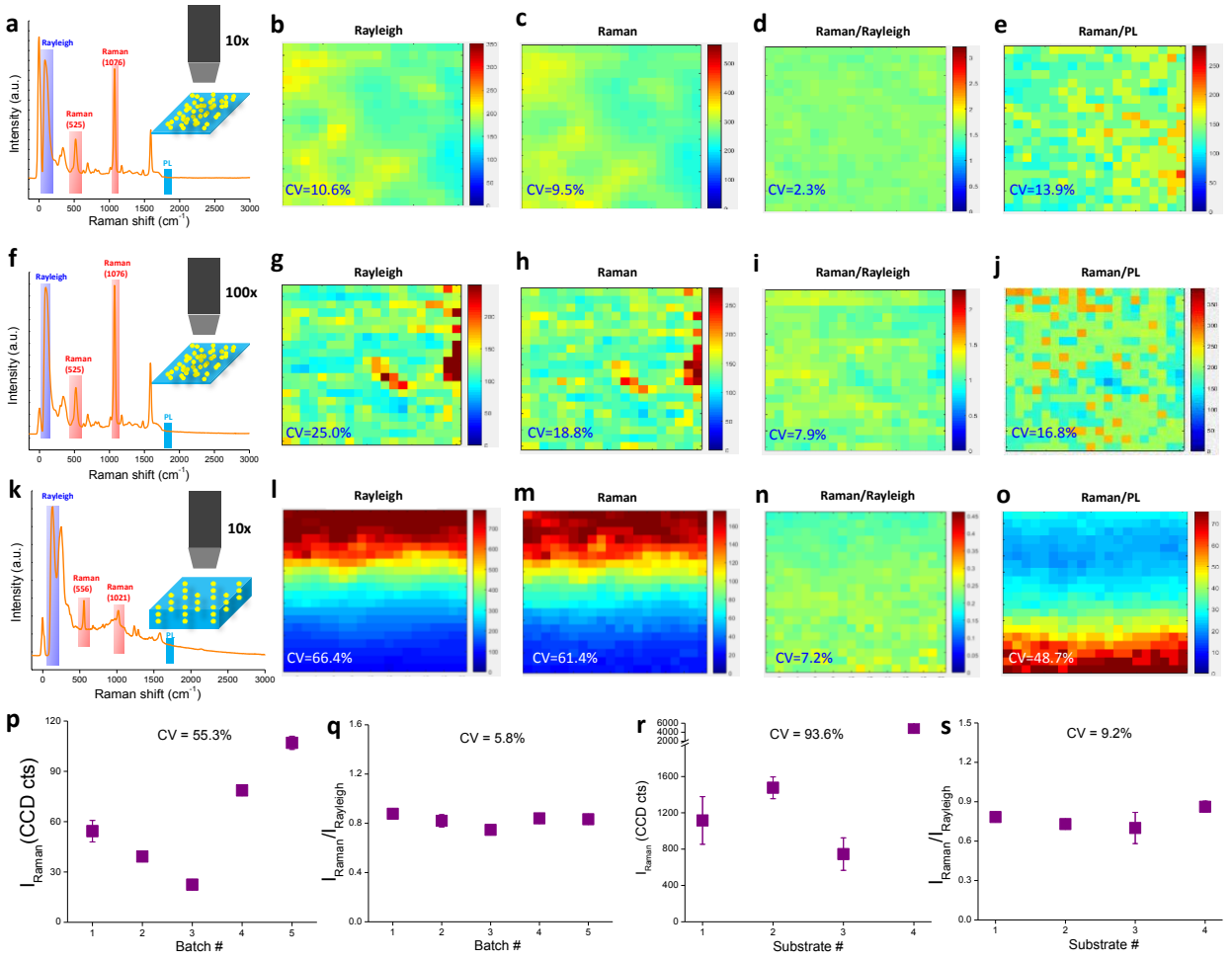

Figure 4.7 SERS spectra and maps of 4-MBA on dry AuNP/BC film collected using 10× (a-e) and 100× (f-j) objectives. Maps of 4-MBA tracking the bands at 84 cm^{-1} (b), 1076 cm^{-1} (c), the ratio between the two bands (I_{1076}/I_{184}) (d), the ratio between the band at 1076 cm^{-1} and the PL background (I_{1076}/I_{1820}) (e). Maps of 4-MBA tracking the bands at 84 cm^{-1} (g), 1076 cm^{-1} (h), the ratio between the two bands (I_{1076}/I_{84}) (i), and the ratio between the band at 1076 cm^{-1} and the PL background (I_{1076}/I_{1820}) (j). Maps of 2-CA from a drying AuNP/BC hydrogel tracking the bands at 126 cm^{-1} (l), 556 cm^{-1} (m), the ratio between the two bands (I_{556}/I_{126}) (n), and the ratio between the band at 556 cm^{-1} and the PL background (I_{556}/I_{1820}) (o). All maps were collected across a 100 µm × 100 µm area and contained 400 single spectra. p) SERS signals of 4-MBA Raman band at 1076 cm^{-1} collected from AuNP/BC substrates prepared by three different people and in five batches; q) The HS normalized (I_{1076}/I_{84}) signal for 4-MBA collected from AuNP/BC substrates prepared in five batches; r) SERS signals of 4-MBA Raman band at 1076 cm^{-1} collected using four different SERS substrates; s) The ratio between the two bands (I_{1076}/I_{84}) of 4-MBA collected using four different SERS substrates. Substrates #1 and #2 are AuNP/BC nanocomposites prepared using 1.2 mM or 12 mM Na_3Cit as reducing agent, respectively; Substrates #3 and #4 are AgNP/BC nanocomposites prepared using 250 mM or 25 mM $NaBH_4$ as reducing agent, respectively; Each substrate was scanned (containing 400 pixels) three times and the error bars reflect the standard deviation of these three scans.

Finally, HS normalization can account for batch-to-batch variability in substrate performance (Figure 4.7p&q) as well as differences in substrate identity without any additional cost (Figure 4.7r&s). To illustrate, Five batches of AuNP/BC were prepared by three separate individuals and scanned after exposure to 50 μM 4-MBA for 2 h. The CV value of the Raman band at 1076 cm^{-1} of 4-MBA decreased from 55.3% to 5.8% after HS normalization (Figure 4.7p&q), indicating that HS normalization can significantly improve batch-to-batch reproducibility of SERS substrates. Four nanocellulose-based SERS substrates prepared using two different metals (Au or Ag) and two different reducing agents (NaCit or $NaBH_4$) were scanned by Raman after exposing to 50 μM 4-MBA for 2 h. The CV value of the 1076 cm^{-1} Raman band decreased from 93.6% to 9.2% after HS normalization (Figure 4.7r&s), indicating that HS normalization can significantly improve the reproducibility across a suite of different SERS substrates.

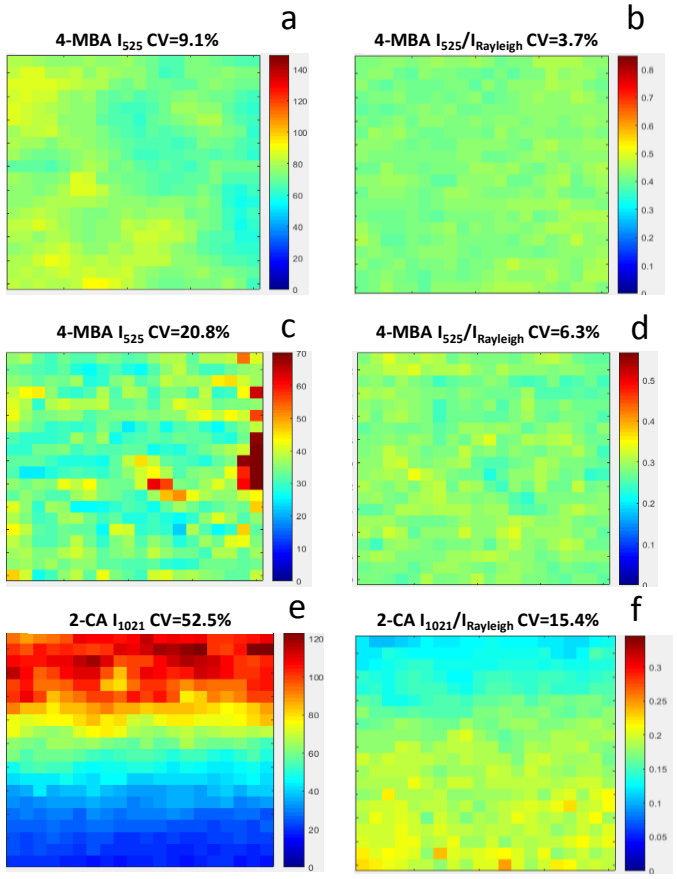

Figure 4.8 Maps of 4-MBA on dry AuNP/BC film tracking the band at 525 cm^{-1} using a) 10× and c) 100× objectives. The ratio between the two bands (I_{525}/I_{126}) using b) 10× and d) 100v objectives. Maps of 2-CA on drying AuNP/BC hydrogel tracking the band at e) 1021 cm^{-1} and f) The ratio between the two bands (I_{1021}/I_{126}). All maps were collected across a 100 µm × 100 µm area and contained 400 single spectra.

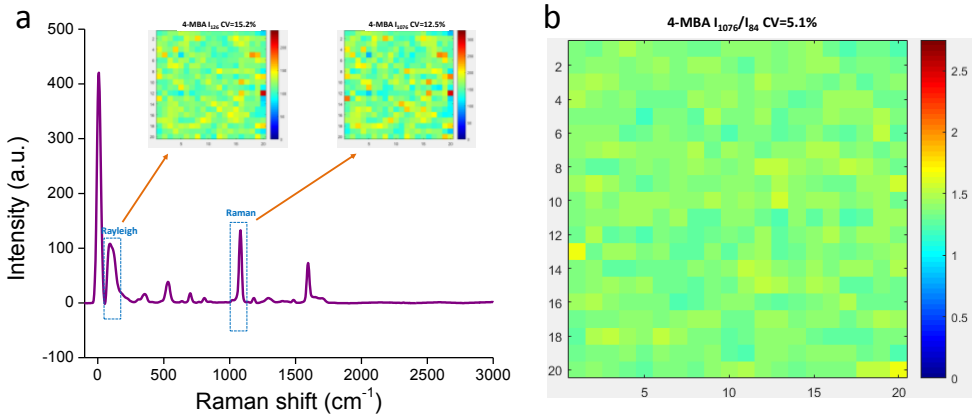

Figure 4.9 Maps of 4-MBA coated AuNP clusters in suspension tracking the band at a) 84 cm^{-1} (ν_e) and 1076 cm^{-1} (Raman band), and b) the ratio between the two bands (I_{1076}/I_{84}) (all maps were collected across a 100 µm × 100 µm area and contained 400 single spectra).

Our measured CV value of 2.3% is, to the best of our knowledge, the lowest reported in the literature (Table 4-1). Such a result is impressive given that the AuNP/BC substrate is heterogeneous with respect to nanoparticle size, shape, and aggregation state and thus the numbers of 4-MBA molecules associated with any given "hot spot" (N_A) will not be 100% identical across the map. Most approaches to achieve low CV values rely on expensive lithographic techniques or apply highly specialized analyte dosing or added internal standards.[241, 268, 269] As shown in Table 4-1, Sepaniak et al. produced a highly homogeneous SERS substrate by electron beam lithography and nanotransfer printing that exhibited a CV value of 13%.[60] Similarly, well-patterned gold nanocluster arrays fabricated via template-guided self-assembly exhibited a CV value of 12%.[270] Most recently, Chen et al. achieved a then record-low CV value (4.3%) by "fixing" analytes in a "hot zone" above an alkanethiolate ligand-regulated AgNP film and using the ligand as internal standards.[241] The fact that HS normalization works well under challenging imaging conditions suggests even lower CV values can be achieved with nano-engineered substrates.

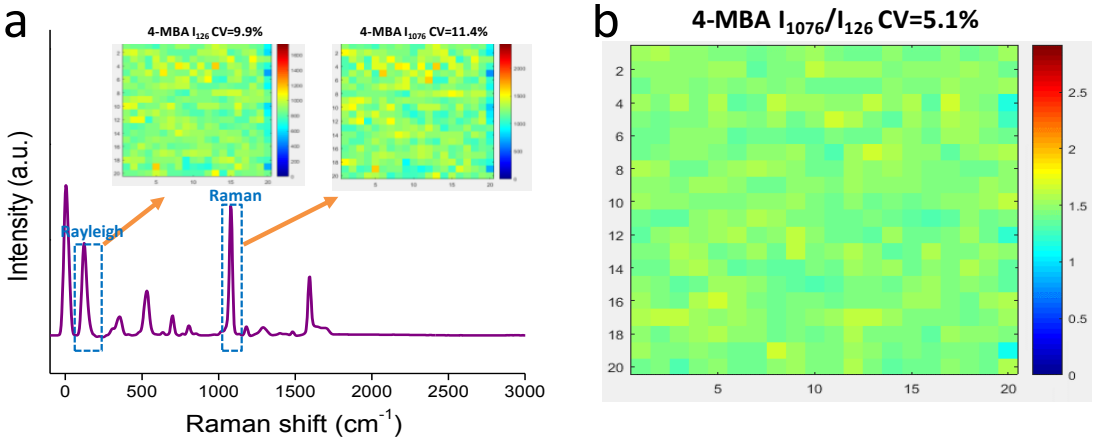

Figure 4.10 Maps of 4-MBA coated AuNP clusters in suspension tracking the bands at a) 126 cm^{-1} (ν_e) and 1076 cm^{-1} (Raman band), and b) the ratio between the two bands (I_{1076}/I_{126}).

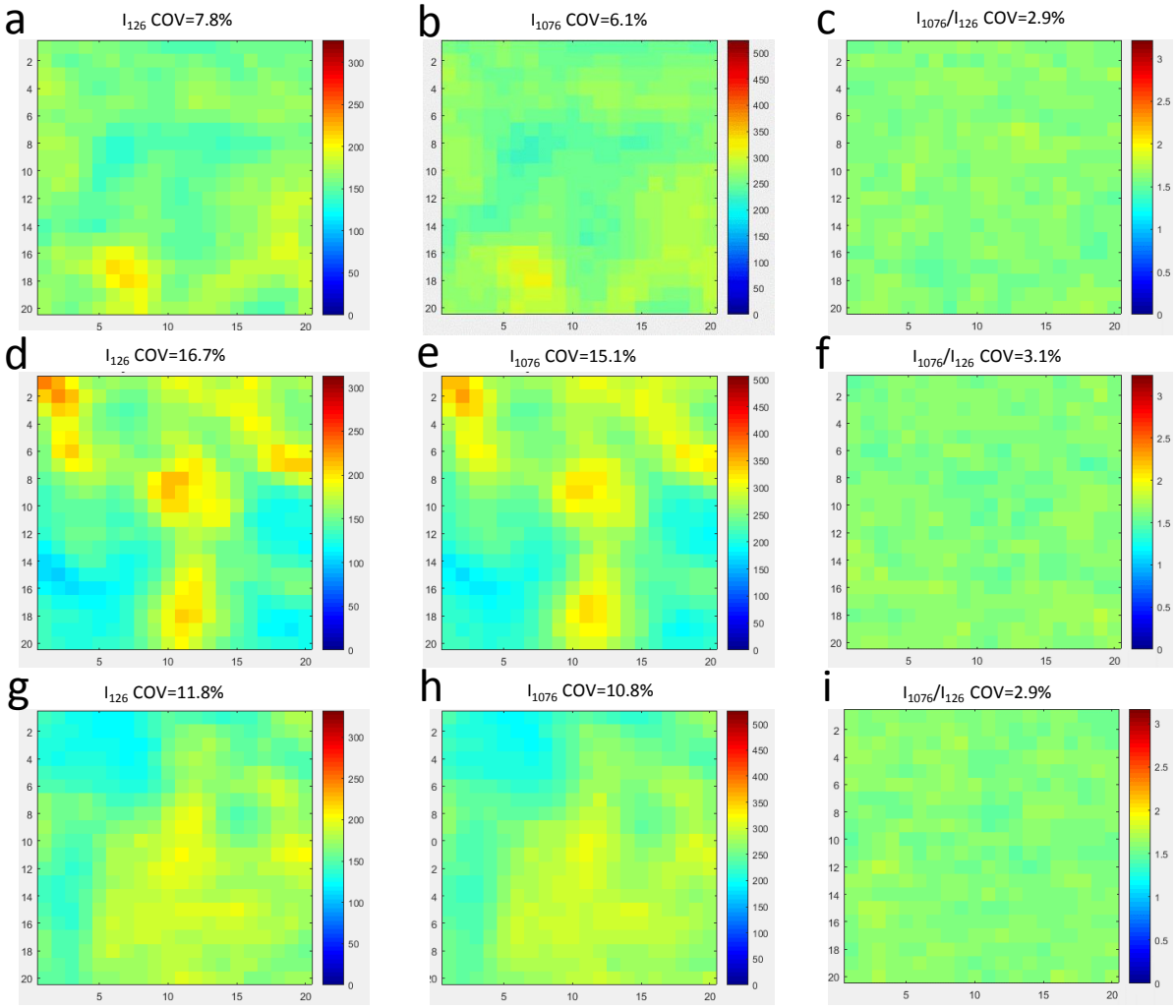

Figure 4.11 Maps of 4-MBA on dry AuNP/BC film tracking the band at 126 cm^{-1}, 1076 cm^{-1}, and the ratio between the two bands (I_{1076}/I_{126}) collected from three different areas (a-c in area 1, d-f in area 2, and g-i in area 3). All maps were collected across a 100 µm × 100 µm area and contained 400 single spectra.

Table 4-1 Comparison of CV values of recently reported SERS substrates

Substrate name	Preparation approach	Analyte	CV (%)	Ref
Nanoparticle cluster arrays	Template-guided self-assembly	4-Mercaptoaniline	12	270
Ordered nanopillars	Reactive ion etching followed by gold coating	Trans-1,2-bis(4-pyridyl)ethylene	8	271
Ligand-regulated silver nanoparticle films	Janus particle layer-by-layer assembly; Analytes in spin-on-glass	Crystal violet	4.3	241
Nanoarrays	E-beam lithography and nanotransfer printing	R6G	13	60
Nanostar on silica pillar	E-beam lithography and reactive ion etching	4-Mercaptoaniline	10	272

AuNP-decorated Si nanorod array	Reactive ion etching and metal assisted chemical etching	R6G	3.9-7.2	[269]
Ag nanostructure pattern	Electrolytic spray deposition	Crystal violet	11-24	[273]
Ordered Ag/Si Nanowires array	Nanosphere lithography, metal-assisted chemical etching and Ag sputter coating	4-Mercaptoaniline	9	[268]
AuNP/BC	In situ reduction	4-MBA	2.3	This study

We have illustrated the applicability of HS normalization for analytes that strongly associate with the AuNP surface via a thiol linkage. However, many analytes only weakly associate with the surface via electrostatic interactions. Due to their lower surface affinities, these analytes present the greatest challenge for SERS based quantitation. To illustrate the broad applicability of HS normalization, SERS maps were acquired by scanning wet AuNP/BC substrates exposed to four structurally similar chloroanilines: 2-chloroaniline (2-CA), 3-chloroaniline (3-CA), 4-chloroaniline (4-CA), and 2,4-dichloroaniline (2,4-DCA). Across this series, the analyte pK_a value changes systematically due to inductive and deductive substituent effects.[274] A pH-triggered approach was applied to enhance surface affinity and ensure consistent molecular alignment on the AuNP surfaces (Figure 4.12).[236] Maps for 2-CA constructed by tracking the intensity of its characteristic band at 556 cm^{-1}, ν_e at 126 cm^{-1}, and the background PL at 1820 cm^{-1} are shown in Figure 4.7k-o. The CV of the SERS signals prior to HS normalization was 61.4%, but was reduced to 7.2% following normalization. Similar improvements in point-to-point variability were observed for the other chloroanilines (Figure 4.13). It is interesting that the CV values were reduced to a level below 10% from whatever large number they initially were by ν_e normalization, which lowered the threshold for making reproducible SERS substrates that are eligible for rapid screen measurements.

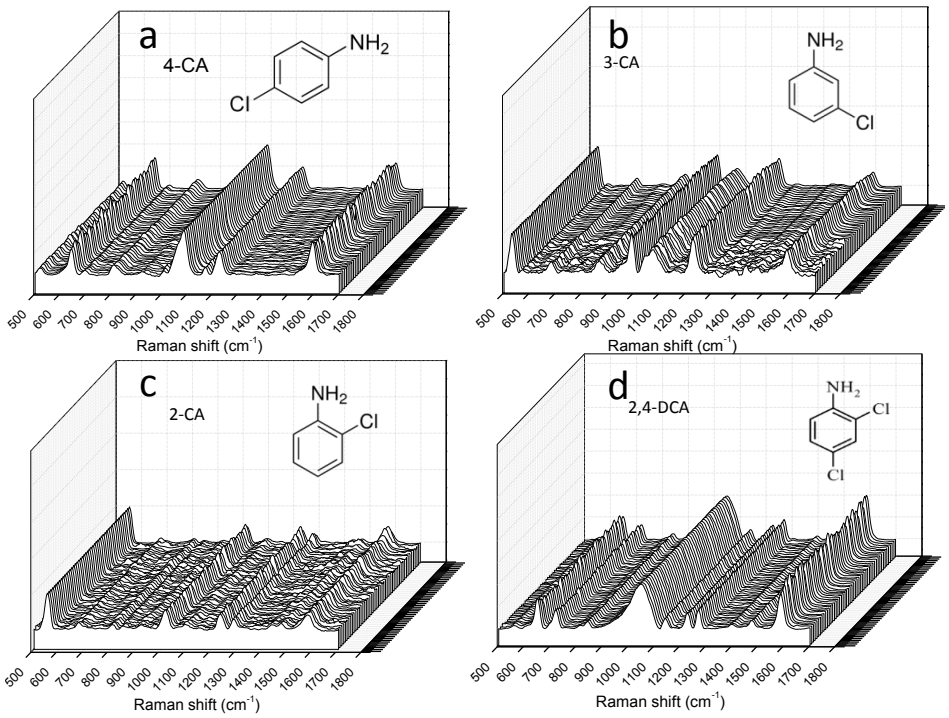

Figure 4.12 Fifty randomly selected Raman spectra from SERS maps acquired on wet AuNP/BC at pH<pK_a for a) 4-CA, b) 3-CA, c) 2-CA, and d) 2,4-DCA.

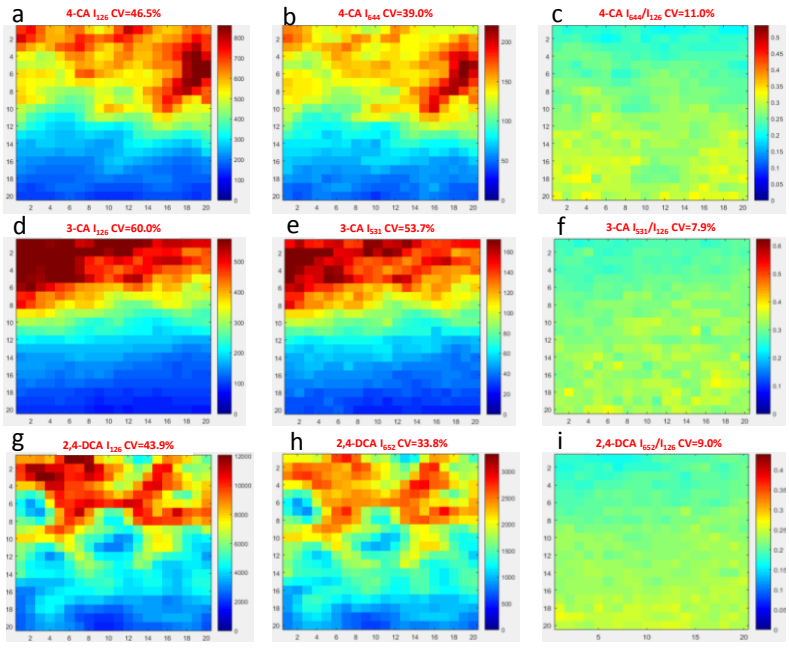

Figure 4.13 Maps of 4-CA on AuNP/BC platform tracking the band at a) 126 cm^{-1} (v_e), b) 644 cm^{-1}, and c) the ratio between the two bands (I_{644}/I_{126}). Maps of 3-CA on AuNP/BC platform tracking the band at d) 126 cm^{-1}, e) 531 cm^{-1}, and f) the ratio between the two bands (I_{531}/I_{126}). Maps of 2,4-DCA on AuNP/BC platform tracking the band at g) 126 cm^{-1}, h) 652 cm^{-1}, and

i) the ratio between the two bands (I_{652}/I_{126}). All maps were collected across a 100 μm × 100 μm area and contained 400 single spectra.

4.2.4 ν_e Enabled SERS Quantitation

The only factor that influences the ratio of the Raman and Rayleigh scattering signals should be the molecular concentration of the target analyte within a "hot-spot". To illustrate, a piece of AuNP/BC hydrogel was fixed at the bottom of a petri dish (Figure 4.14a). Immediately after adding 50 μM 4-MBA to the petri dish, SERS spectra were collected over time. Prior to 4-MBA addition only the ν_e signal was detected in the Raman spectrum (Figure 4.14b). Shortly following 4-MBA addition, the characteristic Raman bands of 4-MBA appear and increase with time. The HS normalized ratio ($=I_{1076}/I_{84}$) increases rapidly over the initial 30 min prior to plateauing after ~60 min (Figure 4.14c). The HS normalized reaction curves obtained using three batches of AuNP/BC virtually overlap, while substantial deviations were observed in the absence of HS normalization (Figure 4.14d). This result illustrates that HS normalization provides a reproducible means to monitor the adsorption kinetics of analytes onto a plasmonic nanoparticle surface. Such a result cannot be achieved by use of IEIS. However, this approach may report "false negative" when AuNP surfaces were blocked by inferent molecules (e.g. protein). Thus the decreased analyte signal was due to its increasing distance from AuNP surface rather than its decreasing concentration. In our future study, a combination between IEIS and ν_e normalization will be conducted to quantify both analyte concentration and distance from AuNP surface in the presence of interferent molecules. Figure 4.14 suggests that HS normalization can be used to study the adsorption and desorption kinetics of many natural or synthetic compounds onto and from plasmonic surfaces.

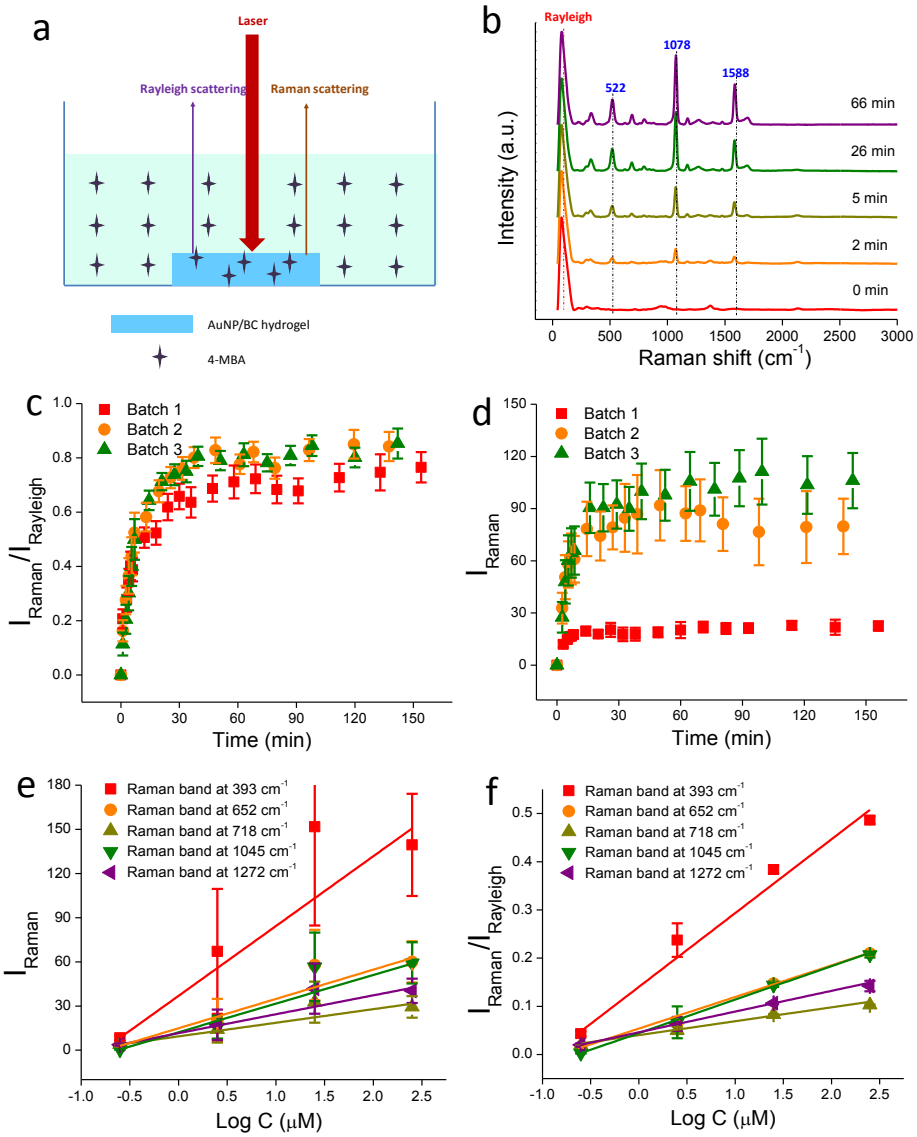

Figure 4.14 a) Schematic of the experimental setup for monitoring 4-MBA adsorption kinetics onto AuNP/BC. b) Selected SERS spectra of 4-MBA collected on AuNP/BC at different time after adding 4-MBA. c) Variation of the ratio between the Raman band at 1076 cm^{-1} and ν_e at 84 cm^{-1} as a function of time. d) Variation of the Raman band at 1076 cm^{-1} as a function of time. e) Variation of non-normalized SERS intensities of 2,4-DCA as a function of their logarithmic concentrations. f) Variation of normalized SERS intensities of 2,4-DCA as a function of their logarithmic concentrations. Error bars reflect the standard deviation of SERS intensities from three collected average spectra. Each average spectrum is the average of 400 spectra in a 100 µm × 100 µm SERS map.

To evaluate how analyte concentration alters the intensity of the SERS spectra, the concentrations of four chloroanilines were varied over a range of 0.25-250 µM and their SERS spectra were collected (Figure 4.15). In the absence of HS normalization, the SERS intensities of

the five prominent bands for 2,4-DCA generally increase with concentration (0.25-250 μM; Figure 4.14e), but exhibit substantial variability. Following HS normalization, the SERS intensities of these characteristic bands exhibit improved linear relationships versus their logarithmic concentrations (R^2>0.95) and substantially reduced error (Figure 4.14f). Similar results were achieved with three other chloroanilines (Figure 4.16) and a series of organic molecules (e.g., anilines with different functional groups, melamine, MGITC; Figure 4.17). As shown, the Raman bands for these compounds primarily occur between 300-1700 cm^{-1} (marked by the red dotted box). Across this suite of chemicals with highly differential functional groups (-Cl, -Br, $-NH_2$, -HS, $-NO_2$), molecular weights (126-486 g/mol), and ring structures (benzene, triazine), ν_e was consistently present at a fixed position with a fixed full width half maximum (FWHM) of 52 cm^{-1}. These results show that HS normalization significantly improved the quantitation performance of SERS.

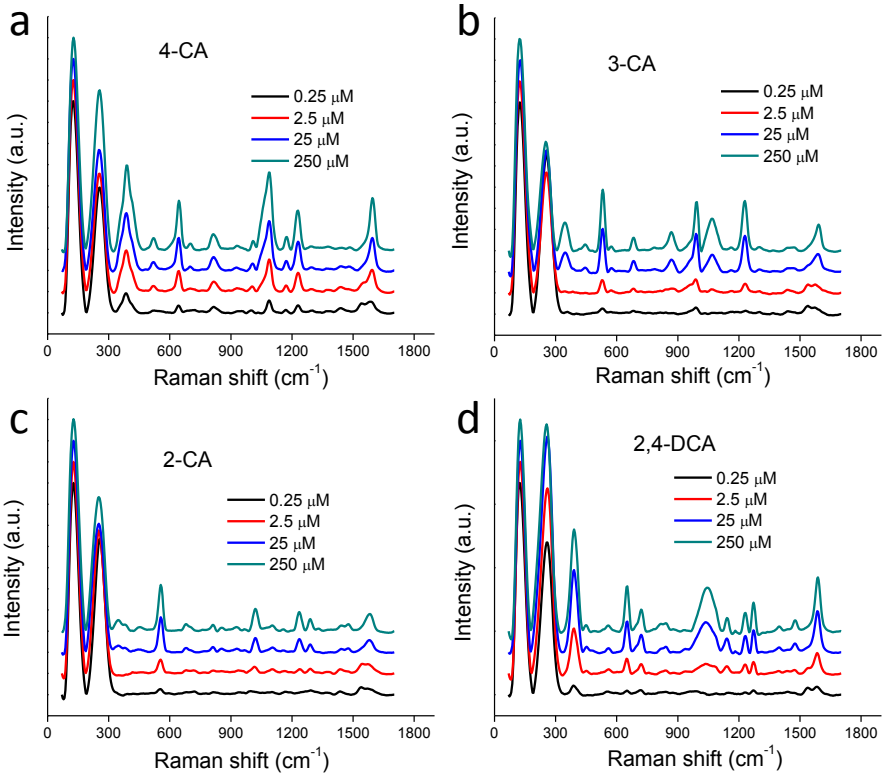

Figure 4.15 SERS spectra of a) 4-CA, b) 3-CA, c) 2-CA, and d) 2,4-DCA acquired on AuNP/BC platform with concentrations from 0.25 - 250 uM (each spectrum is an average of 400 single spectra across a 100 µm × 100 µm area; the spectra were collected at pH = 2.3, 1,9, 1.9, and 1.7, respectively). The spectra are manually baselined for visual convenience.

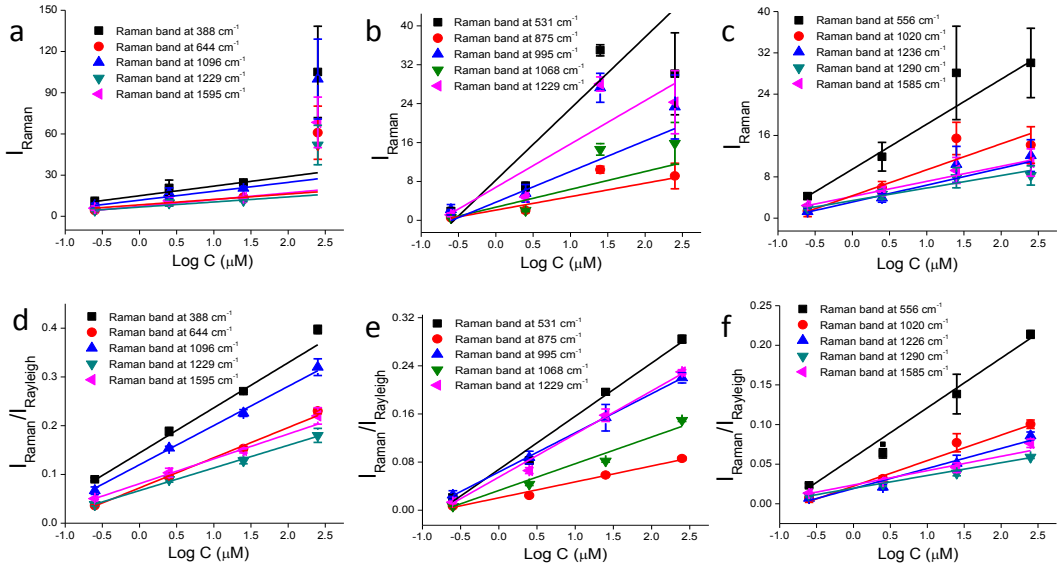

Figure 4.16 Variation of non-normalized SERS intensities of a) 4-CA, b) 3-CA, and c) 2-CA as a function of their logarithmic concentrations. Variation of normalized SERS intensities of d) 4-CA, e) 3-CA, and f) 2-CA as a function of their logarithmic concentrations (error bars

reflect the standard deviation of SERS intensities from three collected average spectra. Each average spectrum is the average of 400 spectra in a 100 µm × 100 µm SERS map. The numbers shown in the figures correspond to the Raman shift of the Raman bands that were monitored here).

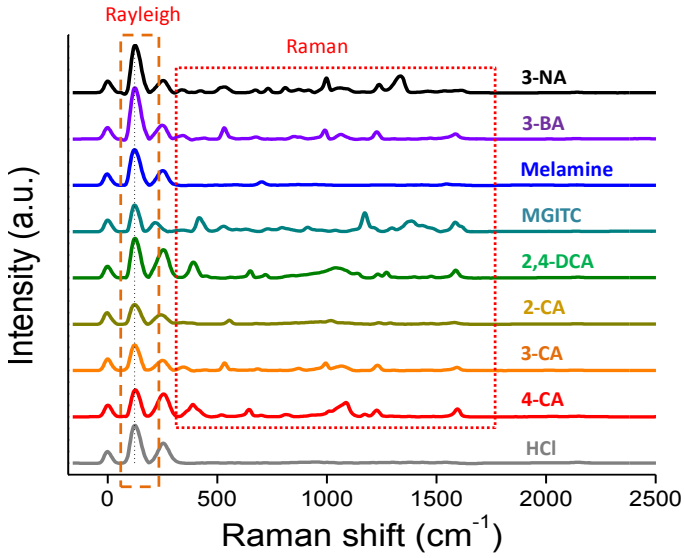

Figure 4.17 SERS spectra of multiple analytes on AuNP/BC platform acquired at pH values below the pK_a. The spectra were manually baseline corrected for visual convenience.

4.2.5 HS Normalization Enables Analyte Quantitation Under Highly Variable Conditions

We have illustrated the capacity for HS normalization to quantify analyte adsorption to stable SERS substrates. To illustrate how HS normalization can be applied under dynamic conditions, we used it to quantify the kinetics of 4-MBA adsorption onto suspended AuNPs. The kinetics of AuNP aggregation in a water/ethanol co-solvent containing 4-MBA are easily controlled and were recently optimized for the production of SERS pH probes.[275] The lower dielectric constant of water/ethanol co-solvent, relative to water alone, facilitates 4-MBA mediated AuNP aggregation.[276] Following 4-MBA addition, the 4-MBA SERS signal increases only slightly during the first 40 minutes and then increases up to 162 min before plateauing. (Figure 4.18a). It is well recognized that the increase in the number of 4-MBA molecules on the AuNP surface and the formation of "hot spots" due to AuNP aggregation simultaneously contribute to the enhancement

in the SERS signal with time, but these two effects cannot be differentiated using existing approaches.

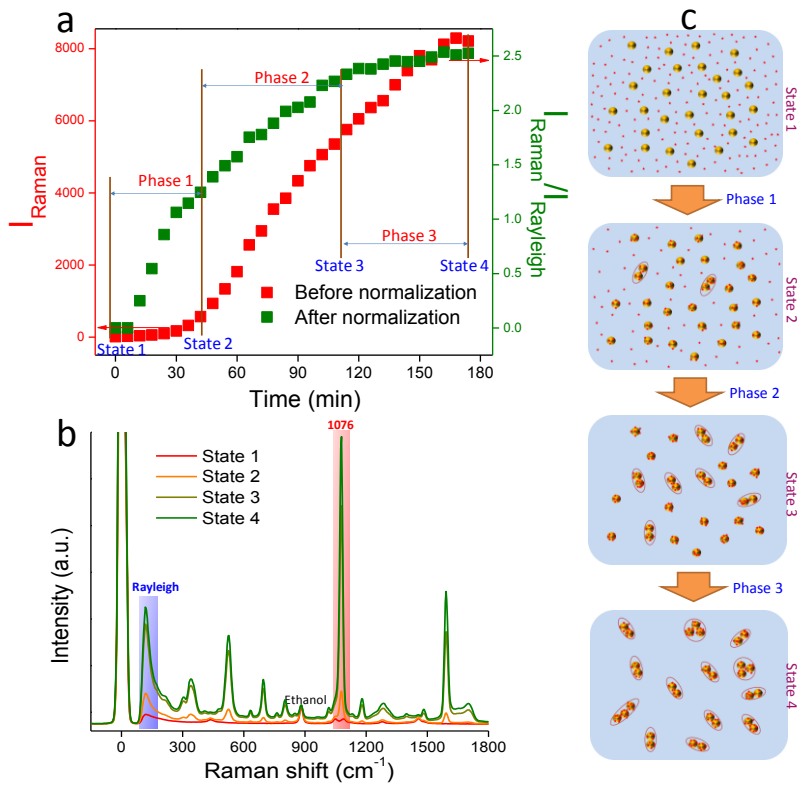

Figure 4.18 a) Variation of SERS intensity of the Raman band at 1076 cm^{-1} of 4-MBA and the ratio of the Raman band at 1076 cm^{-1} to ν_e at 126 cm^{-1} (I_{1076}/I_{126}) as a function of time; b) SERS spectra collected from the 4-MBA, AuNPs, and co-solvent system at the different stages marked in Fig. 5a; c) Schematic of dynamic process of 4-MBA sorption to AuNP surface and AuNP aggregation.

As shown by the green curve in Figure 4.18a, the HS normalized ratio (=I_{1076}/I_{126}) rapidly increases immediately after mixing of the AuNP suspension and 4-MBA solution (Phase 1). This increase continued until 114 min, albeit with a slower rate (Phase 2), prior to plateauing (Phase 3). To explain this process a schematic is shown in Figure 4.18c. At the very beginning, AuNPs were present as monomers with no 4-MBA on their surfaces (State 1). In State 1, the SERS spectrum only exhibits the Raman bands from ethanol (Figure 4.18b). State 2 is reached following 4-MBA adsorption in the first 40 min. In State 2, increasing numbers of 4-MBA molecules adsorb onto the

AuNP surface, but most AuNPs remain as monomers. In this state, the Raman bands of 4-MBA appear, but are weak due to lack of "hot spots". In Phase 2, the surfaces become saturated with 4-MBA and large numbers of SERS "hot spots" form due to AuNP aggregation. This results in a very strong 4-MBA SERS signal for State 3. In Phase 3, fewer 4-MBA molecules remain available to associate with the AuNPs, yet "hot spots" continue to form. The increase in the 4-MBA SERS signal during Phase 3 is attributed primarily to "hot spot" formation and not continued 4-MBA adsorption.

4.3 Conclusions

Theoretical and experimental analysis suggests that ASE light elastically scattered by a SERS "hot spot" quantitatively reflects the integrated strength of the localized electromagnetic field. The ratio between the elastic and inelastic scattering signals is dependent on the number of the target analytes (N_A) within a "hot spot" no matter how the size, shape, pattern, and density of plasmonic nanostructures varies. Surface enhanced Rayleigh scattering can be applied as a truly intrinsic internal standard for SERS. Following HS normalization, the uniformities of colloidal, hydrogel, and solid SERS substrates are improved without additional cost. Internal standards based on surface plasmon enhanced elastic scattering signals are truly intrinsic to the plasmonic nanostructures and provide new features that improve quantitative SERS analysis: (1) ultimate photo-stability (i.e., not photo-bleachable); (2) minimal spectral interference by analyte Raman signals; (3) no spatial competition with analyte molecules for SERS "hot spots"; (4) reduced SERS substrate preparation costs by avoiding the incorporation of extrinsic reference probe molecules; (5) universal applicability for a suite of SERS substrates; and (6) the capacity to differentiate analyte adsorption and "hot spot" formation under dynamic conditions. Accurate measurement of

the surface concentrations of analytes on non-stable colloidal plasmonic nanoparticles is important for many *in vivo* applications and is now possible via HS normalization.

4.4 Methods

4.4.1 Materials

Gold (III) chloride trihydrate ($HAuCl_4 \cdot 3H_2O$), sodium citrate tribasic dehydrate ($Na_3Cit \cdot 2H_2O$), silver nitrate ($AgNO_3$), 4-chloroaniline (4-CA, 98%), 3-chloroaniline (3-CA, 99%), 2-chloroaniline (2-CA, 98%), 2,4-dichloroaniline (99%), 3-bromoaniline (3-BA), 3-nitroaniline (3-NA), melamine, and 4-mercaptobenzoic acid (4-MBA) were purchased from Sigma-Aldrich. Sodium borohydride ($NaBH_4$), hydrochloride acid (HCl) and ethanol were purchased from Fisher Scientific. Malachite green isothiocyanate (MGITC) was acquired from Invitrogen Corp. (Grand Island, NY). Thiolated poly(ethylene glycol) (HS-PEG; 5 kD) was purchased from Nanocs.

4.4.2 Transmission Measurement

SERS spectra of DI water were collected using a transmission mode Raman system equipped with an inverted microscope (WITec alpha 300 RSA+). Two identical objectives were used (20×, NA=0.4) to focus into the sample with a spot size of ≈2.4 um, and collect the signal through the sample. The laser excitation wavelength was 785 nm. We employed a longpass filter (cut-off wavelength: 68 cm^{-1}) before the detector to generate pseudo peak ν_e, and a bandpass filter (center wavelength: 785 nm, Full Width-Half Max: 3 nm) was placed to block the elastic scattering process of ASE fields from the laser. Before the laser and detector, there were two small confocal pinhole apertures that increase optical resolution and suppress out-of-focus light.

4.4.3 Backscattering Measurement

All SERS spectra except the laser emission profile shown in Figure 4.1c were acquired using a confocal Raman spectroscopy system in backscattering mode (WITec alpha 500R). SERS maps were generally collected with a 10× objective. Each SERS map consists of 20×20 spectra across a 100×100 μm^2 area. The laser wavelength was 785 nm and integration time was 0.5 s. The Raman signal was dispersed by a 300 gr/mm grating and detected using a Peltier charge-coupled device. To make HS normalized maps, spectra from a SERS map were imported into Matlab 2015 (The Mathworks, USA) and baseline corrected using in-house scripts. For the maps using PL as normalizing factor, only the dark background (Figure 4.1e) was subtracted. As shown in Figure 4.19, the Au-Cl Raman band at 267 cm^{-1} does not influence ν_e even when an edge filter cutting at 126 cm^{-1} was employed. Integrated intensities from 106-146 cm^{-1} for ν_e at 126 cm^{-1} or 64-104 cm^{-1} for ν_e at 84 cm^{-1} were employed as the normalizing factor. The ratio of the analyte band to ν_e was projected as a normalized SERS map using Matlab.

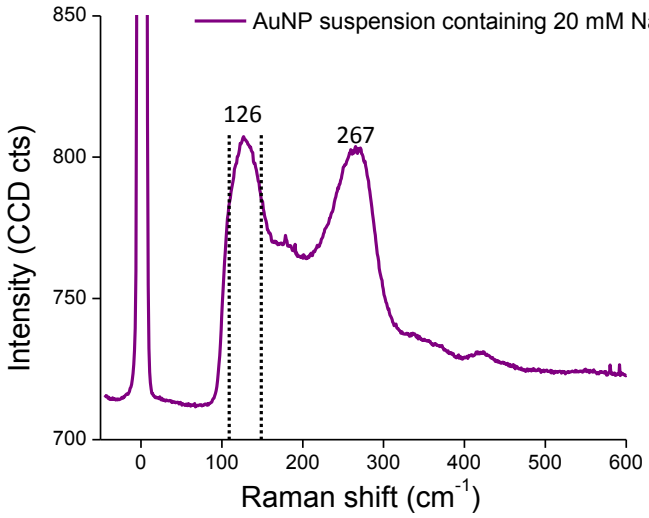

Figure 4.19 The SERS spectrum of AuNP colloid collected at 60 min after adding 20 mM NaCl. The band at 267 cm^{-1} corresponds to Au-Cl.

4.4.4 Preparation of SERS Substrates

Preparation and characterization of the AuNP/BC platform was described previously.[236] Briefly, sixteen pieces of BC (0.5 cm × 0.5 cm) were immersed in 30 mM $HAuCl_4$ solution for 30 s and then transferred to boiling Na_3Cit solution (1.2 mM unless otherwise denoted) for 1.5 h. Scanning electron microscopy images, energy dispersive X-ray spectroscopy, and UV-VIS extinction spectra are shown in Figure 4.20 & Figure 4.21 and in our previous publication.[236] AgNP/BC was prepared by adding 0.7 mL of $NaBH_4$ (25 mM unless otherwise denoted) into a tube containing 0.7 mL $AgNO_3$ and 20 pieces of BC followed by vortex mixing. The preparation method for 14 nm AuNP seeds and 50 nm AuNPs is briefly described as follows: AuNP seeds were synthesized by adding Na_3Cit solution (final conc.: 3.88 mM) to boiling $HAuCl_4$ solution (final conc.: 1 mM) for 15 min. 50 nm AuNPs were synthesized by seed-mediated growth. 100 mL $HAuCl_4$ solution (final conc.: 0.254 mM) was brought to boil, to which 0.818 mL seed solution and 0.44 mL citrate (38.8 mM) were subsequently added. 4-MBA coated AuNP aggregate suspension was prepared by ethanol-induced aggregation followed by thiolated poly(ethylene) glycol (HS-PEG) functionalization.[275]

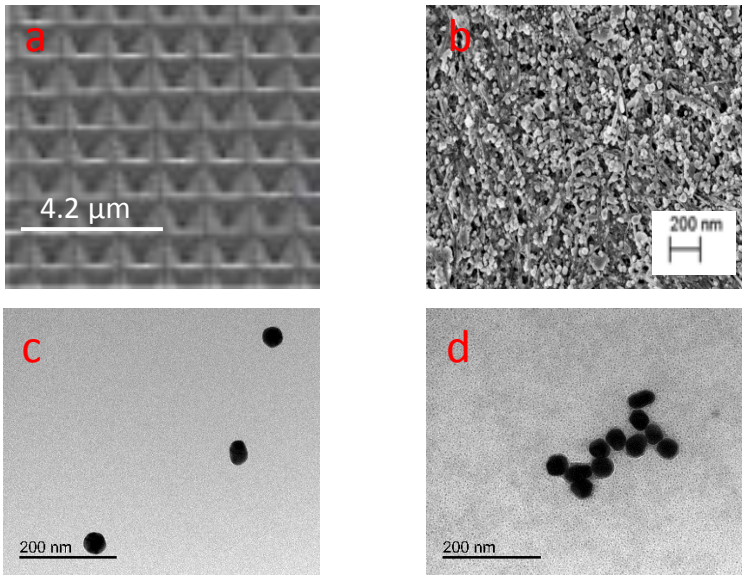

Figure 4.20 SEM images of a) Klarite and b) AuNP/BC nanocomposite in the dry state.[236, 277] TEM images of c) AuNP monomers and d) AuNP aggregates.

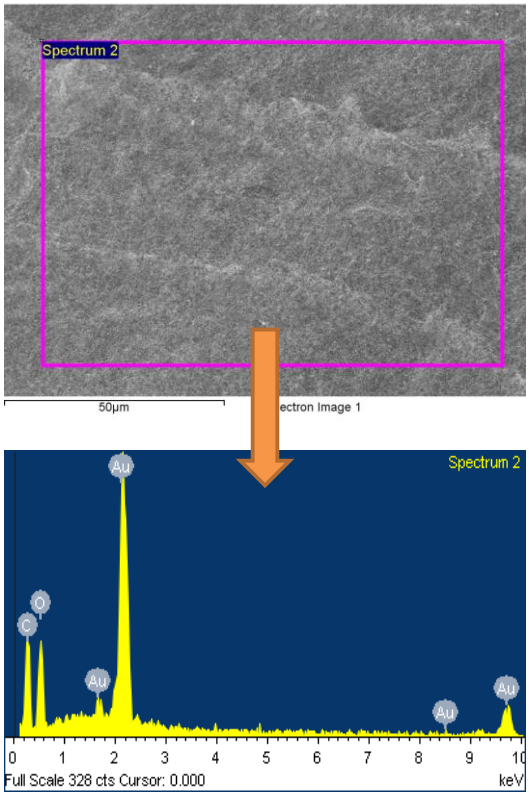

Figure 4.21 Scanning electron microscopy (SEM) image and energy dispersive X-ray spectroscopy (EDS) of AuNP/BC nanocomposite.

4.4.5 Manipulation of Hot Spot Density in AuNP/BC Substrate

One piece of AuNP/BC (0.5×0.5 cm^2) hydrogel was immersed in 5 mL 4-MBA ethanol solution (1 mM) for 3 h. SERS maps were collected from the wet AuNP/BC hydrogel in air every 20 min until 60 min. After the AuNP/BC was completely dry, SERS maps were collected using both 10× and 100× objectives.

4.4.6 pH-Triggered Detection of Four Chloroanilines

Sample aliquots of 1 mL of 4-CA, 3-CA, 2-CA, or 2,4-DCA in ethanol solutions with a concentration of 1 mM were added to 3 mL aqueous solution with pH pre-adjusted to values below their pK_a. The final ethanol concentration (25%) had minimal influence on SERS detection (data not shown). One piece of AuNP/BC (0.5×0.5 cm^2) hydrogel was immersed in chloroaniline solution. After vortex mixing for 30 s, the AuNP/BC hydrogel was taken out for SERS measurement.

4.4.7 Quantitation of Chloroanilines

To determine the dynamic range of four chloroanilines, 1 mL 4-CA, 3-CA, 2-CA, and 2,4-DCA in ethanol with concentrations from 1-1000 μM was added to 3 mL aqueous solution with pH preadjusted to 1.7-2.3. One piece of AuNP/BC (0.5×0.5 cm^2) hydrogel was immersed in the chloroaniline solution. After vortex mixing for 30 s, the AuNP/BC hydrogel was taken out for Raman measurement.

4.4.8 SERS Spectra Collection with a Variety of Analytes and Substrates

SERS spectra of a variety of analytes were acquired using an AuNP/BC platform via a pH-triggered approach.[236] In this process, 1 mL of analyte in ethanol (1 mM) was added to 3 mL aqueous solution of pre-adjusted pH to ensure that solution pH values were below the pK_a. The

final pH values were: MGITC: 5.4; 4-CA: 2.3; 3-CA: 1.9; 2-CA: 1.9; 2,4-DCA: 1.7; Melamine: 2.3; 3-BA: 2.3; and 3-NA: 1.8. One piece of AuNP/BC (0.5×0.5 cm^2) hydrogel was immersed in each solution. After vortex mixing for 30 s, the AuNP/BC hydrogel was taken out for Raman measurement. SERS spectra of blank AuNP/BC were collected at pH values of 5.4 and 2.3 as negative controls.

4.4.9 Monitoring 4-MBA Adsorption to Stable and Dynamic SERS substrates

A piece of AuNP/BC was attached to the bottom of a small petri dish. After collecting the first SERS map (blank), 6 mL 4-MBA ethanol/water solution (50 μM) was added. SERS spectra were collected every 1 min for the first five spectra, every 5 min for the next five spectra, every 10 min for the next five spectra, and every 20 min for the remaining four spectra. To monitor 4-MBA adsorption to aggregating AuNP surface, 0.5 mL 4-MBA ethanol solution (100 μM) was added into 0.5 mL AuNP suspension. After vortex mixing, the mixture was transferred to a quartz cell and scanned. SERS maps (20 × 20 points, 1000×1000 μm^2, 0.5 s int. time) were collected every 5 min until 180 min. Before calculating the ratio between the Raman and Rayleigh bands, the blank spectrum was subtracted from each SERS spectrum to exclude the influence of ASE photons scattered by water.

Chapter 5 Surface Enhanced Rayleigh Band Intensity as an Alternative Evaluation Parameter for SERS Substrate Performance

Haoran Wei,[1,2,3] Alexis McCarthy,[4] Junyeob Song,[5] Wei Zhou,[5] Peter J. Vikesland[* 1,2,3]

[1] Department of Civil and Environmental Engineering, Virginia Tech, Blacksburg, Virginia;

[2] Virginia Tech Institute of Critical Technology and Applied Science (ICTAS) Sustainable Nanotechnology Center (VTSuN), Blacksburg, Virginia;

[3] Center for the Environmental Implications of Nanotechnology (CEINT), Duke University, Durham, North Carolina;

[4] Department of Chemistry, Virginia Tech, Blacksburg, Virginia

[5]Department of Electrical and Computer Engineering, Virginia Tech, Blacksburg, Virginia

(This chapter has been published in ***Faraday Discussions***.[278] – Reproduced by permission of the Royal Society of Chemistry. The publisher - the Royal Society of Chemistry does not require formal reproduction permission when the article is used in the dissertation of the authors.)

Abstract

The performance of surface-enhanced Raman spectroscopy (SERS) substrates is typically evaluated by calculating an enhancement factor (EF). However, it is challenging to accurately calculate EF values since the calculation often requires use of model analytes and requires assumptions about the number of analyte molecules within the laser excitation volume. Furthermore, the measured EF values are target analyte dependent and thus it is challenging to compare substrates with EF values obtained using different analytes. In this study, we propose an alternative evaluation parameter for SERS substrate performance that is based on the intensity of the surface plasmon enhanced Rayleigh band (I_{Rayleigh}) that originates from the amplified spontaneous emission (ASE) of the laser. Compared to EF, I_{Rayleigh} reflects the enhancing capability of the substrate itself, is easy to measure without use of any analytes, and is universally applicable for the comparison of SERS substrates. Six SERS substrates with different states (solid, suspended in liquid, and hydrogel), different plasmonic nanoparticle identities (silver, gold), as well as different nanoparticle sizes and shapes were used to support our hypothesis. The results show that there are excellent correlations between measured SERS intensities and I_{Rayleigh} as well as between SERS homogeneity and the variation of I_{Rayleigh} acquired with the six SERS substrates. These results suggest that I_{Rayleigh} can be used as an evaluation parameter for both SERS substrate efficiency and reproducibility.

5.1 Introduction

Surface-enhanced Raman spectroscopy (SERS) has been applied as an ultrasensitive analytical tool for a variety of analytes.[21, 26, 279, 280] The success of a SERS assay largely relies on the performance of a SERS substrate that consists of a suite of suspended or surface-bound plasmonic

nanostructures. The calculated enhancement factor (EF) is commonly used to describe the performance of SERS substrates. The most commonly calculated EF for evaluating SERS substrate performance, also called the SERS substrate EF (SSEF), is defined as the concentration normalized ratio between the surface-enhanced Raman signal (I_{SERS}) and the normal Raman signal (I_{Normal}) of a single analyte molecule.[271, 281-284] The value of EF is obtained experimentally using Eq. 5.1, where I_{SERS} and I_{Normal} are the Raman signals collected using the SERS substrate and a high concentration analyte solution. N_{SERS} and N_{Normal} are the number of analyte molecules within the excitation volume of the laser when it probes the SERS substrate or analyte solution, respectively.[271, 281, 283-285]

$$SSEF = \frac{I_{SERS} N_{Normal}}{I_{Normal} N_{SERS}} \qquad \text{Equation 5.1}$$

Although SSEF is very useful for evaluating SERS substrate performance, it is not trivial to obtain its value experimentally, mainly due to the difficulty of estimating N_{SERS} accurately.[282, 285] It is generally assumed that analyte molecules form a monolayer that fully covers the plasmonic nanoparticle surface. This is an assumption that sometimes deviates substantially from reality.[271, 284, 285] For example, when a drop of analyte solution is applied to a substrate surface, the analyte molecules can form ~10 nm thick multilayers leading to an overestimation of EF.[283] In addition, the distribution of analyte molecules across a SERS substrate is often not uniform due to the 'coffee ring' effect. In this situation, higher EF values obtained near the periphery relative to the center of the analyte covered area do not fairly reflect the uniformity of the SERS substrate.[271] Even if the analyte molecules truly form a homogeneous monolayer on the SERS substrate, one still has to estimate the area a single molecule occupies on the surface. Such information may not be universally available for all potential analytes as it is highly dependent on the orientation of the analyte molecules relative to the plasmonic surface.[286] For example, crystal violet (CV) – a

commonly used Raman dye - exhibits an orientation parallel to the silver surface, while benezenethiol – another model Raman analyte – orients perpendicularly. This difference results in different molecule numbers within the excitation volume of the laser.[287, 288] In some cases such as single molecule SERS (SMSERS), the focus is on molecules located within SERS hot spots that contribute most to the SERS signals. The EF values obtained within SERS hot spots can be five orders of magnitude larger than the average EF of the whole substrate.[271, 285] Another prerequisite for accurate estimation of N_{SERS} is to fully characterize the morphology of the plasmonic nanostructures that allows us to know the "effective area" the analyte molecules occupy within the excitation laser spot.[271, 288, 289] However, knowledge of this parameter can be extremely challenging when the shapes and sizes of the plasmonic nanostructures of a given SERS substrate are highly heterogeneous. Because of these factors, the estimation of N_{SERS} brings great uncertainty and difficulty to the calculation of EF values.

To circumvent the complexity involved in estimating N_{SERS}, Le Ru et al. proposed the analytical enhancement factor (AEF) as a means to evaluate the efficiency of SERS as a tool for specific analytes.[286] AEF is defined by Eq. 5.2, where c_{normal} and c_{SERS} are the concentrations of the analyte under non-SERS and SERS conditions.

$$AEF = \frac{I_{SERS} c_{normal}}{I_{normal} c_{SERS}} \qquad \text{Equation 5.2}$$

In contrast to SSEF, AEF is particularly useful for colloidal SERS substrates.[290] For solid substrates, large variations in AEF are expected due to variations in the way analyte molecules are added to the substrates, as such variations affect analyte adsorption to the substrate surface. Analyte adsorption to a SERS substrate is generally described using the Langmuir isotherm,[36, 291] such that the coverage of the analyte on the metal surface is only linearly correlated with the analyte solution concentration over a low concentration range. At concentrations above this linear

range, surface coverage of analyte molecules can be significantly overestimated. For example, in a recent study, Fraire et al. reported two AEF values that varied over five orders of magnitudes (1×10^8 vs. 3×10^3) corresponding to two different c_{SERS} (i.e., 10^{-11} vs. 10^{-7} M).[290] Accordingly, AEF reflects the combined properties of both the SERS substrate and the number of analyte molecules on the surface rather than the intrinsic enhancing capability of the SERS substrate. As Le Ru stated, "It is not a good characterization of the SERS substrate itself, and it cannot be used to easily compare the performances of different substrates."

The limit of detection (LOD) for specific analytes is important in terms of the practical applications of SERS. However, in a number of situations (e.g., for the detection of hydrophobic analytes such as atrazine or polyaromatic hydrocarbons), the LOD is not defined by the enhancing capability of the SERS substrate, but instead by the affinities of the analytes to the substrate surface.[31, 174, 178, 236]

For all of the aforementioned reasons, a parameter that can evaluate the enhancing capability of a SERS substrate both quickly and accurately is desired. In this study, we propose an alternative evaluation parameter for SERS substrate performance that is based on the surface plasmon enhanced Rayleigh band ($I_{Rayleigh}$). $I_{Rayleigh}$ reflects the integrated enhancing capability of the SERS substrate itself. Importantly, the determination of the $I_{Rayleigh}$ value does not require analytes or extensive characterization of the substrate morphology. $I_{Rayleigh}$ is a very simple and cost-effective evaluation approach to quickly compare newly developed SERS substrates. It is expected to work for any SERS substrate regardless of their form or morphology. This low wavenumber (< 150 μm) pseudo band, described in detail in a recently submitted manuscript, occurs due to the action of the longpass filter of the Raman instrument on the tail of the amplified spontaneous emission (ASE) of the laser. As illustrated in Figure 5.1, the electromagnetic field of the incident laser ($E_0(\omega_0)$)

excites the collective oscillation of the conductive electrons within a SERS "hot spot" and this is where the highest SERS enhancement occurs.[292-294] The electromagnetic fields for both Raman scattering and Rayleigh scattering ($E_0(\omega_{Rayleigh})$) are enhanced by the same hot spot and reradiated as scattered fields ($E_S(\omega_{Raman})$ and $E_S(\omega_{Rayleigh})$). Recently, it was experimentally shown that Rayleigh scattering from analytes located in a SERS "hot spot" is enhanced by the same electromagnetic mechanism as Raman scattering.[249] The ratio of the enhanced Raman intensity relative to the enhanced Rayleigh intensity is described by Eq. 5.3, where N_A is the number of analyte molecules in the hot spot, N_B is the number of background molecules in the hot spot, α_A is the Raman scattering polarizability of analyte molecules, α_B is the Rayleigh scattering polarizability of background molecules, $I_0(\omega_0)$ and $I_0(\omega_{Rayleigh})$ are the incident light intensity of the laser at frequency ω_0 and ASE at frequency ω_{ASE}. In a SERS experiment, all of these parameters except N_A remain constant. In other words, $I_{Rayleigh}$ is proportional to I_{Raman}, and this is our basis for applying $I_{Rayleigh}$ to evaluate the performance of a SERS substrate. We note that the chemical enhancement mechanism is not considered in this study since the electromagnetic enhancement mechanism is typically the dominant one for SERS.[54, 295-297]

$$\frac{I_{Raman}}{I_{Rayleigh}} = \frac{E_S^2(\omega_{Raman})}{E_S^2(\omega_{Rayleigh})} = \frac{N_A \alpha_A^2(\omega_{Raman}) \mathrm{I}_0(\omega_0)}{N_B \alpha_B^2(\omega_{Rayleigh}) \mathrm{I}_0(\omega_{Rayleigh})} \qquad \text{Equation 5.3}$$

To determine if $I_{Rayleigh}$ can be used to predict SERS substrate performance, six SERS substrates were produced: gold nanoparticle (AuNP) aggregates, a commercial SERS substrate, two gold nanoparticle/bacterial cellulose (AuNP/BC) nanocomposites, and two silver nanoparticle/bacterial cellulose (AgNP/BC) nanocomposites. These SERS substrates were selected because they represent substrates suspended in liquid, solid, or hydrogel states, with different NP identities (gold and silver), and different NP shapes and sizes. These SERS substrates were initially scanned using a 785 nm laser without addition of an external analyte and $I_{Rayleigh}$ was recorded. Following

exposure to 4-mercaptobenzoic acid (4-MBA), the substrates were scanned a second time and the SERS intensity of 4-MBA (I_{Raman}) was recorded. In this manner, the relationship between $I_{Rayleigh}$ and I_{Raman} was established. In addition to SERS intensity, reproducibility is another important factor that dictates SERS substrate performance.[298-300] Accordingly, the variation of $I_{Rayleigh}$ across a Raman map before analytes were added was recorded and compared with the variation in the Raman signal across a SERS map after 4-MBA addition. $I_{Rayleigh}$ is expected to be a predictive factor of both SERS substrate efficiency as well as homogeneity.

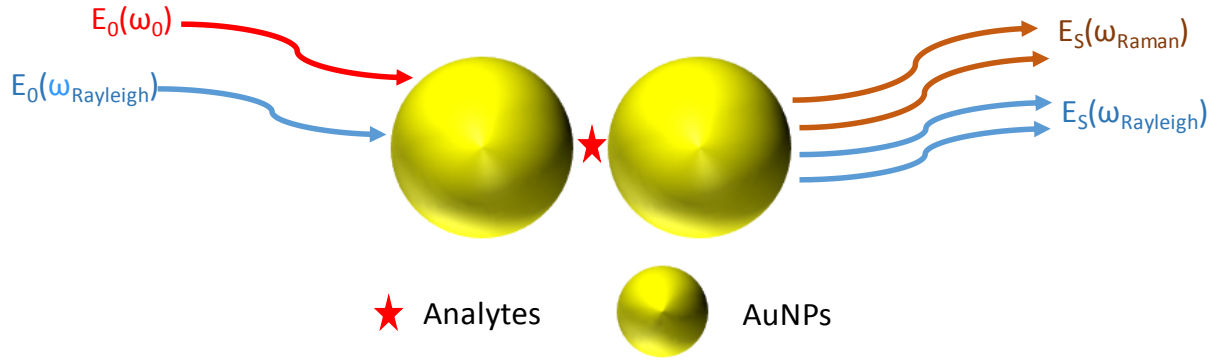

Figure 5.1 Schematic of surface-enhanced Raman and surface-enhanced Rayleigh scattering from the same SERS "hot spot".

5.2 Experimental

5.2.1 Preparation of BC-Based Substrates

AuNP/BC substrates were prepared using the following procedure:[301] 20 pieces of BC (0.5 cm × 0.5 cm) were immersed in 0.7 mL of 30 mM gold (III) chloride trihydrate ($HAuCl_4 \cdot 3H_2O$) solution (Sigma-Aldrich). Following 30 s vortex mixing, the mixture was transferred to 50 mL of sodium citrate tribasic dehydrate ($Na_3Cit \cdot 2H_2O$) solution (Sigma-Aldrich) and then simmered for 1 h. Finally, the obtained nanocomposites were rinsed with copious amounts of DI water. Based on the concentrations of Na_3Cit (1.2 mM or 12 mM) used, the nanocomposites obtained were named AuNP/BC-1.2 and AuNP/BC-12, respectively.

AgNP/BC substrates were prepared using the following procedure: 20 pieces of BC were immersed in 0.7 mL of 25 mM silver nitrate solution (Sigma-Aldrich). Subsequently, 0.7 mL of 25 mM or 250 mM sodium borohydride solution were added. Following vortex mixing for 30 s, the mixture was kept at room temperature for 1 h and then washed with copious amounts of DI water. Based on the concentration of $NaBH_4$ added (25 mM or 250 mM), the nanocomposites were named AgNP/BC-25 or AgNP/BC-250.

5.2.2 Preparation of AuNP Aggregate

AuNP monomer (35±1 nm) suspension was synthesized via seed-mediated growth.[215] AuNP aggregates (A-AuNPs) were then synthesized using the following procedure[302]: 0.5 mL 4-MBA (Sigma-Aldrich) ethanol solution (100 μM) was added into 0.5 mL AuNP monomer suspension. After 100 min, 100 μL of 500 μM thiolated poly(ethylene) glycol (HS-PEG) aqueous solution (Nanocs.) was added to the suspension to endow the aggregates with colloidal stability. After 20 min, the mixture was centrifuged for 15 min at 3000 rcf three times to remove excess reactants.

5.2.3 Exposing SERS Substrates to 4-MBA

The commercial SERS substrate (Ocean Optics) and the four nanocomposites were immersed in 5 mL 4-MBA in ethanol (1 mM) for 1-3 h. Following removal from the solution, the SERS substrates were air dried for 1 h and subsequently scanned by Raman spectroscopy. For A-AuNPs, 4-MBA was added to the substrate during the synthesis process as described in Section 5.2.2.

5.2.4 Instrumentation

All of the Raman spectra were collected using a commercial Raman spectrometer (Alpha500R, WITec). Backscattered photons were dispersed with a 300 groove mm^{-1} grating and detected by a Peltier CCD. The laser wavelength used was 785 nm and the integration time for each single

spectrum was 0.5 s. Each collected Raman map (100 μm × 100 μm) consists of 400 pixels (20 lines and 20 points per line). The Raman maps tracking the intensities of I_{Rayleigh} and I_{Raman} were made using an in-house Matlab script. The photoluminescence background of the SERS spectrum is low under 785 nm laser illumination, so the pseudo band at 84 cm^{-1} does not reflect photoluminescence, but instead the surface-enhanced ASE. The photoluminescence background was subtracted from the collected spectra by baseline correction using an asymmetric least square smoothing based on the published Matlab scripts of Eilers.[263] The morphologies of the nanocomposites were characterized by field emission scanning electron microscope (LEO (Zeiss) 1550).

5.3 Results

5.3.1 $I_{Rayleigh}$ of the SERS Substrates

This study set out to test the capacity for I_{Rayleigh} to predict SERS substrate performance and thus the Raman spectra of the six SERS substrates in the absence of the analytes were initially collected. An exception was A-AuNPs because it was challenging to synthesize colloidally stable AuNP aggregates without addition of 4-MBA. DI water was used as a negative control. As shown in Figure 5.2a, an extremely weak pseudo-band at 84 cm^{-1} was observed for DI water. This pseudo-band originates when the longpass filter of the instrument cuts the ASE of the laser, as discussed previously. As stated in our recent submission, this band was enhanced significantly in the presence of SERS "hot spots" and reflects the integrated efficiency of these "hot spots". It was observed here that I_{Rayleigh} (defined as the maximum measured intensity of the pseudo-band) for all six SERS substrates was much greater than that from DI water (Figure 5.2a).

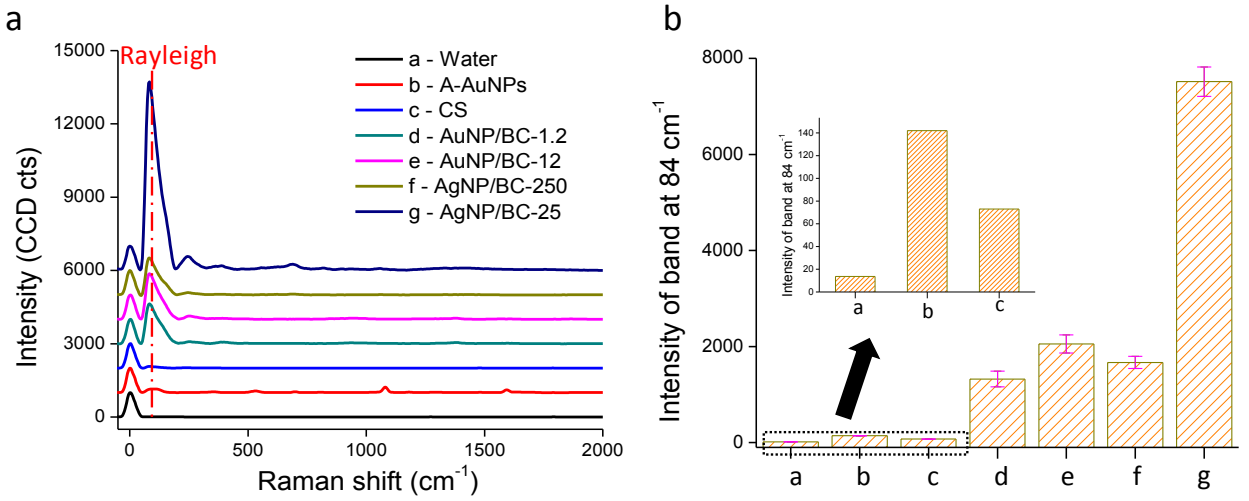

Figure 5.2 a) Raman spectra of the SERS substrates without analyte addition (a. water; b. A-AuNPs; c. commercial substrate (CS); d. AuNP/BC-1.2; e. AuNP/BC-12; f. AgNP/BC-250; g. AgNP/BC-25); b) Intensities of the Rayleigh band at 84 cm^{-1} of all substrates; Inset shows the intensities of the Rayleigh band at 84 cm^{-1} for substrates a-c.

The intensities of the Rayleigh bands at 84 cm^{-1} (I_{Rayleigh}) for each of the SERS substrates are shown in Figure 5.2b. The commercial substrate (CS) exhibited the lowest I_{Rayleigh} amongst the six SERS substrates. This substrate is optimized for SERS detection at lower wavelength laser excitation (i.e., 638 nm), so our use of a 785 nm laser may be one reason why the measured $I_{Rayleigh}$ is low. A-AuNPs also exhibited a low $I_{Rayleigh}$ due to the low "hot spot" density of the aggregates. The four tested nanocomposites exhibited much larger I_{Rayleigh} than either CS or the A-AuNPs because there are large amounts of gold or silver nanoparticles constrained within a film with a thickness of several micrometers.[190, 301] Among the four nanocomposites, AgNP/BC-25 exhibits much larger I_{Rayleigh} than the others because AgNPs are more efficient plasmonic enhancers than AuNPs.[26] The other AgNP-based substrate, AgNP/BC-250, exhibited similar I_{Rayleigh} to the tested AuNP-based substrates because the AgNP density in it is much lower than in the other three nanocomposites (Figure 5.3 & Figure 5.8).

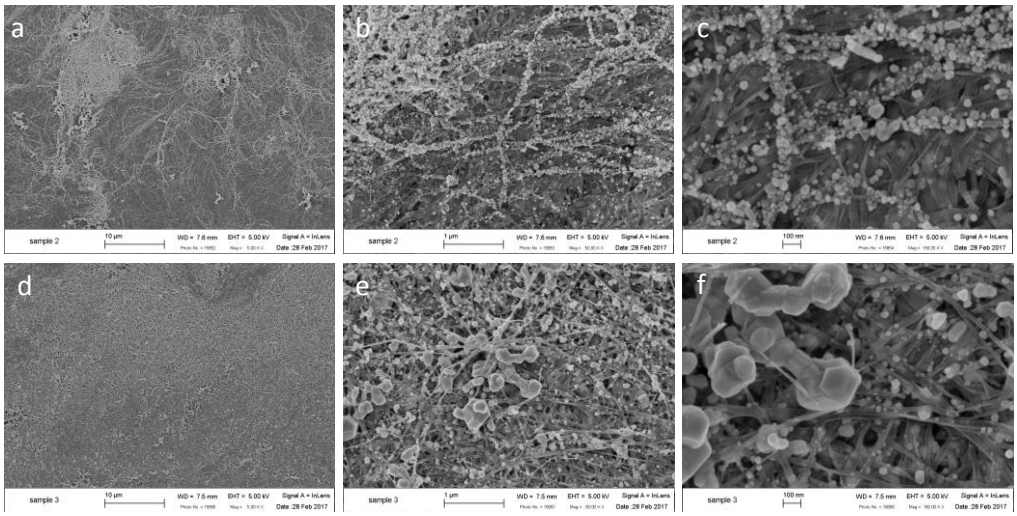

Figure 5.3 SEM images of the AuNP/BC-12 substrate with 5000 (a), 50000 (b), and 150000 (c) magnifications; SEM images of the AgNP/BC-25 substrate with 5000 (a), 50000 (b), and 150000 (c).

5.3.2 $I_{Rayleigh}$ as a Predictive Factor of I_{SERS}

To investigate their SERS efficiency, the six SERS substrates were exposed to 1 mM 4-MBA except for the A-AuNPs, to which 4-MBA was added during synthesis. A relatively high 4-MBA concentration was selected to ensure the NP surfaces were saturated by the analytes. The SERS spectra of the six substrates after exposure to 4-MBA are shown in Figure 5.4a. As a negative control, 1 mM 4-MBA aqueous solution exhibited no Raman signal under these measurement conditions. As shown in Figure 5.4a, all six SERS substrates enhanced the Raman bands of 4-MBA (522, 696, 1076, 1181, and 1590 cm^{-1}).[302] The Rayleigh bands at 84 cm^{-1} are still present in the spectra and the addition of 4-MBA has negligible influence on I_{Rayleigh}. Because the Raman band at 1076 cm^{-1} (benzene ring vibration) is the strongest, it was selected to evaluate SERS substrate efficiency.

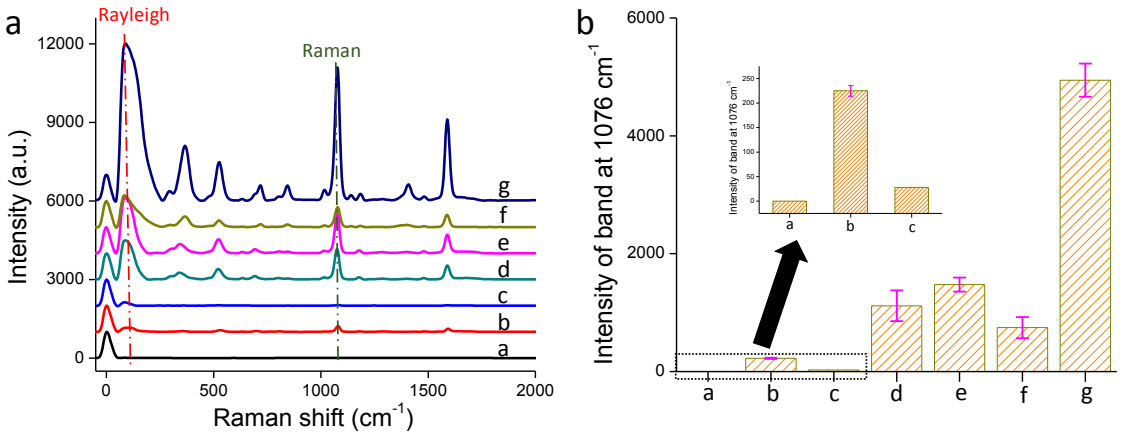

Figure 5.4 a) SERS spectra of 4-MBA on different SERS substrates; b) The intensities of SERS band at 1076 cm^{-1} of all the substrates. Inset shows the intensities of the SERS band at 1076 cm^{-1} for the substrates a-c.

The intensities of the Raman bands at 1076 cm^{-1} of the SERS substrates are shown in Figure 5.4b. A-AuNPs and CS exhibited the lowest $I_{Raman,}$ while also exhibiting the lowest $I_{Rayleigh}$. AuNP/BC-1.2, AuNP/BC-12, and AgNP/BC-250 exhibited similar and moderate $I_{Rayleigh}$ (Figure 5.2b) and they also exhibited similar and moderate I_{Raman} (Figure 5.4b). AgNP/BC-25 exhibited the highest $I_{Rayleigh}$ and coincidently, it also exhibited the highest I_{Raman}. These results collectively suggest that the SERS substrates showing higher intensity Rayleigh bands also show higher intensity Raman bands. In other words, $I_{Rayleigh}$ qualitatively reflects the SERS efficiency of a SERS substrate.

To quantitatively illustrate the relationship between I_{Raman} and $I_{Rayleigh}$, the variation in the intensities of the Raman band at 1076 cm^{-1} as a function of the Rayleigh band at 84 cm^{-1} is shown in Figure 5.5. Because the SERS substrates used to acquire Raman spectra before and after adding 4-MBA were different pieces from the same batch, there were two $I_{Rayleigh}$ measurements obtained for each type of SERS substrate. When using $I_{Rayleigh}$ obtained prior to adding 4-MBA as the abscissa, the I_{SERS} from the six SERS substrates and water roughly follows a linear relationship with $I_{Rayleigh}$. A-AuNPs and CS showed the lowest SERS and Rayleigh signals. The three

nanocomposites AuNP/BC-1.2, AuNP/BC-12, and AgNP/BC-250 showed moderate SERS and Rayleigh signals. AgNP/BC-25 showed both the highest SERS and Rayleigh signals (Figure 5.5). However, if we focus on the three samples exhibiting moderate signals, AgNP/BC-250 showed higher $I_{Rayleigh}$, but lower I_{Raman} than AuNP/BC-0.4. We attribute this to the large piece-to-piece variability of AgNP/BC-250 (details discussed in the following sections). When $I_{Rayleigh}$ measured after addition of 4-MBA was plotted on the abscissa, the measured linear relationships improve because the sample-to-sample variability of a SERS substrate is excluded (i.e., $I_{Rayleigh}$ and I_{SERS} are from the same spectrum). These results support the utility of $I_{Rayleigh}$ as a quantitative tool for predicting SERS efficiency if the sample-to-sample variation of SERS substrates from the same batch is small.

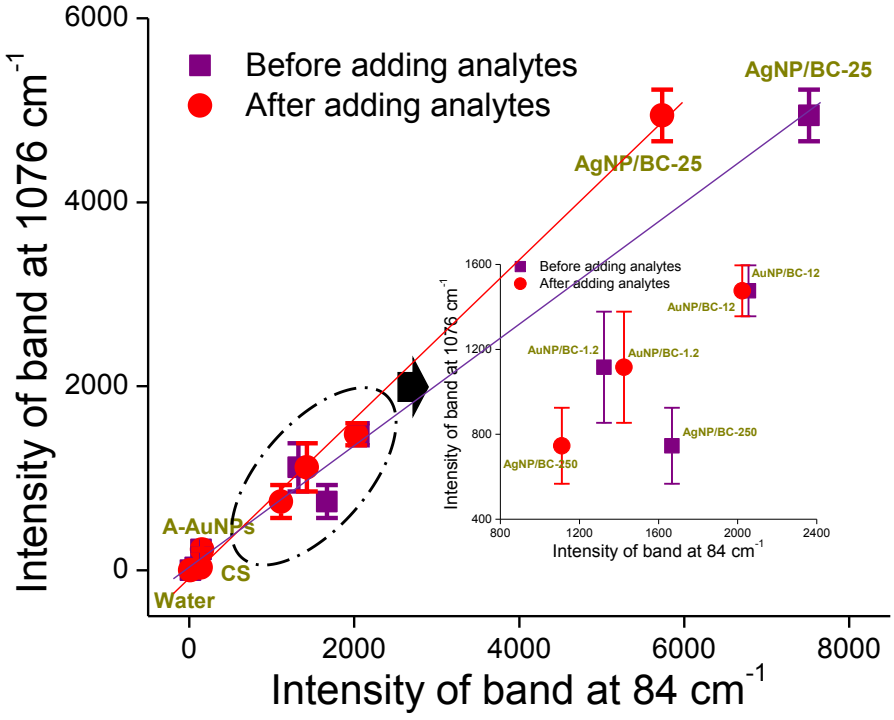

Figure 5.5 Variation of the intensities of Raman band at 1076 cm^{-1} as a function of the Rayleigh band at 84 cm^{-1} before and after adding 4-MBA. Each $I_{Rayleigh}$ or I_{Raman} value is the average of three Raman maps; Each Raman map contains 400 single spectra.

We note that the position of I_{Rayleigh} is dependent on the long pass filter employed. As shown in Figure 5.6, the maximum of I_{Rayleigh} shifts to 126 cm^{-1} when the edge filter of our Raman instrument was replaced with another that cuts at 126 cm^{-1} and to 87 cm^{-1} when a second Raman instrument was employed. As expected, based on instrument-to-instrument variability, $I_0(\omega_{\text{Rayleigh}})$ in Eq. 5.3 changes when switching the Raman instrument. Accordingly, if we define $\omega_{Rayleigh}$ as the wavenumber corresponding to the maximum Rayleigh band intensity then $I_{\text{Raman}}/I_{\text{Rayleigh}}$ changes accordingly (1.70 vs 0.97, Table 5-1). If we define $\omega_{Rayleigh}$ as a fixed wavenumber (e.g., 126 cm^{-1}) for the Rayleigh bands collected with the two instruments, then the ratio $I_{\text{Raman}}/I_{\text{Rayleigh}}$ is much more constant (1.70 vs 1.62, Table 5-1). These results suggest that I_{Rayleigh} has potential to normalize Raman signals collected from different instruments so long as ω_{Rayleigh} is kept constant. Additional experiments to further evaluate this possibility are ongoing.

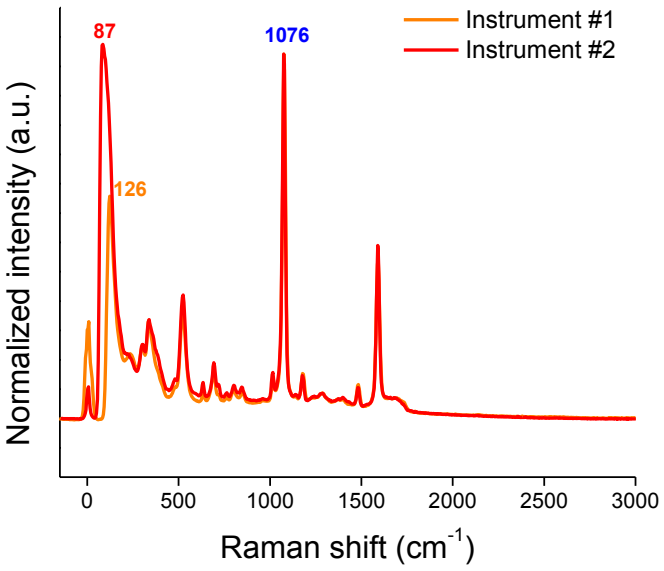

Figure 5.6 SERS spectra of 4-MBA on AuNP/BC-1.2 collected using the Raman instrument in our lab with an alternative edge filter and another Raman instrument in another lab. The spectra were normalized to the Raman intensity at 1076 cm^{-1}.

Table 5-1 $I_{Raman}/I_{Rayleigh}$ acquired using different Raman instruments

Instrument #	$I_{1076}/I_{Rayleigh\text{-}max}$[1]	$I_{1076}/I_{Rayleigh\text{-}126}$[2]
1	1.70	1.70
2	0.97	1.62

This approach defined here performs well for the rapid evaluation of SERS substrate performance when instrumental conditions (edge filters and laser systems) are fixed. However, for SERS substrates characterized using a range of Raman instruments from different labs, it may be challenging to directly compare absolute values of $I_{Rayleigh}$ due to the variability of long pass filters and laser systems. To extend this approach towards a universal evaluation parameter, we suggest the use of readily available SERS substrates (e.g., AuNP aggregated colloids, commercial substrates) as standard test substrates. If our approach is correct, the ratio of the $I_{Rayleigh}$ values for the substrate being evaluated and the standard substrate should remain constant no matter what Raman instrument is used to characterize it. To provide preliminary support of this hypothesis, A-AuNP was used as a standard SERS substrate (substrate #1) and AuNP/BC-1.2 was used as a substrate to be evaluated (substrate #2). As shown in Figure 5.7 and Table 5-2, the ratio of $I_{Rayleigh}$ values for substrate #2 and substrate #1 remained virtually constant for data collected using two different Raman instruments. This result therefore suggests this approach can be extended to evaluate the performance of SERS substrates prepared by different labs or characterized with different Raman instruments.

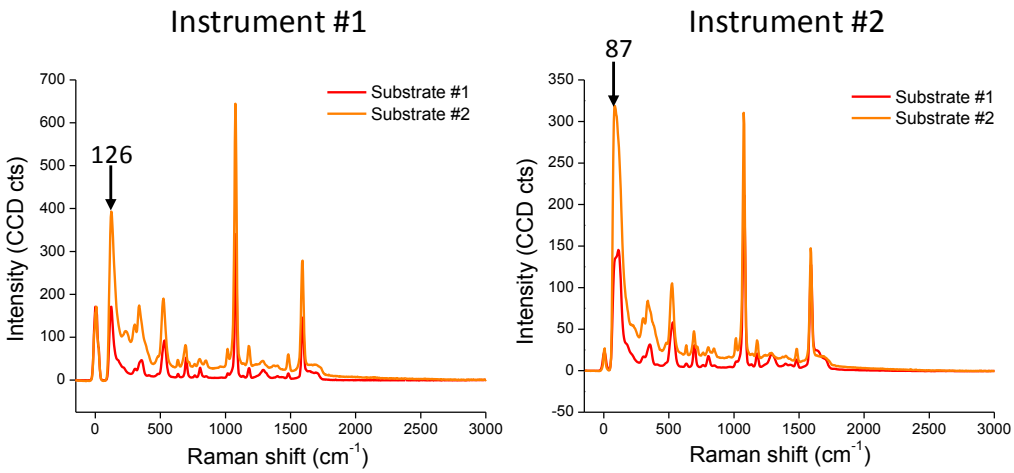

Figure 5.7 SERS spectra of 4-MBA on AuNP/BC-1.2 and A-AuNPs collected using the Raman instrument in our lab with an alternative edge filter and another Raman instrument in another lab.

Table 5-2 $I_{Rayleigh}$ acquired using different Raman instruments

Instrument #	$I_{Rayleigh\text{-}2}$[1] (CCD cts)	$I_{Rayleigh\text{-}2}/I_{Rayleigh\text{-}1}$[2]
1	393	2.20
2	319	2.29

5.3.3 Variation of $I_{Rayleigh}$ across a Raman Map

In addition to intensity, the signal reproducibility across a SERS substrate is another important factor that dictates SERS substrate performance.[303] Since $I_{Rayleigh}$ reflects the "hot spot" efficiency from a single pixel across a SERS substrate, the variation in $I_{Rayleigh}$ is expected to be an indicator of SERS substrate uniformity. To illustrate this, two SERS substrates – AuNP/BC-1.2 and AgNP/BC-250 that exhibited large differences in uniformity, were used as test samples. The morphologies of these nanocomposites were characterized by SEM. As shown in Figure 5.8a, AuNP/BC-1.2 exhibits excellent homogeneity across a 2035 μm^2 area. When the magnification was increased to 50000×, we observe that the nanofibers are fully covered by AuNPs and the homogeneity is excellent across a 21 μm^2 area (Figure 5.8b). When the magnification was further increased to 150000×, we can clearly see AuNPs with heterogeneous shapes and sizes densely

distributed across a 2.3 μm^2 area (Figure 5.8c). The heterogeneity in AuNP size and shape is expected to exert little influence on the homogeneity of the SERS signal because the 10x objective used here has a laser spot size of 2.0 μm^2. The numerous "hot spots" generated by the highly aggregated AuNPs account for the high $I_{Rayleigh}$ and I_{Raman} obtained previously.

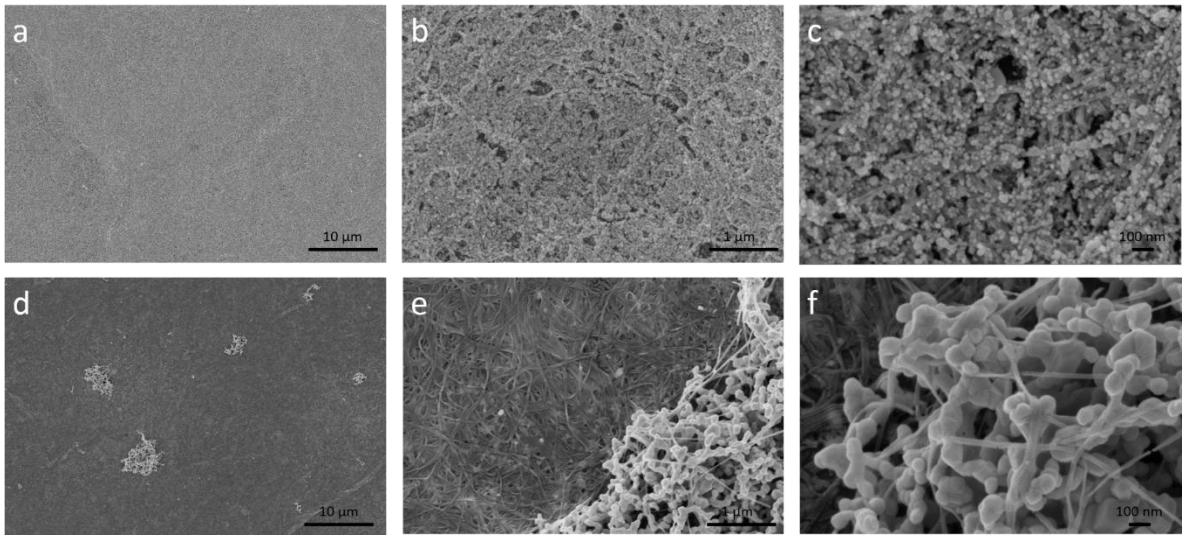

Figure 5.8 SEM images of the AuNP/BC-1.2 substrate with a) 5000×, b) 50000×, and c) 150000× magnifications; SEM images of the AgNP/BC-250 substrate with d) 5000×, e) 50000×, and f) 150000× magnifications. Each substrate was air dried and sputter coated with gold before scanning.

AgNP/BC-250 was much more heterogeneous than AuNP/BC-1.2. As shown in Figure 5.8d, large AgNP clusters were sporadically distributed across a 2035 μm^2 area. When the magnification was increased to 50000×, we can see that a majority of the AgNPs were concentrated in clusters leaving other areas covered with a very low density of AgNPs (Figure 5.8e). When the magnification was further increased to 150000×, we can see the irregular shapes and sizes of the AgNPs. The AgNP size, shape and uniformity of the substrate can be adjusted by changing the $NaBH_4$ concentration. As shown in Figure 5.3d-f, AgNP/BC-25 exhibited much better uniformity than AgNP/BC-250.

As revealed by the SEM images in Figure 5.8, the homogeneity of AuNP/BC-1.2 is much better than that of AgNP/BC-250. We expected that the variation in $I_{Rayleigh}$ across the two SERS substrates would be consistent with their relative uniformities. To test this hypothesis, the two nanocomposites were each scanned across three randomly selected areas and the collected Raman maps are shown in Figure 5.9. As shown in Figure 5.9a-c, a majority of the pixels in the Raman maps of AuNP/BC-1.2 exhibited light blue colors indicating most of the $I_{Rayleigh}$ values are close to the average. Only a small portion of pixels exhibited yellow and red colors that represent $I_{Rayleigh}$ values above the average. We use relative standard deviation (RSD) to describe the variations of $I_{Rayleigh}$ across the Raman maps, which are 18.9%, 17.4%, and 17.3%, respectively.

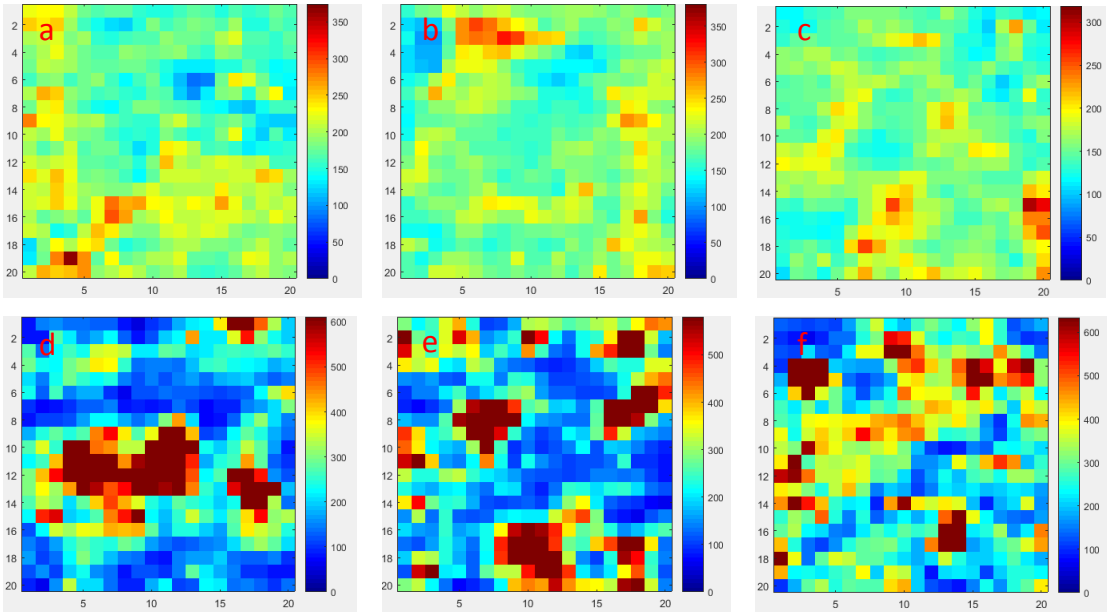

Figure 5.9 a-c) Raman maps made by tracking $I_{Rayleigh}$ at three randomly selected areas of AuNP/BC-1.2; d-f) Raman maps made by tracking $I_{Rayleigh}$ at three randomly selected areas of AgNP/BC-250. Each Raman map contains 400 single spectra.

As shown in Figure 5.9d-f, the Raman maps collected from AgNP/BC-250 were substantially less homogeneous than those collected using AuNP/BC-1.2. Clusters of pixels exhibiting dark red colors corresponding to extremely high $I_{Rayleigh}$ values were present; we speculate these spots represent the locations of the AgNP clusters (Figure 5.8d). Also apparent were pixel areas

exhibiting dark blue colors that correspond to extremely low $I_{Rayleigh}$ values that we speculate reflect the areas generally uncovered by AgNPs (Figure 5.8d). The RSD values of the three Raman maps of AuNP/BC-250 were 95.2%, 78.0%, and 56.3%, respectively, which are significantly greater than those for AuNP/BC-1.2. The variation of RSD values among the three Raman maps collected for AgNP/BC-250 (RSD=25.5%) is much greater than that of AuNP/BC-1.2 (RSD=5.0%). These results collectively demonstrate that AuNP/BC-1.2 is much more uniform than AgNP/BC-250 – a result that is consistent with the SEM observations.

5.3.4 Variation of $I_{Rayleigh}$ as a Predictive Factor for SERS Substrate Uniformity

To determine if the variation in $I_{Rayleigh}$ can effectively predict the variation of I_{Raman}, AuNP/BC-1.2 and AgNP/BC-250 were exposed to 1 mM 4-MBA in ethanol. Following air drying, the SERS maps from three randomly selected areas were collected. As shown in Figure 5.10a-c, the SERS maps made by tracking the Raman band at 1076 cm^{-1} of AuNP/BC-1.2 exhibited RSD values of 18.1%, 22.6%, 15.9%, respectively. In addition, the RSD values of SERS maps collected using AgNP/BC-250 were 55.2%, 55.1%, and 32.4% (Figure 5.10d-f). AuNP/BC-1.2 exhibiting lower variation in $I_{Rayleigh}$ than AgNP/BC-250 also exhibits lower variation in I_{Raman}, which meets our expectation.

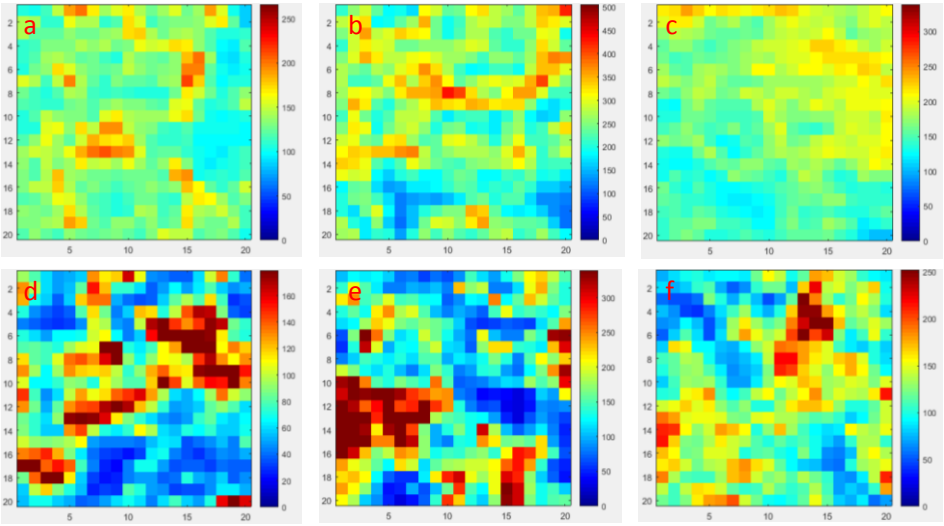

Figure 5.10 a-c) SERS maps made by tracking the band at 1076 cm^{-1} at three randomly selected areas of AuNP/BC-1.2 after exposing to 1 mM 4-MBA solution; d-f) SERS maps made by tracking the band at 1076 cm^{-1} at three randomly selected areas of AgNP/BC-250 after exposing to 1 mM 4-MBA solution.

To confirm that the variation of $I_{Rayleigh}$ can be used to predict the uniformity of a SERS substrate, the variations in the RSD values of the Raman band at 1076 cm^{-1} as a function of the RSD values of the Rayleigh band at 84 cm^{-1} for all the six SERS substrates introduced in Figure 5.2 are shown in Figure 5.11. AgNP/BC-250 not only exhibited the highest RSD value for $I_{Rayleigh}$ but also the largest error bar that represented the standard deviation of RSD values calculated from three SERS maps. In addition to AgNP/BC-250, CS also showed a very high average RSD value for $I_{Rayleigh}$. As expected, these two substrates also exhibited the highest RSD values of I_{Raman}. The other four substrates, including AuNP/BC-1.2, AuNP/BC-12, AgNP/BC-25, and A-AuNPs exhibited similar RSD values ~20% of $I_{Rayleigh}$ and also exhibited similar RSD values ~20% of I_{Raman}. As shown in Figure 5.11, the RSD values of I_{Raman} of the six SERS substrates roughly increased linearly with the increase in RSD values of $I_{Rayleigh}$. Based on the excellent correlation between $I_{Rayleigh}$ and I_{Raman} it appears that the variation of $I_{Rayleigh}$ can be used as a qualitative tool

for predicting the reproducibility of a SERS substrate. Additonal tests are currently ongoing to furhter evaluate the strength of this correlation.

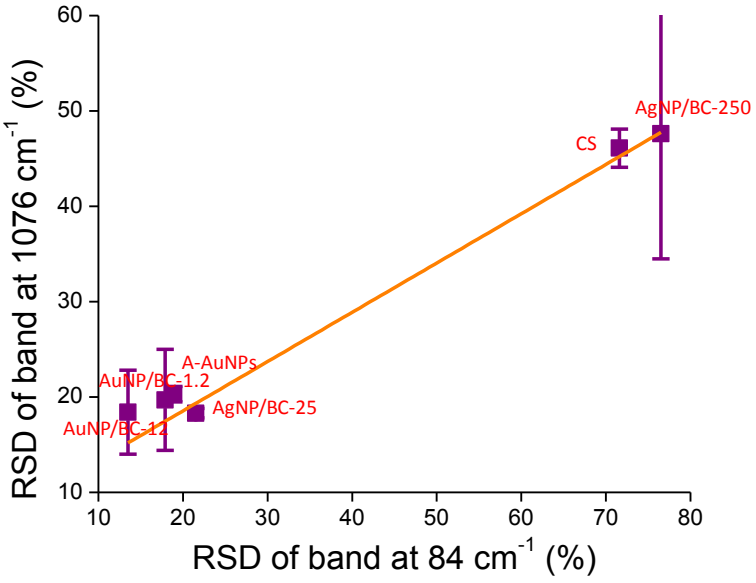

Figure 5.11 The varation of RSD values of the Raman bands at 1076 cm^{-1} as a function of RSD values of the Rayleigh bands at 84 cm^{-1} for the six SERS substrates. Each RSD value is the average of three RSD values calculated from three Raman maps. Each Raman map is collected from a 100 µm × 100 µm area and contains 400 single spectra.

In addition to 785 nm laser, 633 nm laser was also employed in this study. The SERS spectrum of 4-MBA on AuNP/BC-1.2 collected with 633 nm laser is shown in Figure 5.12a. The SERS map constructed by tracking the Rayleigh band at 135 cm^{-1} almost replicates that constructed by tracking the Raman band at 1076 cm^{-1}, i.e., the spot with higher Rayleigh intensity always exhibits higher Raman intensity across the map (Figure 5.12b&c). This result suggests that $I_{Rayleigh}$ can be used to evaluate the performance of SERS substrates when using alternative laser excitation wavelengths.

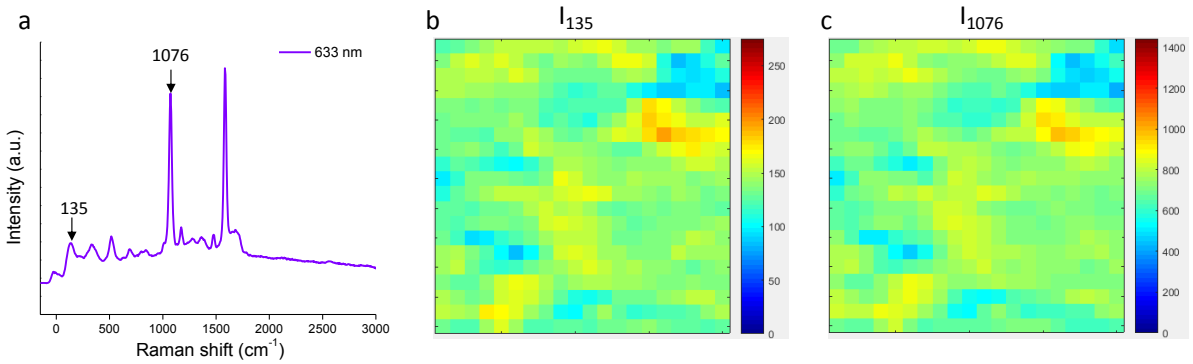

Figure 5.12 a) SERS spectrum of 4-MBA on AuNP/BC-1.2 collected using 633 nm laser; SERS maps tracking b) the Rayleigh band at 135 cm^{-1} and c) the Raman band at 1076 cm^{-1}.

5.4 Conclusions and Discussion

This study proposes an alternative evaluation parameter for SERS substrate performance – the surface plasmon-enhanced Rayleigh band that originates from the ASE of the excitation laser. The intensities of the Rayleigh band (I_{Rayleigh}) of the six SERS substrates follow a linear relationship with the intensities of the primary Raman band of 4-MBA (I_{Raman}), thus indicating I_{Rayleigh} can be used as a quantitative tool for predicting the efficiency of a SERS substrate. The RSD values of I_{Rayleigh} across Raman maps of the six SERS substrates roughly follow a linear relationship with the RSD values of I_{Raman}, indicating that variations in I_{Rayleigh} can be used as a qualitative tool for predicting SERS substrate reproducibility. Accordingly, I_{Rayleigh} can be used as a predictive factor for both SERS substrate efficiency and reproducibility.

As an evaluation parameter for SERS substrate performance, I_{Rayleigh} exhibits several advantages over EF. First, it does not require analyte addition to acquire I_{Rayleigh} values. EF values are typically obtained experimentally by assuming the plasmonic nanostructures are fully covered by the analytes. This assumed condition can substantially deviate from reality when the affinity between a given analyte and the nanostructures is low and the shape and size of the nanostructures are irregular and heterogeneous. For example, it is extremely difficult to measure EF accurately for

our BC-based substrates due to the large variation in NP size and shape. Second, $I_{Rayleigh}$ is an intrinsic property of the SERS substrate, which is independent of the analytes. EF is dependent on the analyte, (i.e., one SERS substrate can have many EF values for different analytes). Therefore, it is challenging to readily compare the large number of SERS substrates reported in the literature. $I_{Rayleigh}$ is intrinsic to a SERS substrate and reflects the integrated "hot spot" efficiency within the laser excitation volume, irrespective of the size, shape, or identity of the plasmonic nanostructures. Overall, $I_{Rayleigh}$ provides an easy but universally applicable "ruler" (with the help of a standard SERS substrate) for evaluating SERS substrate performance.

Chapter 6 Real-Time Monitoring the Kinetics of Ligand Exchange on Gold Nanoparticle Surface Enabled by Hot Spot-Normalized SERS

Haoran Wei,[1,2,3] Weinan Leng,[1,2,3] Junyeob Song,[4] Chang Liu,[1,2,3] Marjorie R. Willner,[1,2,3] Qishen Huang,[1,2,3] Wei Zhou,[4] and Peter J. Vikesland[1,2,3,*]

[1]Department of Civil and Environmental Engineering, Virginia Tech, Blacksburg, Virginia.

[2]Virginia Tech Institute of Critical Technology and Applied Science (ICTAS) Sustainable Nanotechnology Center (VTSuN), Blacksburg, Virginia.

[3]Center for the Environmental Implications of Nanotechnology (CEINT), Duke University, Durham, North Carolina.

[4]Department of Electrical and Computer Engineering, Virginia Tech, Blacksburg, Virginia.

*Corresponding author. Phone: (540) 231-3568, Email: pvikes@vt.edu

(This chapter is to be submitted to ***ACS Nano***.)

Abstract

Surface coatings on engineered nanoparticles determine their fate, transport, and toxicity in aqueous systems. In this effort, we combined gold nanoparticle-bacterial cellulose and "hot spot"-normalized surface-enhanced Raman scattering (HSNSERS) to achieve *in situ* and *real-time* monitoring of ligand exchange on the AuNP surface. By simultaneously improving SERS sensitivity and reproducibility this approach enabled quantification of citrate coverage on the AuNP surface and its desorption kinetics were, for the first time, obtained. Following exposure to different guest ligands (thiolates, amines, carboxylates, inorganic ions, and proteins), the guest ligand signals increased in correspondence to a first-order kinetic model, while the citrate signal decreased followed a first-order decay model. Functional groups on the guest ligands determined the kinetics of citrate desorption, while the guest ligand concentration played only a minor role. As expected, thiolates and BSA were more efficient at ligand exchange than amine-containing chemicals, carboxylate-containing chemicals, and inorganic salts due to their higher binding energies with the AuNP surface. Citrate exhibited low resistance to replacement at high AuNP surface coverage, but high resistance at lower coverage, thus suggesting a transformation of the citrate binding mode during desorption. The high resistance to replacement of citrate in stream water suggests that the role of citrate in AuNP fate and transport should be emphasized.

6.1 Introduction

Gold nanoparticles (AuNPs) have been manufactured for versatile biochemical applications, such as biosensing, labeling, catalysis, drug delivery, and photothermal therapy due to their unique chemical, optical, and electronic properties.[26, 304, 305] In United States, AuNPs, among the other engineered nanomaterials, are regulated under the *Toxic Substances Control Act* concerning their potential acute or chronic toxicity.[306-308] Once released into surface waters, the interactions of AuNPs with natural inorganic/organic chemicals and colloids result in either enhanced colloidal stability or destabilization via homo- or hetero-aggregation.[309-313] Nanoparticle surface coatings directly interact with the environment and are central to their fate and transport in aquatic systems.[309, 310, 314] Surface coatings of AuNPs can alter their cytotoxicity by changing biocompatibility, hydrophobicity/hydrophilicity, surface charge, and other factors that dictate interactions with cell membranes.[314-318] For these reasons, it is important to obtain a clear picture of the stability of AuNP surface coatings.

Techniques that are frequently adopted for AuNP characterization include dynamic light scattering, UV-VIS spectroscopy, transmission/scanning electron microscopies, electrophoresis, and surface charge analysis.[309, 310, 312, 313, 317] Although highly useful, these routine characterizations only provide information about surface coating morphologies and charges, but cannot identify their chemical composition. X-ray photoelectron spectroscopy (XPS) provides chemical identity of surface coatings and has been applied to quantify the ligand density on an AuNP surface.[319] However, it is sensitive to the variation of nanoparticle geometries and is limited to dry powders, thus making it challenging for *in situ* characterization. Second harmonic light scattering, another surface-sensitive technique, was recently used to monitor ligand exchange on colloidal AuNP surfaces.[320] Although *in situ* characterization was achieved, it did not provide any

chemical information regarding the ligands. Nuclear magnetic resonance (NMR) provides high chemical and spatial resolution on ligand identity, arrangement, and dynamics on metal nanoparticle surfaces.[321] However, it is currently only accurate for extremely small NPs (<200 atoms). For common AuNPs, digestion is required, making it challenging for *real-time* measurement. A surface-sensitive technique that can identify and quantify AuNP surface coatings *in situ* and in real time is highly desired.

Surface-enhanced Raman spectroscopy (SERS) is an emerging analytical tool with single-molecule sensitivity and fingerprint chemical identity.[24, 26, 322] SERS originates from the amplified electromagnetic field within the nanoscale vicinity of a plasmonic nanoparticle surface due to the collective oscillation of conduction electrons.[24, 322] SERS has been widely applied for environmental analysis, disease diagnosis, and homeland security protection.[173, 185, 323] SERS provides abundant vibrational bond information and nanoscale surface sensitivity, making it an ideal platform for surface coating characterization. However, to date, only two studies have utilized SERS to monitor ligand exchange kinetics on an AuNP surface.[324, 325] These studies both used thiolated guest ligands, thus minimizing their environmental significance. In addition, they only measured the adsorption kinetics of the guest ligand onto the AuNP surface. The other side of "ligand exchange" (i.e., desorption kinetics of the existing coating (e.g. citrate) from the AuNP surface), has never been reported. It is urgent that we extend the suite of guest ligands to encompass environmentally and medically relevant chemicals and consider the other half of the "ligand exchange" puzzle.

It is highly challenging to apply colloidal AuNPs for *real time* SERS measurement for the following two reasons: 1) the poor colloidal stability of AuNPs in the presence of guest ligands (especially electrolytes); 2) the low enhancing capability of AuNP monomers. The first problem

can be solved by immobilizing NPs onto a solid matrix. For example, silver nanoparticles (AgNPs) were immobilized onto solid supports using nanosphere lithography and plasma polymerization.[326-328] The dissolution and transformation of these AgNPs were subsequently investigated using atomic force microscopy and X-ray absorption spectroscopy. Although very useful, these substrates exhibited low "hot spot" (HS) density, making them inefficient SERS enhancers.[288] To improve both the stability and sensitivity of SERS substrates we employed a rigid hydrogel – bacterial cellulose (BC) – as a matrix for AuNP immobilization (Figure 6.1a). The BC structure forms a three-dimensional network for growth of a high density of AuNPs *in situ*, thus creating a large number of HS sites for efficient SERS detection.[29] AuNPs restrained within the BC scaffold remain stable and hydrated during a SERS measurement, thus making them great surrogates for colloidal NPs.

Another bottleneck for SERS application is its poor reproducibility. The size, shape, density, and aggregation states of AuNPs define the enhancing capability of a SERS substrate.[26, 322, 329] Therefore, the variation of these factors (heterogeneous HS distribution) oftentimes overwhelms the signal variation induced by changes in ligand concentration on the AuNP surface. To improve the reproducibility of SERS, our recently developed technique – hot spot-normalized SERS (HSNSERS) was adopted herein (Figure 6.1b).[233] Surface-enhanced Rayleigh scattering (ν_e) located in the region of laser amplified spontaneous emission (ASE) reflected the integrated enhancing efficiency of SERS HS within the laser excitation volume. Using ν_e as an internal standard, signal variations arising from heterogeneous HS distributions across a substrate or among different substrates can be minimized. In this study, three types of signals were generated and collected during ligand exchange reactions on AuNP/BC (Figure 6.1b): 1) Raman signals of the

existing coating on AuNP surface (i.e., citrate); 2) Raman signals of the guest ligand adsorbed on the AuNP surface; 3) A ν_e signal that was used as the internal standard for both Raman signals.

In this effort, we coupled the AuNP/BC platform and HSNSERS with the intent to monitor the kinetics of ligand exchange on an AuNP surface *in situ*. Citrate-coated AuNPs (cit-AuNPs) were selected as the model system because citrate is arguably the most common surface coating on as-synthesized colloidal AuNPs. Recently, citrate binding to an AuNP surface was characterized by infrared and XPS, from which a conclusion was drawn that citrate exhibited high resistance to thiolate replacement.[330, 331] However, another report challenged this conclusion by using XPS and SERS to show that citrate was readily replaced by thiolates and other chemicals.[332] Obviously, the measurement of the kinetics of citrate desorption from AuNP surface will be highly valuable to settle this debate. Herein, cit-AuNPs restrained in BC were exposed to a variety of chemicals including aromatic thiolates with different functional groups, amine (4-chloroaniline), carboxylate (4-chlorobenzoic acid), protein (bovine serum albumumin), nucleobase (adenine), environmental pollutant (melamine), and inorganic ion (Cl^-). In addition, the ligand exchange kinetics in stream water were also quantified.

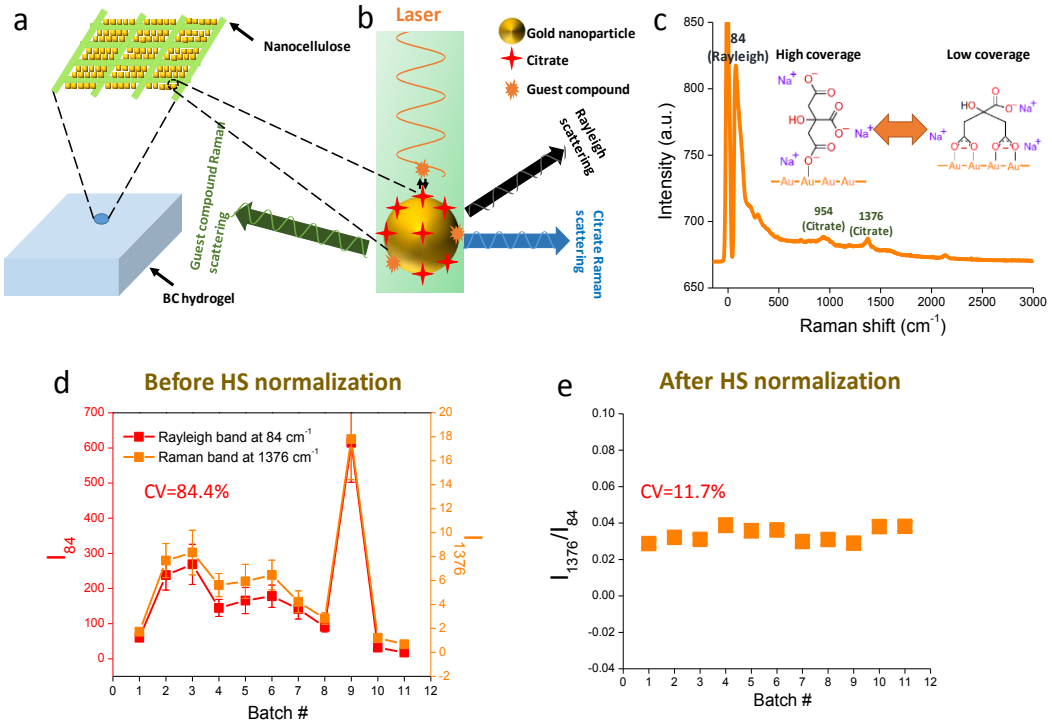

Figure 6.1 a) Schematic of AuNPs constrained within a BC hydrogel that produce a large number of SERS hot spots; b) Schematic of the exchange between guest ligands and citrate layer on AuNP surface monitored by HSNSERS. The photons collected in this study include the Rayleigh scattering of laser ASE, Raman scattering of citrate, and Raman scattering of guest ligands. c) A representative SERS spectrum of citrate collected from AuNP/BC substrate; d) The covariance of surface-enhanced Rayleigh scattering of laser ASE at 84 cm^{-1} and the surface-enhanced Raman scattering of citrate at 1376 cm^{-1} for 11 batches of AuNP/BC substrates prepared by three individuals; e) Variation of HS-normalized citrate Raman band intensity within 11 batches of AuNP/BC substrates.

6.2 Experimental Section

6.2.1 Materials

Gold chloride trihydrate ($HAuCl_4 \cdot 3H_2O$), sodium citrate tribasic dihydrate ($Na_3Citrate \cdot 2H_2O$), 4-aminothiophenol (4-ATP), 4-mercaptobenzoic acid (4-MBA), 4-chloroaniline (4-CA), 4-chlorobenzoic acid (4-CB), adenine, melamine, and bovine serum albumin (BSA) were purchased from Sigma-Aldrich. Sodium chloride (NaCl) was purchased from Fisher Scientific. Stream water was collected from a creek flowing through Virginia Tech campus in Blacksburg. Deionized water (18.2 MΩ) was used as solvent.

6.2.2 Preparation of AuNP/BC

BC used in this study were synthesized in our lab using a protocol described in detail as follows: Gluconacetobacter Xylinus was used in this study to produce bacterial nanocellulose with ATCC 459 media. Specifically, 40 g of fructose, 5 g of yeast extract, and 12.5 g of $CaCO_3$ were dissolved in 1000 mL of DI water. The media was autoclaved at 121℃ for 15 min and then cooled down for use. 1 ml of Gluconacetobacter Xylinus and 150 ml of the fresh media were mixed in cell culture flask with vented cap. Then the flask was transferred to an incubator and the temperature was set at 30 ℃. To maintain a high relative humidity, an autoclaved open container with soapy water was placed at the bottom of the incubator. A BC pellicle formed on the surface of the cell culture flask after 3 days. The pellicle was vigorously shaken to extract the bacteria from the pellicle to the media. The bacteria enriched media was transferred to centrifuge tubes, which were saved as pre-culture for future use. When the pre-culture was obtained, mix 2 ml of the prepared pre-culture with 300 ml of fresh ATCC 459 media and then cultivate the mixture at 30 ℃ with humidity in petri dishes. After 10 days growth, the obtained BC pellicles were removed from the petri dishes and washed thoroughly with 0.5 M NaOH solution for 5 days. NaOH solution need to be refreshed regularly to remove the bacteria left in the pellicles. Then the pellicles were washed using DI water for 7 days until the pH reached neutral. AuNP/BC nanocomposites were synthesized using the *in situ* citrate reduction approach that was described in our previous publication.[29]

6.2.3 Principle of HSNSERS for Monitoring Ligand Exchange Kinetics

The detailed theoretical rationale of HSNSERS was described in our recent publication. Briefly, the ratio of intensities of ν_e at 84 cm^{-1} ($I_{Rayleigh}(r_\infty,\omega_1)$) and Raman band of citrate or guest ligand at specific Raman shift ($I_{Raman}(r_\infty,\omega_0\pm\omega_{vib})$) is shown in Eq. 6.1:

$$\frac{I_{Raman}(r_\infty,\omega_0\pm\omega_{vib})}{I_{Rayleigh}(r_\infty,\omega_1)} \approx \frac{N_A|\alpha_A(\omega_0\pm\omega_{vib},\omega_0)|^2 I_0(r_0,\omega_0)}{N_B|\alpha_B(\omega_1)|^2 I_0(r_0,\omega_1)} \quad \text{Equation 6.1}$$

where N_A and N_B are the molar concentration of the molecules of interest (citrate or guest ligands) and the background molecules (e.g. water) within SERS HS located in laser excitation volume, respectively; $\alpha_A(\omega_0\pm\omega_{vib},\omega_0)$ and $\alpha_B(\omega_1)$ are Raman scattering polarizability of molecules of interest and Rayleigh scattering polarizability of background molecules, respectively; $I_0(r_0,\omega_0)$ and $I_0(r_0,\omega_1)$ are the intensities of incident laser at 0 cm^{-1} and incident laser ASE at 84 cm^{-1}, respectively. Herein we assume that all of these parameters remain constant during the period of time for ligand exchange except N_A and thus the surface concentration of molecules of interest can be quantified in real time using ν_e at 84 cm^{-1} as a normalizing factor.

6.2.4 Monitoring the Ligand Exchange on AuNP Surface

One piece of AuNP/BC hydrogel (0.5 cm × 0.5 cm) was immobilized on the bottom of a small petri dish. The laser spot was focused on top of the hydrogel followed by the collection of the first Raman spectrum (defined as time: 0 min). Subsequently, 6 mL of 4-ATP (50 μM), 4-MBA (0.5 – 50 μM), 4-CA (50 μM), 4-CB (50 μM), Cl^- (50 μM and 10 mM), adenine (50 μM and 1 mM), BSA (15 μM), or melamine (1 mM) in DI water or stream water were separately added to the petri dish. The petri dish was covered to prevent water evaporation during Raman scanning. The laser spot was refocused on top of the hydrogel after solution addition and the Raman maps were collected every 1 min for the first 5 min, every 5 min for the next 25 min, every 10 min in the following 50 min, and every 20 min in the following 100 min.

6.2.5 Instrumentation

Raman spectra were collected using a confocal Raman spectrometer (WITec Alpha 500R). A 10× objective was employed that has a laser spot diameter of ~10 μm. The laser wavelength employed

was 785 nm and integration time for a single Raman spectrum was 0.1 s. The collected photons were dispersed by a 300 gr/mm grating and detected using a Peltier charge-coupled device. For each time point, a 20 × 20 Raman map in a 200 × 200 μm^2 area was collected. The reported spectrum was the average of the 400 spectra and the error bar denoted the standard deviation. The morphology of AuNP/BC was characterized using scanning electron microscopy (FESEM, LEO (ZEISS) 1550). The AuNP mass (3.9±0.5 mg) in one piece of AuNP/BC was measured using inductively coupled plasma – mass spectrometry (Thermo Electron X-Series ICPMS, Waltham, MA, USA). Chemical oxygen demand and NH_3-N of stream water were measured by a colorimeter (Hach DR/890, Hach Company, Loveland, CO, USA). Stream water conductivity was measured using a benchtop conductivity meter (Mettler-Toledo, Columbus, OH, USA).

6.3 Results and Discussion

6.3.1 Quantitation of Citrate on AuNP Surface

Citrate acts as not only reducing agent in AuNP synthesis, but also as a stabilizing agent that provides a strong electrostatic repulsive forces between AuNPs.[217] As shown in Figure 6.1c, the SERS spectrum of cit-AuNPs exhibited a strong Rayleigh band at 84 cm^{-1} and two weak citrate Raman bands at 1376 cm^{-1} (symmetric COO^- stretching) and 954 cm^{-1} (skeletal C-C stretching).[333] The intensity ratio of these two citrate bands remained constant across a SERS map, indicating citrate ions bind onto the AuNP surface in a consistent orientation (Figure 6.2). Using a combined experimental and calculation approach, Al-Johani et al. recently determined that the binding mode of citrate to the AuNP surface was dictated by the citrate/Au molecular ratio.[334] As shown in the Inset of Figure 6.1c, at low citrate/Au ratio (0.2:1), the citrate binds to Au via dicarboxylate bridging, while at higher citrate/Au ratio (1:1), the mode changes to monocarboxylate

monodentate.[334] In our case, the initial citrate/Au ratio was 2.9:1, so the citrate binds to the AuNP surface via consistent monocarboxylate monodentate.

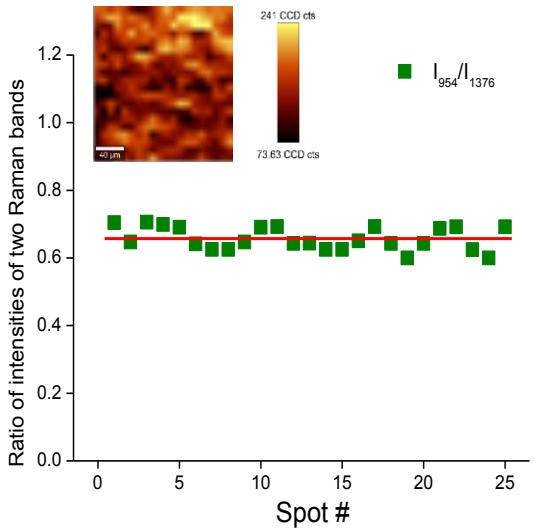

Figure 6.2 Variation of the intensity ratio of the two citrate bands at 954 cm^{-1} and 1376 cm^{-1} as a function of location across a SERS map collected from AuNP/BC. Inset is the SERS map tracking the band at 1376 cm^{-1}.

To monitor the citrate desorption kinetics, we need to quantify the initial citrate concentration (coverage) on the AuNP surface. As shown in Figure 6.1d, the intensities of the citrate band at 1076 cm^{-1} varied significantly for eleven batches of AuNP/BC prepared by three individuals with a large coefficient of variation (CV) of 84.4%. The high signal variation can be attributed to the large differences in HS density, thus making the absolute Raman intensity inaccurate for citrate quantitation. As expected,[233] the Rayleigh band at 84 cm^{-1} varied in the same manner as the citrate band (Figure 6.1d). As shown in Figure 6.1e, the signal variation was significantly reduced after HS normalization (CV=11.7%). The ratio of the maximum to minimum intensities before normalization was 26.2, but decreased to 1.35 after HS normalization. These results suggest that citrate quantitation was enabled by HSNSERS.

6.3.2 Visualization of SAM Formation Using HSNSERS

4-Aminothiophenol (4-ATP), a thiolate and a common SERS label,[325] was employed to evaluate the efficiency of HSNSERS for monitoring ligand exchange kinetics on the AuNP surface. Before exposure to 4-ATP solution, the SERS spectrum for the cit-AuNPs only contained ν_e and citrate Raman bands (Figure 6.3a). Following addition of 50 μM 4-ATP solution, 4-ATP Raman bands at 393 cm^{-1} (Au-S vibration), 1083 cm^{-1} (C-S stretching), and 1589 cm^{-1} (benzene ring stretching) appeared immediately (Figure 6.3a).[100, 324] Because it took ~1 min to refocus the laser spot on the AuNP/BC surface, the first data point collected was set as 1 min. Representative snapshots of SERS spectra demonstrate the increase in the 4-ATP Raman bands and the simultaneous decrease in the citrate bands as exposure time increased, corresponding to the citrate replacement by 4-ATP (Figure 6.3a).

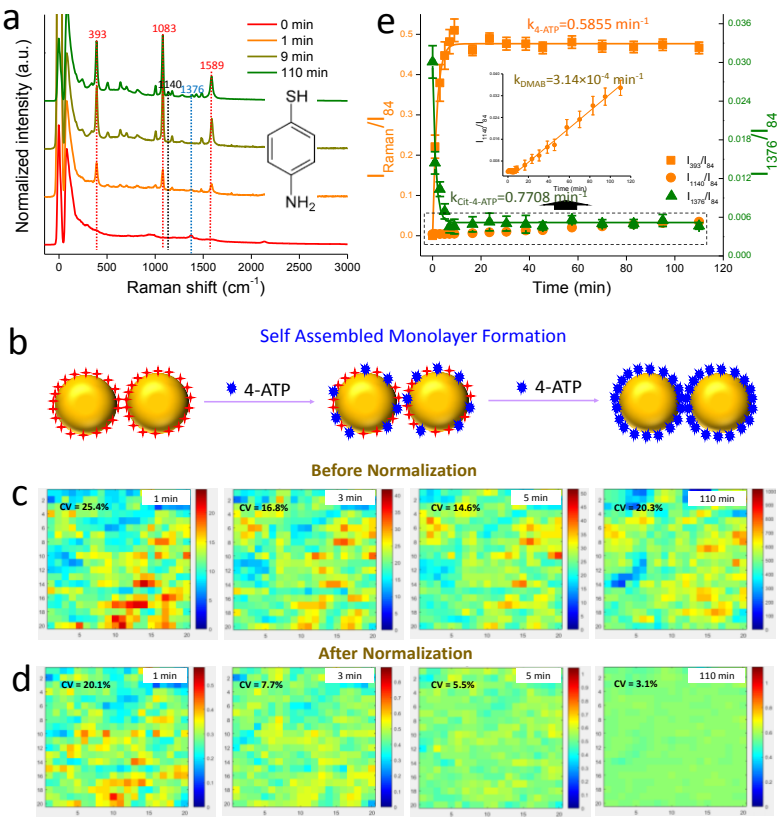

Figure 6.3 a) Representative snapshots SERS spectra collected from AuNP/BC with different exposure time to 6 mL 4-ATP aqueous solution (50 μM); b) Schematic of the formation of 4-ATP self-assembled monolayer (SAM) on AuNP surface; c) Variation of SERS maps constructed by tracking 4-ATP Raman band at 393 cm^{-1} as a function of exposure time; d) Variation of maps constructed by tracking HS-normalized SERS signals (I_{393}/I_{84}) as a function of exposure time; e) Variation of normalized 4-ATP Raman band (I_{393}/I_{84}), DMAB Raman band at 1140 cm^{-1}, and citrate Raman band at 1376 cm^{-1} as a function of exposure time.

Thiolates form a self-assembled monolayer (SAM) on AuNP surface via covalent Au-S bonds (Figure 6.3b).[335] By tracking the 4-ATP band at 393 cm^{-1}, 200 × 200 μm^2 SERS maps across AuNP/BC were obtained (Figure 6.3c). As shown in Figure 6.3c, the SERS maps at any time point all exhibited yellow (even red) and blue pixels corresponding to spots with substantially stronger and weaker intensities compared to the average, respectively. As exposure time increased, (i.e., as more and more 4-ATP molecules were adsorbed onto the AuNP surface), the CV values of SERS maps fluctuated within 14.6-25.4% (Figure 6.3c). The large CV of the SERS map after SAM

formation illustrates the heterogeneous HS distribution across the substrate as evidenced by the heterogeneities in AuNP size, shape, and aggregation state of AuNP/BC (Figure 6.4).

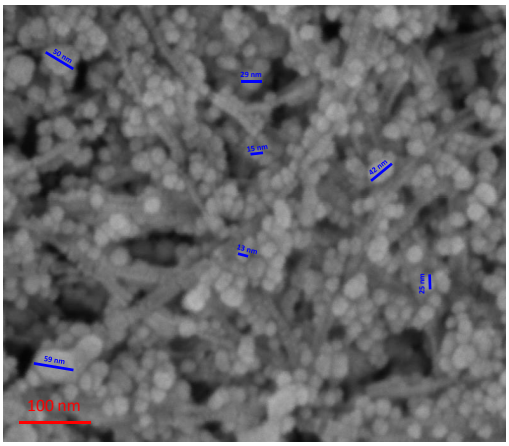

Figure 6.4 SEM image of AuNP/BC.

Maps tracking the HS-normalized 4-ATP band (I_{393}/I_{84}) are shown in Figure 6.3d. As shown, the CV of the maps decreased from 20.1% to 3.1% as exposure time increased, indicating the map uniformity gradually improved as additional 4-ATP was adsorbed onto the AuNP surface. In the map at 110 min, all of the yellow and blue pixels disappeared because of SAM completion (Figure 6.3d). HSNSERS thus enabled visualization of SAM formation on the AuNP surface. These results collectively demonstrate that the SERS signals were dominated by the enhancing capability of the HS. Following HS normalization, the signals were dominated by the analyte concentration on AuNP surface, further confirming the usefulness of HSNSERS for improving SERS quantitation performance.

6.3.3 Monitoring Ligand Exchange Kinetics Using HSNSERS

HS-normalized signals (I) solely reflect the surface coverage of a ligand at time t (θ_t). Therefore, by tracking the variation in the normalized signal as a function of time ($I(\theta_t)$), the kinetics of ligand adsorption/desorption onto/from AuNP surface can be obtained. As shown in Figure 6.3e, the

normalized Au-S signal (I_{393}/I_{84}), also known as the surface coverage of 4-ATP ($\theta_{4\text{-}ATP}$), increased rapidly during the initial 10 min, then reached a plateau as a result of surface saturation. The kinetics of 4-ATP adsorption onto the AuNP surface can be described using a first-order kinetic model (Eq. 6.2), (i.e., the adsorption rate is proportional to the deficit between the saturated surface coverage (θ_s) and the real surface coverage (θ_t)). $k_{4\text{-}ATP}$ is the adsorption rate constant for 4-ATP. The data points shown in Figure 6.3e perfectly fit the numerical form of Eq. 6.2 (Eq. 3, R^2=0.99), confirming that 4-ATP adsorption can be described by a first-order model. The adsorption kinetics were similar with 4-ATP adsorption onto cetyl trimethylammonium chloride-coated AuNPs with high surface curvatures.[324]

$$\frac{dI(\theta_t)}{dt} = k_{4-ATP}[I(\theta_s) - I(\theta_t)] \qquad \text{Equation 6.2}$$

$$I(\theta_t) = I(\theta_s)(1 - e^{-k_{4-ATP}t}) \qquad \text{Equation 6.3}$$

In addition to adsorption, kinetics of by-product formation on the AuNP surface were also monitored using HSNSERS. As shown in Figure 6.3a, the spectrum at 110 min exhibited three additional Raman bands at 1140 cm^{-1}, 1389 cm^{-1}, and 1428 cm^{-1}, which were the ag_{12}, ag_{16}, and ag_{17} vibrational modes of dimercaptoazobenzene (DMAB) generated from the photothermal coupling reaction between two amine groups of 4-ATP molecules.[336] By tracking the normalized DMAB Raman band at 1140 cm^{-1} (I_{1140}/I_{84}), the kinetics of DMAB formation were obtained. $I(\theta_{t\text{-}DMAB})$ almost remained constant in the initial 10 min and then increased linearly with time (Inset Figure 6.3e). The linear trend indicates that DMAB formation followed a zero-order kinetic model (Eq. 6.4), which is reasonable since the AuNP surface was saturated by 4-ATP within 10 min. The rate constant for DMAB formation (k_{DMAB}) was much smaller than that describing 4-ATP adsorption (3.14×10^{-4} min^{-1} vs 0.5855 min^{-1}), thus indicating this reaction was minor during ligand

exchange. The intensity ratio between the 4-ATP Raman band at 1480 cm^{-1} (C-N, C-H, and C-$C_{aromatic}$) and the band at 393 cm^{-1} (Au-S) decreased by ~30% during the initial 10 min, which was tentatively attributed to the change in 4-ATP orientation on the AuNP surface from parallel to upright during SAM formation (Figure 6.5).

$$I(\theta_t) = k_{DMAB}t \qquad \text{Equation 6.4}$$

In addition to providing the capacity to study coverage, reaction, and orientation of guest ligands on the AuNP surface, HSNSERS was subsequently used to monitor citrate desorption kinetics. As shown in Figure 6.3e, the normalized citrate signal (I_{1076}/I_{84}) decreased rapidly during the initial 10 min and then reached a constant value of ~0.005. The desorption kinetics were well described by a first-order exponential decay model (R^2=0.97, Eq. 6.5), where $I(\theta_e)$ is the normalized citrate signal at equilibrated surface coverage θ_e. The non-zero value of $I(\theta_e)$ indicates that there was a small portion of citrate left on AuNP surface after 4-ATP replacement. The bond energy of Au-S (~31 kcal/mol) is much higher than that of Au-COO^- monodentate (~2 kcal/mol).[320, 325, 337] Accordingly, 4-ATP easily replaced 83% (calculated simply by dividing the $(I(\theta_0)-I(\theta_e)$ by $I(\theta_0)$) of the initial citrate from the AuNP surface. However, as the citrate coverage decreased, citrate changed its binding mode to dicarboxylate bridging with covalent Au-O bond with binding energy up to 55 kcal/mol[334], making it thermodynamically challenging to be fully broken by 4-ATP. This demonstrated that citrate exhibits high resistance for replacement even to thiolates, which is consistent with Shumaker-Parry's study using XPS.[330]

$$I(\theta_t) = I(\theta_e) + Ae^{-k_{Cit}t} \qquad \text{Equation 6.5}$$

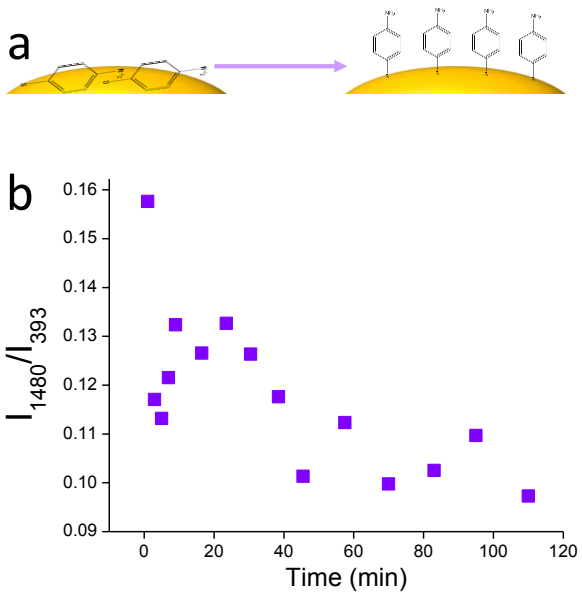

Figure 6.5 a) Schematic for the change of 4-ATP orientation on AuNP surface from parallel to upright; b) Variation of the intensity ratio between the Raman band at 1480 cm^{-1} and the Raman band at 393 cm^{-1} (I_{1480}/I_{393}) as a function of time.

6.3.4 Influence of Ligand Concentration on Citrate Replacement

Following exposure to 50 μM 4-MBA solution, the SERS spectrum exhibited strong 4-MBA Raman bands at 1076 cm^{-1} (benzene ring vibration)[302] while the citrate band at 1376 cm^{-1} substantially decreased (Figure 6.6a). The kinetics of 4-MBA adsorption followed the first-order model (Eq. 3). The fitting parameters are listed in Table 6-1. The adsorption rate constant for 4-MBA ($k_{4\text{-}MBA}$) was smaller than $k_{4\text{-}ATP}$ (0.099 vs 0.59 min^{-1}) indicating that completion of the 4-MBA SAM was slower than for 4-ATP (~30 min vs. ~10 min). Similarly, the citrate desorption rate constant for 4-MBA ($k_{Cit\text{-}4\text{-}MBA}$) was also smaller than that of 4-ATP ($k_{Cit\text{-}4\text{-}ATP}$; 0.17 min^{-1} vs 0.77 min^{-1}). Since the only difference between 4-MBA and 4-ATP is that 4-MBA has a –COOH group rather than $–NH_2$ group, these results demonstrate that $–NH_2$ was much more efficient than –COOH in accelerating citrate replacement. Despite the 4.5× lower k_{Cit}, the citrate residues

remaining on AuNP surface ($\theta_{e\text{-}4\text{-}MBA}$) following 4-MBA replacement were only 23% greater than that of 4-ATP (Table 6-1), indicating θ_e was determined by –HS group.

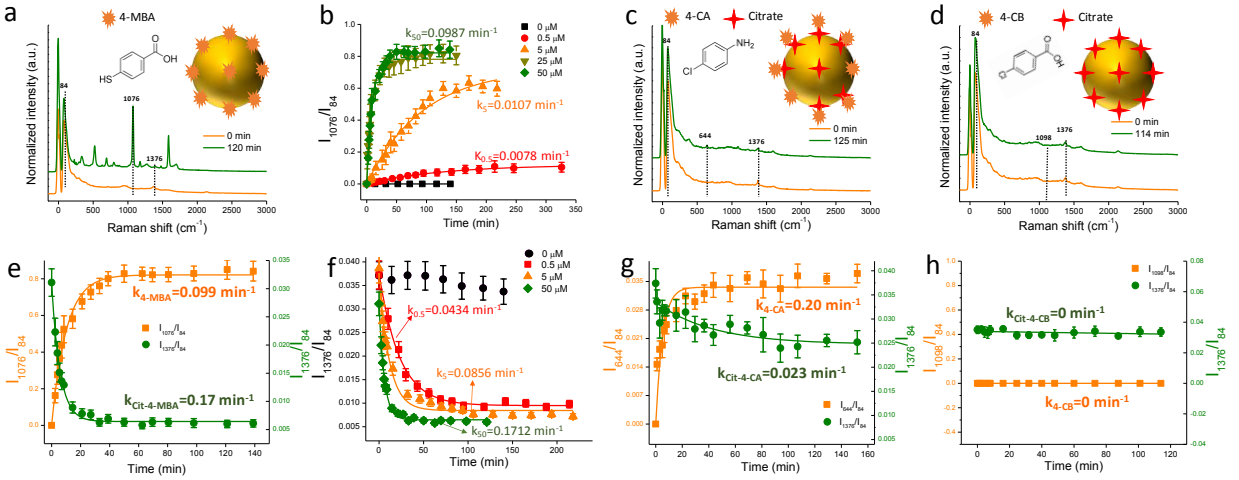

Figure 6.6 a) SERS spectra collected from AuNP/BC before and after its exposure to 50 μM 4-MBA solution for 120 min; b) Variation of normalized Raman band at 1076 cm^{-1} (I_{1076}/I_{84}) as a function of time with different 4-MBA concentrations; c) SERS spectra collected from AuNP/BC before and after its exposure to 50 μM 4-CA solution for 125 min; d) SERS spectra collected from AuNP/BC before and after its exposure to 50 μM 4-CB solution for 114 min; e) Variation of normalized 4-MBA Raman signal (I_{1076}/I_{84}) and citrate Raman signal (I_{1376}/I_{84}) as a function of exposure time; f) Variation of normalized Raman band at 1376 cm^{-1} (I_{1376}/I_{84}) as a function of time with different 4-MBA concentrations; g) Variation of normalized 4-CA Raman signal (I_{644}/I_{84}) and citrate Raman signal (I_{1376}/I_{84}) as a function of exposure time; h) Variation of normalized 4-CB Raman signal (I_{1098}/I_{84}) and citrate Raman signal (I_{1376}/I_{84}) as a function of exposure time.

Table 6-1 Fitting parameters of the adsorption/desorption of guest ligand/citrate onto/from AuNP surface

Guest ligands	Adsorption			Desorption		
	$I(\theta_s)$	$k_{Guest\ ligand}$ (min^{-1})	R^2	$I(\theta_e)$	k_{Cit} (min^{-1})	R^2
4-ATP (50 μM)	0.48	0.59	0.99	0.0052	0.77	0.97
4-MBA (50 μM)	0.82	0.099	0.99	0.0064	0.17	0.99
4-MBA (5 μM)	0.70	0.011	0.99	0.0085	0.086	0.98
4-MBA (0.5 μM)	0.12	0.0078	0.99	0.0095	0.043	0.99

4-CA (50 μM)	0.034	0.20	0.89	0.025	0.023	0.75
4-CB (50 μM)	0			0.034		
NaCl (50 μM)	0			0.034		
NaCl (10 mM)	0.042	0.41	0.96	0.019	0.55	0.86
Adenine (1 mM)	0.21	0.21	0.98	0.016	1.3	0.99
Adenine (50 μM)	0.068	0.15	0.95	0.021	1.1	0.97
Melamine (1 mM)	0.046	0.31	0.92	0.017	0.70	0.88
BSA (1 g/L)	0.39	0.095	0.96	0.0083	0.046	0.98
Stream	0			0.028		

To further understand the role of –HS in replacing citrate, 4-MBA/citrate adsorption/desorption at different 4-MBA solutions of different concentrations were obtained. As 4-MBA concentration increased from 0.5 – 50 μM, the rate constant increased from 0.0078 to 0.099 min^{-1} (Figure 6.6b). Villarreal et al. recently observed the inverted U-shaped adsorption kinetics of 4-ATP on AuNP surface at low 4-ATP concentration (2 μM) and attributed this to the hierarchy in SERS enhancing capabilities at different adsorption sites on AuNP surfaces.[324] HSNSERS mitigated the heterogeneity arising from SERS HS and isolated the analyte surface concentration as the only variable, thus providing us a clear picture of SAM formation kinetics even at low thiolate concentrations. The final coverages of 4-MBA on AuNP surface ($\theta_{s\text{-}4\text{-}MBA}$) at different 4-MBA concentrations can be described using the Langmuir adsorption isotherm (R^2=0.99), indicating that thiolate indeed formed a monolayer on the AuNP surface (Figure 6.7).

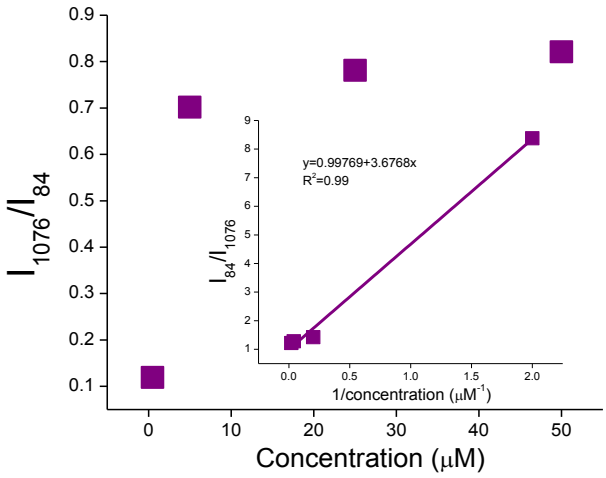

Figure 6.7 Variation of normalized SERS band (I_{1076}/I_{84}) at saturated surface coverage (θ_s) as a function of 4-MBA concentrations.

As the 4-MBA concentration increased from 0.5 – 50 μM, the rate constant describing citrate desorption increased from 0.0434 to 0.1712 min^{-1} (Figure 6.6f). It is interesting that it was not one citrate molecule replaced by one 4-MBA molecule. For example, AuNP surface was covered only by 15% of 4-MBA at initial 4-MBA concentration of 0.5 μM while 75% of citrate already desorbed from AuNP surface at the same time (Figure 6.6b&f). Increasing the concentration to 50 μM resulted in 680% more 4-MBA adsorption while only 33% more citrate desorption. These results confirm that the binding energy of citrate on the AuNP surface depended on its surface coverage. At high coverage, citrate bound to AuNP through a monocarboxylate monodentate linkage and was easily displaced. At low coverage, dicarboxylate bridging played a major role, thus making it difficult to be replaced even by thiolates. This statement is further supported by the shift in the citrate band wavenumber from 1379 cm^{-1} to 1366 cm^{-1} as the citrate band was replaced by 4-MBA (Figure 6.8).

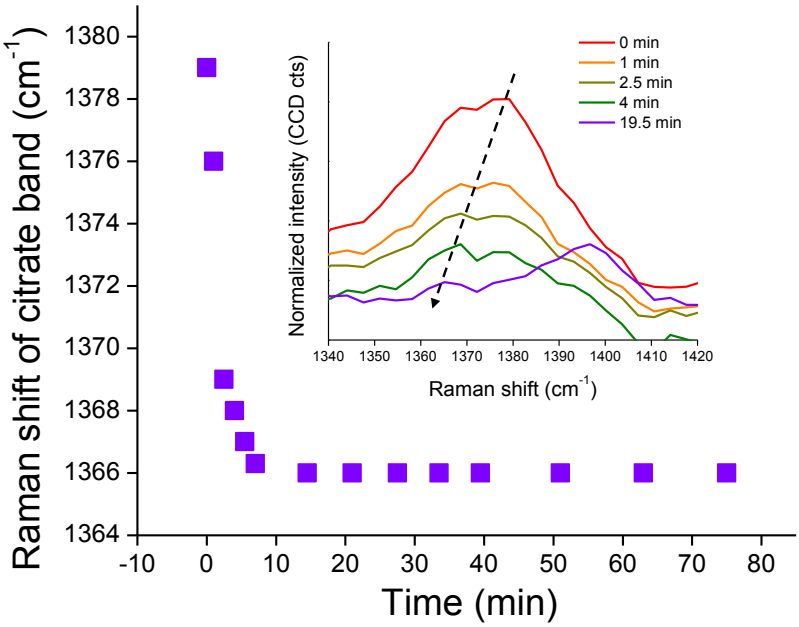

Figure 6.8 Variation of Raman shift of citrate band as a function of time for exposing to 4-MBA solution; Inset is the enlarged Raman spectra for citrate band.

6.3.5 Influence of Ligand Functional Group on Citrate Replacement

To examine the efficiency of $-NH_2$ in replacing citrate, 4-CA was selected as the guest ligand (inset Figure 6.6c). Following AuNP/BC exposure to 50 µM 4-CA solution for 125 min, the 4-CA Raman band at 644 cm^{-1} (benzene ring bending)[338] appeared and the citrate band at 1376 cm^{-1} was attenuated (Figure 6.6c). The adsorption of 4-CA on the AuNP surface was fast with a rate constant in the middle between that of 4-ATP and 4-MBA (Figure 6.6g). Considering the much lower binding energy of Au-NH_2 (8 kcal/mol)[337] than Au-HS (31 kcal/mol)[325], their similar adsorption rates indicated that 4-CA developed an overcoat of the citrate layer via the electrostatic attractive force between the $-NH_2$ of 4-CA and the –COOH of citrate rather than replacing it. Evidence supporting this hypothesis was that $I(\theta_s\text{-}_{4\text{-}ATP})$ was ~14× greater than $I(\theta_s\text{-}_{4\text{-}CA})$ (Table 6-1). Because these two compounds have highly similar chemical structure, their Raman cross sections should not vary much. Because electromagnetic enhancement decays exponentially with increasing

distance from AuNP surface, separation between 4-CA and AuNP by citrate probably resulted in the lower signals of 4-CA compared to 4-ATP that directly interacts with the AuNP surface.[339] The rate constant for citrate desorption induced by 4-CA was much smaller than for the thiolates, indicating $–NH_2$ was much less efficient than –HS in replacing citrate. A large amount of citrate remained on the AuNP surface following 4-CA replacement, as evidenced by the much higher $\theta_{e\text{-}cit\text{-}4\text{-}CA}$ than $\theta_{e\text{-}cit\text{-}4\text{-}MBA}$ (0.025 vs. 0.0064; Figure 6.6e&g). These results collectively demonstrate that a majority of 4-CA molecules overcoated the citrate layer instead of replacing it (Inset Figure 6.6c).

To examine the efficiency of –COOH in replacing citrate, 4-CB was used as the guest ligand (Inset Figure 6.6d). The Raman spectrum of 4-CB solid exhibited Raman bands at 630 cm^{-1}, 805 cm^{-1}, and 1098 cm^{-1} (Figure 6.9), but none of these bands were observed in the SERS spectrum of AuNP/BC after its exposure to 50 μM 4-CB for 114 min (Figure 6.6d). This result indicates that there was no detectable amount of 4-CB located near the AuNP surface. Normalized citrate signal remained constant after 114 min, indicating the citrate layer remained intact in the presence of 4-CB (Figure 6.6h). The low effectiveness of the carboxylate group in replacing citrate can be attributed to its low binding energy to the AuNP surface (~2 kcal/mol). In addition, the electrostatic repulsion force between –COOH groups in 4-CB and citrate prevented 4-CB from forming an overcoating of the citrate layer.

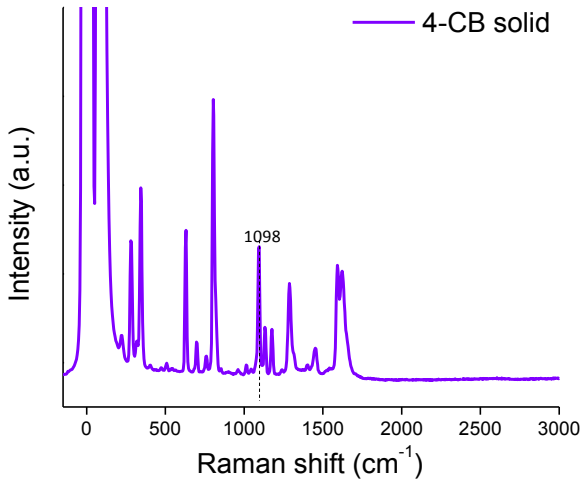

Figure 6.9 Normal Raman spectrum collected from 4-CB solid.

6.3.6 Citrate Replacement by Environmental-Relevant Chemicals

In addition to model compounds with different functional groups, chemicals that are of environmental significance were also selected as guest ligands. Chloride (Cl^-) forms an Au-Cl bond with AuNPs that is reflected by the Raman band at ~250 cm^{-1}.[333, 340] As shown in Figure 6.10a, the Au-Cl band was not observed in the Raman spectrum collected from AuNP/BC following its exposure to 50 μM NaCl solution for 114 min. Meanwhile, the citrate band remained constant (Figure 6.11). These results suggest that Cl^- was much less efficient than $–NH_2$ and –HS for citrate replacement. Because the Cl^- concentration of stream waters in urban areas often exceeds 250 mg/L (~7 mM) due to road deicing,[341] we further increased the Cl^- concentration to 10 mM. As shown in Figure 6.10a, the Au-Cl band at 252 cm^{-1} was observed following exposure of AuNP/BC to 10 mM NaCl solution for 105 min. Both Cl^- adsorption and citrate desorption occurred rapidly (Figure 6.10e). However, a large amount of citrate remained on the AuNP surface after 105 min even at such a high Cl^- concentration, further corroborating the poor performance of Cl^- for citrate replacement.

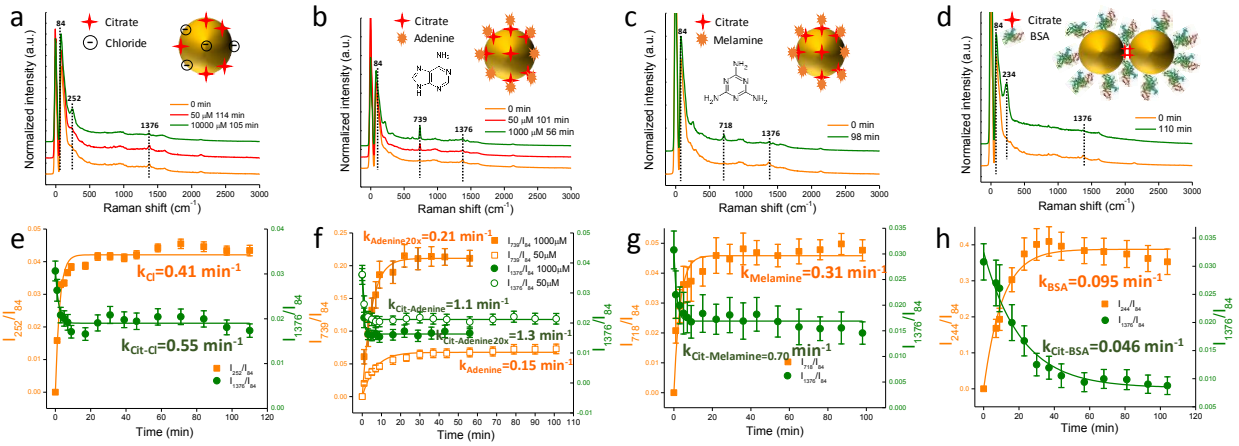

Figure 6.10 a) SERS spectra collected from AuNP/BC before and after exposing to 50 μM and 10 mM NaCl solution for 114 min and 105 min, respectively; b) SERS spectrum collected from AuNP/BC before and after exposing to 50 μM and 1 mM adenine solution for 101 min and 56 min, respectively; c) SERS spectrum collected from AuNP/BC before and after exposing to 1 mM melamine solution for 98 min; d) SERS spectrum collected from AuNP/BC before and after exposing to 0.15 μM BSA solution; e) Variation of normalized Cl^- and citrate Raman signals collected from AuNP/BC exposing to 10 mM NaCl solution as a function of time; f) Variation of normalized adenine and citrate signals collected from AuNP/BC exposing to 50 μM and 1 mM adenine solution as a function of time; g) Variation of normalized melamine and citrate Raman signals collected from AuNP/BC exposing to 1 mM melamine solution as a function of time; h) Variation of normalized BSA and citrate Raman signals collected from AuNP/BC exposing to 1 g/L BSA solution as a function of time.

Decomposition of dead plants release nucleic acids into surface water. SERS has made a great progress recently in detecting both single-stranded and double-stranded DNA with single nitrogenous base sensitivity.[342-344] SERS signals of nucleic acids primarily arise from adenine,[343, 344] and thus we selected adenine as a guest ligand here. As shown in Figure 6.10b, the adenine band at 739 cm^{-1} (ring breathing mode)[344] appeared when the citrate band attenuated following AuNP/BC exposure to 50 uM adenine solution for 101 min. The remaining citrate ($I(\theta_{e\text{-}Adenine})=0.021$) was close to that of 4-CA exposure ($I(\theta_{e\text{-}4\text{-}CA})=0.025$) because adenine and 4-CA both have amine groups. As the adenine concentration was increased to 1 mM, both adenine adsorption and citrate desorption were accelerated (Figure 6.10f). The final adenine coverage increased by 310% while the remaining citrate only decreased by 24% (Figure 6.10f), indicating

that the increase in adenine coverage did not replace the same amount of citrate from the AuNP surface. These "excess" adenine molecules presumably overcoated the citrate layer, just as 4-CA did.

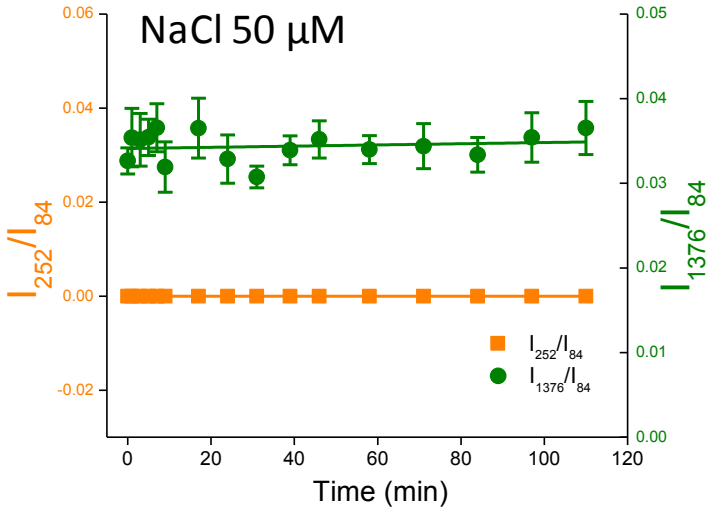

Figure 6.11 Variation of normalized Au-Cl Raman signal (I_{252}/I_{84}) and normalized citrate signal (I_{1376}/I_{84}) as a function of time (NaCl solution concentration: 50 µM).

Melamine was recently spotlighted in China's milk adulteration scandal in 2008 and was selected here as a representative environmental pollutant. As shown in Figure 6.10c, the melamine band at 718 cm^{-1} (in-plane ring breathing mode)[345] was observed in the Raman spectrum collected from AuNP/BC after its exposure to 1 mM melamine solution for 98 min. Accompanied with the fast melamine adsorption onto AuNP surface was the fast citrate desorption from the AuNP surface as evidenced by the large rate constants (Figure 6.10g & Table 6-1). Again, a large percentage of citrate remained on the AuNP surface after equilibrium was reached ($I(\theta_{e\text{-}Melamine}) = 0.017$), which was similar with the other $-NH_2$-containing chemicals (4-CA and adenine).

Adsorption of proteins onto the NP surface ("protein corona") alters their colloidal stability, dissolution, and biocompatibility.[346, 347] Herein, BSA was selected as a representative protein to investigate the kinetics of "corona" formation and citrate replacement. As shown in Figure 6.10d,

the BSA Raman band at 244 cm^{-1} (Au-S) was observed in the spectrum following AuNP/BC exposure to 15 μM BSA solution for 110 min. Meanwhile, the citrate Raman band significantly attenuated. Citrate desorption induced by BSA ($k_{Cit\text{-}BSA}$=0.046 min^{-1}) was much slower than that by 4-ATP ($k_{Cit\text{-}4\text{-}ATP}$=0.77 min^{-1}) despite the fact that it contained a large number of $–NH_2$ and disulphide bonds (–S-S-) (Figure 6.10h). This result was attributed to the larger molecular size of BSA (66.5 kDa), making it difficult to diffuse into very small gaps between AuNPs within the BC matrix. The amount of citrate remaining on the AuNP surface following BSA replacement ($I(\theta_{e\text{-}BSA})$=0.0083) was slightly higher than that replaced by 4-ATP ($I(\theta_{e\text{-}4\text{-}ATP})$=0.0052), which was also a result of the large size of BSA molecules (Inset Figure 6.10d). However, the remaining citrate following BSA replacement was still much less than 4-CA ($I(\theta_{e\text{-}4\text{-}CA})$=0.025) and adenine ($I(\theta_{e\text{-}Adenine})$=0.021) replacement, indicating that BSA replaced rather than overcoated the citrate layer.

6.3.7 High Resistance of Citrate to Replacement in Stream Water

It is well known that the interactions AuNPs with natural organic matter (NOM) significantly influences their fate and transport in aquatic systems.[310] However, whether NOM or other chemicals present in natural water replace the citrate coatings of AuNPs remains unknown. Herein, cit-AuNPs were exposed to a stream water sample collected from a creek flowing through Virginia Tech campus to determine if the replacement of the citrate layer from the AuNP surface happens. Parameters of this water sample including pH, COD, conductivity, and NH_3-N are shown in Figure 6.12a and fall in the range typical for stream water.

Following exposure to stream water for 99 min, no additional Raman bands were observed from the spectrum collected from AuNP/BC (Figure 6.13), indicating that NOM could not penetrate the citrate barrier and arrive at the enhancing zone. This observation was consistent with Pallem et al, where they concluded that humic acid overcoated on the citrate layer according to the enhancement

of fluorescence in the presence of cit-coated AuNPs.[348] However, the slight decrease of the citrate band was observed, indicating citrate desorbed from AuNP surface (Figure 6.13). The kinetics of citrate desorption did not follow the first-order exponential decay model due to the complexity of the stream water (Figure 6.12b). The remaining citrate in stream water ($I(\theta_{e\text{-}Stream})$ = 0.028) was much higher than that in thiolate solution (<0.01) and slightly higher than that in amine solution (<0.025), demonstrating the strong resistance of citrate layer to replacement in stream water.

Recently, remaining citrate on the AuNP surface was observed by XPS and attenuated total reflectance infrared spectroscopy (ATR-IR) following their exposure to 1 mM 1-dodecanethiol ethanol solution, suggesting the strong resistance of citrate to thiolate replacement.[330] This study was challenged more recently by the disappearance of citrate Raman bands following cit-AuNP exposure to thiolates, adenine, and halides.[332] This study, for the first time, provided the kinetics of citrate desorption from AuNP surface in the presence of a variety of chemicals. Owing to the improved SERS reproducibility by HS normalization, the desorption kinetics obtained using different AuNP substrates could be quantitatively compared. As shown in Figure 6.12c, 4-CB and Cl^- exhibited no citrate replacement capability due to their low binding affinity to AuNP surface (~2 kcal/mol). Using $–NH_2$-containing chemicals, i.e. improving the binding energy by ~6 kcal/mol, replaced 53% of citrate. Another 32% citrate were replaced by using –HS or –S-S-containing molecules, i.e. further improving binding energy by 23 kcal/mol. Since the binding energy of citrate onto the AuNP surface at low coverage was up to 55 kcal/mol,[334] it required 24 kcal/mol more binding energy to replace all the citrate. As shown in Figure 6.12, guest ligand concentration plays a less important role than ligand functional group. These results experimentally confirm that citrate has different binding modes, i.e. binding energies, to the AuNP surface, which result in the increasing resistance to replacement as the citrate coverage decreases.

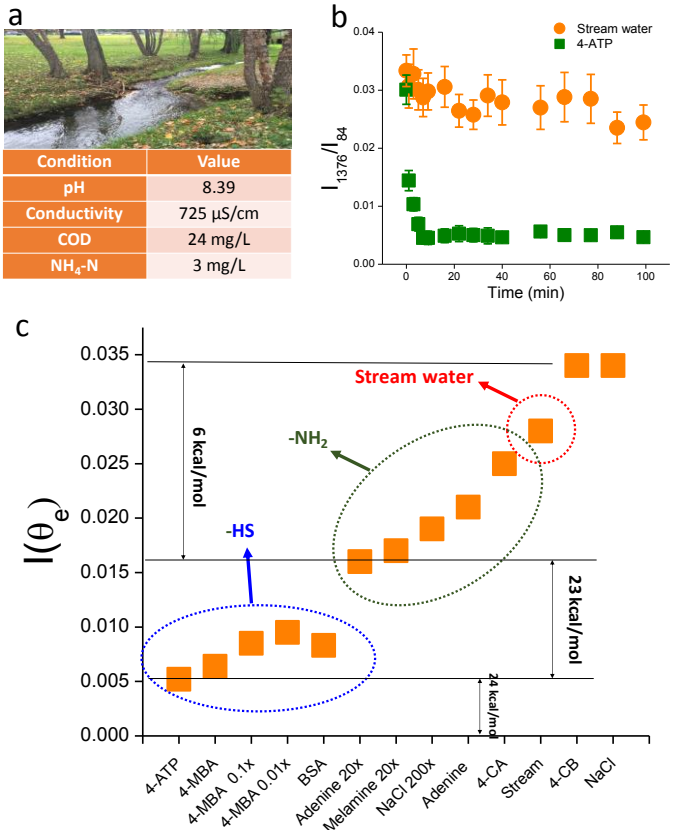

Figure 6.12 a) Parameters of the characterization of the stream water sample; b) Variation of HS-normalized citrate signals collected from AuNP/BC exposed to surface water and 4-ATP solution as a function of time; c) The remaining citrate on AuNP surface following replacement by a variety of chemicals.

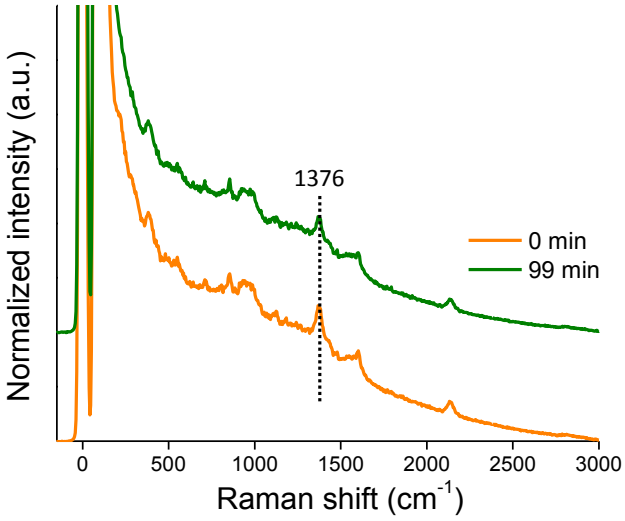

Figure 6.13 Raman spectra collected from AuNP/BC before and after its exposure to stream water for 99 min.

6.3.8 Environmental Implications

The combination of HSNSERS and the AuNP/BC platform enabled *in situ* and real time monitoring of the ligand exchange kinetics on the AuNP surface. This approach can potentially be generalized to a wide range of plasmonic nanoparticles, such as silver nanoparticles (AgNPs), transition metal nanoparticles, and semiconductor nanostructures. AgNPs, a better SERS enhancer than AuNPs, are well known for their strong antimicrobial effects.[349] Quantifying ligand exchange on an AgNP surface would be very useful for understanding their fate and transport in aquatic systems. In addition, this approach can be used to investigate the transformation/reactions occurring on plasmonic nanoparticle surfaces. Recently, it was reported that AgNPs promoted the formation of disinfection byproducts and AuNPs altered the nonsystemic behavior of pesticides.[350, 351] Quantifying the reaction products or intermediates could help us to understand the mechanisms behind such phenomenon.

One important conclusion in this study was that citrate on AuNP surface layer exhibited strong resistance to replacement in stream water, which had important implications for the colloidal stability of cit-AuNPs in aquatic systems. It was reported that NOM stabilizes cit-AuNPs under a wide pH range or in the presence of natural colloids by providing electrostatic and steric repulsion.[309, 310] This stabilizing effect is dependent on the physicochemical properties of the NOM used. NOMs with larger molecular weight better stabilized cit-AuNPs than those of smaller molecular weight.[311, 312] In these studies, how NOM or natural colloids interact with the citrate layer on the AuNP surface remains unknown due to the lack of analytical tools that can achieve *in situ* and real-time quantitation of AuNP surface coatings. This study provides such an analytical tool and suggests that the role of citrate in the fate and transport of cit-AuNPs should be more greatly emphasized.

Chapter 7 pK_a Determines the Affinity of Aromatic Amines to Citrate–Coated Gold Nanoparticles: In Situ Observation using HSNSERS

Haoran Wei,[1,2,3] Qishen Huang,[1,2,3] Weinan Leng,[1,2,3] Peter J. Vikesland[1,2,3*]

[1]Department of Civil and Environmental Engineering, Virginia Tech, Blacksburg, Virginia.

[2]Virginia Tech Institute of Critical Technology and Applied Science (ICTAS) Sustainable Nanotechnology Center (VTSuN), Blacksburg, Virginia.

[3]Center for the Environmental Implications of Nanotechnology (CEINT), Duke University, Durham, North Carolina.

*Corresponding author. Phone: (540) 231-3568, Email: pvikes@vt.edu

(This section is to be submitted to ***Environmental Science & Technology Letters***.)

Abstract

Aromatic amines associate with citrate coated gold nanoparticles (cit-AuNPs) via electrostatic attraction between amine and carboxylate groups and potentially alter the fate, transport, and toxicity of cit-AuNPs in aquatic systems. pK_a determines the protonation extent of amine groups and thus is expected to influence its affinity of aromatic amines to cit-AuNPs. In this study, the relationship between amine pK_a and their affinity to cit-AuNPs was systematically investigated *in situ* using "hot spot"-normalized surface-enhanced Raman spectroscopy (HSNSERS). Hot spot (HS) normalization minimizes the HS heterogeneity across SERS substrates and enables us to isolate solution pH as the only stimuli to the changing SERS signal. With the assistance of HS normalization, the SERS responses of four chloroanilines at different pH were well differentiated and the relationship of aniline pK_a and their affinity to cit-AuNPs was for the first time revealed. The results demonstrated that the anilines with lower pK_a exhibited lower affinity to cit-AuNPs at circumneutral pH but this affinity can be significantly improved at $pH<pK_a$. HSNSERS, as an in situ analytical tool, can be easily extended to studying the affinity of a variety of pollutants to AuNP surfaces under different environmental stimuli (temperature, pH, ionic strengths etc.).

7.1 Introduction

Aromatic amines are precursors and metabolites of azo dyes, herbicides, and pharmaceuticals.[352-354] Due to their mutagenic and carcinogenic effects,[352, 354, 355] the release of aromatic amines into surface water poses great concern for ecological safety and thus attracts great research effort for their transformation in natural systems.[356-358] Recently, sorption of aromatic amines onto

environmental solid - Montmorillonite[359] and pyrogenic carbonaceous materials[360] have been investigated. These two studies both employed cationic amines as target analytes and highlighted the important role of electrostatic forces and $\pi^{+}-\pi$ interactions in amine-solid affinity. However, the affinity of neutral aromatic amines to negatively-charged citrate-coated gold nanoparticles (cit-AuNPs) have not been explored.

Cit-AuNPs have been massively manufactured in both laboratories and industries for a variety of optical, electronic, therapeutic, and catalytic applications.[361-363] Accumulation of chemicals onto Au surface can alter their fate, transport, and toxicity in aqueous environments[315, 364] and thus largely determines their risk for human health. Our recent study showed that 4-chloroaniline with a comparatively high pK_a (4.2) overcoated on the citrate layer of AuNP surface. However, two amines with comparatively low pK_a (1.7 and 2.3) – atrazine and carbamazepine exhibited little affinity to cit-AuNP at circumneutral pH.[236] This intriguing phenomenon leads to the hypothesis that pK_a dictates the affinity of aromatic amines to cit-AuNP surface by controlling the electrostatic forces between them. However, systematic investigation on the influence of aromatic amine pK_a on their affinity to cit-AuNP surface has not been reported.

Surface-enhanced Raman spectroscopy (SERS) is a fast, sensitive, and information-abundant analytical technique arising from the collective oscillation of conductive electrons (localized surface plasmon resonance, LSPR) of plasmonic nanoparticles.[21, 365, 366] Due to the near-field characteristics of LSPR, SERS is particularly powerful for detecting molecules located within nanometer scale from nanoparticle surface. Considering cit-AuNPs themselves are SERS-active, it is a niche to apply SERS to investigate the interactions between aromatic amines and AuNP surface. However, the poor reproducibility of SERS caused by heterogeneous distribution of "hot spots" (HS) across a substrate makes quantitation challenging.[147, 367] Various chemicals have been

incorporated in SERS substrates as internal standards and thus improved the performance of SERS quantitation.[37, 242] However, introducing an external compound as internal standard adds to the cost and complexity while sacrifice sensitivity. Recently, we introduced surface-enhanced Rayleigh light as internal standard for SERS that overcomes the aforementioned disadvantages, which was called hot spot-normalized SERS (HSNSERS). This approach was subsequently applied for monitoring the kinetics of citrate replacement in presence of various chemicals from AuNP surface and evaluating the SERS substrate efficiency.[278]

In this study, influence of aromatic amine pK_a and solution pH on their affinity to cit-AuNP surface was investigated using HSNSERS. Four chloroanilines – 4-chloroaniline (4-CA), 3-chloroaniline (3-CA), 2-chloroaniline (2-CA), and 2,4-dichloroaniline (DCA) were selected as representative aromatic amines due to their simple structure and frequent occurrence in surface water.[352] Due to the inductive and deductive substituent effects,[368] the pK_a values of these four anilines systematically changed from 2.06 to 4.15 (Figure 7.1a). HSNSERS was applied to minimize the heterogeneous "hot spot" distribution across SERS substrate, making normalized SERS signal changed solely as a function of solution pH. The relationship between analytes` pK_a and their affinity to cit-AuNPs was for the first time revealed.

7.2 Materials and Methods

7.2.1 Reagents

Gold chloride trihydrate ($HAuCl_4 \cdot 3H_2O$) was purchased from MP Biomedicals. Sodium citrate tribasic dihydrate ($Na_3Cit \cdot 2H_2O$), 3-bromoaniline (3-BA, 98%), 4-chloroaniline (4-CA, 98%), 3-chloroaniline (3-CA, 99%), 2-chloroaniline (2-CA, 98%), and 2,4-dichloroaniline (99%) were

purchased from Sigma-Aldrich. Sodium hydroxide (NaOH) and Hydrochloric acid (HCl) were purchased from Fisher Scientific and used for adjusting solution pH.

7.2.2 Preparation of AuNP/BC Platform

Synthesis of bacterial cellulose (BC) and gold nanoparticle/bacterial cellulose (AuNP/BC) nanocomposites were described in detail in our previous publications. AuNP/BC nanocomposites were used as SERS substrates in this study.

7.2.3 Sampling

1 mL 4-CA, 3-CA, 2-CA, or 2,4-DCA ethanol solution with a concentration of 1 mM was added to 3 mL water solution with pH preadjusted to 1-10. One piece of AuNP/BC (0.5 cm × 0.5 cm) was immersed in the analyte solution. After vortex mixing for 30 s, the AuNP/BC hydrogel was taken out for Raman measurement. For quantitative analysis, 1 mL analyte ethanol solution with concentrations from 1 μM - 1 mM was added to 3 mL water solution with pH from 1.7-2.3. The following steps are the same as before. For analysis of analyte mixture, 1 mL of two or four analyte mixture ethanol solution (the concentration of each analyte is 0.125 and 0.25 mM for two aniline mixture and four aniline mixture, respectively) was added to 3 mL water solution with pH from 1.2-5.2. The following steps are the same as before.

7.2.4 SERS Measurement

After sampling, the AuNP/BC hydrogel is placed on sample holder of Raman spectrometer (WITec alpha 500R) and kept for 10 min before collecting data. The Raman maps were acquired every 5 min till 25 min with a 10× objective. Each Raman map contains 20 × 20 spectra in a 100 μm × 100 μm area. Laser wavelength is 785 nm and integration time for each spectrum is 0.5 s. The Raman

signal was dispersed by a 300 gr/mm grating and detected by a Peltier charge-coupled device (CCD).

7.2.5 HS-Normalization

For hot spot (HS) normalization, each spectrum was baseline corrected and the peak height at 126 cm^{-1} and 644 (4-CA), 531 (3-CA), 556 (2-CA), and 652 cm^{-1} (2,4-DCA) were recorded. The height ratio between the analyte peak and 126 cm^{-1} peak is the normalized value.

7.3 Results and Discussion

7.3.1 Improving Chloroaniline Quantitation using HSNSERS

The SERS spectra of the four chloroanilines were shown in Figure 7.1a. The slight difference of the four chloroanilines in the relative position of chlorine to amine group resulted in obvious different SERS spectra, making it easy to differentiate them. The strong band located at consistent wavenumber of 126 cm^{-1} in the SERS spectra was the surface-enhanced Rayleigh band from the amplified spontaneous emission of laser, which was used as internal standard here and after. As far as we know, it is the first time that the SERS spectra of these four chloroanilines were reported. Assignment of these Raman bands are beyond the scope of this study.

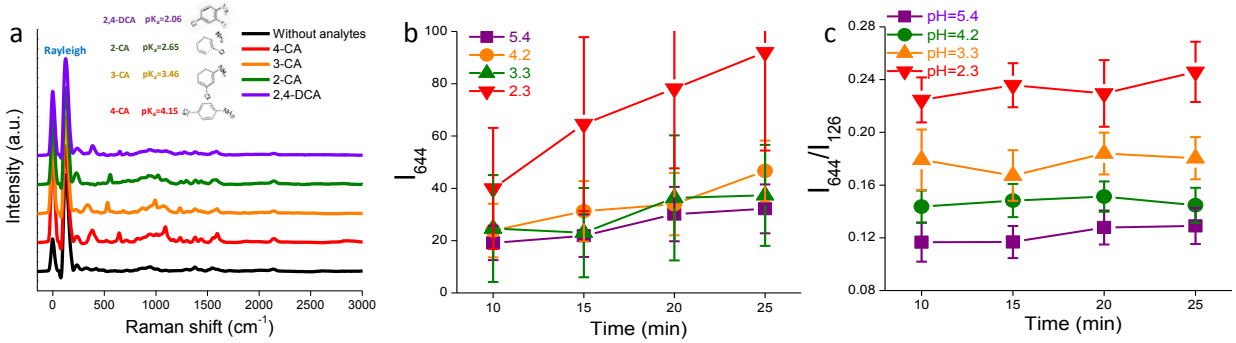

Figure 7.1 a) Average SERS spectra of 4-CA, 3-CA, 2-CA, and 2,4-DCA collected on AuNP/BC substrate at circumneutral pH; The spectra were normalized to the Rayleigh band at 126 cm^{-1}; b) Variation of SERS intensity of Raman band at 644 cm^{-1} of 4-CA as a function

of the drying time of AuNP/BC hydrogel acquired at different solution pH; c) Variation of ratios of Raman band at 644 cm^{-1} to Rayleigh band at 126 cm^{-1} (I_{644}/I_{126}) as a function of the drying time of AuNP/BC hydrogel at different solution pH.

By tracking one characteristic Raman band of each chloroaniline, its SERS map (100×100 μm^2) was obtained. The data points shown in Figure 7.1b were the average intensities of 4-CA band at 644 cm^{-1} over 400 spectra across its SERS maps. The error bar of each date point reflected the coefficient of variation (CV) of the band intensities across each map. As shown in Figure 7.1b, the large error bars (CV = 24.9%-83.0%) suggested that the variations of 4-CA Raman signal across the maps were very high. As shown in Figure 7.1c, following HS-normalization, the signal variations across the maps were significantly reduced indicated by the much smaller error bars (CV = 7.1%-12.8%).

After being placed onto the sample stage of the Raman spectrometer, more and more HS formed within AuNP/BC as the hydrogel was drying due to decreasing distance between nanoparticles.[190] SERS maps were collected every 5 min at different locations within the substrate until 25 min, when the hydrogel was still hydrated (a prerequisite for maintaining constant solution pH inside the hydrogel). At circumneutral pH of 5.4 (no additional HCl was added), the variation of the averaged Raman signals collected at different time and locations was high (CV=24.5%), which was significantly reduced following HS normalization (CV=5.5%) as shown in Figure 7.1b&c. The significant improvement of the temporal and spatial uniformity of Raman signals following HS normalization were repeatedly observed at the other three pH values (4.2, 3.3, and 2.2), suggested by the decrease of CV values from 24.8%-32.4% to 2.4%-5.5%. As shown in Figure 7.1b&c, the averaged signals at different pH (especially 5.4-3.3) entangled together due to the large signal variation induced by HS heterogeneity. However, after HS-normalization, the signals at different pH were well differentiated, enabling us to study the influence of pH on the SERS

signals of the chloroanilines. Similar results were observed for the other three chloroanilines (Figure 7.2).

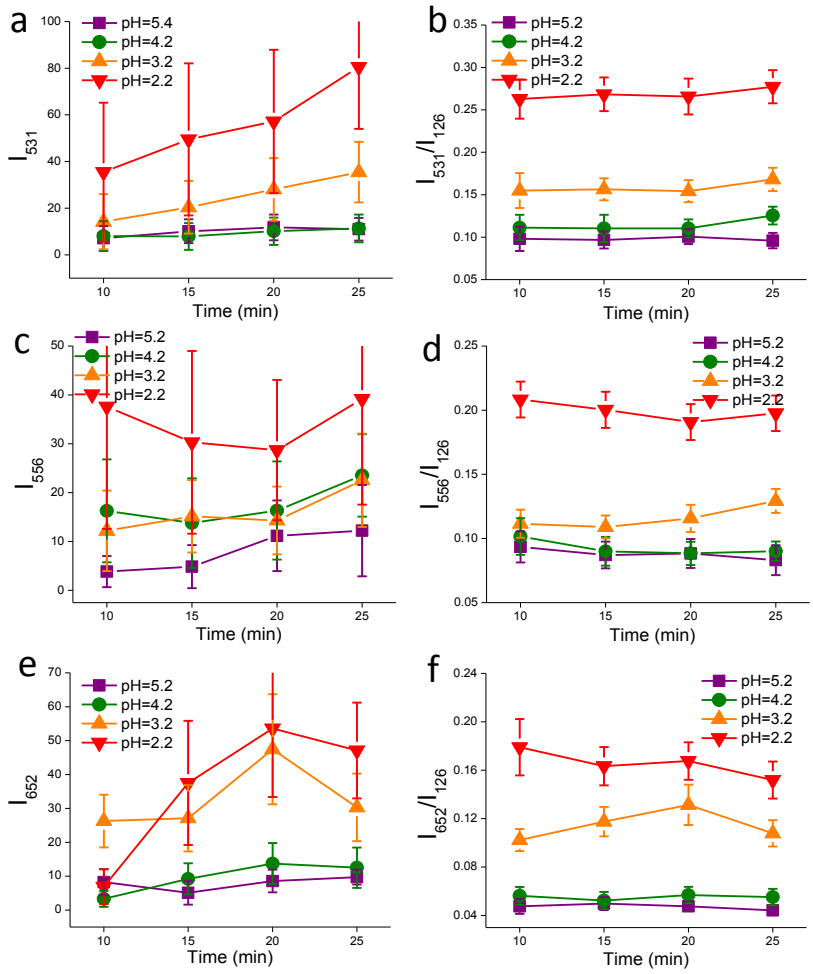

Figure 7.2 a) Variation of SERS intensity of Raman band at 531 cm^{-1} of 3-CA as a function of the drying time of AuNP/BC platform acquired at different solution pH; b) Variation of ratios of Raman band at 531 cm^{-1} to I_{126} as a function of the drying time of AuNP/BC platform at different solution pH; c) Variation of SERS intensity of Raman band at 556 cm^{-1} of 2-CA as a function of the drying time of AuNP/BC platform acquired at different solution pH; d) Variation of ratios of Raman band at 556 cm^{-1} to I_{126} as a function of the drying time of AuNP/BC platform at different solution pH; e) Variation of SERS intensity of Raman band at 652 cm^{-1} of 2,4-DCA as a function of the drying time of AuNP/BC platform acquired at different solution pH; f) Variation of ratios of Raman band at 652 cm^{-1} to I_{126} as a function of the drying time of AuNP/BC platform at different solution pH.

7.3.2 pH-Triggered Adsorption of Anilines to Cit-AuNP Surface

Affinity between analytes and plasmonic NPs significantly influence their SERS detection due to the exponential decay of SERS signal with distance of analytes from NP surface.[174, 369, 370] Recently, lowering pH below pK_a was used to improve the affinity of atrazine and carbamazepine to cit-AuNP.[236] Here we applied HS normalization to quantify the pH-triggered adsorption of four chlroanilines to AuNP surfaces. 4-CA has a pK_a value of 4.2, so the electrostatic affinity between 4-CA and citrate-coated AuNPs (negatively charged) should increase with the decreasing solution pH (Figure 7.3a). To prove this, average spectra from different time and locations under different pH were shown in Figure 7.3b. When the spectra were normalized at the band at 126 cm^{-1}, the intensities of 4-CA Raman bands collectively increased when pH decreased from 5.4 to 2.3. Similar results were observed for the other three chloroanilines (Figure 7.3c and Figure 7.4). These results were consistent with our previous observation of pH-triggered SERS detection of carbamazepine and atrazine and corroborated that the electrostatic forces dominated the affinity between chloroanilines and cit-AuNP surfaces.

However, 4-CA and 2,4-DCA exhibited significantly different behaviors in their pH-triggered adsorption. As shown in Figure 7.3b&c, under circumneutral pH, the SERS signal of 4-CA had already been very strong while the SERS signal of 2,4-DCA was almost overwhelmed by the background (citrate) signal. However, when solution pH was lowered to values below the analyte pK_a, SERS signals of 4-CA and 2,4-DCA were both enhanced significantly (Figure 7.3b&c). The pH-triggered adsorption of these two chloroanilines were quantified by inserting the normalized signals ($I_{Raman}/I_{Rayleigh}$) to their concentration calibration curves (Figure 7.5). The conclusion reached is that for 4-CA and 2,4-DCA, lowering the pH value to 3.3 was equal to increasing their concentrations by 7 and 16× for SERS detection. Further lowering the pH below the pK_a was equal

to increasing their respective concentrations by 36 and 1087× for their SERS detection. The great difference between pH-triggered adsorption was expected as a result of the different pK_a values of these two chloroanilines (4.2 vs 2.1). To prove this hypothesis, the relationship between aniline pK_a and their SERS response was systematically studied in the following section.

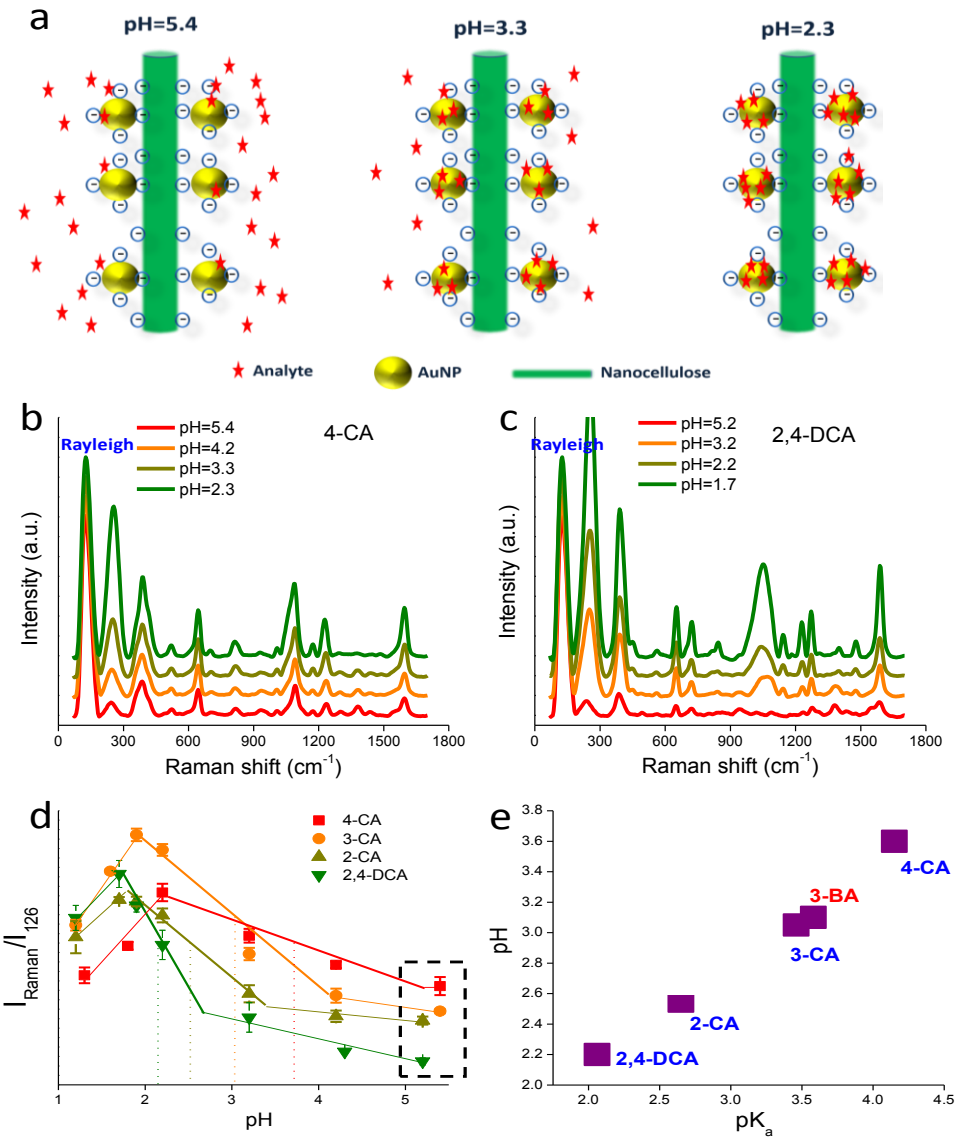

Figure 7.3 a) Schematic of the sorption process of 4-CA to AuNP surface at different pH; SERS spectra of b) 4-CA and c) 2,4-DCA acquired on AuNP/BC platform at different pH values. Each spectrum is an average of 400 single spectra across a 100 µm × 100 µm area; d) Variation of normalized SERS intensity of four chloroanilines as a function of solution pH; e) Variation of middle point of the linearly increasing ranges of five anilines as a function of their pK_a.

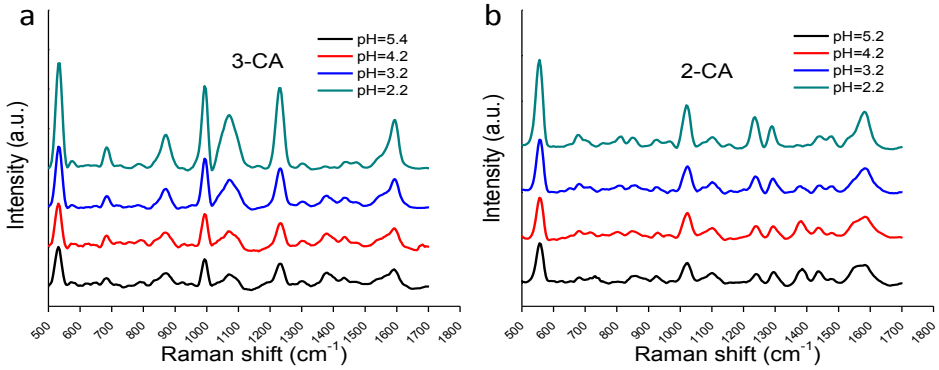

Figure 7.4 SERS spectra of a) 3-CA and b) 2-CA acquired on AuNP/BC platform at different pH values. Each spectrum is an average of 400 single spectra across a 100 µm × 100 µm area. All the spectra were normalized to the band at 126 cm^{-1}.

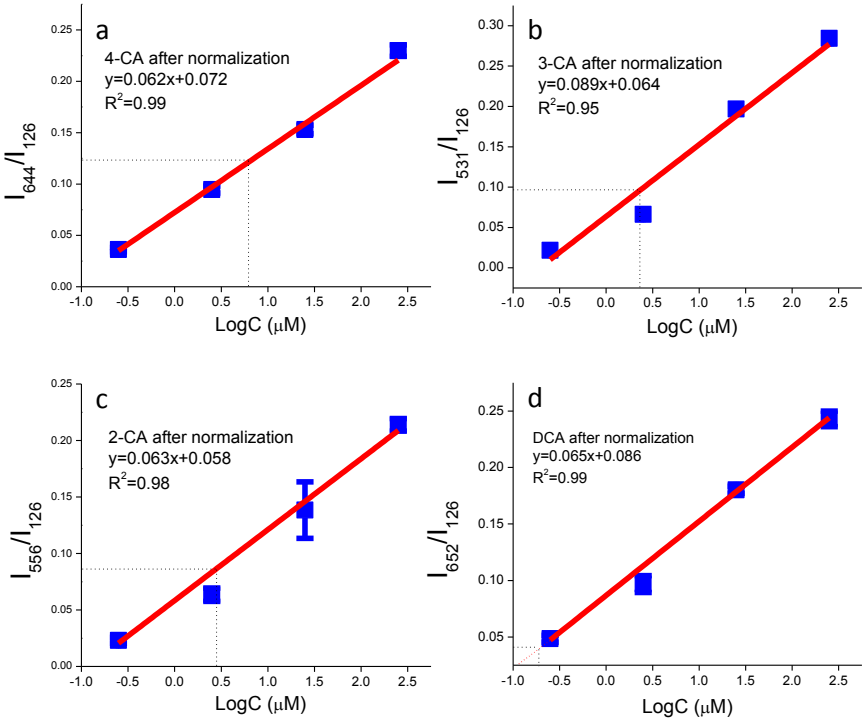

Figure 7.5 Variation of normalized SERS intensities of a) 4-CA, b) 3-CA, c) 2-CA, and 2,4-DCA as a function of their logrithmic concentrations (error bars reflect the standard deviation of SERS intensities from three collected average spectra; Each average spectrum is the average of 400 spectra in a 100 µm × 100 µm SERS map. The numbers shown in the figures correspond to the Raman shift of the Raman bands that were monitored here). This figure was readapted from the data reported in our previous publication.

7.3.3 Relationship between Aniline pK_a and Their Affinity to Cit-AuNPs

The normalized SERS signal of four chloroanilines with different pK_a acquired from pH 1-6 were shown in Figure 7.3d. This range was selected because the analytes` pK_a all located in this range and the SERS intensity acquired at pH values beyond this range kept constant (Figure 7.6). For all the four chloroanilines, normalized SERS intensities first increased slowly and subsequently increased linearly with the decreasing pH (Figure 7.3d). The reason for the linear increase is attributed to the enhanced electrostatic attraction between analytes and AuNP surface at lower pH. After the intensity reached the maximum, it dropped down as the pH further decreased, which may be due to the competitive adsorption of the excess protons on AuNP surface.

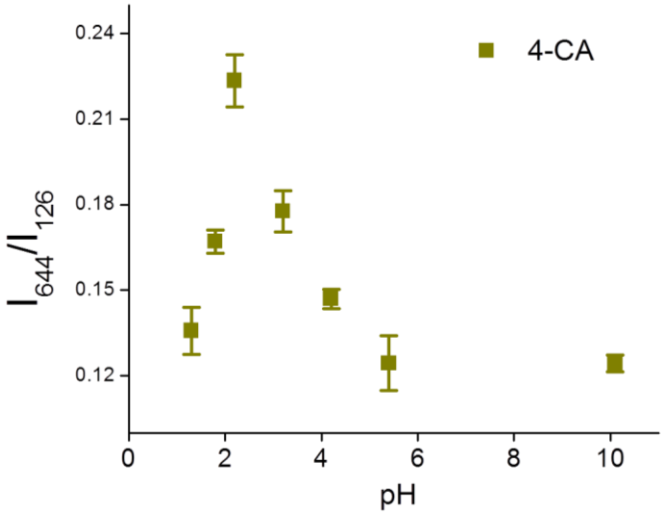

Figure 7.6 Variation of normalized SERS intensity of 4-CA as a function of solution pH.

In order to clearly show the pK_a dependence of their SERS responses, the middle points of the linearly increasing range for the four chloroanilines were shown in Figure 7.3e. The corresponding pH values of the middle points decreased as the pK_a of the compounds decreased, exhibiting the blue shift of the pH-sensitive range of these compounds (Figure 7.3e). It was notable that the middle points of the linearly increasing ranges were close to the pK_a values of the four anilines, highlighting the potential of this platform for detecting the pK_a of amine-containing compounds.

These results demonstrated the strong dependence of the SERS responses on aromatic amine` pK_a. The pH value corresponding to the linear increasing range of 3-bromoaniline (3-BA, pK_a=3.58) lies on the linear line shown in Figure 7.3e, indicating this pK_a-SERS relationship is independent of the identity of the halogen substituents (Figure 7.7).

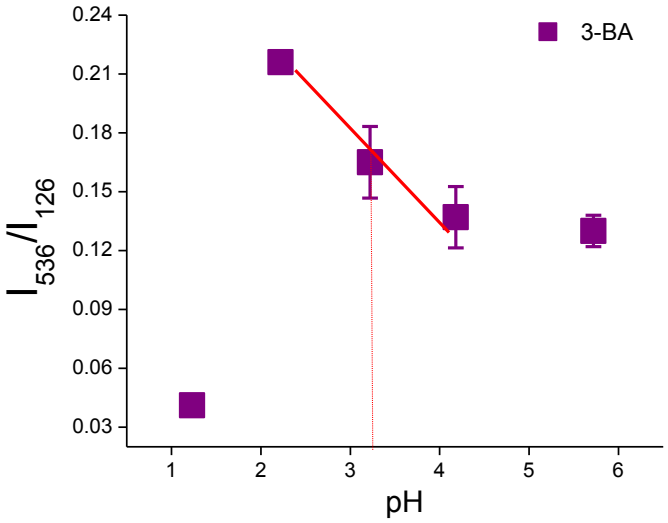

Figure 7.7 Variation of normalized SERS intensity of 3-BA as a function of solution pH.

Marked by the black dashed rectangle in Figure 7.3d, the normalized SERS signal of chloroanilines at circumneutral pH increased with their pK_a, suggesting that the lower pK_a the aniline has, the harder can it associate with cit-AuNPs. This is consistent with our observation that the SERS spectrum of 2,4-DCA (having the lowest pK_a) exhibited much lower SERS signals than 4-CA at circumneutral pH (Figure 7.3b&c). This phenomenon can be explained by the extent of protonation of amine groups of the four anilines. Amine group of 4-CA, with the highest pK_a value, was protonated easiest, thus facilitating its adsorption onto cit-AuNP surface. Amine group of 2,4-DCA, with the lowest pK_a, was protonated hardest, thus limiting its electrostatic attraction onto cit-AuNP surface. To put it simply, anilines with lower pK_a need more protons to "activate" their amine groups.

7.3.4 SERS Spectra of a Mixture of Anilines

One environmental implication of pK_a-SERS relationship is that anilines with low pK_a (<3) can barely associate with cit-AuNPs at circumneutral pH even when their concentration were considerably high. To further confirm this statement, SERS spectra of a mixture of two chloroanilines with different pK_a were acquired at different pH. The concentration of each aniline was 125 µM. As shown in Figure 7.8a, the SERS spectrum of 4-CA (pK_a=4.2) and 2,4-DCA (pK_a=2.1) mixture only exhibited the characteristic bands of 4-CA at circumneutral pH. As the pH decreased to 2.2, 2,4-DCA Raman bands, e.g. bands at 1042 cm^{-1} and 1273 cm^{-1} appeared and developed. The ratios between 2,4-DCA bands and 4-CA bands (I_{1042}/I_{1094} and I_{1273}/I_{1239}) almost remained constant from pH 5.0 to 3.3 and significantly increased from 3.3 to 2.2 (Figure 7.8b), which was consistent with our observation in Figure 7.3d.

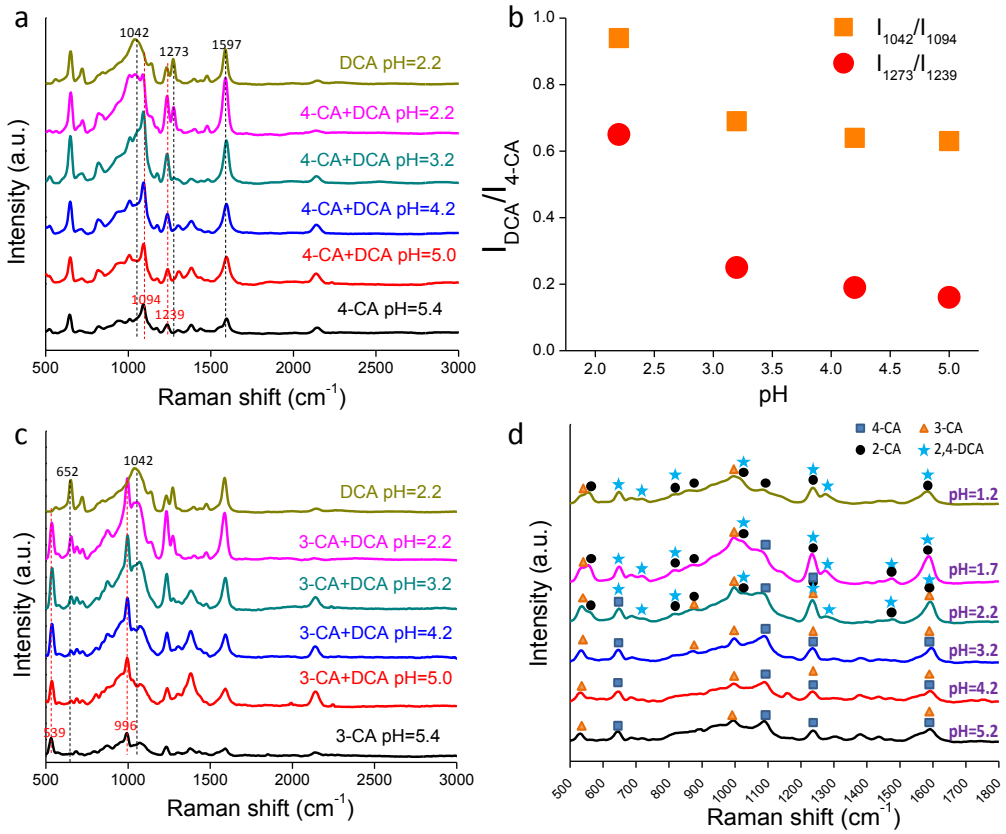

Figure 7.8 a) SERS spectra of a mixture of the two anilines (4-CA and 2,4-DCA) acquired at different solution pH; b) Variation of the ratios between 2,4-DCA and 4-CA Raman bands at 1042 cm^{-1} to 1094 cm^{-1} and 1273 cm^{-1} to 1239 cm^{-1} as a function of pH; c) SERS spectra of a mixture of the two anilines (3-CA and 2,4-DCA) acquired at different solution pH; d) SERS spectra of a mixture of the four anilines acquired at different solution pH.

Similar results were observed in a mixture of 3-CA (pK_a=3.5) and 2,4-DCA (pK_a=2.1). As shown in Figure 7.8c, the SERS spectrum of the mixture exhibited predominantly the feature of 3-CA at circumneutral pH. As the pH decreased to 2.2, the characteristic Raman bands of 2,4-DCA gradually increased. These results clearly demonstrated that 2,4-DCA was almost "invisible" at circumneutral pH while the two anilines with higher pK_a (4-CA and 3-CA) can be readily detected by SERS.

To further confirm this conclusion, SERS spectra of a mixture of four anilines (each with a concentration of 62.5 μM) at different pH were collected. As shown in Figure 7.8d, the most prominent Raman bands for 2-CA (556 cm^{-1}) and 2,4-DCA (1031 cm^{-1}) were not observed at pH

of 5.2 and 4.2, indicating these two compounds with lower pK_a (2.1 and 2.7) were not detected at these pH values. However, when pH decreased from 3.2 to 1.7, 2-CA and 2,4-DCA bands (marked by black circle and blue star) appeared and became dominant in the spectrum. When pH further decreased to 1.2, the intensities of all Raman bands decreased due to the competitive adsorption of H^+, which is consistent with our observation in Figure 7.3d. Since most of SERS analysis was carried out at circumneutral pH, some amine-containing compounds may escape the detection because of their low pK_a. Since aromatic amines with low pK_a exhibit negligible affinity to cit-AuNP surface, they are not likely to alter the fate, transport, and toxicity of cit-AuNP at circumneutral pH.

Chapter 8 pH-Triggered Molecular Alignment for Reproducible SERS Detection of Atrazine and Carbamazepine via An AuNP/BC Platform

Haoran Wei[1,2,3] and Peter J. Vikesland[1,2,3*]

[1]Department of Civil and Environmental Engineering, Virginia Tech, Blacksburg, Virginia

[2]Virginia Tech Institute of Critical Technology and Applied Science (ICTAS) Sustainable Nanotechnology Center (VTSuN), Blacksburg, Virginia

[3]Center for the Environmental Implications of Nanotechnology (CEINT), Duke University, Durham, North Carolina

*Corresponding author. Phone: (540) 231-3568, Email: pvikes@vt.edu

(This chapter has been published in ***Scientific Reports***.[29] *Scientific Reports* is an open access journal, so reproduction permission is not required)

Abstract

The low affinity of neutral and hydrophobic molecules towards noble metal surfaces hinders their detection by surface-enhanced Raman spectroscopy (SERS). Herein, we present a method to enhance gold nanoparticle (AuNP) surface affinity by lowering the suspension pH below the analyte pK_a. We developed an AuNP/bacterial cellulose (BC) nanocomposite platform and applied it to two common pollutants, carbamazepine (CBZ) and atrazine (ATZ) with pK_a values of 2.3 and 1.7, respectively. Simple mixing of the analytes with AuNP/BC at $pH<pK_a$ resulted in consistent electrostatic alignment of the CBZ and ATZ molecules across the nanocomposite and highly reproducible SERS spectra. Limits of detection of 3 nM and 11 nM for CBZ and ATZ, respectively, were attained. Tests with additional analytes (melamine, 2,4-dichloroaniline, 4-chloroaniline, 3-bromoaniline, and 3-nitroaniline) further illustrate that the AuNP/BC platform provides reproducible analyte detection and quantification while avoiding the uncontrolled aggregation and flocculation of AuNPs that often hinder low pH detection.

8.1 Introduction

Surface-enhanced Raman spectroscopy (SERS) has been proposed for ultrasensitive chemical analyses ever since the technique exhibited the capacity for single molecule detection.[24, 25] Compared to other analytical techniques, SERS does not necessarily require laborious sample pretreatment nor expensive instrumentation, and thus is promising for rapid field and point of use detection.[26, 55, 68] To date, however, the hoped for utilization of SERS for rapid detection of

environmental pollutants has yet to be realized due to the challenges and costs associated with the production of reproducible SERS substrates[371-373] as well as the intrinsic requirement that the analyte consistently associates with the substrate to generate a strong, reproducible Raman signal.[31, 173] Because of these factors, many SERS studies continue to utilize model analytes with high surface affinity to test assay performance.[26, 33, 61, 100, 114, 121, 155] Unfortunately, many relevant analytes are moderately hydrophobic and thus exhibit low affinity to gold or silver nanoparticle (AuNP or AgNP) surfaces. To overcome this drawback, molecular "traps" have recently been used to bind target molecules to the AuNP/AgNP surface.[173-176, 178, 374] Modification of the noble metal surface with these "traps" adds complexity to the material synthesis and produces a potentially interfering background signal that makes data analysis more challenging. To mitigate this issue, some investigators manipulate electrostatic forces, either by altering the AuNP/AgNP surface coating or adjusting the solution pH to enhance the affinity of the analyte for the plasmonic nanoparticle surface.[109, 375] Unfortunately, surface coatings can decrease the SERS signal intensity due to the increased distance between the analyte and the surface,[376] and AuNP/AgNP suspensions generally exhibit uncontrolled aggregation and flocculation at low pH values and are thus inappropriate SERS enhancers under these conditions. For analytes with low pK_a values it is necessary to develop a SERS platform that is stable at low pH.

Bacterial cellulose (BC) is a low-cost bacterial by-product that is biodegradable and exhibits minimal to no toxicity.[194] Compared to common cellulosic materials, BC fibers are nanoscale in radial diameter (<100 nm) and are tightly interwoven as a layered high mechanical strength hydrogel.[194, 202] Importantly, unlike paper, BC retains its 3D structure in water and is resistant to both acidic and alkaline pH.[190] Recently, its role as a scaffold for nanoparticles for SERS and other applications has been realized.[190, 377, 378] Our prior studies with this nanocomposite suggest that the

coupling of AuNPs with BC may be a promising approach for the development of a stable low pH SERS platform since the AuNPs are immobilized within the BC matrix and both components are acid-resistant.

In this study, AuNP/BC nanocomposites were synthesized by boiling $HAuCl_4$-treated BC in sodium citrate (Na_3Cit) solution to produce AuNPs that are fully intercalated within the BC network. These nanocomposites were then tested as a SERS platform under acidic pH conditions. To illustrate the capacity of this substrate, two common environmental contaminants - carbamazepine (CBZ; pK_a=2.3) and atrazine (ATZ; pK_a=1.7) - were used as model, environmentally relevant analytes.[379-382] CBZ is an micropollutant of emerging concern and is one of the most frequently detected pharmaceuticals in surface water.[381] ATZ is widely used for weed control in corn acreage and is the most frequently detected herbicide in surface water.[380] Each of these analytes are moderately hydrophobic (K_{ow} > 1.5; refs.[383, 384]) with low pK_a values and exhibit low AuNP surface affinity under neutral pH conditions.

8.2 Results

8.2.1 Material Characterization

Our AuNP/BC nanocomposite was synthesized by vortexing BC in 0.7 mL of 30 mM $HAuCl_4$ and then boiling in 50 mL of 1.2 mM Na_3Cit. As shown schematically in Figure 8.1a, the as produced AuNP/BC nanocomposite is a rigid hydrogel with large numbers of 63±17 nm (n=200) diameter AuNPs widely distributed throughout the BC matrix (Figure 8.2a&b). The extinction spectrum shows a broad LSPR band with two maxima at 589 and 637 nm indicating the in situ formed AuNPs are highly aggregated (Figure 8.2c). The AuNP/BC nanocomposite exhibits an extremely flat surface topography that facilitates XY image scan collection (Figure 8.2d). Furthermore, the AuNP/BC platform is remarkably stable as shown by a pH invariant extinction spectrum (Figure

8.2c) and the lack of any detectable variation in AuNP size (Figure 8.3) following exposure to either neutral or acidic pH. This stability is reflected by the consistency of our previously acquired MGITC SERS spectra at neutral and acidic pH.[190] Compared with suspension-based SERS, AuNP/BC provides a rigid scaffold that prevents uncontrolled aggregation and flocculation and thus has potential for use as a low pH SERS substrate.

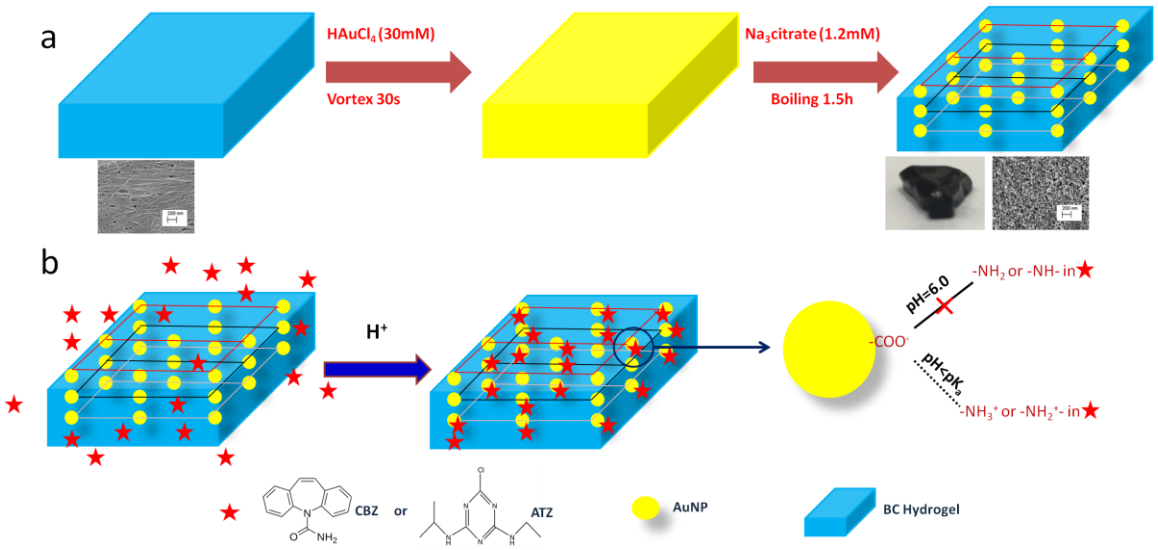

Figure 8.1 a) Schematic of synthesis of AuNP/BC nanocomposites and b) schematic of pH-induced adsorption of CBZ and ATZ on AuNP/BC.

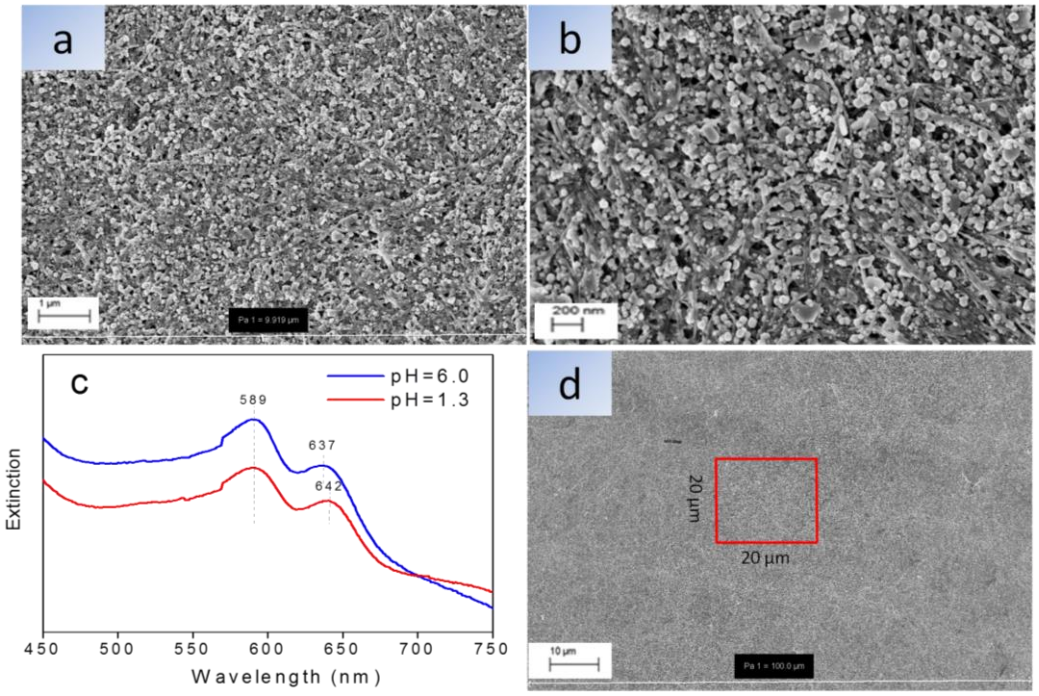

Figure 8.2 SEM images of AuNP/BC dry film at a) 28000×, and b) 50000× magnification. c) Extinction spectra of AuNP/BC hydrogel exposed to aqueous solution with pH=1.3 or 6.0 for 15 s. d) SEM images of AuNP/BC dry film at 2800× magnification.

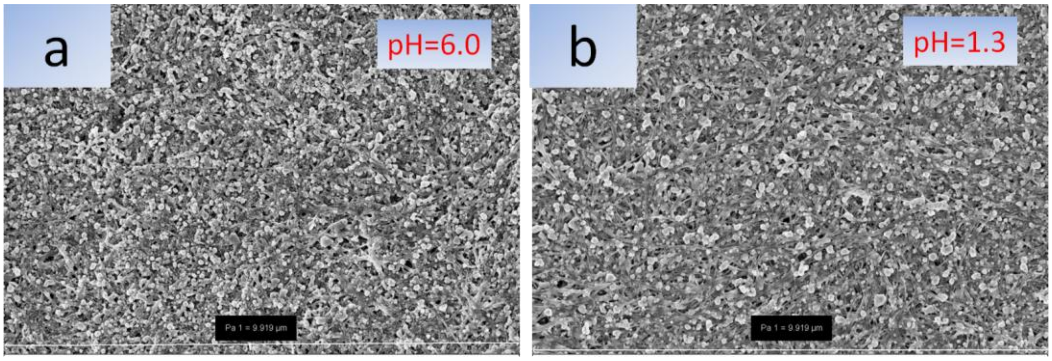

Figure 8.3 SEM images of AuNP/BC dry film exposed to aqueous solution with a) pH=6.0 or b) pH=1.3 for 15 s.

8.2.2 pH-Triggered SERS

Many analytes used to test novel SERS substrates (e.g., rhodamine 6G, crystal violet, Nile blue, etc.) are positively charged at neutral pH and either covalently or electrostatically associate with negatively charged AuNPs. However, both CBZ and ATZ are neutral molecules at environmental pH and thus exhibit low affinity to the AuNP surface due to the lack of an electrostatic attraction.

No Raman signal for either CBZ or ATZ could be observed following exposure of an AuNP suspension to CBZ or ATZ at pH = 6.0 (Figure 8.4). CBZ and ATZ contain primary and secondary amine groups, respectively, that are protonated at pH values below their respective pK_a values (Figure 8.1b). Unfortunately, under these pH conditions many AuNPs uncontrollably aggregate and are thus unsuitable for use as SERS enhancers.[375] We speculated, however, that the stability of AuNP/BC at low pH would enable the protonated amine groups of CBZ and ATZ to associate with the carboxylate groups of AuNP bound citrate via electrostatic attraction (Figure 8.1b) and that this would facilitate their SERS detection.

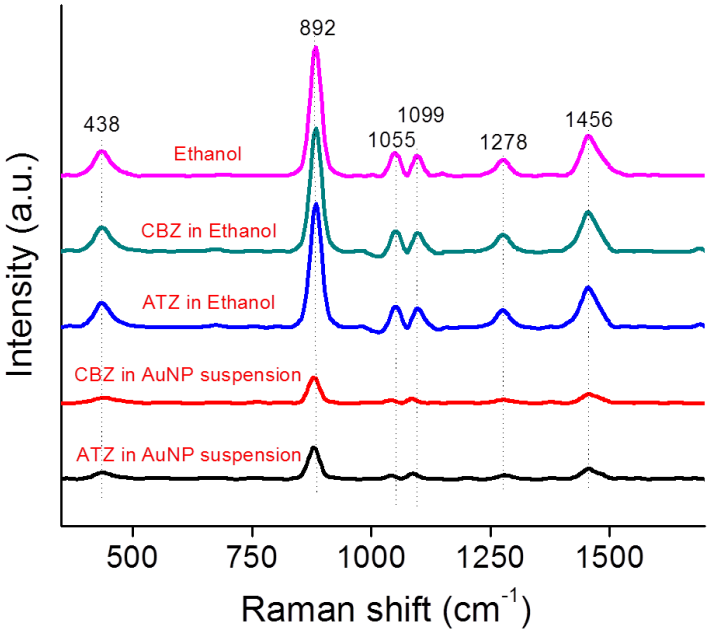

Figure 8.4 Average Raman spectrum of 250 µM CBZ and ATZ in a 50 nm AuNP suspension, in an ethanol solution and pure ethanol. (Average of 400 spectra in a 100 µm × 100 µm area, laser 785 nm, 5 mW, 10× objective).

At neutral pH neither CBZ nor ATZ exhibit a detectable SERS signal (Figure 8.5a&b, Figure 8.6). However, when the pH decreases from 6.0 to 3.0, the signal intensity increases and at pH values below an analyte's pK_a there is a substantial enhancement in the SERS signal for both CBZ and ATZ. To quantify the influence of pH on the SERS signal, the intensity of the CBZ peak at

1222 cm^{-1} and the intensity of the ATZ 961 cm^{-1} peak were used to reflect the signal from the two compounds (I_{signal}), while the small peak at 1371 cm^{-1} was used to represent the BC support ($I_{background}$). As shown in Figure 8.5c, the ratio of the peak intensity for the analyte relative to the background increased 47× for CBZ and 68× for ATZ with a decrease in pH from 6.0 to below the analyte's pK_a. Because of the chemical and colloidal stability of the AuNPs restrained within the BC scaffold, AuNP aggregation cannot account for this pH-induced Raman signal enhancement (Figure 8.2c and Figure 8.3). Furthermore, the stability of the Raman band at 1371 cm^{-1} under varying pH conditions supports our contention that the AuNP/BC platform is stable at acidic pH (Figure 8.5a&b). We did not observe any temporal variations in signal intensity, thus indicating the platform did not degrade at acidic pH. We thus conclude that the significant SERS enhancement for CBZ and ATZ at low pH is due to an increase in their surface affinity. For $pH<pK_a$, the protonated $-NH_2$ and -NH- groups in CBZ and ATZ facilitate analyte association with the negatively charged carboxylate groups of the AuNP citrate coating (Figure 8.1b). To affirm this speculation, benzoic acid (pK_a = 4.2), an aromatic compound without an amine group, was used as a negative control. Under similar conditions as used for CBZ, no Raman signal for BA could be observed, thus further suggesting the role of pH sensitive amine groups in the SERS detection of CBZ and ATZ (Figure 8.7). In contrast, our positive control MGITC, which associates with AuNP via a thiol linkage, exhibited pH insensitive SERS.[190, 385]

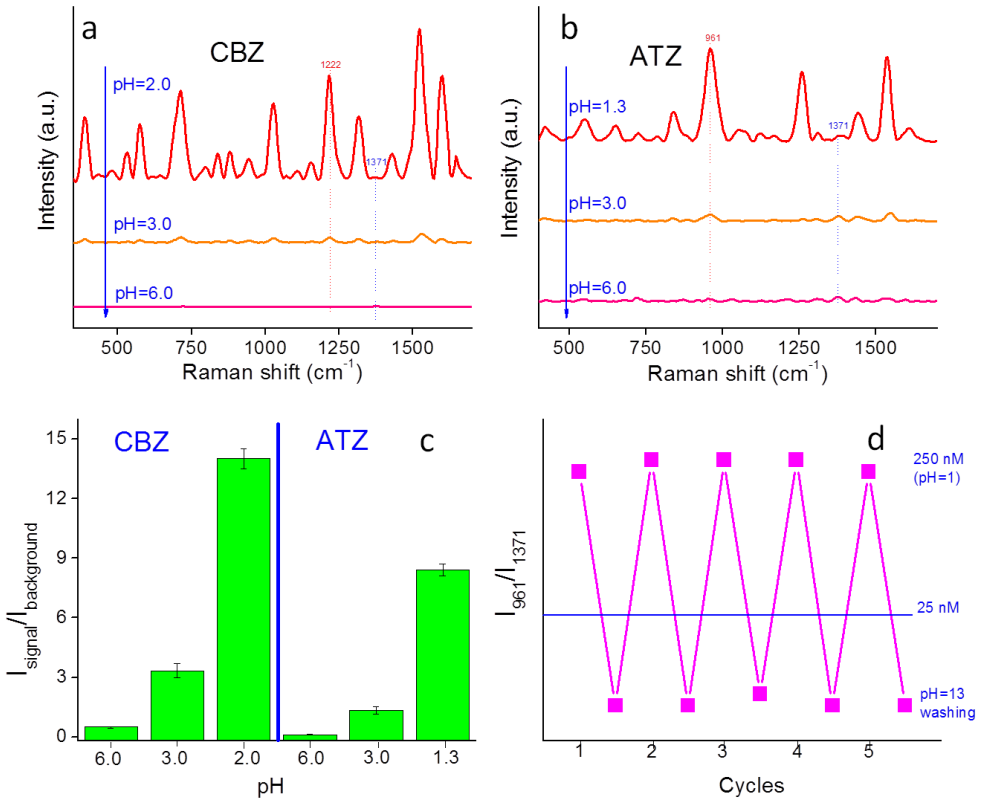

Figure 8.5 Average Raman spectra of AuNP/BC exposed to a) 250 µM CBZ and b) ATZ solutions of different pH; c) Change of signal/background ratio (I_{1222}/I_{1371} for CBZ and I_{961}/I_{1371} for ATZ) as a function of solution pH; d) Change of signal/background ratio for ATZ with five consecutive exposure to ATZ at pH=1.3 and NaOH washing at pH=13. (Average of 400 spectra in a 20 µm × 20 µm area, laser 785 nm, 5 mW, 10× objective).

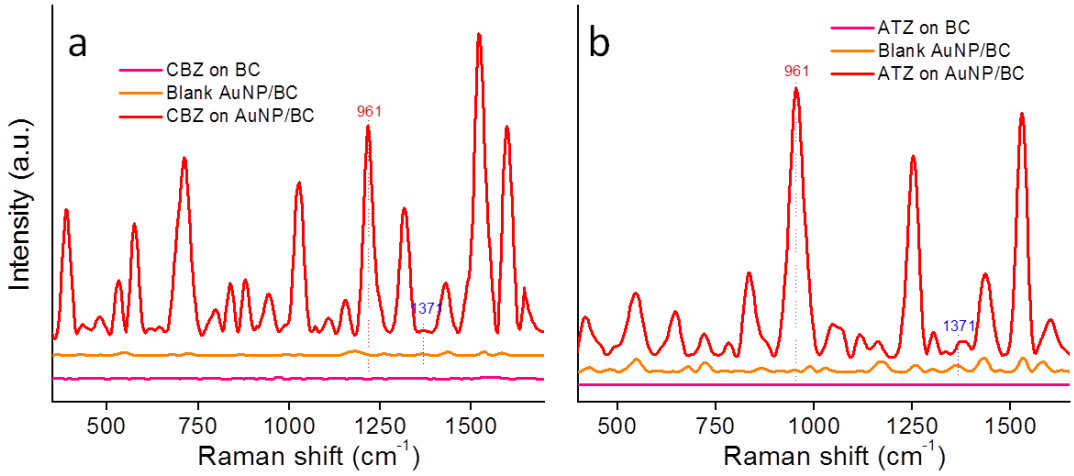

Figure 8.6 Average Raman spectrum of 250 µM a) CBZ and b) ATZ on BC and AuNP/BC and blank AuNP/BC at pH=1.3 or 2.0. (Average of 400 spectra in a 20 µm × 20 µm area, laser 785 nm, 5 mW, 10× objective).

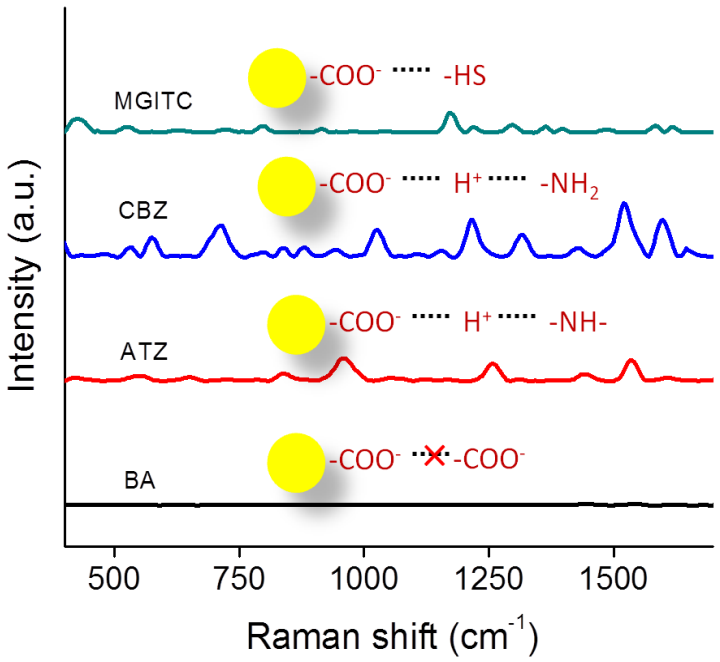

Figure 8.7 Average Raman spectra of AuNP/BC exposed to 2.5 µM MGITC at pH=6.0, 250 µM CBZ and BA at pH=2.0, and 250 µM ATZ at pH=1.3.

To further support our contention that CBZ and ATZ associate with the surface via their nitrogen groups we examined the collected SERS spectra and compared them to the normal Raman spectrum of each compound (Figure 8.8a&b). For each analyte, the prominent peaks in the normal Raman spectra appear in the respective SERS spectra, but exhibit substantial signal enhancements, thus validating that the spectra reflect the SERS of the target analytes. The measured Raman shift reflects the vibrations of chemical bonds, and thus significant differences in Raman shift between the SERS spectrum and the normal Raman spectrum indicate the change in the vibration of a particular chemical bond that is caused by an interaction between the analyte and the NP surface.[386, 387] In the SERS spectra of CBZ and ATZ, there is very little shift in the Raman peaks relative to their normal Raman spectra in the 400-1400 cm^{-1} range (these peaks primarily reflect covalent interactions within the six-member rings and C-C bonds)[59], thus indicating the main mechanism for the SERS of these bands is via long distance electromagnetic enhancement.[388] However, there are detectable blue shifts and significant enhancement of the peaks in the range

1500-1600 cm^{-1} (N-H and C-N bonds),[59] indicating shorter distance chemical SERS enhancements in addition to the longer range electromagnetic enhancement.[387] SERS spectral analysis thus supports our speculation that CBZ and ATZ associate with the AuNPs through an electrostatic attraction between amine groups and the citrate coating of the AuNPs. The $-NH_2$ group in CBZ and the two protonated -NH- groups of the ATZ ring substituents are in close proximity to the AuNP surface, while the six-member rings are further away from the AuNP surface (Figure 8.8c). Our speculation that the positively-charged amine groups of CBZ and ATZ associate with the negatively-charged carboxylate groups on AuNP surface is supported by the following: 1) The significant enhancement in the SERS intensity of CBZ and ATZ was observed at pH values below their respective pK_a values, thus highlighting the important role of positively-charged amine groups (Figure 8.5). 2) A similar phenomenon was observed for a variety of amine-containing compounds (positive controls) with low pK_a values, but not for carboxylate-containing compounds (negative controls; Table 8-1 and Figure 8.7), further corroborating the role of positively-charged amine groups. 3) The substantial enhancement and shift of the amine SERS bands of CBZ (1521 cm^{-1} and 1596 cm^{-1}) and ATZ (1538 cm^{-1} and 1598 cm^{-1}) relative to their normal Raman bands indicate that the amine groups were close to the AuNP surface and thus subject to chemical enhancement.

The SERS enhancement factor (EF) for AuNP/BC was estimated using Eq. 8.1 and the simplifying assumption that all of the CBZ and ATZ initially added associated with the AuNPs:

$$EF = \frac{I_{SERS} N_{NR}}{I_{NR} N_{SERS}} \qquad \text{Equation 8.1}$$

where I_{SERS} and I_{NR} are the peak intensities at 1222 cm^{-1} for CBZ and 961 cm^{-1} for ATZ on AuNP/BC and solid, respectively, and N_{SERS} and N_{NR} are estimates for the number of analyte

molecules within the laser probe volume for both AuNP/BC and the solid. Using this relationship EF was calculated to be 1×10^5 for CBZ and 3×10^5 for ATZ. We note that our calculated EF is a lower bound of the actual EF due to that fact that substantial amounts of free CBZ and ATZ both remain in solution and associate with the BC matrix. As stated in the highly cited and comprehensive study of SERS EF by Etchegoin and colleagues,[286] an EF of 10^7 is sufficient to enable single molecule SERS detection and thus our calculated value of 10^5 reflects a substantial enhancement. We note that a recent study[389] coupling capillary chromatography with SERS for ATZ detection reported an EF value of only 8 and that we determined a comparable EF of 10 using a commercially available substrate (Figure 8.9 & Figure 8.10). Our value is nearly five orders of orders of magnitude larger. Large variations in the reported SERS spectra for atrazine in the literature and their obvious differences relative to the normal Raman and theoretical spectra of atrazine illustrate the challenges that to date have plagued reproducible atrazine detection by SERS.[59, 390-392] Furthermore, the lack of information about temporal and spatial SERS signal variations makes the reproducibility of these studies questionable.

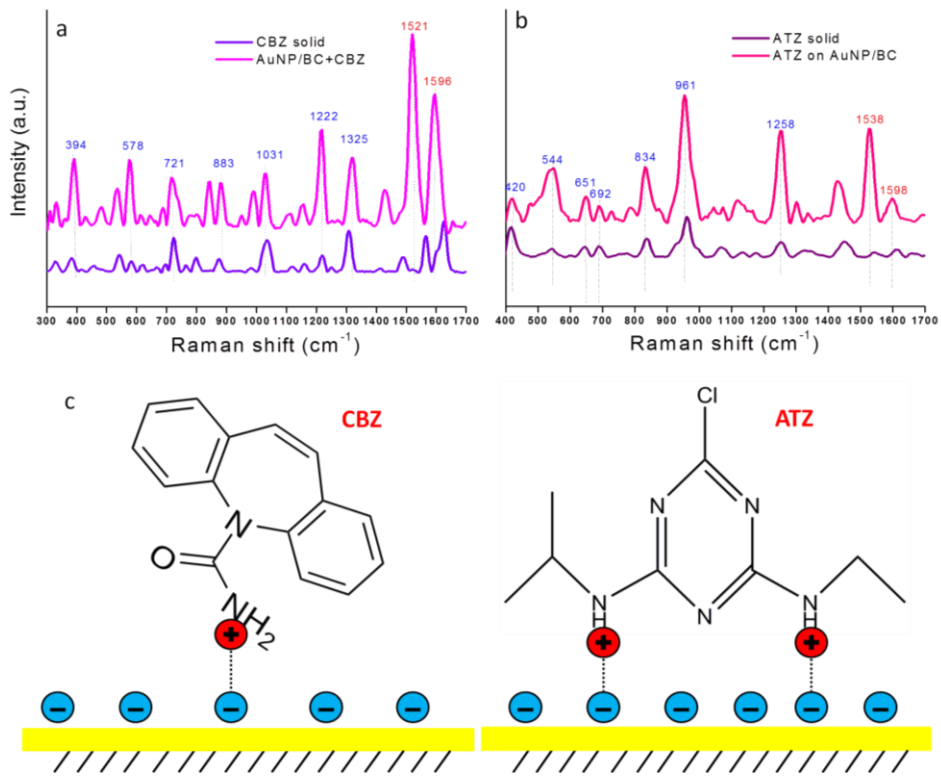

Figure 8.8 a) Average Raman spectra of CBZ solid, and CBZ on AuNP/BC hydrogel; b) Average Raman spectra of ATZ solid, and ATZ on AuNP/BC hydrogel; c) The molecular orientation of CBZ and ATZ on AuNPs. (Average of 400 spectra in a 20 µm × 20 µm area, laser 785 nm, 5 mW, 10× objective; For ATZ solid, 11.1 mW, 100× objective).

Table 8-1 pH-triggered SERS detection of five additional compounds with low pK_a

Compound	pK_a	Signal peak	Background peak	$I_{signal}/I_{background}$ at pH=6.0	$I_{signal}/I_{background}$ at pH<pK_a	Enhancement*
Melamine (MEL)	5.0	703	1371	2.5	5.8	2.3×
2,4-dichloroaniline (DCA)	2.0	1584	1371	0.7	95	136×
4-chloroaniline (4-CA)	4.15	1598	1371	2	16	8×
3-bromoaniline (3-BRA)	3.58	1588	1371	0.8	6.0	7.5×
3-nitroaniline (3-NA)	2.5	1250	2143**	0.5	21	42×

*Enhancement is the ratio of $I_{signal}/I_{background}$ at pH<pK_a to that at neutral pH;
**For 3-NA, background peak is 2143 cm^{-1} because there is overlap between signal and background at 1371 cm^{-1}.

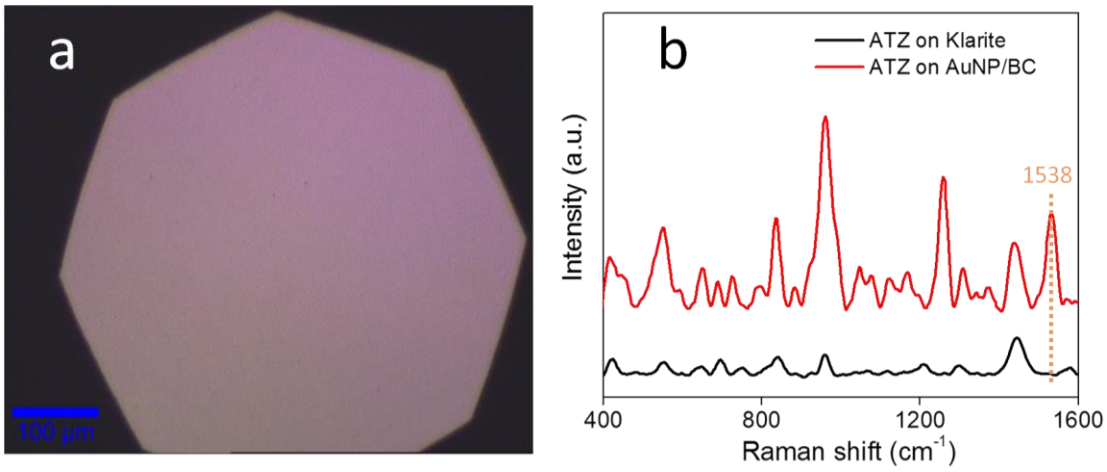

Figure 8.9 a) Optical image of Klarite; b) Average Raman spectra of atrazine (250 uM) on AuNP/BC and Klarite`s coffee ring. (Average of 400 spectra in a 100 µm × 100 µm area, laser 785 nm, 5 mW, 10× objective.)

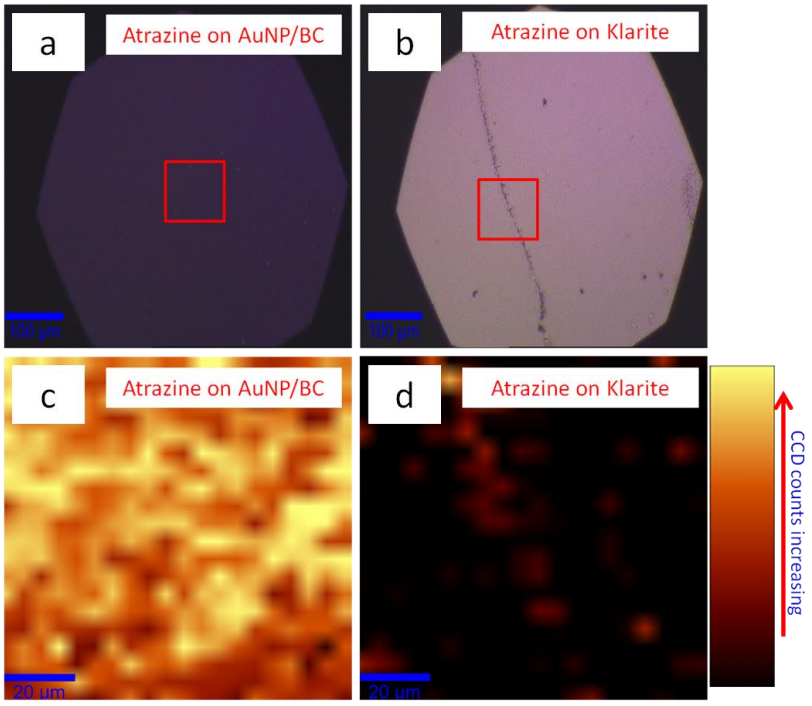

Figure 8.10 Optical images of a) AuNP/BC hydrogel and b) Klarite exposed to 250 µM atrazine; Raman XY maps of the atrazine 961 cm^{-1} peak on c) AuNP/BC and d) Klarite obtained from the noted areas of the corresponding optical images. (Average of 400 spectra in a 100 µm × 100 µm area, laser 785 nm, 5 mW, 10× objective.)

8.2.3 Reproducibility, Reusability, and Quantitation

The electrostatic attraction between the amine groups of CBZ and ATZ and the AuNP surface results in spatially and temporally repeatable binding of these analytes to the nanocomposite as evinced by both XY Raman imaging as well as SERS barcodes. We produced XY image scans by tracking the intense peaks at 1222 cm^{-1} (CBZ) and 961 cm^{-1} (ATZ). Prior to adding CBZ or ATZ, the Raman maps were completely blank thus demonstrating no observable signal (Figure 8.11a). After adding CBZ or ATZ, the maps become bright yellow indicating strong CBZ and ATZ signals (Figure 8.11a). The uniform distribution of the SERS signal across the Raman maps illustrates the homogeneity and reproducibility of the binding. To further illustrate the extreme reproducibility of our substrate we constructed "SERS barcodes" for each analyte. Such barcodes have recently been proposed as a tool to succinctly illustrate the relative intensities of all the peaks in a set of collected Raman spectra.[393] Herein we randomly selected 50 spots from our collected XY Raman maps (Figure 8.11b). As shown in Figure 8.11b, higher intensity Raman bands are brighter, while lower intensity bands are darker. For both CBZ and ATZ perfect barcodes were readily obtained. For comparison, we illustrate the barcode for the MGITC positive control, which was expected to be highly legible because of the covalent Au-S linkage that results in reproducible binding to the surface. For $pH<pK_a$, CBZ and ATZ, our two analytes with low surface affinity, exhibited similar reproducible behavior thus further suggesting that they align in consistent orientations across the AuNP surface.

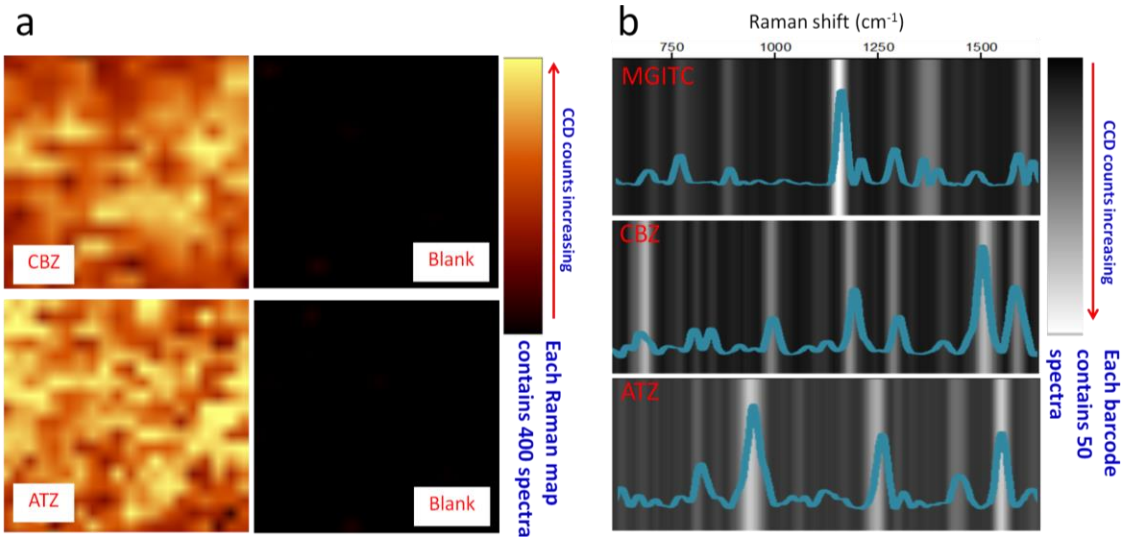

Figure 8.11 a) Raman XY maps of CBZ, ATZ and blank solutions at pH = 2.0 or 1.3 on AuNP/BC nanocomposite; b) SERS barcodes of 50 randomly selected spectra in a Raman map overlapping together for MGITC, CBZ and ATZ.

Reusability is important, yet difficult to achieve for many SERS substrates due to the irreversible binding of the analyte to the sensor surface. However, because this platform relies on electrostatic attractions it is possible to regenerate and reuse it by simply cycling the pH between 1.3 and 13 (Figure 8.5d). As shown, a consistent SERS signal intensity for ATZ at pH 1.3 is easily recovered through five cycles. This capacity is the result of the acidic and alkaline resistance of the BC matrix as well as the AuNPs.

Using the intensity of the background band at 1371 cm^{-1} as an internal standard we established the minimum quantitation level for CBZ and ATZ using the aforementioned peaks at 1222 cm^{-1} and 961 cm^{-1}. Accordingly, intensity ratios for signal and background peaks (I_{1222}/I_{1371} and I_{961}/I_{1371}) were used for CBZ and ATZ quantification, respectively. For each analyte a series of concentrations from 25 nM to 250 μM were used to test the AuNP/BC substrate. Over this concentration range the background peak at 1371 cm^{-1} exhibits little change in intensity, while the CBZ and ATZ peaks at 1222 cm^{-1} and 961 cm^{-1} increase monotonically (Figure 8.12a&b). For both analytes, the intensity ratio increased significantly from 25 nM - 25 μM and then began to

level off between 25-250 μM (Figure 8.12c). We attribute this latter phenomenon to nanocomposite saturation at high CBZ and ATZ concentrations. When the concentration was plotted in logarithmic form, a linear relationship results (Figure 8.12d). The limits of detection (LOD; defined as the signal-to-noise ratio = 3; ref.[394]) are 3 nM and 11 nM for CBZ and ATZ, respectively. US EPA has set a regulation limitation for ATZ in drinking water of 3 μg/L. Although our LOD for ATZ (11 nM or 2.3 μg/L) by SERS is slightly higher than that of GC-MS (0.12 μg/L, EPA standard method),[395] the SERS method is considerably more rapid, is easier and shows potential for on-site detection.

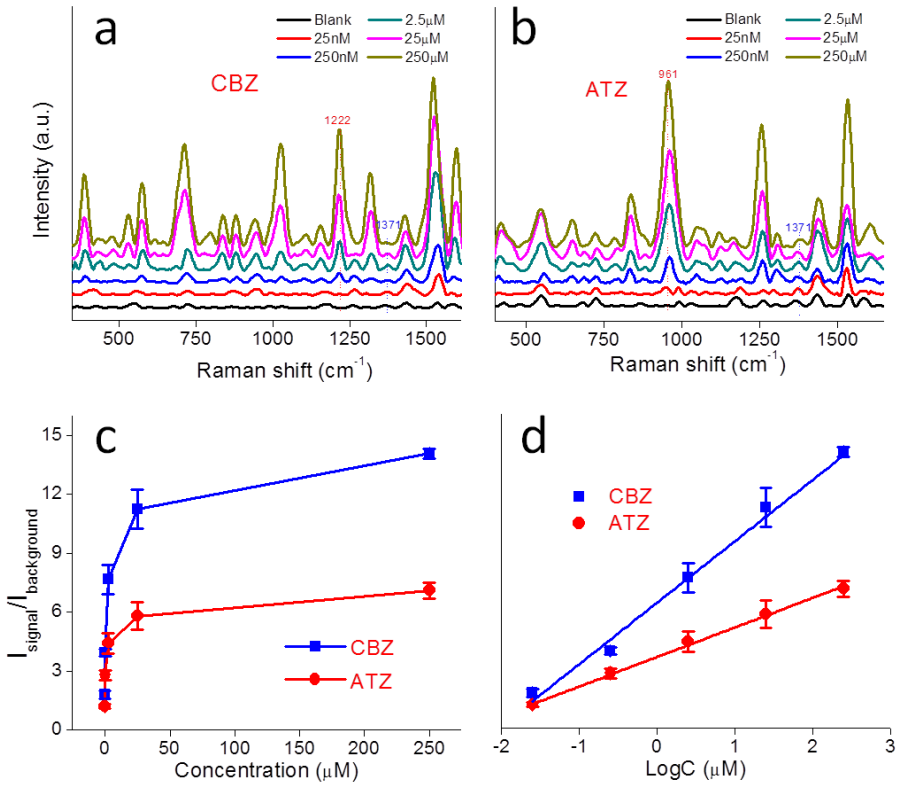

Figure 8.12 Average Raman spectra for a) CBZ and b) ATZ concentrations of 25 nM-250 μM on AuNP/BC hydrogel; c) The 1222 cm^{-1}/1371 cm^{-1} ratio and the 961 cm^{-1}/1371 cm^{-1} ratio increase as a function of analyte concentration; d) The 1222 cm^{-1}/1371 cm^{-1} ratio and the 961 cm^{-1}/1371 cm^{-1} ratio increase linearly with analyte concentration in logarithmic form.

To illustrate the applicability to employ AuNP/BC for real environmental samples, it was tested using surface water acquired from a local creek. For this effort, 100 nM of CBZ and 250 nM of ATZ were spiked into unpurified surface water. Following 15 s of mixing of AuNP/BC with the solution, the nanocomposite was taken out for Raman testing. From the sample spiked with low concentration CBZ (100 nM) and ATZ (250 nM), the characteristic bands of CBZ (394, 578, 1030, 1222, 1325 cm^{-1}) and ATZ (544, 651, 692, 834, 961, 1258, 1538 cm^{-1}) were clearly observed while from the blank sample no such bands appeared (Figure 8.13). These results indicate that AuNP/BC can be applied in real world surface waters.

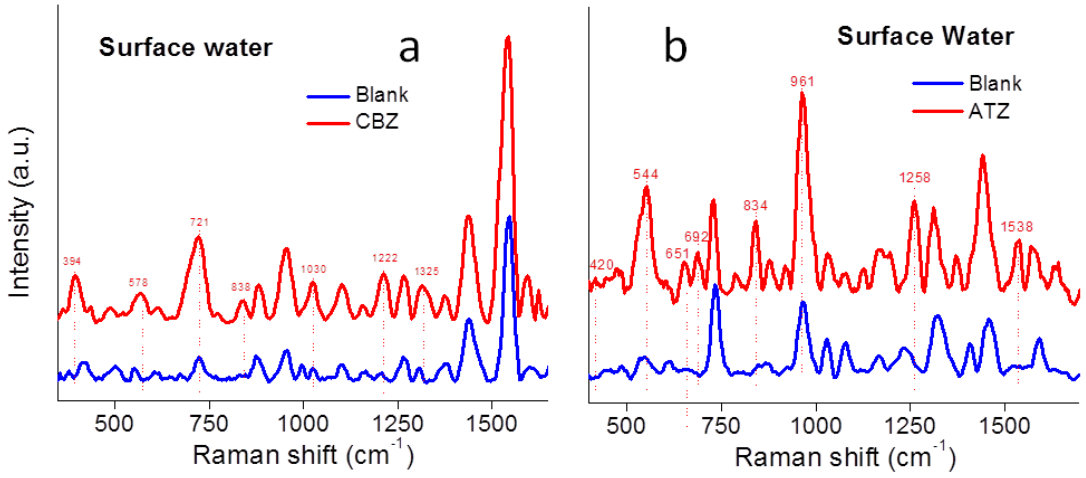

Figure 8.13 Average a) CBZ and b) ATZ spectra obtained using surface water (ATZ concentration: 250 nM; CBZ concentration: 100 nM; Average of 400 spectra in a 20 µm × 20 µm area, laser 785 nm, 5 mW, 10× objective.)

8.2.4 Hydrogel Deformation-Induced Intensity Changes

In the hydrated state, AuNP/BC is a three-dimensional hydrogel with a height 5500 ± 100 µm. When fully dried the hydrogel shrinks in the vertical direction into a thin film with a height of 16 ± 1 µm. In our previous study, the drying of AuNP/BC produced significant signal enhancements for MGITC and Rhodamine 6G due to drying induced formation of SERS "hot spots".[190] Interestingly, CBZ exhibited similar behavior, while ATZ did not. As shown in Figure 8.14a, the

SERS intensity of CBZ gradually increased from 0 (wet) to 90 min (dry) indicating that positively charged CBZ associates with the AuNP surface during the drying process. However, for ATZ the Raman signal decreases and ultimately disappears when the drying time is increased from 0 (wet) to 90 min (dry; Figure 8.14b).

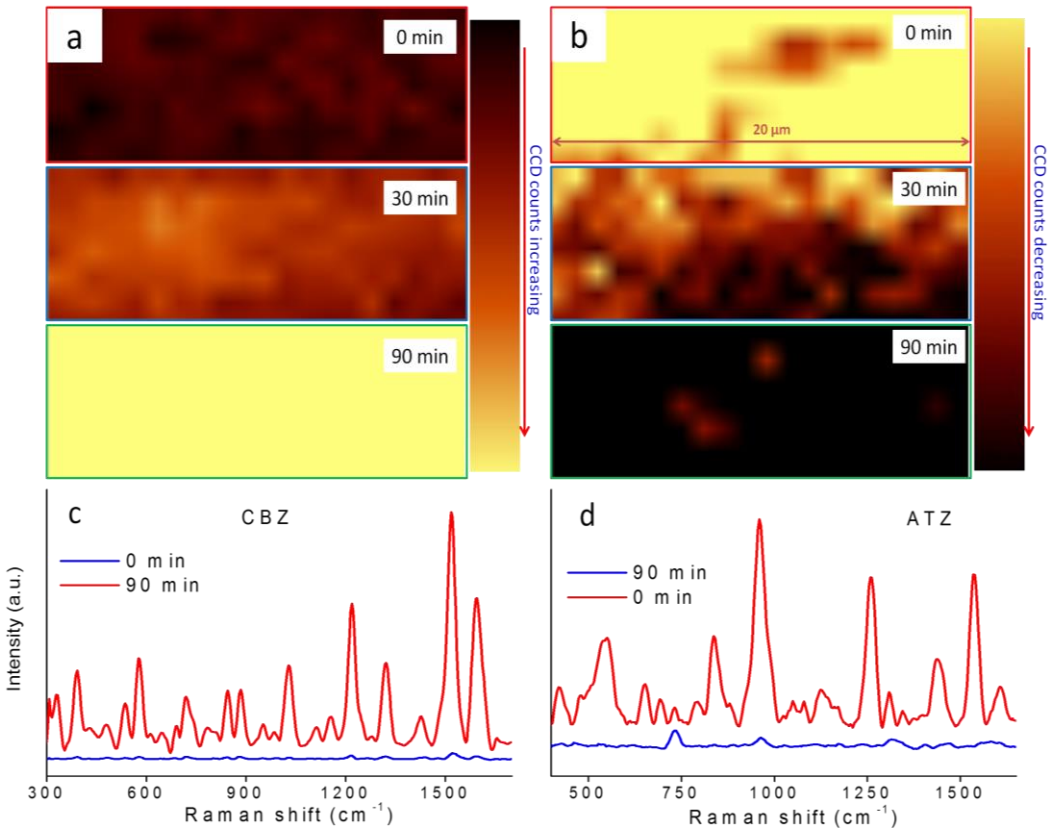

Figure 8.14 Raman XY maps of the a) CBZ 1222 cm^{-1} peak and b) ATZ 961 cm^{-1} peak for the AuNP/BC hydrogel under wet (0 min and 30 min) and dry (90 min) conditions; (Average of 140 spectra in a 20 µm × 7 µm area, laser 785 nm, 5 mW, 10× objective.) Average Raman spectra of c) CBZ and d) ATZ for the AuNP/BC hydrogel under wet and dry conditions.

Spatially averaged spectra for CBZ and ATZ under both wet and dry hydrogel conditions are shown in Figure 8.14c&d. The spectra of CBZ at 0 and 90 min are similar except for the observed change in SERS intensity (Figure 8.14c), while the ATZ spectrum at 0 min is completely lost at 90 min (Figure 8.14d). These data suggest that ATZ was transported away from the AuNP surface during drying due to capillary forces generated by water evaporation. We therefore searched for

the ATZ signal near the edges of the dry substrate and found it to be heterogeneously distributed across the edge (Figure 8.15a). Collected Raman maps of the edge were highly heterogeneous and could not be used to generate clear SERS barcodes (Figure 8.15b).

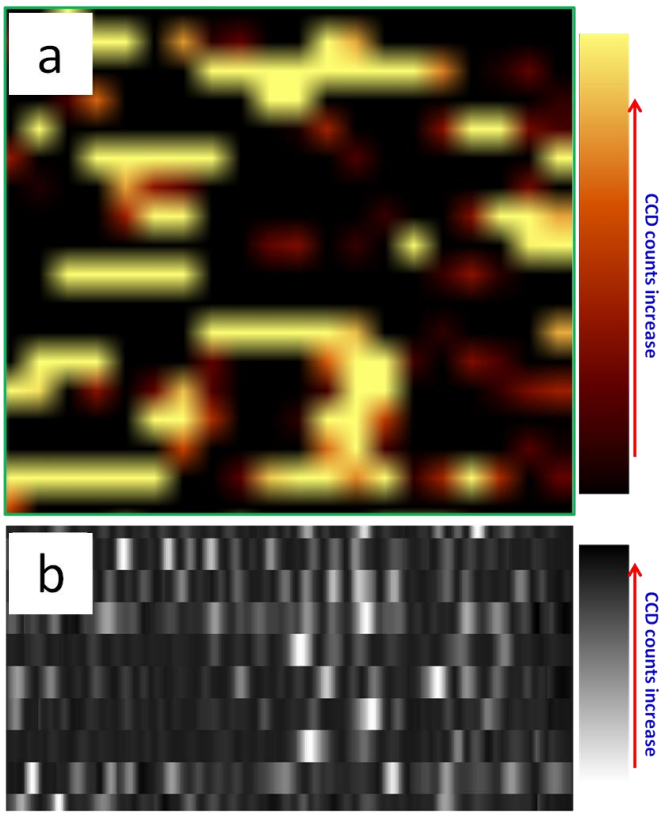

Figure 8.15 a) Raman XY map of one of the edge areas of dry AuNP/BC substrate; b) SERS barcode of 10 randomly selected spectra in the edge area. (Average of 400 spectra in a 100 µm × 100 µm area, laser 785 nm, 5 mW, 10× objective.)

Clearly, AuNP/BC needs to be hydrated for ATZ detection. The much weaker interaction force between ATZ and the AuNP surface relative to CBZ can be attributed to the following reasons: 1) The secondary amine group of ATZ shows less affinity to carboxylate group than the primary amine of CBZ; 2) In addition to the amine groups of ATZ, there are also one isopropyl group and one ethyl group. These hydrophobic groups are expected to decrease the affinity of ATZ to the polar surface of AuNPs and may provide steric hindrance that restricts the binding of the secondary amine to the surface carboxylate groups (Figure 8.8). In contrast, the primary amine group of CBZ

is in the far end of the molecular structure without any alkyl groups around, and thus it has greater capacity to bind to the AuNP surface. 3) The K_{ow} of ATZ (2.68) is higher than that of CBZ (1.51) indicating that ATZ is more than one order of magnitude more hydrophobic than CBZ.[383, 384] The AuNP/BC platform is extremely hydrophilic due to the large number of hydroxyl groups on the nanocellulose fibers. Due to the capillary forces generated during water evaporation, the more hydrophobic ATZ is more likely to recrystallize from the system (Figure 8.10) while the more hydrophilic CBZ is more likely to stay in the system. The above three factors may act synergistically to result in this phenomenon. In the future, we intend to systematically examine the influence of molecular structure on SERS using a series of chemically similar compounds.

8.2.5 Broad Applicability

To examine the broad applicability of our SERS platform, five additional analytes (melamine, 2,4-dichloroaniline, 4-chloroaniline, 3-bromoaniline, and 3-nitroaniline) with low pK_a values were tested under both neutral and the $pH<pK_a$ conditions (Table 8-1). For these compounds, the signal/background ratio ($I_{signal}/I_{background}$) increased by 2-136× at $pH<pK_a$ compared to neutral pH (Table 8-1), further supporting the pH-triggered affinity enhancement of compounds with amino groups. SERS barcodes (Figure 8.16) of these compounds were acquired under low pH conditions thus demonstrating the perfect reproducibility of their SERS spectra. These results further indicate that pH-triggered SERS using the AuNP/BC platform can be applied to a range of pollutants.

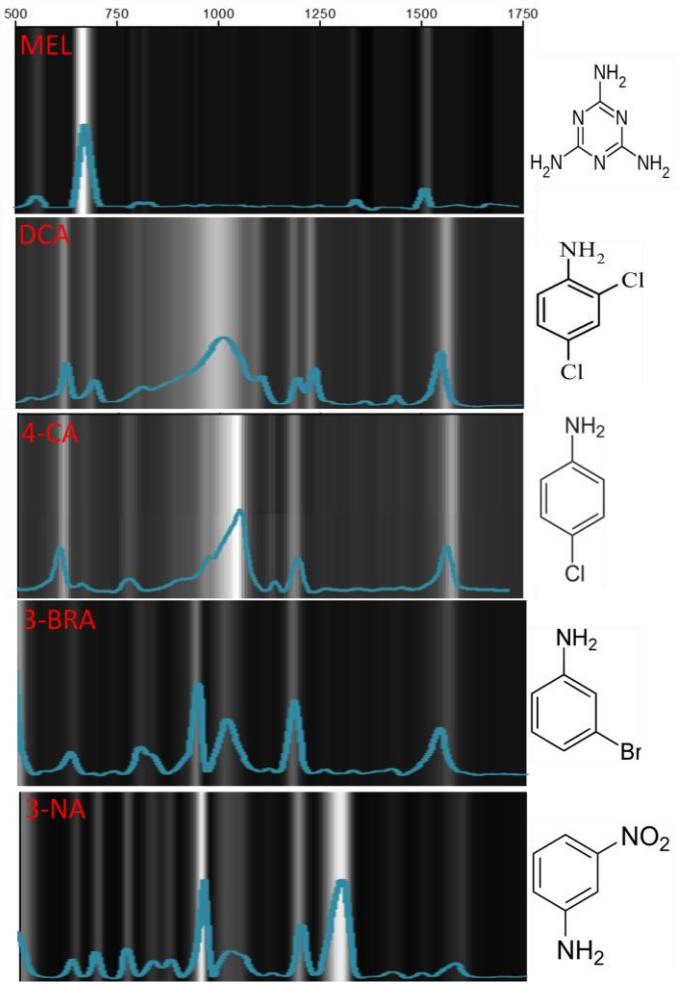

Figure 8.16 SERS barcodes of 50 randomly selected spectra in a Raman map overlapping together for melamine (MEL), 2,4-dichloroaniline (DCA), 4-chloroaniline (4-CA), 3-bromoaniline (3-BRA), and 3-nitroaniline (3-NA).

8.3 Discussion

A facile and stable AuNP/BC nanocomposite was synthesized and used as a low pH SERS substrate. SERS detection of carbamazepine and atrazine was achieved using this platform by lowering the solution pH to a value below the analyte's pK_a. The enhanced affinity and higher SERS intensity are triggered simply by adjusting solution pH without the need to modify the AuNP surface. The electrostatic interaction between the analyte and the AuNP surface can be reversed by adjusting the solution pH. At $pH<pK_a$, the consistent molecular alignment on the AuNP surface

results in highly reproducible SERS spectra. This protocol simplifies and reduces the cost of detecting amine-containing compounds with low pK_a. The sampling and detection time is short (<1 min) and the preparation procedure is simple, thus making this platform promising for real world application. Compared with conventional suspension-based SERS substrates, AuNPs are restrained in BC matrix and are not subject to uncontrolled aggregation and flocculation at acidic pH. Meanwhile, the AuNP/BC is readily stored and transported due to its small volume. Compared with solid SERS substrates such as Klarite, AuNP/BC is easier and cheaper to synthesize and shows much higher EF values and improved reproducibility (Figure 8.9 & Figure 8.10). Because AuNP/BC is a 3D hydrogel, drying-induced deformation generates additional SERS hot spots in the vertical direction and can lead to stronger SERS intensities for relatively hydrophilic compounds. After drying, the AuNP/BC SERS platform shrinks into a thin (16 μm) and light (0.4 mg) film, which reduces waste compared with solid SERS substrates. This is the first report on the pH-triggered SERS detection of real contaminants with relatively low affinity to AuNP surface. Quantitative analysis was achieved using common citrate-AuNPs without any surface modification. Different from the mainstream literature focusing on the design of intricate nanostructures to enhance the intrinsic SERS EF, this paper emphasizes the importance of surface affinity, especially electrostatic interactions for SERS detection of real-world contaminants. We expect that the AuNP/BC nanocomposite will serve as an ideal platform for studying the influence of solution pH on SERS detection of a broad suite of analytes.

Recently reported SERS substrates with AuNPs embedded in polymeric matricies are summarized in Table 8-2.[160, 162, 190, 396-402] Herein, we focus on flexible SERS substrates due to their intrinsic advantages for real world application relative to rigid substrates.[163] Our AuNP/BC platform is compared to existing AuNP/polymer composites in terms of the following: 1) Support

material: Compared with cellulose and synthetic polymer nanofibers, the nanocellulose used in this study is a naturally produced polymer that not only can house greater number of AuNPs due to its nanoscale size, but also exhibits the potential for biocompatible application. 2) Preparation method: Most AuNP/polymer composites are synthesized by multi-step methods. First, the AuNPs are synthesized based on an existing protocol. Second, the polymers are impregnated by exposure to an AuNP suspension or the polymer precursors are polymerized onto the AuNPs by gelation or electrospinning. Our AuNP/BC nanocomposite was synthesized by a one step in situ reduction method that is considerably faster and easier. 3) Application form: A majority of the reported AuNP/polymers have only been used under dry conditions due to their low stability in water. The AuNP/BC platform is a rigid hydrogel with high water stability. It can accumulate analytes directly from water and be reused many times without losing its stability. The hydrogel can "replicate" the pH of the bulk solution that is the basis for our later pH-triggered detection. 4) Application pH: Due to the chemical and water stability of both AuNPs (compared with AgNPs) and nanocellulose, our material can be used at acidic pH (as low as 1.3 for ATZ detection) while the other materials in Table 8-2 have only been tested at neutral pH. At low pH values, amine-containing compounds with low pK_a are protonated and easily associate with the citrate-coated AuNP surface. This low-pH stable SERS platform extends the application of SERS to the detection of low pK_a compounds in an easy and reproducible manner. Further, by manipulating solution pH, this material can be easily regenerated and reused, which to our knowledge cannot be achieved by other AuNP/polymer materials. 5) Target analyte: According to Table 8-2, most of AuNP/polymer substrates reported to date have been tested using Raman resonant dyes or compounds with sulfur atoms. These compounds either exhibit large Raman cross sections or have a strong affinity to the AuNP surface. In our study, two neutral environmental contaminants - atrazine and carbamazepine

with low affinity to AuNPs were tested. Excellent SERS reproducibility and sensitivity were achieved for these compounds by simply adjusting solution pH.

Table 8-2 AuNPs embedded in various polymer matrix used for SERS detection of chemicals

Support material	Preparation method	Application form	Application pH	Target analyte	LOD	Ref
Cellulose	Impregnation	Paper	Neutral	1,4-Benzenedithiol	0.1 nM	[160]
Cellulose	Impregnation	Paper	Neutral	4-aminothiolphenol	1 nM	[162]
Cellulose	Impregnation	Paper	Neutral	1,2-bis(4-pyridyl)ethene	0.5nM	[402]
Cellulose/Polyvinyl chloride	Deposition+Stamping	Paper/Plastic	Neutral	4-aminothiolphenol/Crystal violet	1 μM/5 nM	[399]
Chitosan	Electrospinning +In situ reduction	Dry mat	Neutral	2-naphthalenethiol/R6G/Glucose	1 fM/1 μM/5 μM	[396]
Poly(vinyl alcohol)+ Polyethyleneimine	Electrospinning+Impregnation	Dry mat	Neutral	Rhodamine B	1 nM	[397]
Poly(vinyl alcohol)	Electrospinning	Dry mat	Neutral	3,3′-diethylthiatricarbocyanine iodide	100 nM	[398]
Poly(acrylic acid)	Polymerization+Washing with HF	Hydrogel	Neutral	2-naphthalenethiol/paraquat	50nM/100nM	[401]
Poly(vinyl alcohol)	Polymerization	Dry gel	Neutral	Crystal violet	1 pM	[400]
Nanocellulose	In situ reduction	Dry mat	Neutral	MGITC	400 fM	[190]
Nanocellulose	In situ reduction	Hydrogel	Acidic	Atrazine/Carbamazepine	11 nM/3 nM	This study

8.4 Methods

8.4.1 Reagents

Gold chloride trihydrate ($HAuCl_4 \cdot 3H_2O$) was purchased from MP Biomedicals. Sodium citrate tribasic dihydrate ($Na_3Cit \cdot 2H_2O$), benzoic acid (BA), melamine, 2,4-dichloroaniline, 4-chloroaniline, 3-bromoaniline, and 3-nitroaniline were purchased from Sigma-Aldrich. Atrazine (98.9%) and carbamazepine (99.0%) were purchased from Chem. Service and Acros Organics, respectively. Malachite green isothiocyanate (MGITC) was acquired from Invitrogen Corp. (Grand Island, NY). HCl and ethanol were purchased from Fisher Scientific. BC was grown by culturing *Gluconacetobacter xylinus* in corn steep liquor for 14 days.[403] Surface water was obtained from Tom`s Creek near the Virginia Tech campus and was used without pretreatment.

8.4.2 Preparation of AuNP/BC

Sixteen pieces of BC (0.5 cm × 0.5 cm) were incubated in 0.7 mL $HAuCl_4$ solution (30 mM) and vortexed for 30 s. Subsequently, they were transferred into 50 mL of boiling 1.2 mM Na_3Cit and kept for 1.5 h. The resultant AuNP/BC was rinsed 10× with 25 mL aliquots of DI water. In parallel, a suspension of AuNPs with a uniform size of 50 nm was synthesized via seed-mediated growth.[214]

8.4.3 Control Experiments

Control experiments were conducted to exclude potential background interferences in the normal Raman spectra of CBZ and ATZ. CBZ or ATZ (250 μM) when dissolved in ethanol only exhibit the Raman peaks of the ethanol solvent (Figure 8.4) thus indicating the normal Raman spectrum of CBZ and ATZ in solution is challenging to obtain. Under our operating conditions the normal Raman spectrum of CBZ and ATZ could only be acquired using CBZ or ATZ solids and a high

energy laser. Assignments of the Raman bands for CBZ and ATZ are found in Table 8-3 and Table 8-4. Raman spectra of CBZ and ATZ on pure BC were acquired to verify all the Raman signals obtained previously were from AuNP-enabled SERS. As shown in Figure 8.6, no Raman signal was obtained using only BC, thus indicating the spectra originate from AuNP-enabled SERS. Furthermore, exposure of AuNP/BC to solutions without CBZ or ATZ produces only a weak Raman signal that corresponds to citrate (Figure 8.6).

Table 8-3 Assignment of the prominent peaks in normal Raman spectrum and SERS spectrum of ATZ (all assignments are based upon those defined elsewhere[59]).

Normal Raman (cm^{-1})	SERS (cm^{-1})	Assignment
647	651	τ (CH_2)
690	692	Φ (6a)
841	834	ω (CH_3) + ν(CC)
964	961	Φ (12) + ν(CC)
1257	1258	Φ (14) + τ (CH_2)
1452	1437	δ (CH_2) + δ(CH_3)
1553	1538	Φ (8a) + δ (NH)
1610	1598	δ (NH) + ν(CN)

Table 8-4 Assignment of the prominent peaks in normal Raman spectrum and SERS spectrum of CBZ.

Normal Raman (cm^{-1})	SERS (cm^{-1})	Assignment
581	578	$\delta(CC)_{ring}$[404]
723	721	ω(CH)[405]
876	883	ν(CCN)[406]
1036	1031	ν(C-C=C)[405]
1221	1222	ν(CC)[407]
1311	1325	ν(CN)[408]
1569	1521	δ (NH)[59]
1627	1596	δ (NH) + ν(CN)[59]

8.4.4 Sampling

To study the influence of pH on SERS, one piece of AuNP/BC was immersed in 4 mL of 250 μM CBZ or ATZ solution at pH=1.3-6.0 and vortexed for 15 s. As control experiments, AuNP/BC was exposed to 4 mL of 2.5 μM MGITC solution at pH = 6.0 and 250 μM BA solution at pH = 2.0. To

quantify CBZ and ATZ, AuNP/BC was immersed in 4 mL 0.025-250 μM CBZ and ATZ solution at pH=2.0 or 1.3. To test the substrate in real environmental waters, AuNP/BC was immersed in 4 mL surface water spiked with 100 nM CBZ or 250 nM ATZ at pH=2.0 or 1.3, respectively. A blank surface water sample pH adjusted with HCl was used as a control.

8.4.5 Regeneration

Following exposure to 4 mL of 250 nM ATZ solution at pH = 1.3, one piece of AuNP/BC was characterized via Raman spectroscopy. Subsequently, the sample was washed 3× with 10 mL DI water, 3× with 2 mL NaOH solution (pH = 13), and copiously washed with DI water to remove NaOH. Following alkaline washing, the sample was immersed in 4 mL HCl solution (pH = 1.3) and tested again with Raman spectroscopy. The whole process described above was repeated five times.

8.4.6 Comparison with Suspension and Solid-Based Substrate

AuNPs with uniform particle size (50 nm) were prepared and used to represent suspension-based SERS. Following addition of 1 mL of 1 mM CBZ or ATZ solution into 3 mL AuNP suspension and vortexing for 15 s, the suspensions were subjected to Raman measurement. A commercial SERS substrate (Klarite) was also tested. A Raman map was obtained at the edge of the coffee ring formed by drop deposition of 10 μL of 1 mM ATZ solution on the Klarite substrate.

8.4.7 Instrumentation

Following sampling, the AuNP/BC was put onto aluminum foil and tested via Raman spectroscopy (WITec alpha 500R). For each measurement, a XY area (20 μm × 20 μm) of 400 points was scanned. A 785 nm wavelength laser and a 10× objective (5 mW, 0.5 s integration time) were used to collect each spectrum in the Raman map. The signal was transmitted through a 300 gr/mm

grating and detected using a Peltier CCD. Unlike the single spectra reported in most of the SERS literature, each of the spectra reported herein represent the average of the 400 baseline corrected (Origin 8.0) spectra in the collected Raman maps. Each of the calculated "SERS barcodes"[393] contains 50 randomly selected spectra from one XY Raman map. Each spectrum (352 data points) was normalized to the most intense peak before all the data points (352 × 50) were converted into a matrix that was subsequently projected into "barcode" images using Origin 8.0. To monitor Raman signal changes due to the deformation of the AuNP/BC hydrogel, Raman maps were scanned every 30 min. The morphologies of AuNP/BC were characterized by field emission scanning electron microscopy (FESEM, LEO (ZEISS) 1550). Extinction spectra of AuNP/BC were measured with a UV-Vis spectrophotometer (Cary 5000, Agilent) after pasting the hydrogel on the inner wall of a cuvette.

Chapter 9 Synthesis of Highly Stable SERS pH Nanoprobes Produced by Co-Solvent Controlled AuNP Aggregation

Haoran Wei[1,2,3], Marjorie R. Willner[1,2,3], Linsey C. Marr[1,2,3], and Peter J. Vikesland[1,2,3*]

[1] Department of Civil and Environmental Engineering, Virginia Tech, Blacksburg, VA, USA.

[2] Institute for Critical Technology and Applied Science (ICTAS) Center for Sustainable Nanotechnology (VTSuN), Virginia Tech, Blacksburg, VA, USA.

[3] NSF-EPA Center for the Environmental Implications of Nanotechnology (CEINT).

*Corresponding author E-mail: pvikes@vt.edu; 540-231-3568; Fax: 540-231-791

(This chapter has been published in ***Analyst***.[302] – Reproduced by permission of the Royal Society of Chemistry. The publisher - the Royal Society of Chemistry does not require formal reproduction permission when the article is used in the dissertation of the authors.)

Abstract

Production of gold nanoparticle (AuNP) surface-enhanced Raman spectroscopy (SERS) nanoprobes requires replicable aggregation to produce multimers with high signal intensity. Herein, we illustrate a novel, yet simple, approach to produce SERS nanoprobes through control of co-solvent composition. AuNP multimers were produced by mixing AuNP monomers in water:ethanol co-solvent for variable periods of time. By varying the water:ethanol ratio and the amount of 4-mercaptobenzoic acid (4-MBA) present, the aggregation rate can be systematically controlled. Thiolated poly(ethylene glycol) was then added to halt the aggregation process and provide steric stability. This approach was used to produce pH nanoprobes with excellent colloidal stability in high ionic strength environments and in complex samples. The pH probe exhibits broad pH sensitivity over the range 6-11 and we calculate that a single AuNP dimer in a 35 fL volume is sufficient to generate a detectable SERS signal. As a proof-of-concept, the probes were used to detect the intracellular pH of human prostate cancer cells (PC-3). The internalized probes exhibit a strong 4-MBA signal without any interfering bands from either the cells or the culture media and produce exceptionally detailed pH maps. pH maps obtained from 19 xy surface scans and 14 yz depth scans exhibit highly consistent intracellular pH in the range of 5 to 7, thus indicating the greater reliability and reproducibility of our pH probes compared with other probes previously reported in the literature. Our water:ethanol co-solvent production process is fast, simple, and efficient. Adjustment of solvent composition may become a powerful way to produce SERS tags or nanoprobes in the future.

9.1 Introduction

Gold nanoparticles (AuNPs) are widely used for surface-enhanced Raman scattering (SERS) based sensing due to their strong localized surface plasmon resonance (LSPR), low toxicity, and long-term stability.[190, 409-412] It is generally accepted that the largest SERS signals or "hot spots" are generated in the narrow gap between two AuNPs as a result of the strong electromagnetic coupling in that region.[413, 414] Reproducible production of SERS "hot spots" is non-trivial and requires that AuNP aggregation be neither too minimal (leaving too many monomers and a weak signal), nor too extensive (resulting in an unstable colloid). Controlled aggregation as a mechanism to produce "hot spots" has attracted extensive research attention and the use of small organic molecules as nanoparticle linkers has been deemed to be one of the more efficient ways to bridge nanoparticles.[386, 415-420] For example, Taylor et al. used a cucurbit [n]uril "glue" to produce reproducible and controlled AuNP aggregates with a gap distance of 0.9 nm.[419] Aggregation inducers occupy a portion of the "hot spot" volume and generate peaks in the SERS spectrum. For this reason, SERS nanoprobes (defined as an AuNP multimer containing two or more AuNP monomers) are often produced using a Raman active linker. We and others have illustrated that malachite green isothiocyanate (MGITC), 2-aminothiolphenol (2-ATP), and 3,5-dimercaptobenzoic acid linkers can produce nanoprobes with intense, but reproducible SERS signals.[386, 415, 421] One substantial challenge, however, is that not all desired SERS applications utilize organic molecules that induce aggregation and bridge nanoparticles.

To date, a number of nanoparticles for SERS based determination of pH have been reported in the literature.[415, 420-428] The pH sensing capacity of these nanoparticles is generally realized via surface functionalization of the particle with a pH sensitive molecule whose SERS spectrum changes as a function of pH. For example, 4-aminothiolphenol, 2-aminothiolphenol, 3-amino-5-

mercapto-1,2,4-triazole, and 4-mercaptobenzoic acid (4-MBA) are often employed due to the pH sensitivity of the SERS band of the amine or carboxyl groups of these molecules. Amongst these, 4-MBA exhibits a broad pH sensitive range, simple structure, high photochemical stability, and thiol mediated AuNP surface affinity.[422, 427-430] Arguably the most common way to synthesize 4-MBA-AuNPs is to dilute a concentrated 4-MBA ethanol solution in an aqueous AuNP suspension.[422, 429, 431] Unfortunately, 4-MBA does not effectively induce AuNP aggregation and thus the SERS probes produced by this approach exhibit a weak and irreproducible signal. Lawson et al. improved probe reproducibility and signal intensity by utilizing 3,5-dimercaptobenzoic acid as both the pH indicator and aggregation inducer.[415] However, the three step organic reaction required for the synthesis of 3,5-dimercaptobenzoic acid is mechanistically challenging and thus not feasible for widespread use. While there is substantial interest in the production and potential application of SERS based pH sensors, the syntheses reported to date have generally resulted in particles of only transient colloidal stability and weak signal due to the limited ability for the aforementioned molecules to induce nanoparticle aggregation and form stable nanoprobes.

Past studies have shown that AuNPs aggregate more rapidly in the presence of ethanol than in water due to the lower polarity of the alcohol.[432] We hypothesized that addition of ethanol to an aqueous suspension of AuNPs would reproducibly change the solvent properties and thus enable controlled AuNP aggregation. Such an approach has three potential advantages: 1) Coordinated changes in solvent properties should enable control of the aggregation rate such that reproducible aggregates can be produced both in the presence and absence of a SERS active organic molecule; 2) Once stable aggregates are formed, excess ethanol can be removed by centrifugation; and 3) Because no complicated organic syntheses are required, this method may be more sustainable and thus more cost-efficient than many extant methods. With this rationale, we set out to test whether

a water:ethanol co-solvent system could be used to control AuNP aggregation and produce AuNP-based SERS nanoprobes.

Through the use of water:ethanol co-solvent mixtures we can systematically produce AuNP multimers of controlled size (Figure 9.1). Multimers of size appropriate for SERS were formed in 50:50 water:ethanol co-solvent and then following functionalization with a protective HS-PEG layer a highly stable SERS pH probe was produced. Compared with previously used BSA and silica coatings, PEG has a long hydrophilic chain that does not inhibit proton diffusion to the SERS hot spots.[425, 431] This pH nanoprobe illustrates high SERS activity, high pH sensitivity, a broad pH sensitive range, and excellent stability in high ionic strength environments. To our knowledge this is the first time that co-solvents have been used for SERS pH probe production. This approach can be easily extended to produce numerous types of SERS probes through controlled adjustment of co-solvent type and concentration.

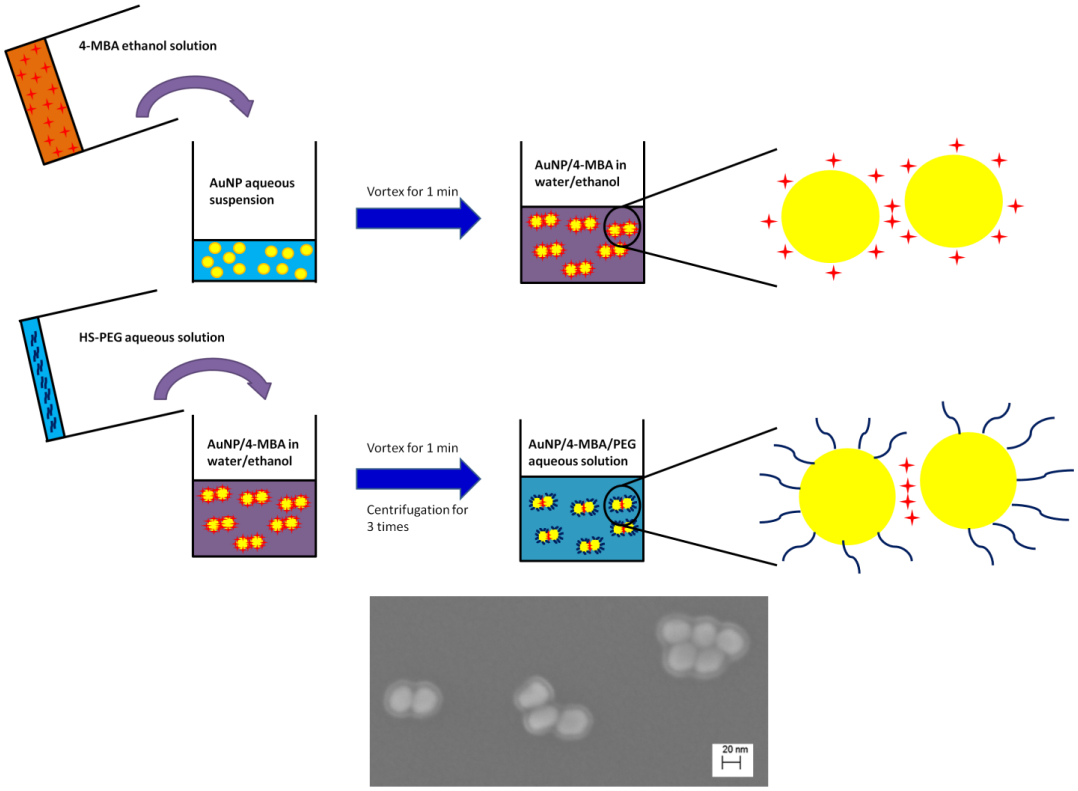

Figure 9.1 Production of AuNP/4-MBA/PEG nanosensor.

9.2 Experimental Section

9.2.1 Materials

Gold chloride trihydrate ($HAuCl_4 \cdot 3H_2O$), sodium citrate tribasic dihydrate ($Na_3Citrate \cdot 2H_2O$), 4-Mercaptobenzoic acid (4-MBA), and phosphate buffer (PB) solution were purchased from Sigma-Aldrich. Thiolated poly(ethylene glycol) (HS-PEG; 5 kD) was purchased from Nanocs. Anhydrous ethanol was purchased from Fisher Scientific.

9.2.2 AuNP Synthesis

AuNPs were synthesized using the seed-mediated approach. Briefly, 13 nm gold nanoparticle seeds were synthesized according to Frens.[214] $Na_3Citrate \cdot 2H_2O$ (final concentration 3.88 mM) was added to 100 mL of boiling 1 mM $HAuCl_4 \cdot 3H_2O$ under vigorous mixing conditions. The reaction

was allowed to run until the solution color changed to wine red, indicating completion. During seed synthesis the pH was controlled at 6.2-6.5 to improve their monodispersity.[217] Following seed synthesis, 35 nm AuNPs were synthesized by seed-mediated growth.[215] A 250 mL flask containing 100 mL of $HAuCl_4 \cdot 3H_2O$ solution (0.254 mM) was heated to boil under vigorous stirring. To this flask was added 2.02 mL seed suspension and 0.44 mL $Na_3Citrate \cdot 2H_2O$ (final concentration 0.17 mM). After a 40 min reaction time the flask was cooled to room temperature.

9.2.3 AuNP Aggregation in Water:Ethanol Co-Solvent

AuNPs suspended in water:ethanol mixtures of varying ethanol content were prepared by adding 0.5 mL of a water:ethanol mixture (ethanol content 0-100%) to 0.5 mL of aqueous AuNP suspension. The mixture was then vortexed for 1 min to ensure complete mixing of the components. The kinetics of AuNP aggregation in the water:ethanol mixtures were investigated by monitoring the variation in the UV-VIS extinction spectra and the DLS determined hydrodynamic diameter over a two day period. 4-MBA-AuNPs in water:ethanol co-solvent were prepared by adding 0.5 mL 4-MBA in ethanol (100 μM) to 0.5 mL AuNP aqueous suspension. We emphasize that the 4-MBA solution and the AuNP suspension were mixed at a 1:1 volumetric ratio. Equal volume mixing of the two components results in more homogeneous adsorption of 4-MBA and more highly controlled AuNP aggregation.[433] The aggregation kinetics of 4-MBA functionalized AuNPs in water:ethanol co-solvent were investigated by both UV-VIS extinction spectra and DLS. SERS spectra of 4-MBA-AuNPs in solutions with different ethanol contents were collected at 100 min after the mixing of 0.5 mL AuNP suspensions and 0.5 ml 4-MBA solutions with ethanol contents 12.5-100%.

9.2.4 Production of Colloidally Stable SERS pH Probes

The procedure for production of our SERS probe is shown in Figure 9.1. First, 0.5 mL of 100 μM 4-MBA in ethanol was added to 0.5 mL of aqueous AuNP suspension and then fully mixed by vortexing. After 10, 55, 100, or 140 min, 100 μL of HS-PEG aqueous solution (500 μM) was added to the mixture. The suspension was kept for 20 min at room temperature and subsequently washed by centrifugation 3× to remove excess 4-MBA, HS-PEG, and ethanol. Following centrifugation, the supernatant was discarded and the sediment was redispersed in 1 mL water.

9.2.5 Evaluation of the Sensitivity and Stability of the pH Probe

To evaluate the pH sensitivity of our probe, 1 mL of probe was added to 1 mL of PB solution (20 mM) with different pH. The pHs of the mixtures were also measured by a commercial pH meter (Accumet AB15 plus, Fisher Scientific) and their corresponding SERS spectra were recorded. A pH calibration curve was produced by plotting the change in the SERS spectra versus pH. To evaluate the colloidal stability of the probe, 1 mL probe was added to 1 mL PB solution (20 mM) and variations in DLS determined hydrodynamic diameter, UV-VIS extinction spectra, and pH indicator values were monitored for one hour. To further test the capacity of the probe (200 μL) it was also added to 800 μL of two different soft drinks (Fanta orange and club soda) and tap water. SERS spectra were acquired and the derived pH values were compared with those measured by the commercial pH meter.

9.2.6 Intracellular pH Monitoring

A human prostate cancer cell line, PC-3, was cultured in F-12K Medium (Kaighn's Modification of Ham's F-12 Medium) (ATCC) supplemented with 10% fetal calf serum and 1% penicillin/streptomycin. Cells were grown to confluence in an incubator at 37 °C with 5% CO_2 prior to harvesting using trypsin/EDTA. A cell concentration of 2.4 x 10^4 cells/mL was then seeded

into a 6-well plate (volume of cell medium). Cells were then incubated overnight in an incubator at 37 °C with 5% CO_2. Each well was then inoculated with 20 µl of nanoprobes and left in the incubator overnight. After approximately 24 hours the cells were washed three times with PBS before being imaged.

9.2.7 Instrumentation

Pristine AuNP size (35±1 nm, n=40) was measured by field-emission scanning electron microscopy (FESEM, LEO (Zeiss) 1550) and transmission electron microscopy (TEM, JEOL JEM-1400) with the assistance of Image J (Figure 9.2). Pristine AuNP size (39 nm) was also measured by dynamic light scattering (DLS, Nano Zetasizer, Malvern). The LSPR of the AuNPs as well as AuNP aggregates was characterized by UV-VIS spectroscopy (Cary 5000, Agilent). Raman spectra were acquired by a Raman spectrometer (Alpha500R, WITec) with a 10× objective and 0.5 s integration time. The 785 nm laser light was dispersed by a 300 gr/mm grating and detected by a Peltier CCD. Each Raman spectrum reported (unless noted otherwise) was an average of 400 single spectra acquired across a 1000 µm × 1000 µm Raman map. The cells were directly imaged in the 6-well plate using a 785nm laser, 50x objective and a 0.05 second integration time.

9.2.8 SERS Data Processing

The SERS data for the calibration curve and cell experiments was imported into MATLAB® 2015b (The Mathworks, USA). The spectra were first baseline corrected using an asymmetric least squares fitting,[434] the intensities of the peaks of interest (1084cm^{-1}, 1410 cm^{-1} and 1710 cm^{-1}) were tracked and ultimately ratios between the pH insensitive and pH sensitive peaks were plotted. A calibration curve with a Boltzmann fit was established using Origin 8.0 to describe the relationship between the pH and SERS peak ratios. The pH was then calculated at each of the points in the

SERS maps and a visual representation was rendered in Matlab. The data from all the cell experiments was further compiled and analyzed in Matlab.

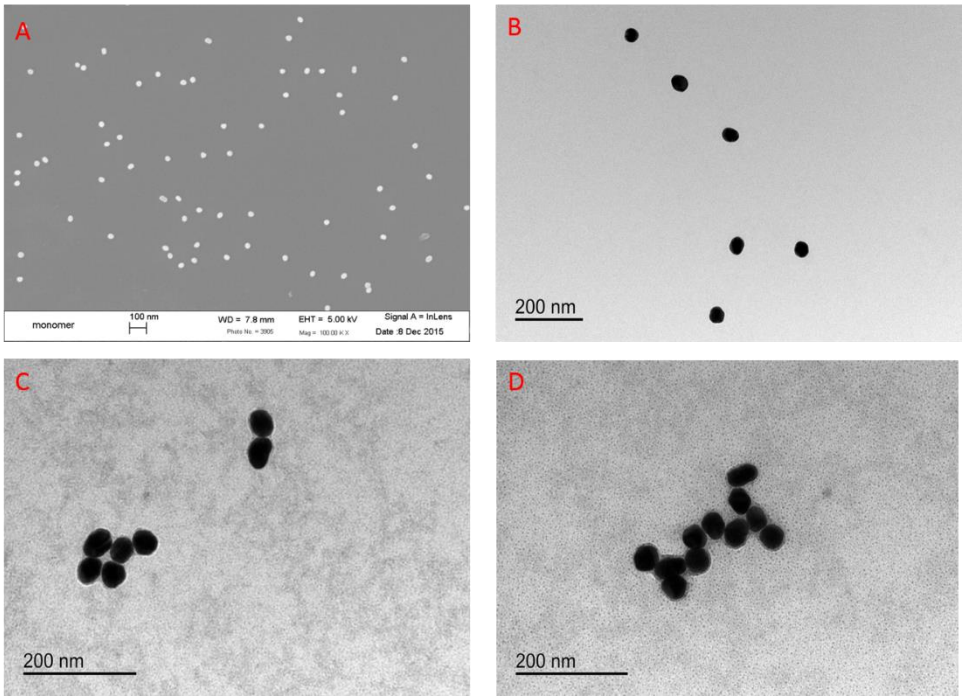

Figure 9.2 A) Scanning electron microscopy image of the pristine AuNPs spin coated on a silicon wafer; Transmission electron microscopy images of pristine AuNP monomer (B), and PEG-coated AuNP aggregates (C&D).

9.3 Results and Discussion

9.3.1 Controlled AuNP Aggregation in Water:Ethanol Co-Solvent

AuNPs synthesized by sodium citrate reduction are stable in the absence of salt due to the negative charge imparted by surface associated citrate and its degradation products.[217, 435] Ethanol, however, is known to induce AuNP aggregation due to dipole-dipole attractive interactions.[432] Herein, we observed that changes in the ethanol co-solvent concentration greatly affected AuNP size and colloidal stability. For ethanol co-solvent concentrations of 0-25% the hydrodynamic diameter proportionally increased with the ethanol content (Figure 9.3). AuNP multimers produced in

water:ethanol cosolvent mixtures below 50:50 were stable over a two day period, while those produced at a 50:50 water:ethanol ratio exhibited more extensive aggregation. Because aggregate formation is vitally important for "hot spot" formation and SERS nanoprobe production, we focused on the 50:50 water:ethanol mixture (referred to as a water:ethanol co-solvent hereafter).

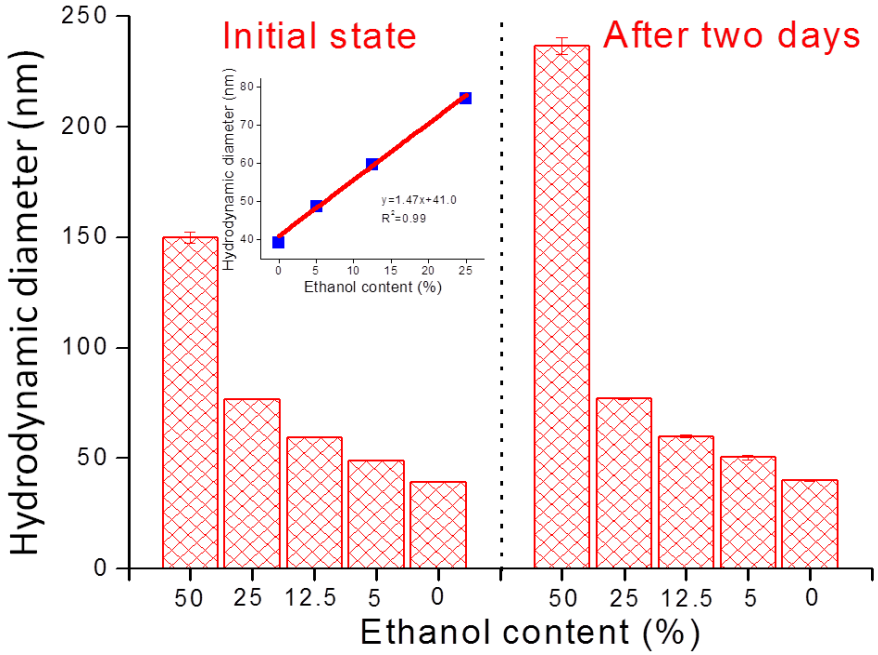

Figure 9.3 Size of AuNPs dispersed in water/ethanol mixture with different ethanol content; Inset figure shows the linear relationship between AuNP size and the ethanol content when it is below 25%.

An immediate increase in the AuNP hydrodynamic diameter from 39 to 150 nm was observed in water:ethanol co-solvent, while no change was observed in water alone (Figure 9.4A). In co-solvent, the AuNP hydrodynamic diameter increased slowly from 150 to 188 nm during the first hour. After two days the AuNP size ultimately reached 236 nm and the colloid was colloidally stable (Figure 9.3 and inset of Figure 9.4A). We attribute the rapid AuNP aggregation in water:ethanol co-solvent to the systematic variation of the solvent dielectric constant. As shown in Eq. 9.1, the electrostatic repulsive force (V_{elec}) supporting AuNP stability is proportional to the solvent dielectric constant ε when other parameters (φ is the surface potential, h is the gap between

two particles, and k is the inverse of Debye length) remain constant.[436] Addition of ethanol (ε=24.4) to water (ε=80.1) leads to a smaller dielectric constant in co-solvent than in water alone, which in turn decreases the electrostatic repulsive force between AuNPs.

$$V_{elec} = 2\pi\varepsilon a\varphi^2 \ln(1+e^{-kh}) \qquad \text{Equation 9.1}$$

4-MBA functionalized AuNPs exhibited completely different aggregation kinetics compared with the pristine AuNPs. The 4-MBA-AuNP hydrodynamic diameter slightly decreased in the initial ~40 min and then increased from 40 to 180 min, thus indicating that aggregation is minimal for the first ~40 min and then proceeded more rapidly until the colloids were no longer colloidally stable. Control suspensions of AuNPs and 4-MBA-AuNPs in DI water exhibited no sign of aggregation (Figure 9.4A).

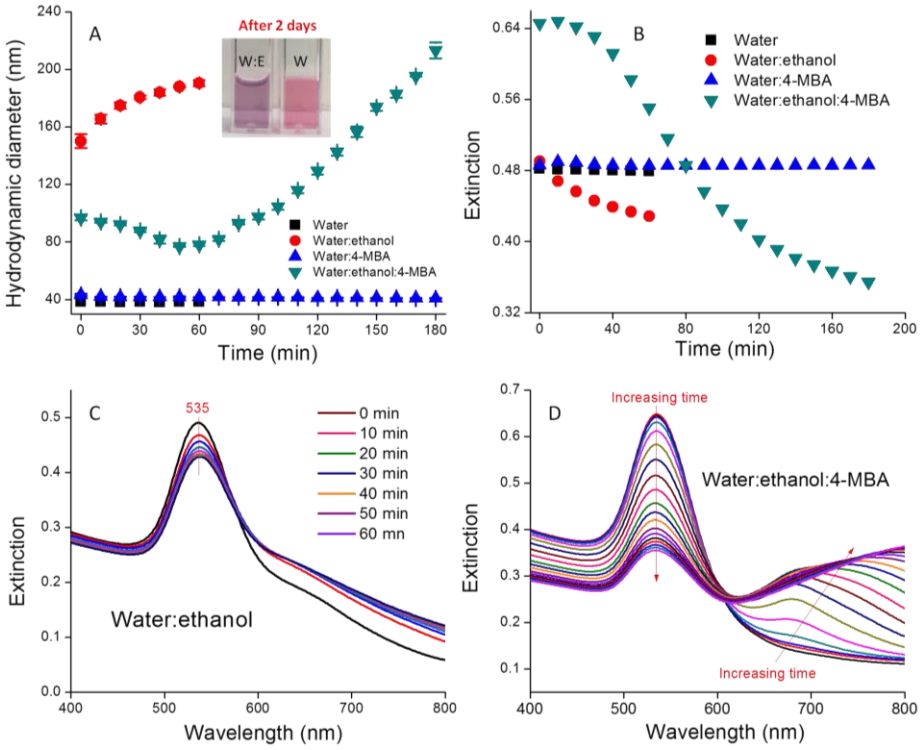

Figure 9.4 A) Temporal variation of the DLS determined hydrodynamic diameter of AuNPs dispersed in water and 50:50 water:ethanol in the presence and absence of 4-MBA; Inset photos are of AuNPs in water and 50:50 water:ethanol after two days; B) Temporal variation in the extinction of the primary LSPR band for AuNPs dispersed in water and 50:50 water:ethanol in the presence

and absence of 4-MBA; C) Extinction spectra of AuNPs in water:ethanol as a function of time, and D) Extinction spectra of AuNPs in water:ethanol:4-MBA as a function of time.

UV-VIS spectroscopy results are consistent with the DLS data. The extinction spectra of AuNPs in water:ethanol co-solvent exhibited a primary LSPR band at 535 nm and a secondary LSPR band at ~650 nm, thus indicating AuNP aggregation (Figure 9.4C). As time increased from 0 to 60 min, the primary LSPR band gradually decreased in magnitude, while the secondary band simultaneously increased (Figure 9.4C). To quantitatively illustrate this change we plot the height variation of the primary LSPR band as a function of time in Figure 9.4B. This figure demonstrates that AuNP aggregation in water:ethanol co-solvent occurs rapidly at the beginning and then occurs more slowly, thus resulting in the long-term stability of the suspension.

Similar to the DLS results, the extinction spectra of 4-MBA-AuNPs in water:ethanol co-solvent exhibited different time-dependent variation relative to pristine AuNPs (Figure 9.4B&D). Over the first 40 min, the spectra remained almost constant, thus indicating no obvious aggregation. Following this short delay, the LSPR band at 535 nm decreased at a rate comparable to the increase in the intensity of the band at 650 nm until 2 h. After 2 h, the bands at 535 nm and 650 nm decreased, while a third band at 750 nm developed. Unlike pristine AuNPs, the 4-MBA-AuNPs in water:ethanol co-solvent were initially stable and then once aggregation was initiated it proceeded until the colloidal stability was completely lost by 12 h (data not shown). We attribute the delay in aggregation to the increase in solvent dielectric constant that occurs due to addition of a high concentration of 4-MBA (100 μM), which in turn results in an increase in V_{elec} (Eq. 9.1). At extended reaction times increasingly larger amounts of 4-MBA have adsorbed onto the AuNPs and this leads to a decrease in the local dielectric followed by the onset of aggregation. Such speculation is supported by the fact that no delay in the onset of aggregation was observed when the 4-MBA concentration was decreased by 10×, 100×, or 1000×, thus suggesting that low 4-MBA

concentrations are insufficient to change the local dielectric (Figure 9.5). For low 4-MBA concentrations, the initial AuNP size is highly dynamic because of rapid initial aggregation (data not shown). Because of the delay in the onset of aggregation that occurs in the presence of high 4-MBA concentrations, the point at which aggregation is initiated can be easily pinpointed and the entire aggregation process can be well controlled.

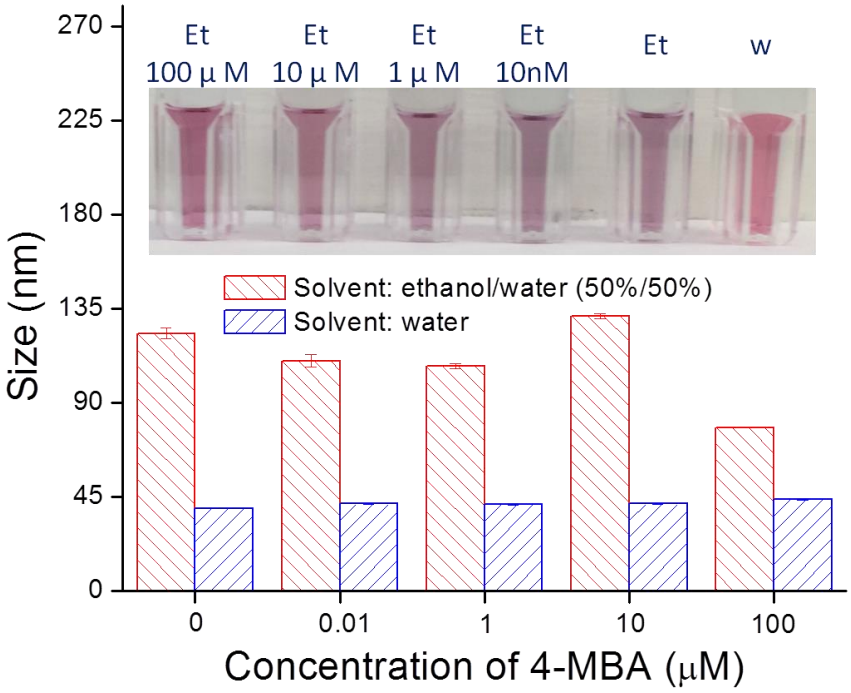

Figure 9.5 Size of 4-MBA coated AuNPs in water and water:ethanol co-solvent with different 4-MBA concentrations; Insets are photos of MBA coated AuNPs in water and water:ethanol co-solvent with different 4-MBA. All the results are at time = 0 h.

The extinction spectra of the AuNPs and 4-MBA-AuNPs in water remain stable over a three-hour period (Figure 9.6), thus demonstrating the important role of ethanol to accelerate aggregation. The role of 4-MBA in AuNP aggregation in water:ethanol co-solvent can thus be concluded: 1) to stabilize the colloid in the first 40 min due to the increase in solvent dielectric constant; 2) to promote aggregation after 40 min due to the decreased stabilizing capacity of 4-MBA relative to the citrate AuNP surface coating. The synergistic interplay between the ethanol

and 4-MBA concentrations in dictating AuNP aggregation enables reproducible and stable pH probe production, as shown in the following sections.

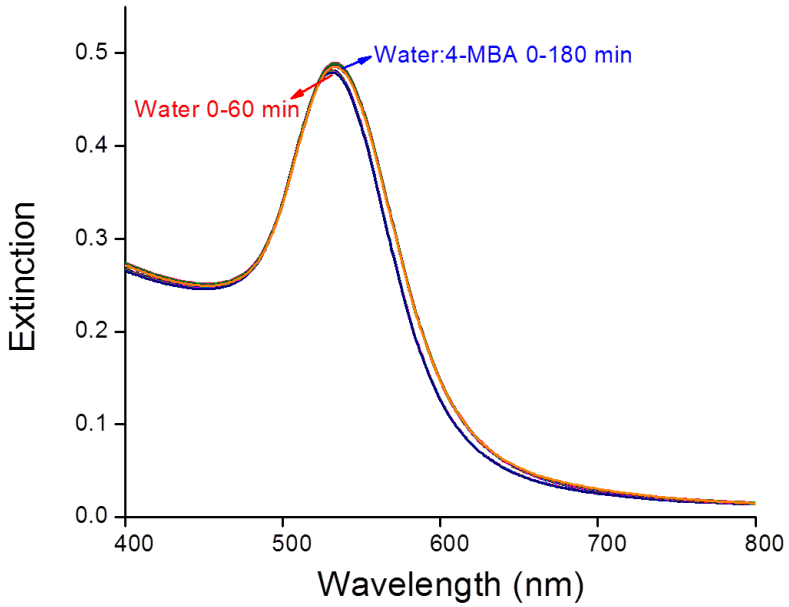

Figure 9.6 Extinction spectra of AuNPs and 4-MBA coated AuNPs in water as a function of time.

9.3.2 SERS of 4-MBA-AuNPs in Water:Ethanol Co-Solvent

The variation in the SERS spectra for 4-MBA-AuNPs in water:ethanol co-solvent was monitored every 6 min for 3 h (Figure 9.7). At t=0, only the ethanol spectrum was apparent with a prominent band at 886 cm^{-1}. The intensity of this band remained constant over the 3 h reaction period because of the fixed ethanol content. With time, the characteristic bands of 4-MBA (528, 698, 1084, 1286, and 1597 cm^{-1}) appeared and increased in magnitude from 0 to 168 min (Figure 9.7A). In comparison, the Raman bands of 4-MBA-AuNPs in water alone were approximately 260× weaker than in water:ethanol co-solvent. Such a result highlights the importance of producing multimers containing "hot spots" to achieve an intense SERS signal and succinctly illustrates the important role that ethanol plays in AuNP aggregation and in the generation of a strong 4-MBA SERS signal.

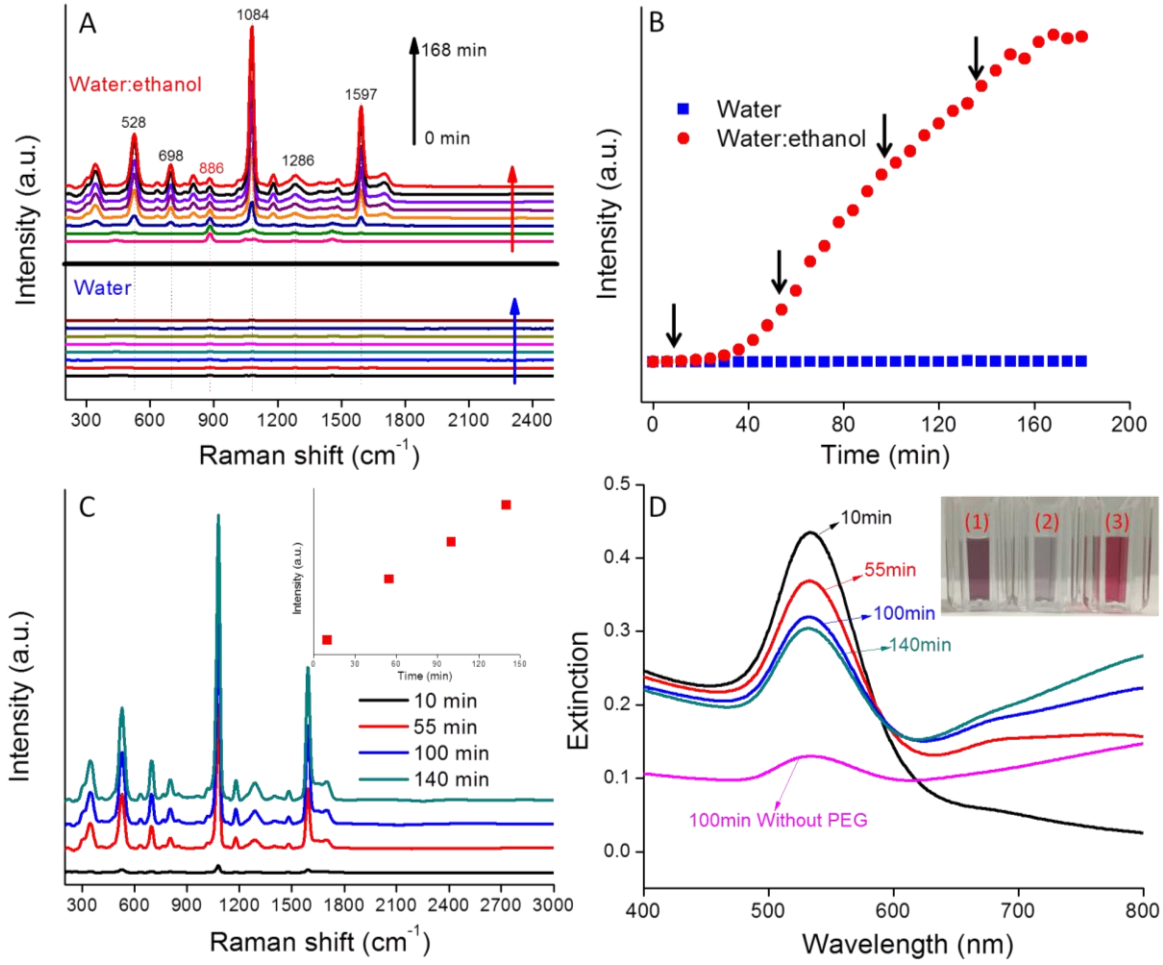

Figure 9.7 A) Selected SERS spectra of 4-MBA-AuNPs in water and water:ethanol mixture over three hours; B) SERS intensity variation of band at 1084 cm^{-1} as a function of time; C) SERS spectra of 4-MBA-AuNPs after PEG coating at different times; D) UV-VIS extinction spectra of 4-MBA-AuNPs coated with HS-PEG at different times as well as without the HS-PEG coating; Inset is the photo of (1) AuNP monomer colloid, (2) 4-MBA-AuNPs without HS-PEG coating after centrifugation; and (3) 4-MBA-AuNPs with HS-PEG coating after centrifugation.

To quantitatively show the time-dependent variation in SERS signal, the intensities of the Raman band at 1084 cm^{-1} for 4-MBA-AuNPs in water and in water:ethanol co-solvent were compared (Figure 9.7B). In water:ethanol co-solvent, the SERS intensity was constant for the initial 40 min, a period that corresponds to the aggregation delay depicted in Figure 9.4A&B. This result demonstrates that AuNP aggregation is crucial for the generation of a strong SERS signal. Between 40 and 160 min, the SERS intensity increased steadily, due to enhanced coupling between

the developing LSPR band in the NIR region and the 785 nm incident laser wavelength (Figure 9.4D).[386] Between 160 and 180 min the SERS intensity plateaued, a result that may be due to the depletion of sufficient numbers of AuNP monomers to feed the growing multimer population (Figure 9.7B). We note that all the 4-MBA Raman bands varied simultaneously with a change in aggregation state, thus indicating aggregation state had no influence on the peak ratios, a result that is consistent with the literature.[425]

SERS spectra of 4-MBA-AuNPs in solutions with different ethanol contents were also collected. As shown in Figure 9.8, the SERS signal generally decreased with the decrease of ethanol content, which was attributed to the ineffective aggregation of AuNPs in solutions with lower ethanol contents. There is a substantial SERS signal enhancement when ethanol content increased from 25-50%. This indicates the ethanol content threshold that could effectively induced AuNP aggregation lies in between 25-50%, which is supported by the results in Figure 9.3. Overall, these results suggested that the change of solution dielectric constant induced by ethanol can be effectively applied to control AuNP aggregation and thus enhance their SERS signal.

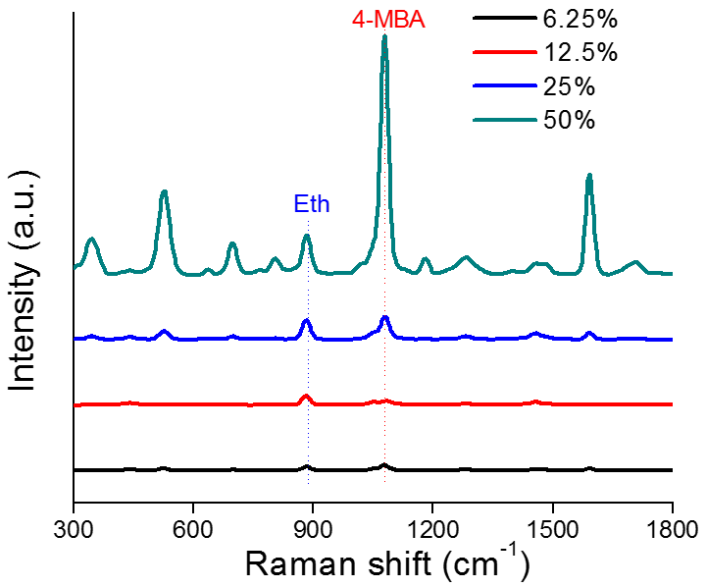

Figure 9.8 SERS spectra of 4-MBA coated AuNPs in solutions with different ethanol contents.

9.3.3 Production of Colloidally Stable SERS pH Probe

Uncontrolled aggregation and flocculation limit the broad application and use of most of the currently described SERS pH probes.[421, 422, 429] A stable pH probe with broad pH sensitivity is desired to enhance reproducibility and enable real world applications. HS-PEG is recognized for its capacity to sterically stabilize AuNPs and thus we used it as a means to stabilize our nanoprobes.[246] We specifically investigated the addition of HS-PEG to arrest nanoprobe aggregation. Accordingly, HS-PEG was added to aliquots of the reacting system depicted in Figure 9.7B at the times denoted by the black arrows (10, 55, 100, and 140 min). Each of these times corresponds to a different extent of aggregation and thus variable SERS intensity. Two days after adding HS-PEG, the 4-MBA-AuNP extinction spectra remained virtually unchanged, thus indicating that HS-PEG can effectively quench the aggregation of the 4-MBA-AuNPs in water:ethanol (Figure 9.9).

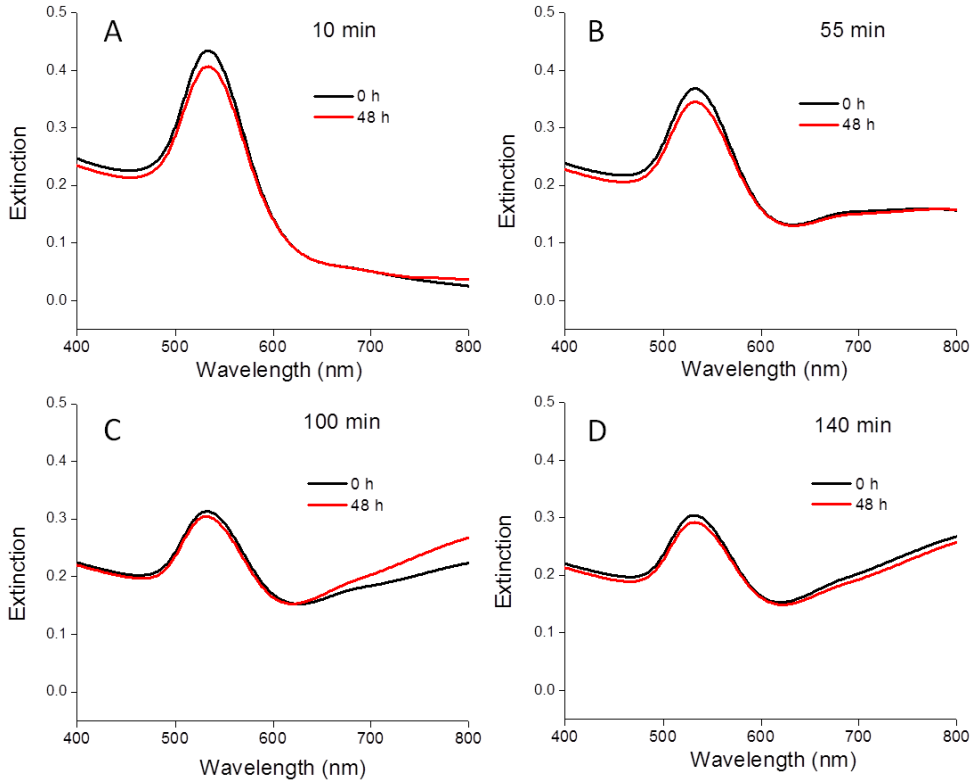

Figure 9.9 UV-VIS extinction spectra of 4-MBA coated AuNPs in water/ethanol co-solvent 0 h and 48 h after adding HS-PEG.

After addition of HS-PEG, the nanoprobes were washed by centrifugation three times to remove excess 4-MBA, HS-PEG, and ethanol. Following each centrifugation, the supernatant was discarded and the solids were redispersed in water. Assuming each 4-MBA molecule occupies a 0.2 nm^2 area on the AuNP surface, the maximum number of 4-MBA molecules each AuNP can hold is 24,000.[428] Under our synthesis conditions the concentration of 4-MBA exceeded 300,000 molecules per AuNP and thus the AuNP surface should be saturated by 4-MBA. The added amount of HS-PEG was of similar concentration to that of 4-MBA and there was some concern that HS-PEG could replace 4-MBA on the AuNP surface and thus lower the SERS intensity. However, as shown in Figure 9.10, the addition of HS-PEG had no detrimental effect on the measured SERS intensity. This result suggests that HS-PEG either does not replace surface associated 4-MBA or does so only on the periphery of the AuNP clusters and not within the "hot spots" responsible for

the intense SERS signal. Of these two hypotheses, the latter is supported by SEM images that illustrate 4-MBA-AuNP clusters consistently wrapped by a ~5.6 nm thick PEG layer (a thickness consistent with the 5k molecular weight[437]), but with interparticle junctions of only a few angstroms that are consistent with the expected spacing for SERS "hot spots" (Figure 9.1). These results are corroborated by TEM images that show small AuNP clusters with PEG coatings (Figure 9.2C&D).

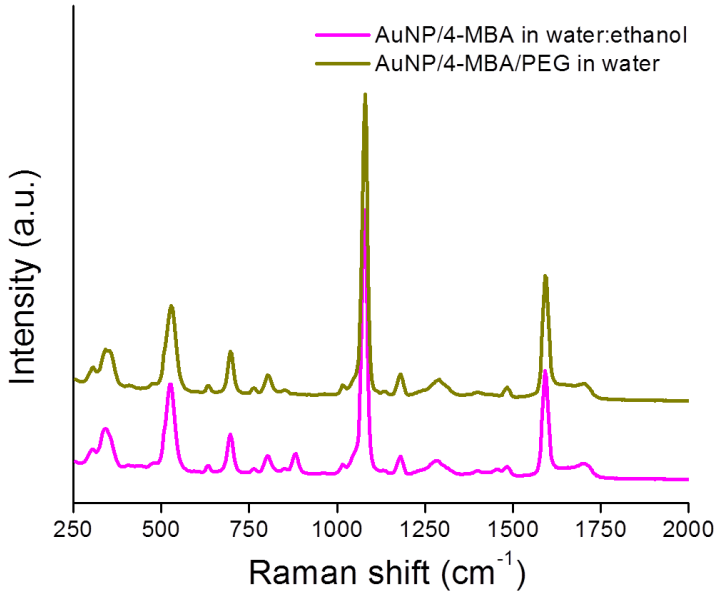

Figure 9.10 SERS spectra of AuNP/MBA in water:ethanol co-solvent and AuNP/4-MBA/PEG in water at 100 min.

The absence of a peak at 886 cm^{-1} in the spectra for the washed probes (Figure 9.7C) indicates that a majority of the ethanol initially present in the system was removed by centrifugation. We note that it is highly advantageous that the reagent used to induce AuNP aggregation can be easily removed following probe synthesis since it then does not occupy the SERS "hot spot" volume. The SERS intensity increased almost linearly with the coating time (Inset of Figure 9.7C), which is consistent with the trend observed in the absence of the HS-PEG coating (Figure 9.7B).

UV-VIS extinction spectra of HS-PEG coated 4-MBA-AuNPs after centrifugation are shown in Figure 9.7D. With an increase in the HS-PEG coating time, the LSPR band at 535 nm gradually decreased while the band in the NIR region gradually increased, leading to the increase in SERS intensity (Figure 9.7C). As a negative control, 4-MBA-AuNPs without HS-PEG were also washed by centrifugation. After washing, the extinction spectrum became almost flat (Figure 9.7D) and the colloid color significantly faded (Inset of Figure 9.7D), thus indicating that most of the 4-MBA-AuNPs were lost by the irreversible formation of large aggregates during centrifugation. As a comparison, the colloid with a HS-PEG coating showed dark purple color (Inset of Figure 9.7D), highlighting the important role of HS-PEG for colloid stability. An ideal pH probe should be able to generate high SERS intensity as well as stay suspended in water for an extended period of time (i.e., the aggregates cannot be too large). Balancing these two aspects, 4-MBA-AuNPs coated with HS-PEG at 100 min were selected as the best pH probe and further tested.

9.3.4 pH Nanoprobe Sensitivity and Stability

The pH sensitivity of our nanoprobe was tested in phosphate buffer (PB) solutions of different pH. As shown in Figure 9.11A, the SERS spectra varied with pH. The bands at 1410 ($-COO^-$) and 1710 cm^{-1} (-COOH) increased or decreased in intensity, respectively, as well as slightly shifted with an increase of solution pH, while the Raman band at 1084 cm^{-1} (benzene ring) remained constant. This result indicates that the protective PEG layer is permeable to H^+ and does not detrimentally affect the pH sensitivity of the probe. We note that this probe exhibits high SERS intensity at both extremely acidic (pH=1.2) and basic (pH=12.6) conditions. These high ionic strength conditions normally result in colloidal instability, thus the high signal intensities demonstrate the excellent stability conferred by the PEG coating (Figure 9.12).

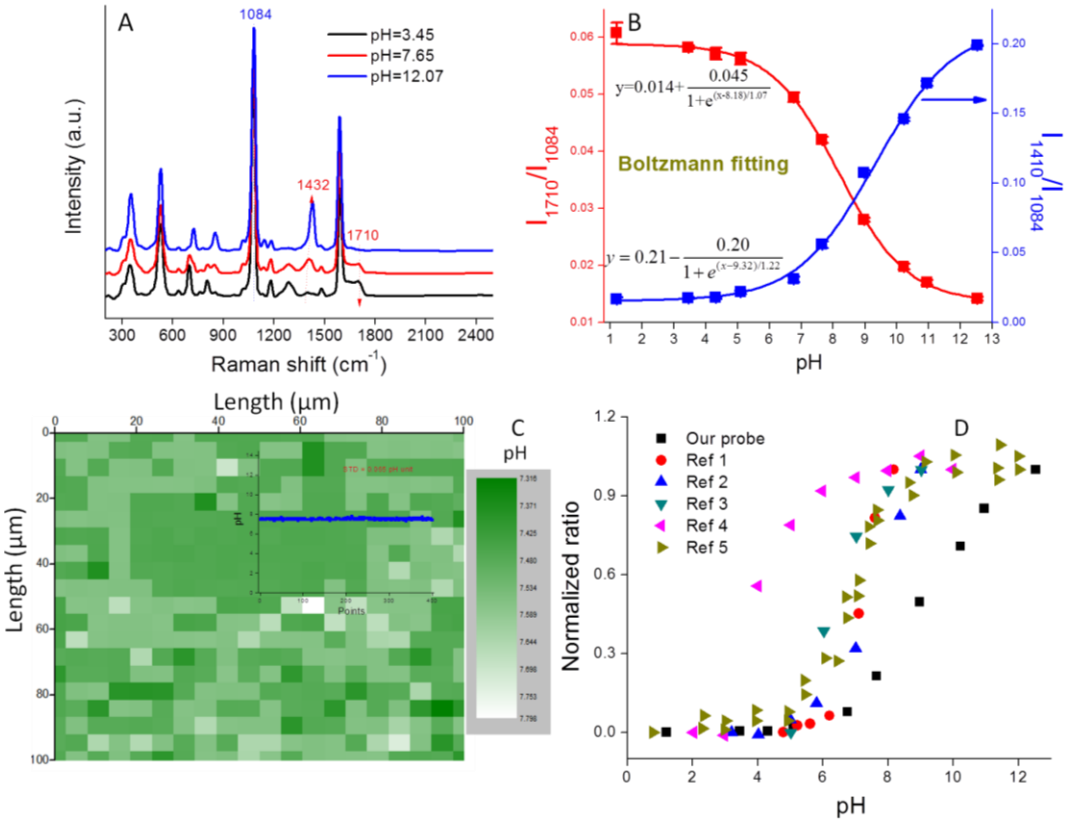

Figure 9.11 A) SERS spectra of pH probe in PB buffer of different pH; B) pH calibration curve in the range 1-13; C) A Raman map containing 400 pixels, each pixel shows a pH value for a 3.5×10^{-11} mL volume; Inset figure: pH value variation of the 400 pixels from the Raman map; D) pH calibration curves from both our study and the literature for 4-MBA functionalized pH probes. The curves are normalized to their maximum values.[420, 422, 427, 429, 431]

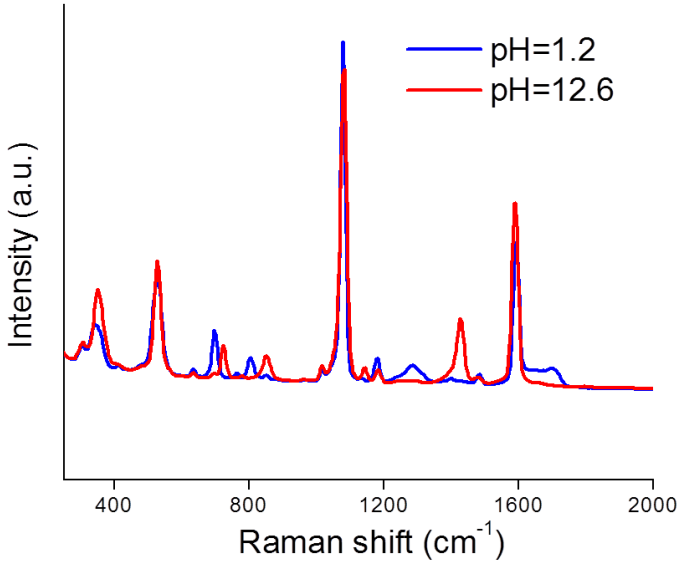

Figure 9.12 SERS spectra of probe at pH=1.2 and 12.6.

Ratios of each of the pH-sensitive peaks (1410 cm^{-1} or 1710 cm^{-1}) relative to the pH-insensitive peak (1084 cm^{-1}) were plotted as a function of pH from 1 to 13 (Figure 9.11B). In the acidic pH range of 1-6 and the basic range of 11-13, the intensity ratios (I_{1410}/I_{1084} and I_{1710}/I_{1084}) increase or decrease minimally, while in the 6-11 pH range, the ratios change much more dramatically, thus indicating that this is the most sensitive pH range for this probe. The pH calibration curves could be perfectly fitted using the Boltzmann expression (Figure 9.11B) that has been previously applied to fit sigmoid shaped pH curves.[430] The linear portion of the curve covers five pH units, a range that is much broader than those reported in the literature for other 4-MBA based nanoprobes (Figure 9.11D). This result can be attributed to both the high SERS intensity of our probes and their unique colloidal stability. We note that the derived pK_a value (8.75) is nearly 4 pH units higher than that of bulk 4-MBA (4.79). Such a large pK_a discrepancy between nanostructure associated 4-MBA and its bulk value has been previously reported and can be attributed to changes in surface topography and electron density.[438, 439] pH measurements obtained with this nanoprobe are highly reproducible (STD<5% for three parallel measurements) due to their well controlled aggregation and stability (Figure 9.11B).

Most recently, Zheng et al. utilized bovine serum albumin (BSA) to stabilize their pH nanoprobes.[425] However, due to the nonspecific mechanism by which BSA associates with the nanoprobes, the resulting nanoprobes were difficult to reproduce and had limited shelf stability. Importantly, Zheng et al. attributed the majority of their SERS signal to the presence of small numbers of dimer and trimer AuNP aggregates that formed following BSA addition. Such a result supports our focus on the systematic production of colloidally stable AuNP aggregates of fixed size. Wang et al. developed silica shell-coated AgNP pH probes and successfully prevented BSA from contaminating the AgNP surface.[431] However, the reverse microemulsion method utilized for

this synthesis is chemical-intensive and time-consuming. Also the silica shell limited the diffusion of protons to the AgNP surface, making the pH sensitive range very narrow (pH 3-6). We note that none of the previously reported probes exhibit stability over the broad pH range of 1-13 that we report here.

A significant advantage of nano-sized pH probes is their capacity to provide high spatial resolution and their potential to quantify pH within microenvironments. The laser spot size of a Raman microscopy system limits the resolution that can be achieved by a SERS probe. For our probe and our microscope objective this spot size is described in the lateral ($\delta_{lateral}$ = 1.6 μm) and axial (vertical) dimensions (δ_{axial} = 17.4 μm) using Eqs. 9.2 and 9.3, where λ is the laser wavelength, and NA (numerical aperture) is the characteristic parameter of an objective. Assuming a cylindrical laser spot, the minimum volume that can be detected is 35 fL. This volume is much smaller than that can be detected by commercial pH meter.

$$\delta_{lateral} = \frac{0.61\lambda}{NA} \qquad \text{Equation 9.2}$$

$$\delta_{axial} = \frac{2\lambda n}{(NA)^2} \qquad \text{Equation 9.3}$$

A 1000 μm × 1000 μm Raman map collected in PB solution contains 400 pixels as shown in Figure 9.11C. Using the pH calibration curve in Figure 9.11D, a pH map illustrates the pH value within the 35 fL volume derived from a single Raman spectrum. As shown in Figure 9.13, such a single spectrum exhibits an excellent signal/noise ratio. Because the concentration of AuNPs used in this study is known (1.3×10^{11} mL^{-1}) each detection volume contained on average 2.3 NPs. This result demonstrates that each multimer exhibits extremely high SERS intensity. When all 400 pH values from the Raman map were plotted (inset to Figure 9.11C), an extremely flat line was obtained. The

small standard deviation (STD = 0.065 pH units) demonstrated the high pixel-to-pixel reproducibility of the SERS spectra. The pH sensitivity of our probe is defined as three fold of the STD,[394] i.e., about 0.2 pH units.

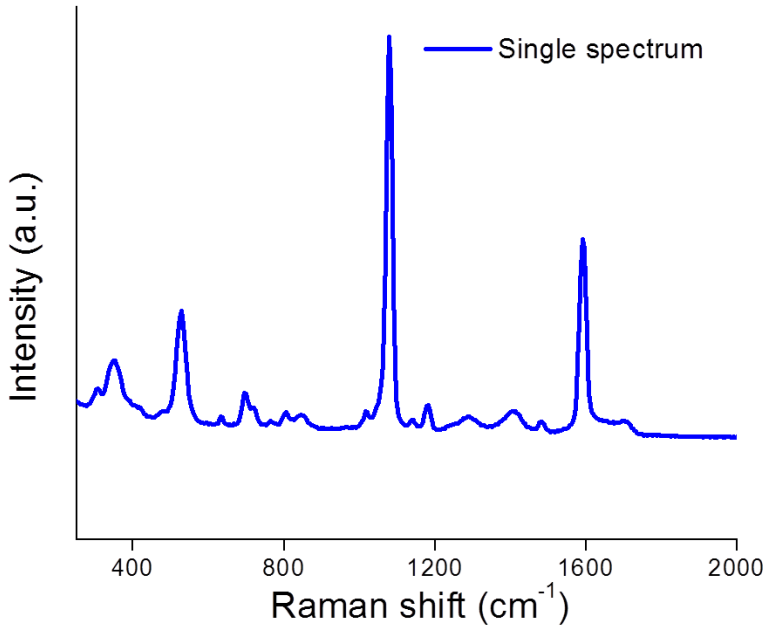

Figure 9.13 Single Raman spectrum from a random selected pixel in the Raman map.

Probe stability is important for real world application of AuNP-based pH probes. The HS-PEG coating is expected to prevent AuNP aggregation and nonspecific chemical adsorption on the AuNP probes, thus improving both the spatial and temporal reproducibility of the probe response. To evaluate their stability, the probes were suspended in PB solution (0.01M) and the variation of their extinction spectra, size, and pH indicator values (I_{1410}/I_{1084} and I_{1710}/I_{1084}) were monitored for one hour. As shown in Figure 9.14A-C, the extinction spectra, hydrodynamic diameter, and pH indicator values each remained constant during one hour thus indicating that the probes were highly stable in pH buffer. In addition, the stability of the probe was tested in two soft drinks (Fanta orange and club soda) and tap water. As shown in Figure 9.14D, the pH values measured by our pH probe are consistent with those measured by a commercial pH meter. Impressively, the probes

generated high quality and reproducible SERS spectra in each of these matrices, thus indicating that they were very stable in these complex matrices and that the other constituents present exhibited no interferences to probe response (Figure 9.15).

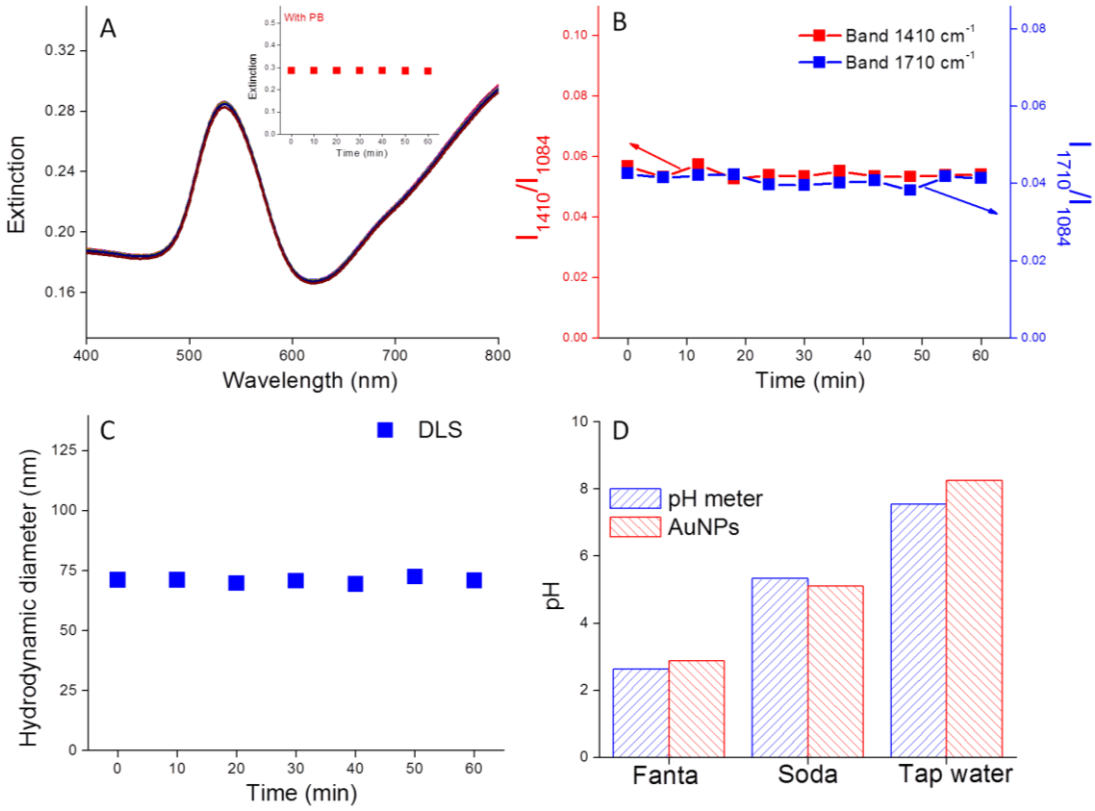

Figure 9.14 A) Variations of the UV-VIS extinction spectra, B) pH indicator values, and C) hydrodynamic diameter of the pH probe in 0.01 M PB solution as a function of time; D) pH values of three real water samples measured by our pH probe and a commercial pH meter in our lab.

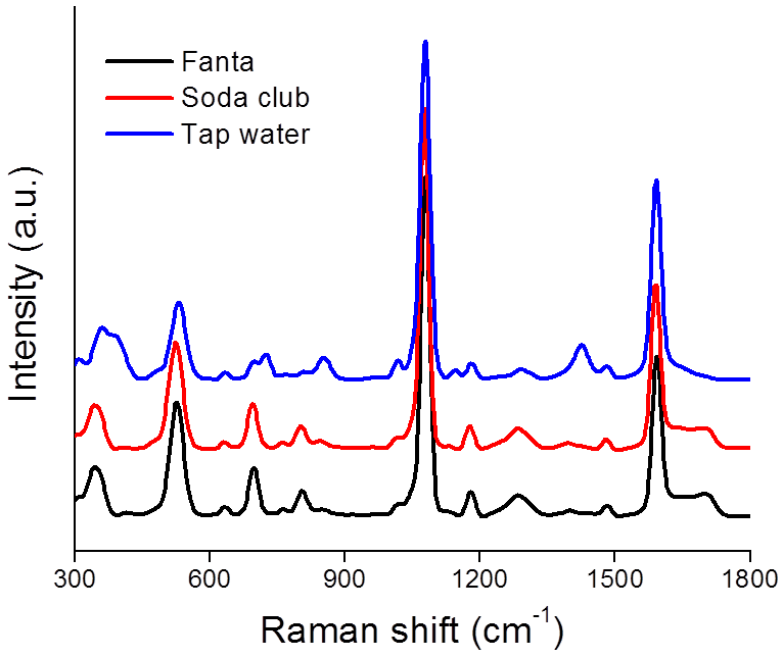

Figure 9.15 SERS spectra of our pH probe suspended in Fanta, club soda, and tap water.

9.3.5 Intracellular pH Monitoring

As a proof-of-concept, we utilized our pH probes to detect the intracellular pH of the clinically relevant PC-3 human prostate cancer cell line. Nanoparticle uptake by PC-3 cells has been demonstrated numerous times in the literature[440] with endocytosis, a broad term encompassing many distinct pathways, considered the predominant method of AuNP uptake.[441, 442] Briefly, our pH probes were incubated with PC-3 cells for 24 hours, washed, and then imaged using Raman spectroscopy. As shown in Figure 9.16A, the sizes and shapes of the cancer cells were heterogeneous, as expected for an adherent cell-line incubated for nearly two days.[443] The most prominent 4-MBA Raman band (1084 cm^{-1}) was used to identify the internalized nanoprobe locations and as shown in Figure 9.16B, the probe position was co-located with that of the cancer cells. Intracellular localization of the nanoprobes was verified by depth scanning (Figure 9.17). The nearly uniform SERS intensity within the cell, ~25 μm in depth, provides evidence that the probes were located inside the cell and not on the cell surface. These results demonstrate that the

cancer cells can easily take up the pH sensitive PEG-4-MBA-AuNP probes described herein and can be readily imaged.

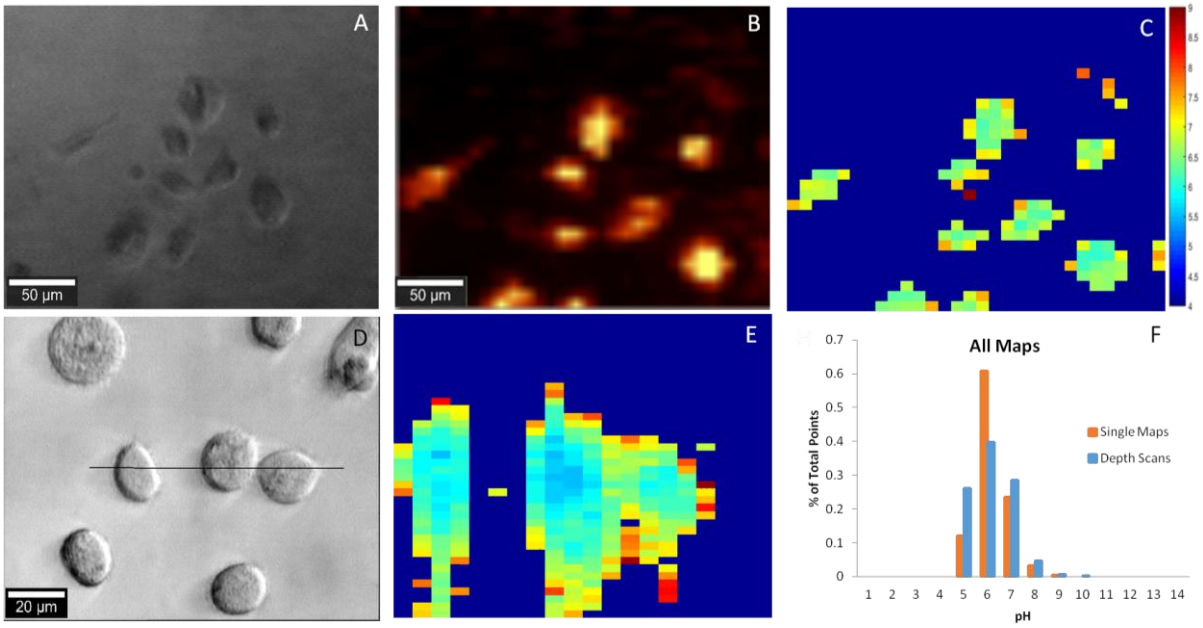

Figure 9.16 A) Optical 10X image of PC3 cancer cells; B) SERS map of Figure A based on intensity of the 1084^{-1} cm peak; C) pH map rendered in MATLAB of Fig A derived from the signal of Fig B. D) Optical 50X image of PC3 cancer cells with black line indicating position of YZ plane; E) In-depth pH map indicated by the black line in Fig D and F) Summary of pH distribution for single maps and depth scans.

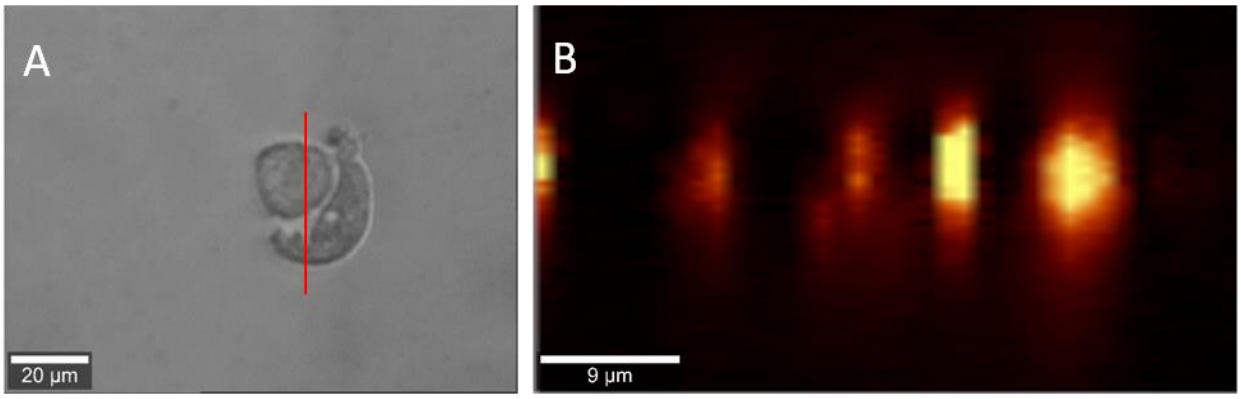

Figure 9.17 A) Optical image of prostate cancer cell and B) Y-Z cross section Raman scan (marked by the red line) of the cancer cell.

To determine the intracellular pH of the cancer cells in rapid and automated fashion, the collected SERS maps were imported into Matlab and baseline corrected and analyzed using in-house scripts. At each point in every SERS map, the ratio between the pH insensitive peak (1084 cm^{-1}) and the pH sensitive peak (1410 cm^{-1}) was determined. Using a calibration curve established in cell culture media (Figure 9.18), the pH was calculated at each point and then rendered into a XY map (Figure 9.16C). The SERS spectrum of the internalized pH probes includes the 4-MBA Raman bands with good signal-to-noise ratio with no interference from either the cell or the culture medium, thus indicating the excellent stability and protection capability of the PEG layer. A typical SERS spectrum is shown in Figure 9.19. Ultimately, 19 unique pH maps were collected. The intracellular pH range calculated over the whole sample set, Figure 9.16F, agrees with the intracellular pH range reported in the literature of pH 4 to 9.[420, 422, 429, 430] Additionally, fourteen depth scans, YZ cross sections, were collected and demonstrate the three-dimensional spatial consistency of our probes (Figure 9.16D&E). Again, for both single maps and depth scans across the dataset (Figure 9.16F) more than 95% of the pH points fall between pH 5-7 and 99% of the points fall within the expected range for intracellular pH.

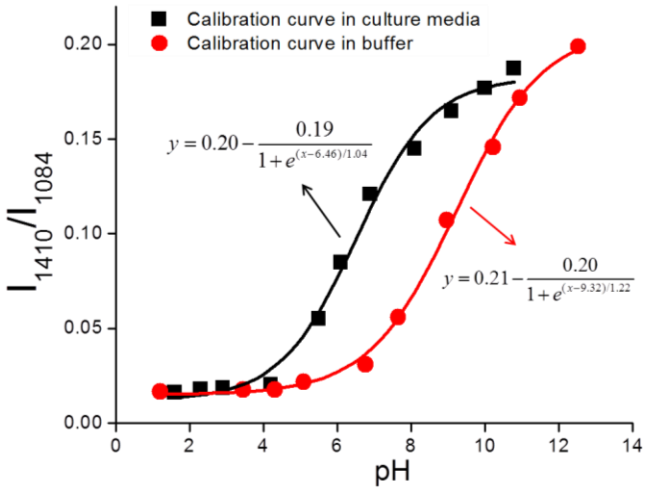

Figure 9.18 pH calibration curves for pH probes in cell media (black squares) and in buffer (red circles).

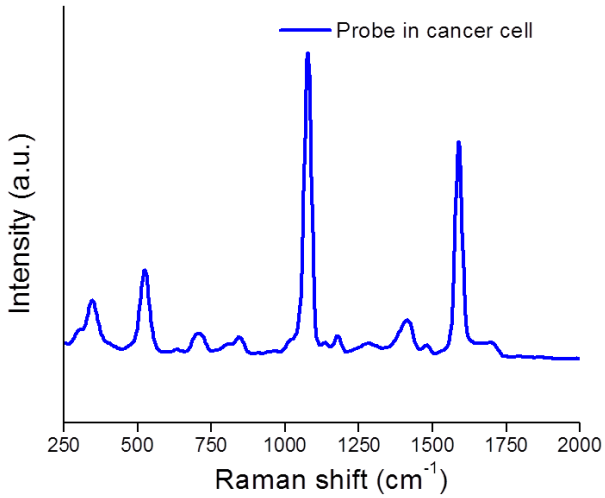

Figure 9.19 SERS spectrum of the pH probe inside the cancer cell.

We found it necessary to develop a pH calibration curve in cell culture media. As shown in Figure 9.18, there is a substantial difference in both the shape of the calibration curve and pH sensitive range in cell culture media relative to PB. We attribute this fact to the presence of proteins in the culture media as we observed a similar phenomenon in milk (data not shown). To our knowledge the observation that pH nanoprobes should be calibrated in culture media has not been addressed in a majority of the prior studies detailing their development. In Figure 9.20 we compare

internal cell pH values measured using a calibration curve obtained in cell culture media relative to PB media alone. The lack of consideration of this effect may be partially responsible for many of the extant reports of low pH zones in cells mapped using nanoprobes.

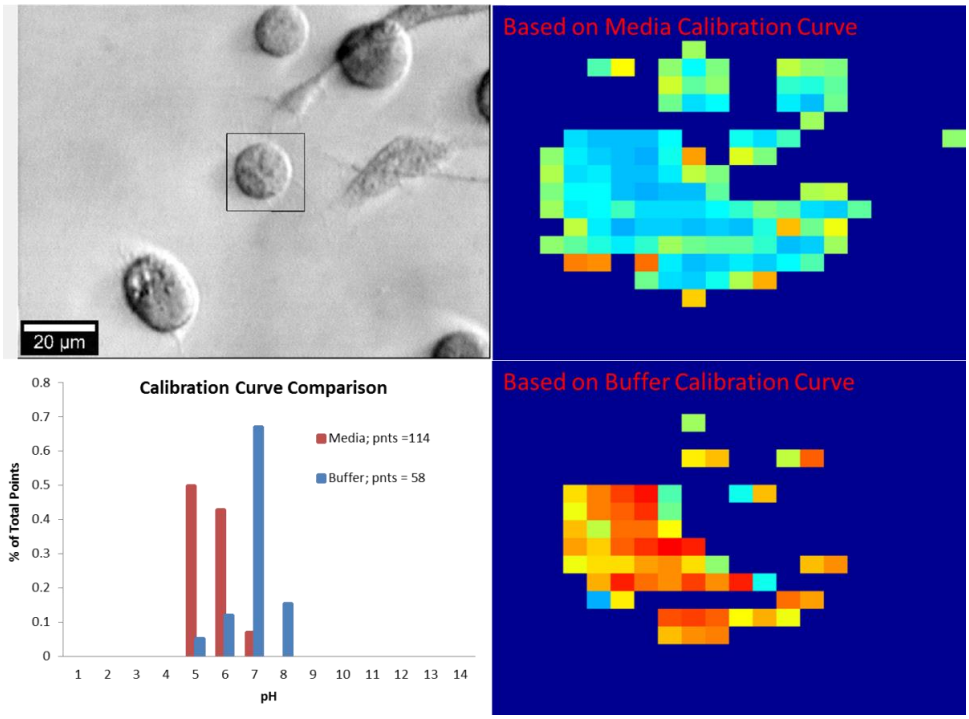

Figure 9.20 Comparison of the pH calculated for a given cell with the two different calibration curves.

Compared to previously reported intracellular pH probes, our probe exhibits several advantages: 1) the Raman spectrum exhibits higher signal-to-noise ratio than those produced by uncontrolled aggregation (Figure 9.7A, Figure 9.19)[422, 429] due to our use of co-solvents to control the extent of aggregation. 2) The SERS spectra collected from probes internalized by PC3 cells only contain Raman bands for 4-MBA (Figure 9.19) because the PEG protective layer prevents cellular components from reaching the surface. In contrast, many reported probes that do not have a protective layer exhibit potentially interferent Raman bands due to the biomolecules inside the cells.[421] 3) This paper demonstrates clear evidence that the probes are internalized by the PC3 cells

by providing co-located optical and SERS images and is the first to present depth scans (Figure 9.16 & Figure 9.17), while none of extent literature provides this information.[422, 427, 429, 431] As a comparison, in a recently published paper, 4-MBA-coated AuNPs without controlled aggregation and PEG protection were applied for detecting pH in EA.hy926 cells.[429] Due to lacking in SERS signal optimization through controlled aggregation and stability through PEG protection, the probes exhibited much lower signal-to-noise ratio in cells compared to ours. SERS maps exhibited the tendency of the probes to locate in several limited areas inside the cells and reported several abnormally high pH values, which could be attributed to the severe aggregation of the unprotected probes and interferences from the biomolecules inside the cells or the culture media.

9.4 Conclusions

Herein we have described a novel, highly reproducible approach to control AuNP aggregation using water:ethanol co-solvent and 4-MBA mixtures. By using this approach, and by coating the resulting multimers with PEG to provide steric stability we were able to produce highly stable pH nanoprobes. Because of their colloidal stability these nanoprobes exhibit a broader pH sensitive range of 6-11 than existing pH nanoprobes described in the literature. An individual dimer within a 3.5 fL volume generates high SERS intensity, which is ideal for detecting pH changes within microenvironments. To provide proof of concept, we utilized the pH nanoprobes to detect the intracellular pH of PC-3 cancer cells. Using a Raman mapping approach and data processing we establish that intra-cellular pH is highly consistent across multiple cells and we have produced the most robust database of intracellular pH obtained by SERS to date. Because the protective PEG layer can be replaced with bifunctional PEG (i.e., both thiol and carboxy terminated) our nanoprobes can be further functionalized to provide multiplex sensing capacity. In our ongoing

studies we seek to utilize this capacity to measure not only pH, but also to detect and quantify cells.

Chapter 10 Aerosol Microdroplets Exhibit a Stable pH Gradient

Haoran Wei,[a,b,c] Eric P. Vejerano,[a,b,c,d] Weinan Leng,[a,b,c] Qishen Huang,[a,b,c] Marjorie R. Willner,[a,b.c] Linsey C. Marr,[a,b,c] Peter J. Vikesland[a,b,c,1]

[a] Department of Civil and Environmental Engineering, Virginia Tech, Blacksburg, Virginia;

[b] Virginia Tech Institute of Critical Technology and Applied Science (ICTAS) Sustainable Nanotechnology Center (VTSuN), Blacksburg, Virginia;

[c] Center for the Environmental Implications of Nanotechnology (CEINT), Duke University, Durham, North Carolina;

[d] Arnold School of Public Health, University of South Carolina, Columbia, South Carolina.

[1] Corresponding author, email: pvikes@vt.edu

Manuscript Prepared for ***PNAS***

Physical Sciences: Environmental Sciences

(This chapter is upon revision in ***Proceedings of National Academic of Sciences***.)

Abstract

Suspended aqueous aerosol droplets (<50 μm) are micro-reactors for many important atmospheric reactions. In droplets, and other aquatic environments, pH is arguably the key parameter dictating many chemical and biological processes. The nature of the droplet air/water interface has the potential to significantly alter droplet pH relative to bulk water values. Historically, it has been challenging to measure the pH of individual droplets due to their inaccessibility to conventional pH probes. In this study, we scanned droplets containing 4-mercaptobenzoic acid (4-MBA) functionalized gold nanoparticle (AuNP) pH nanoprobes by 2D and 3D laser confocal Raman microscopy. Using surface-enhanced Raman scattering (SERS), we acquired the pH distribution inside ~20 μm diameter, phosphate-buffered aerosol droplets and found that the pH in the core of a droplet is higher than that of bulk solution by up to 3.6 pH units. This finding suggests the accumulation of protons at the air/water interface and is thus consistent with recent thermodynamic model results. The existence of this shift in pH was corroborated by the observation that a catalytic reaction that only occurs under basic conditions (i.e., the dimerization of 4-aminothiophenol to produce dimercaptoazobenzene) occurs within the high pH core of a droplet, but not in bulk solution. Our nanoparticle-derived probe enables quantification of pH through the cross-section of an aerosol droplet, revealing a spatial gradient that has important implications for acid-base catalyzed atmospheric chemistry.

10.1 Introduction

At high relative humidity (RH), aerosols containing liquid water are ubiquitous and have a profound influence on local, regional, and global atmospheric processes.[444-446] For example, aerosol droplets in clouds influence the global radiation budget and the hydrological cycle, which have uncertain feedbacks linked to factors driving climate change.[447, 448] At both local and global scale, sea spray and anthropogenic aerosols impact coastal and inland communities as well as climate through their capacity to absorb and scatter solar radiation and their role in cloud formation.[449, 450] In addition, anthropogenic aerosols contribute to air quality problems in urban areas across the globe.[451]

To quantify the impacts of these aerosols, we need to characterize their physical and chemical properties to understand how they influence *in situ* aerosol chemical reactions. In particular, the formation of organosulfates, acetals, esters/amides and other compounds affects secondary organic aerosol (SOA) production.[452-454] pH is arguably the key parameter defining droplet chemistry because of its central role dictating chemical speciation, partitioning, and reactivity.[274, 455, 456] pH is known to affect reactive uptake of atmospheric gases, phase separation, and surface tension.[457-460] Nonetheless, it is analytically challenging to measure the pH of individual aerosol droplets due to the current dearth of tools that can detect pH within the confined, micron-scale droplet environment.[461]

It is well known that water at the air-water interface exhibits different structure and hydrogen bond dynamics relative to bulk water and that these differences affect the pH of the near-surface region.[462] Unfortunately, it is both experimentally and theoretically challenging to probe the air/water interface, and even more so the acidity of that interface.[463] Electrophoretic mobility measurements of oil droplets and air bubbles in water indicate that this interface is negatively

charged. The simplest explanation for this observation is the accumulation of hydroxide (OH^-) at the interface and the electrostatic repulsion of hydronium (H_3O^+). This conceptual model, however, is inconsistent with surface sensitive experimental techniques such as second harmonic generation (SHG) and sum-frequency generation (SFG) that indicate that the interface is enriched in H_3O^+.[464] Molecular dynamics[465] and continuum solvent model[464] simulations further support the argument that H_3O^+ has greater affinity for the air/water interface than does OH^- and that the water surface of an aerosol droplet is expected to be acidic.[465, 466]

Currently, aerosol pH values are typically calculated using thermodynamic models, such as E-AIM and ISORROPIA-II[455, 456, 467, 468] that assume equilibrium between dissolved inorganic ions in the aqueous aerosol environment. However, these equilibrium models require measurement of the concentrations of multiple inorganic ions, along with temperature and relative humidity, to estimate aerosol water content.[469] ISORROPIA-II also neglects the impacts of organic ions, as well as particle phase and morphology. Furthermore, because aqueous aerosol particles are externally mixed, there is a significant need to obtain individual aerosol particle measurements in place of ensemble average or bulk measurements. Because aqueous aerosol particles can also be internally mixed, the ability to probe spatial heterogeneities within a single particle is critical, too.[461]

A number of spectroscopic and microscopic techniques such as electron microscopy, X-ray microscopy, fluorescence microscopy, single-particle aerosol mass spectroscopy, and Raman microscopy have the potential for single particle characterization.[461] Raman spectroscopy, in particular, provides the capacity to differentiate the vibrational states of acids and their conjugate bases under ambient conditions that are not accessible with other techniques. Recently, Rindelaub et al. used Raman spectroscopy to determine the pH of aerosol particles by tracking the ratio of the Raman bands of SO_4^{2-} and HSO_4^-.[470] Unfortunately, this approach was only useful in the highly

acidic pH range near the HSO_4^-/SO_4^{2-} pK_a of 2. To extend this approach to a broader pH range (-1 to 10), Craig et al. used a variety of acid-base pairs with different pK_a values and determined the pH of individual particles at sizes down to 1 μm.[471] Recently, surface-enhanced Raman spectroscopy (SERS) has been suggested as a means to sensitively probe atmospheric aerosols.[472, 473] SERS is an *in situ* method that can be used to probe water matrices, it exhibits extreme sensitivity,[474] and it provides a highly stable signal.[475]

We and others[420, 476, 477] have recently shown that SERS provides the capacity to measure pH in confined aqueous environments. Using a plasmonic nanoparticle that has been surface functionalized with a pH sensitive amine or carboxylic acid it is possible to collect SERS spectra that change as a function of the local pH. Solution pH is then determined based upon relative peak heights or changes in the band locations of specific vibrational modes. Herein, we employed nano-sized pH probes to characterize the pH of individual phosphate-buffered aerosol droplets and found that they exhibited a stable pH gradient across a droplet that often exceeded three pH units. Phosphorous is an important, yet underappreciated, component of many aerosols.[478-480] Phosphate is also useful as a buffer as, in contrast to ammonium, it exhibits minimal gas-particle partitioning. By combining the spatial resolution of a confocal Raman microscope with the inherent sensitivity of these probes, we were able to obtain the first two-dimensional (2D) and three-dimensional (3D) characterization of the pH distribution of micron-sized aerosol droplets under *in situ* conditons. The information acquired by this approach provides improved quantification of the pH of aerosol droplets.

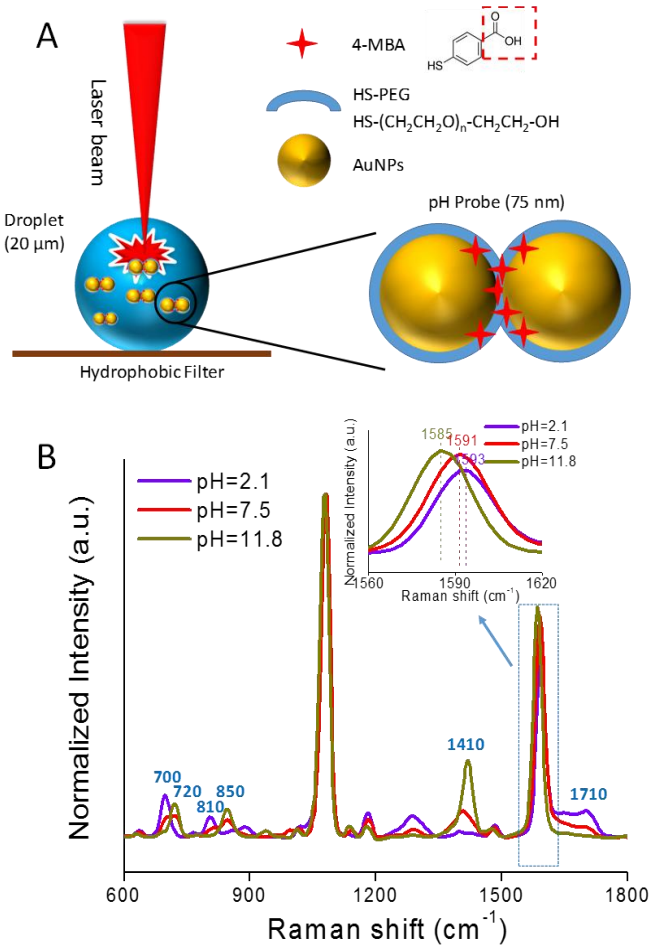

Figure 10.1 Principle for the pH detection of aerosol droplets using pH SERS nanoprobes. A) Schematics illustrating SERS probing of aerosol droplets collected on a superhydrophobic PVDF filter and of SERS pH nanoprobes; B) SERS spectra of pH nanoprobes in bulk phosphate buffer (PB) solutions (0.6 M) that were adjusted to different pH values.

10.2 Results

10.2.1 Principle of Droplet pH Detection by SERS

Our experimental design is illustrated in Figure 10.1. Aqueous microdroplets were generated from a 0.6 M phosphate buffer (PB) solution containing pH nanoprobes (2×10^{10} particles/mL) using a commercial atomizer (TSI 3076). Produced droplets were collected on a superhydrophobic surface prepared by drop-coating polydimethylsiloxane-treated silica nanoparticles onto a 0.22 μm polyvinylidene difluoride (PVDF) filter (Figure 10.1A). The filter with the collected droplets was

then placed in a humidity controlled flow cell. Unless otherwise indicated, all of the experiments were conducted at a RH of 97±0.5%.

As shown in Figure 10.1A, the pH nanoprobes consist of an AuNP optical antenna, a thiolated polyethylene glycol (PEG) stabilizing layer, and the 4-mercaptobenzoic acid (4-MBA) pH indicator.[477] 4-MBA is bifunctional, with a thiol group to covalently bind to the AuNP surface and a carboxylate group to detect changes in pH. SERS spectra collected from nanoprobes in bulk solutions of 0.6 M PB with different initial pH values are shown in Figure 10.1B. There are six characteristic Raman bands that change in intensity as the solution pH increases: 1) bands at 720 (out-of-plane ring hydrogen wagging), 850 (COO^- bending), and 1410 cm^{-1} (COO^- stretching) increase; and 2) bands at 700 (OCO bending), 810 (C-COOH stretching), and 1710 cm^{-1} (CO stretching) decrease.[423] Simultaneously, the band at 1590 cm^{-1} (benzene ring breathing and axial deformation) shifts to a lower wavenumber.[427] The other Raman bands in the spectrum are pH-insensitive, with the band at 1080 cm^{-1} (benzene ring breathing and axial deformation) the strongest. Because the pH-sensitive bands at ~1410 and 1710 cm^{-1} slightly shift with a change in solution pH, the maxima of the two peaks irrespective of position were used for pH calculation. The ratios of the Raman bands at 1710 cm^{-1} to 1080 cm^{-1} (I_{1710}/I_{1080}) and 1410 cm^{-1} to 1080 cm^{-1} (I_{1410}/I_{1080}) were used to construct pH calibration curves and are well described by the Boltzmann equation (Figure 10.2).

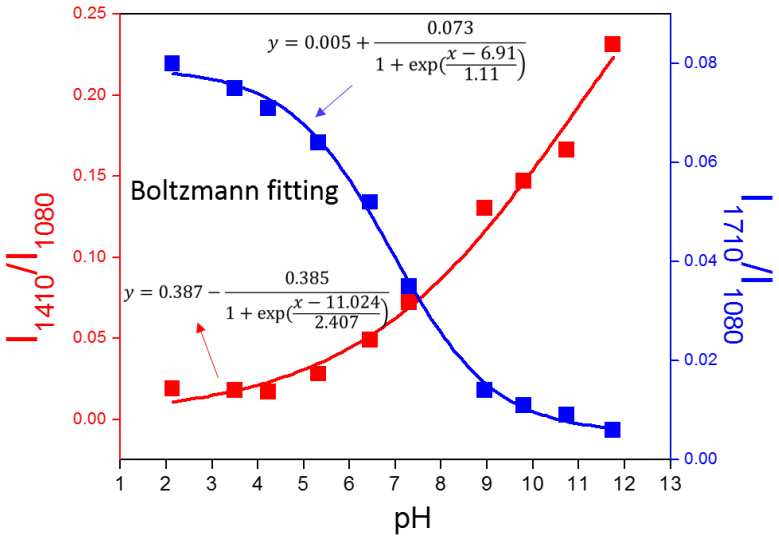

Figure 10.2 pH calibration curves constructed by fitting the variation of ratios I_{1410}/I_{1080} and I_{1710}/I_{1080} as a function of solution pH in Boltzmann equation.

10.2.2 Collection and Raman Scan of Microdroplets

Following aerosolization, micrometer-sized aqueous droplets were observed across the filter, indicating successful droplet generation and collection (Figure 10.3). The droplets were highly spherical owing to the high contact angle of 157.3º imparted by the superhydrophobic substrate. Using ImageJ,[481] we calculated an average droplet size of 19.5±6.2 μm for 155 droplets collected on five separately prepared superhydrophobic filters, although droplets <10 μm were not enumerated due to their poor contrast against the substrate. Control experiments indicate that the presence of the pH nanoprobes did not significantly alter the droplet size distribution.

A key consideration for *in situ* droplet scanning is the stability of a droplet over the course of a measurement. We monitored droplet diameter as a function of time and, as shown in Figure 10.4, observed that it remained stable over a 44 min period due to our control of RH in the flow cell. The droplet diameter remained unchanged after an entire Raman scan using a 50× objective (Figure 10.6), thus indicating a droplet is stable enough for laser confocal Raman interrogation.

In contrast, droplets scanned under supersaturated conditions grew in size over the course of an hour (Figure 10.5).

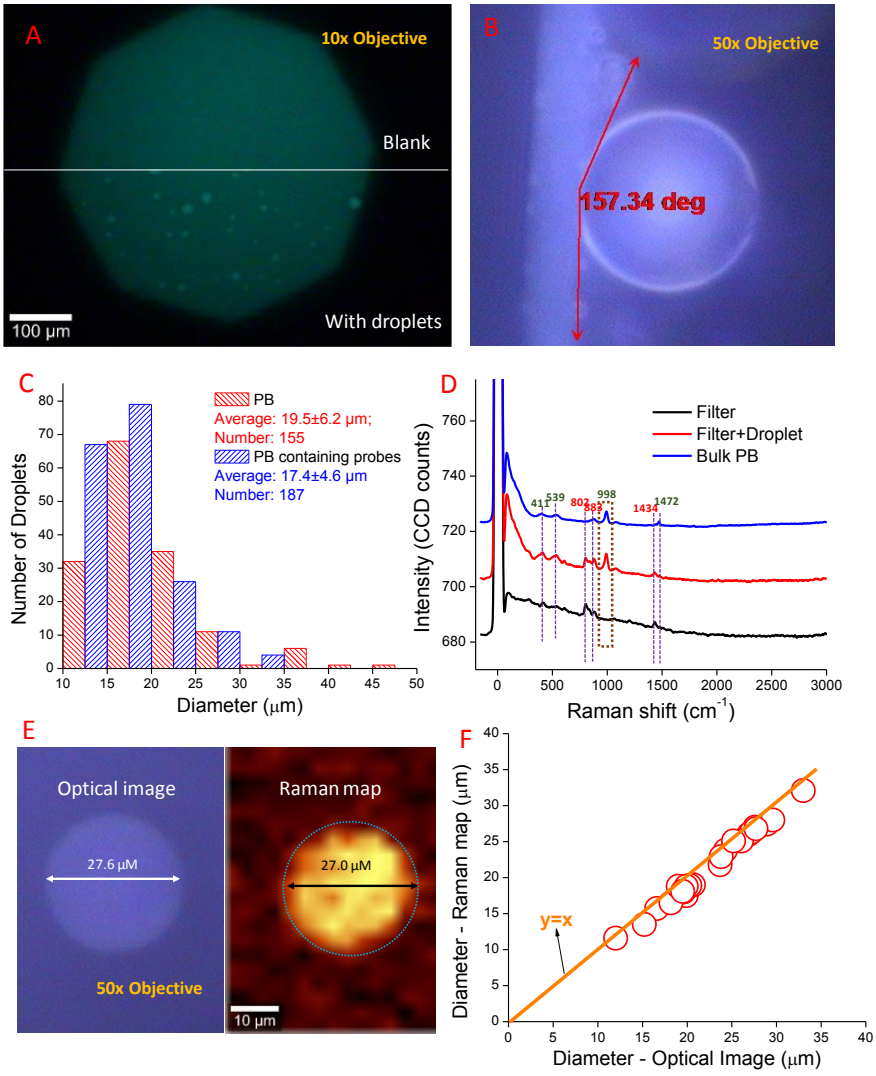

Figure 10.3 Generation, collection, and Raman scan of the aerosol droplets. A) Optical images of a blank superhydrophobic PVDF filter (top) and aerosol droplets collected on a superhydrophobic PVDF filter (bottom); B) The optical image of the side view of a droplet that was used to measure contact angle; C) Size distribution of aerosol droplets generated from 1 M PB solution and 0.6 M PB solution + pH nanoprobes; D) Raman spectra of 1M bulk PB solution, superhydrophobic PVDF filter, and 1M PB aerosol droplet on a superhydrophobic PVDF filter; E) Optical image and Raman map of a droplet generated from 1 M PB solution constructed by tracking the Raman band at 998 cm^{-1}; F) Relationship between droplet diameters measured using Raman maps and optical images.

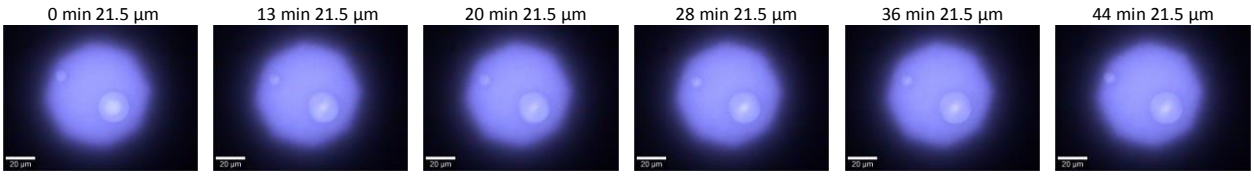

Figure 10.4 Optical images of one microdroplet taken at different time under well controlled RH of 97%.

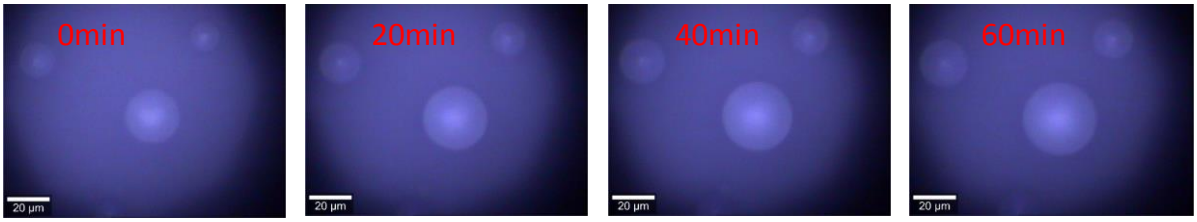

Figure 10.5 Optical images of one microdroplet taken at different time under oversaturated RH caused by the wet paper in the cell.

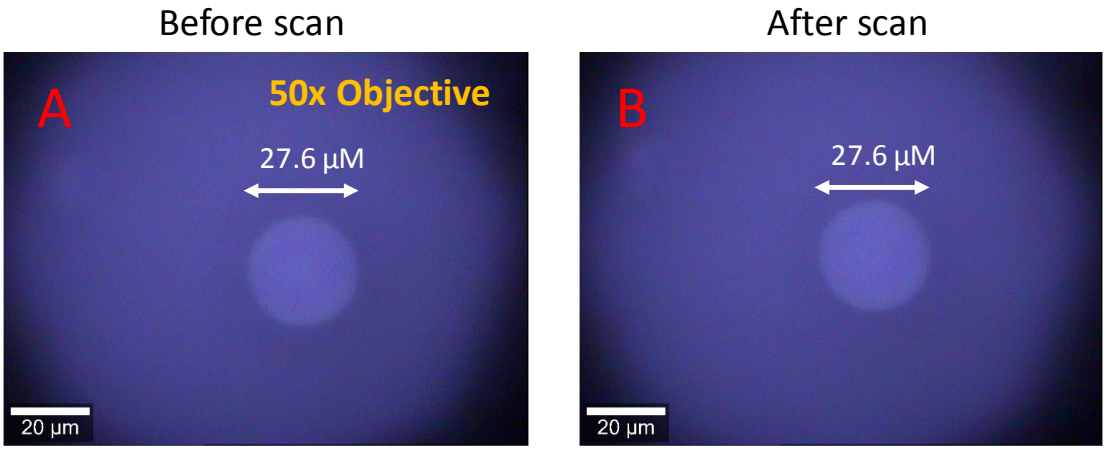

Figure 10.6 Optical images of one aerosol droplet under 50x objective (A) before and (B) after laser interrogation.

Following the successful generation and collection of droplets, we scanned them individually by confocal Raman microscopy using collection areas slightly larger than their respective diameters. As shown in Figure 10.3D, the normal Raman spectrum of a droplet generated from a PB solution without added nanoprobes contains Raman bands for both PB (411, 539, 998, and 1472 cm^{-1}) and the PVDF filter (802, 883, and 1434 cm^{-1}). A Raman map made by tracking the intense band at 998 cm^{-1} (PO_4^{3-} stretch) is shown in Figure 10.3E.[482] The area defined by the

Raman signal is illustrated by the dotted circle. This circle is comparable to the droplet diameter determined from the optical image (27.0 vs 27.6 µm, Figure 10.3E), and the consistency of the signal across the droplet illustrates the uniform distribution of phosphate throughout the droplet. As shown in Figure 10.3F, there is a linear relationship between the droplet diameter determined optically and that obtained by Raman imaging.

10.2.3 The Core pH of a Droplet is Higher Than Bulk pH

In the presence of the pH nanoprobes, the Raman signals arising from either the PB or the PVDF substrates were weak and were overwhelmed by the 4-MBA SERS signal (Figure 10.7). SERS maps of droplets can however be obtained by tracking the benzene ring breathing and axial deformation mode of 4-MBA at 1080 cm^{-1}.[483] As shown in Figure 10.8A, the SERS maps of five different droplets exhibited variable patterns indicating the pH nanoprobes were not as uniformly distributed within each droplet as the phosphate molecules were (Figure 10.3E).

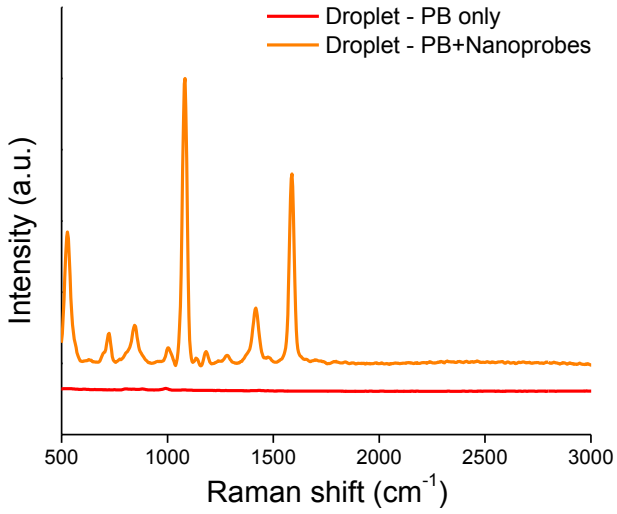

Figure 10.7 Raman spectra collected from aerosol droplets containing only 1 M PB and 0.6 M PB + nanoprobes.

We note that the droplet diameter determined from the SERS signal was consistently smaller than that from the comparable optical images (Figure 10.8B; Figure 10.9). This observation cannot

be a result of the droplet being thicker in the middle and thinner at the edges because the laser focal depth (3.2 μm) was much smaller than the droplet diameter. As shown in Figure 10.10, for a 20-μm droplet, the signals within a SERS map primarily arise from a cylindrical region with a width of 3.2 μm. In our system, the thickness of the laser excitation region should begin to decrease approximately 0.13 μm from the droplet edge (Figure 10.10). This distance is much smaller than the difference between the droplet diameters determined from the SERS signal and the optical image (several microns, Figure 10.9). In addition, the homogeneous signal distribution within the phosphate Raman map (Figure 10.3E) further suggests minimal influence of the change in droplet thickness on the collected Raman signals. These results suggest that the PEG-coated AuNPs preferentially partition towards the droplet centroid and away from the comparatively hydrophobic air/water interface. It was recently suggested that polyvinylpyrrolidone (PVP) coated AgNPs preferentially accumulate at the air/water interface.[484] We tested this hypothesis by synthesizing PVP-coated pH nanoprobes, but determined that these nanoprobes still preferentially partition towards the droplet centroid (Figure 10.11). We are currently working to develop nanoparticle based pH probes that target the air-water interface.

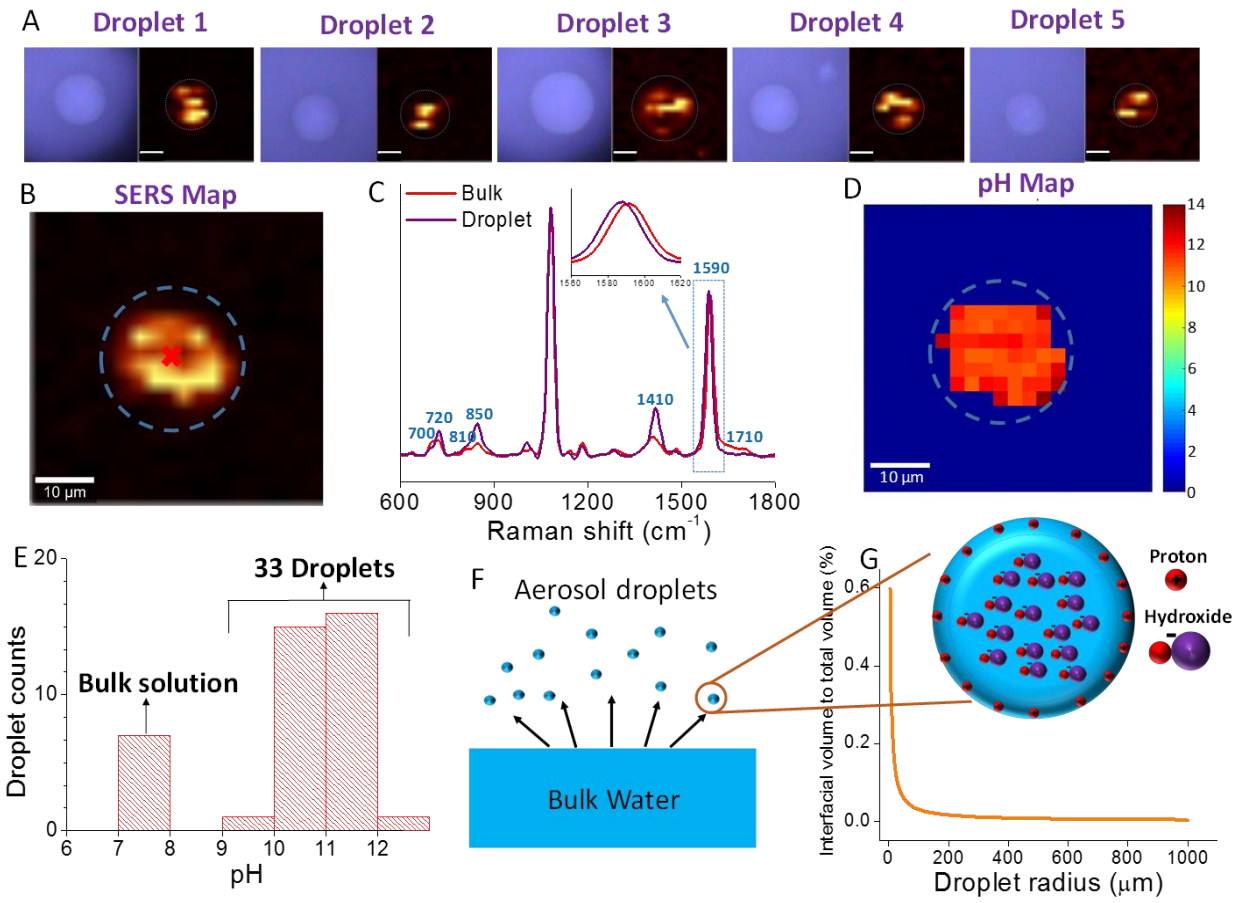

Figure 10.8 2D characterization of the pH inside aerosol droplets. A) Optical images and Raman maps of droplets generated from 0.6 M PB + pH nanoprobes by tracking the 4-MBA Raman band at 1080 cm^{-1}; B) One Raman map of a droplet by tracking the 4-MBA Raman band at 1080 cm^{-1}; the dashed circle is the outline of the droplet; Inset is the optical image of the droplet; The diameter determined by SERS signal is smaller than that determined by optical image (18.8 vs 23.5 μm); C) SERS spectra collected from bulk solution with pH of 7.4 and droplet generated from that bulk solution; D) pH map of the droplet shown in Fig. 3B; E) pH at the centroid of 33 different droplets generated from bulk solutions with pH of 7.4; F) Schematic of the aerosol droplets generated from a bulk solution and the accumulation of protons at air/water interface in aerosol droplets; G) Variation of interfacial volume to total volume of droplets as a function of droplet radius.

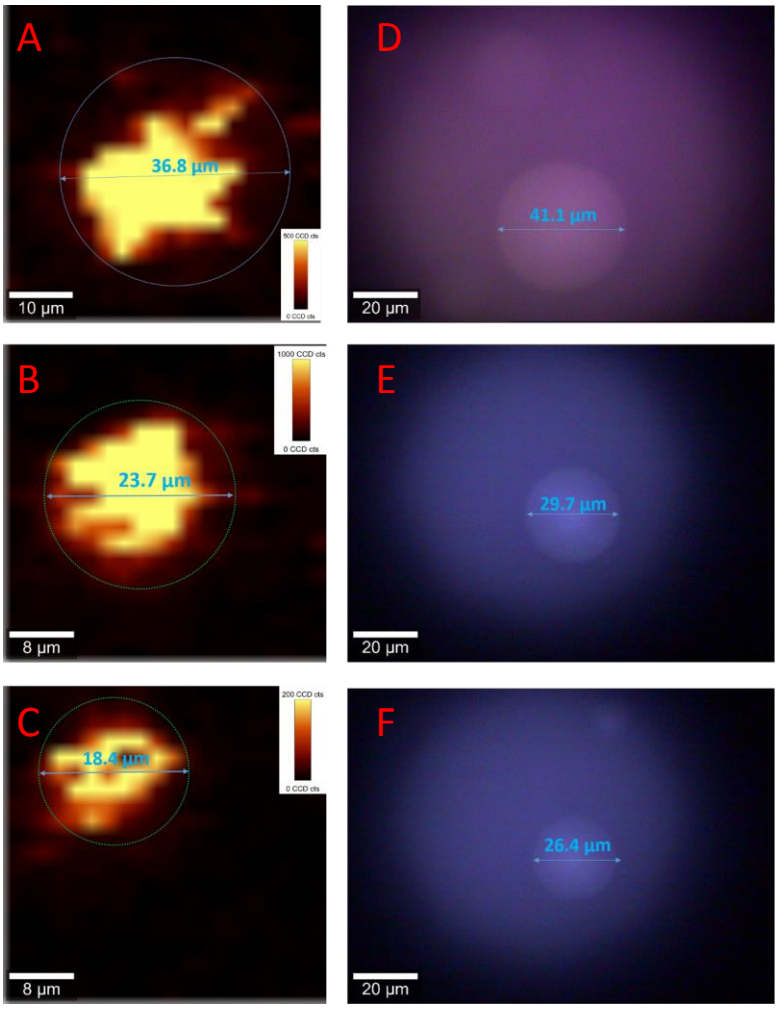

Figure 10.9 A-C) SERS maps tracking 4-MBA band at 1080 cm^{-1} of three droplets; D-F) Optical images of the three droplets.

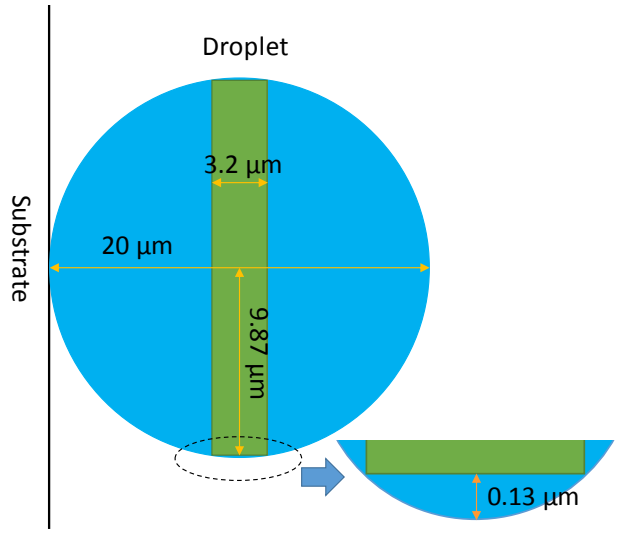

Figure 10.10 Schematic of the laser excited volume of a 20-µm droplet when collecting a 2D SERS map.

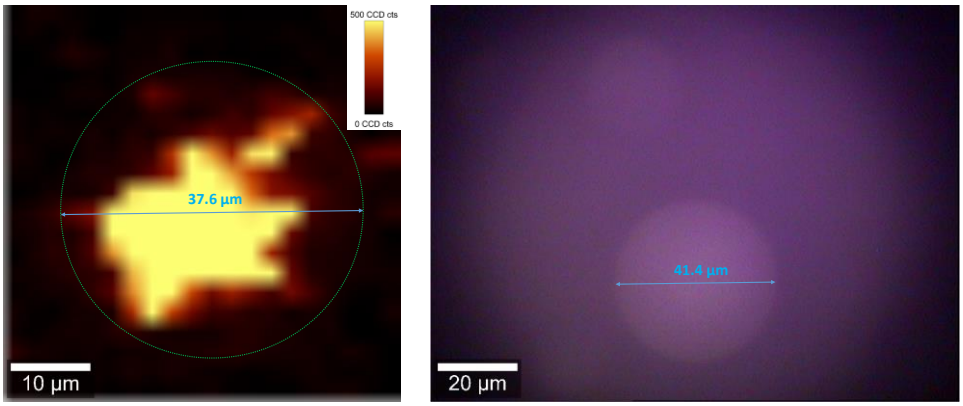

Figure 10.11 SERS map and optical image of droplet containing PVP-coated pH nanoprobes.

A representative SERS spectrum collected from the center of a droplet is shown in Figure 10.8C along with the SERS spectrum for nanoprobes dispersed in bulk PB. As shown, all seven pH indicators suggest that the pH at the droplet centroid was much higher than the bulk solution (pH=7.4) from which the droplet was generated (i.e., the bands at 720, 850, and 1410 cm^{-1} increase in magnitude while the bands at 700, 810, and 1710 cm^{-1} decrease in magnitude and the band at 1590 cm^{-1} shifts to a lower wavenumber). The measured SERS signals were converted into pH values using the calibration curve shown in Figure 10.2 to produce 2D pH maps that reflect the

measured pH distribution within the planar region bisecting the droplet (Figure 10.8D). Interestingly, all of the pixels exhibit pH values higher than the bulk solution pH of 7.4. This same result is illustrated in pH maps collected for 33 individual droplets (Figure 10.12). The measured average pH at the droplet centroid of 33 separate droplets was 11.0±0.49 (Figure 10.8E). This value is 3.6 pH units higher than the initial bulk pH. Control experiments in which the probe concentration was varied by 0.5-2× (our experimentally accessible range) indicate that the measured pH was not affected by the nanoprobe concentration (Figure 10.13). In addition, experiments using a range of initial pH values (2.1-10.7) indicate that the pH at the droplet centroid was consistently higher than the bulk (Figure 10.14).

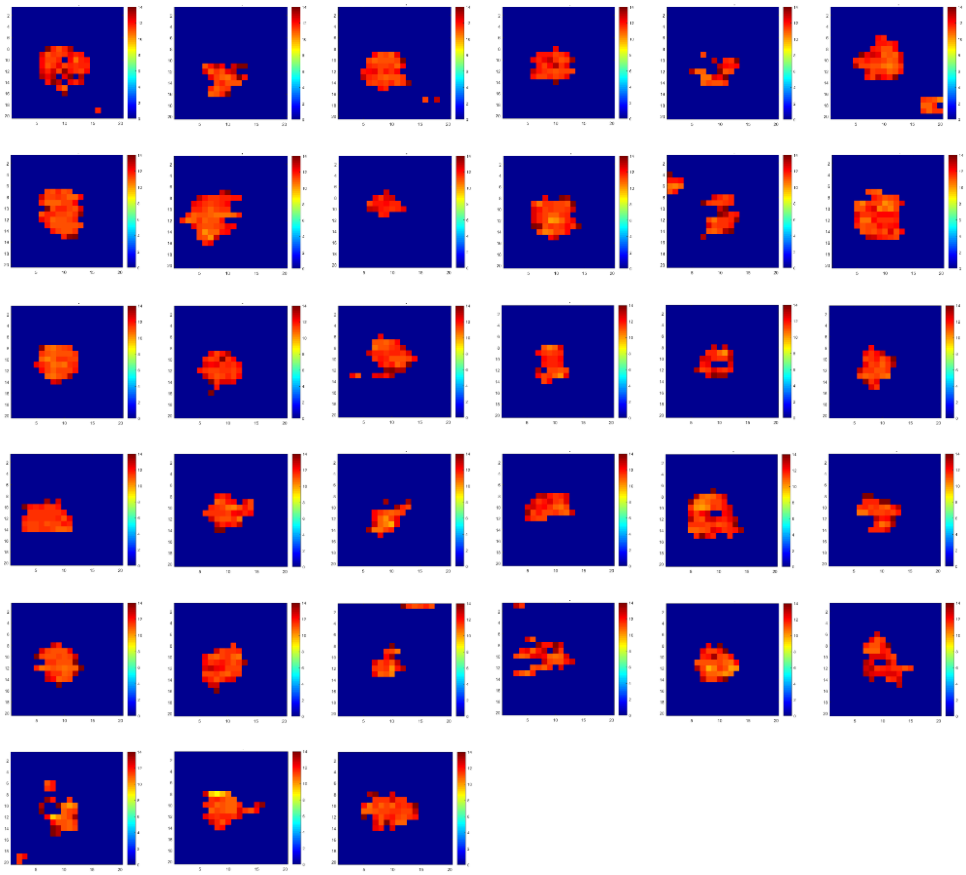

Figure 10.12 pH maps of 33 droplets containing 0.6 M PB and pH nanoprobes.

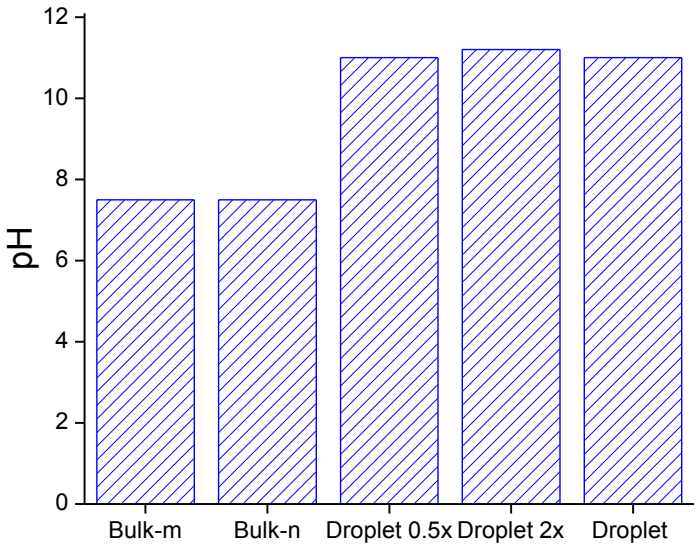

Figure 10.13 pH values at the centroid of droplets containing half and twice probe concentrations. Bulk-m: bulk solution pH measured using commercial pH meter; Bulk-n: bulk solution pH measured using pH nanoprobes; Droplet 0.5×: droplet containing half probe concentration; Droplet 2×: droplet containing twice probe concentration.

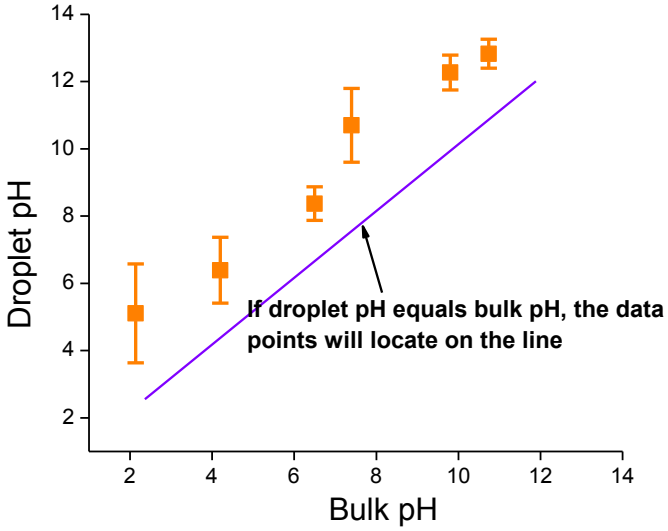

Figure 10.14 pH of droplets (in a petri dish without controlling RH) generated from bulk solution with different pH.

An aerosol droplet should be considered a high surface area object with a substantial portion of its volume in the near vicinity of the air/water interface (Figure 10.8F). The ratio of the interfacial to total volume (Y) as a function of droplet radius (r) can be mathematically expressed as:

$$Y = 1 - \left(\frac{r-a}{r}\right)^3 \qquad \text{Equation 10.1}$$

where *a* is the depth relative to the interface. As shown in Figure 10.8G, *Y* is essentially constant for a droplet radius between 100-1000 μm. However, when the radius is further decreased from 100 to 5 μm, *Y* increases exponentially. For example, in a 1000 μm spherical water droplet ($V_{droplet}$ = 5.2 × 10^{-10} m^3) approximately 0.003% of the total volume is within 10 nm of the surface. This percentage increases to 0.6% for a 10 μm droplet ($V_{droplet}$ = 5.2 × 10^{-16} m^3). The large air/water interfacial volume could lead to a large number of protons residing at this region, leaving a higher pH zone in the droplet interior. We investigated the relationship between droplet diameter and the pH of the centroid and did not find any correlation (Figure 10.15). We attribute this fact to the 1) the limited range of droplet diameters (16-25 μm) investigated; and 2) the uncertainty of the height (*Z*) for the scans. As shown below, *Z* exhibits significant influence on droplet pH.

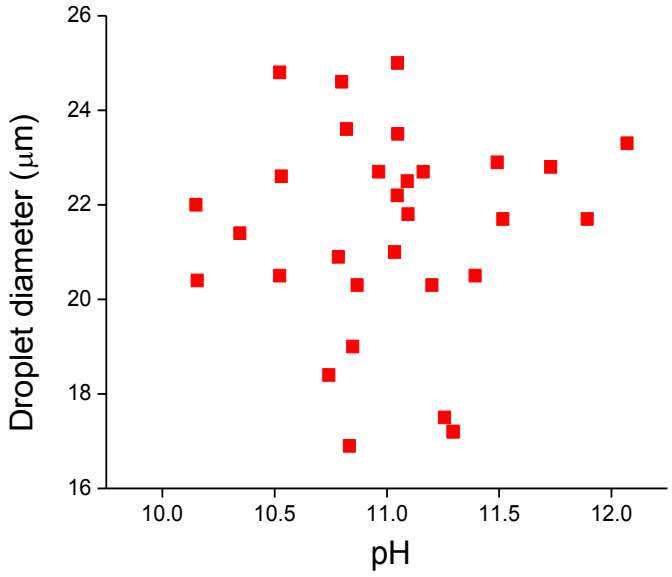

Figure 10.15 pH values at the centroid of 31 droplets as a function of droplet diameter.

10.2.4 3D pH Distribution

2D scans of a microdroplet (Figure 10.8B&D) do not provide information about the pH of the interfacial region. This fact arises from two phenomena: 1) the pH nanoprobes preferentially partition towards the droplet centroid; 2) at the droplet edge the excitation laser is parallel to the air/water interface and thus relatively few photons can be backscattered by the interfacial region and collected by the detector. This second limitation can be partially overcome by 3D droplet scanning.

As illustrated schematically in Figure 10.16A, we systematically varied the *Z* height of the objective both above and below the planar region bisecting the droplet. This approach was first tested by tracking the phosphate band at 998 cm^{-1} for a droplet that did not have nanoprobes added. As shown in Figure 10.17, the maps get smaller and smaller as the *Z* height was increased – thus demonstrating the feasibility of 3D scanning of a microdroplet. Subsequently, 3D scans of a droplet containing nanoprobes were collected. As the objective moved upward, the optical images of a droplet (22 μm) became increasingly blurry (Figure 10.16B). The SERS maps of the droplet exhibit different patterns due to the Brownian motion of the nanoprobes (Figure 10.16C). As shown in Figure 10.16E, the pH at the center of each map generally decreased as the objective moved from 0 to 20 μm. This phenomenon was repeatedly observed for a number of different droplets (Figure 10.18). As the objective moves upward, it gradually approaches the air/water interface. Therefore, the nanoprobes residing there make an increasingly larger contribution to the SERS signals that are collected, leading to the lower pH values. Although the interfacial depth is small (10 nm) compared to the focal depth (3.2 μm), the relative contribution of the interfacial region to the measured signal is expected to be larger than might be expected on a volume basis because of its significantly different nature compared to the bulk.[485, 486] Assuming all the depleted

protons from the non-interfacial volume migrate to the interfacial region, a high proton concentration within the interfacial region could induce the pH decrease illustrated in Figure 10.16E. In addition, when the focal point is above the top of the droplet, the ratio of the interfacial to the total excited volume within the droplet increases, which further increases the contribution of the interfacial region to the detected pH values (Figure 10.19). This observation supports our speculation that the air/water interface can accumulate protons.

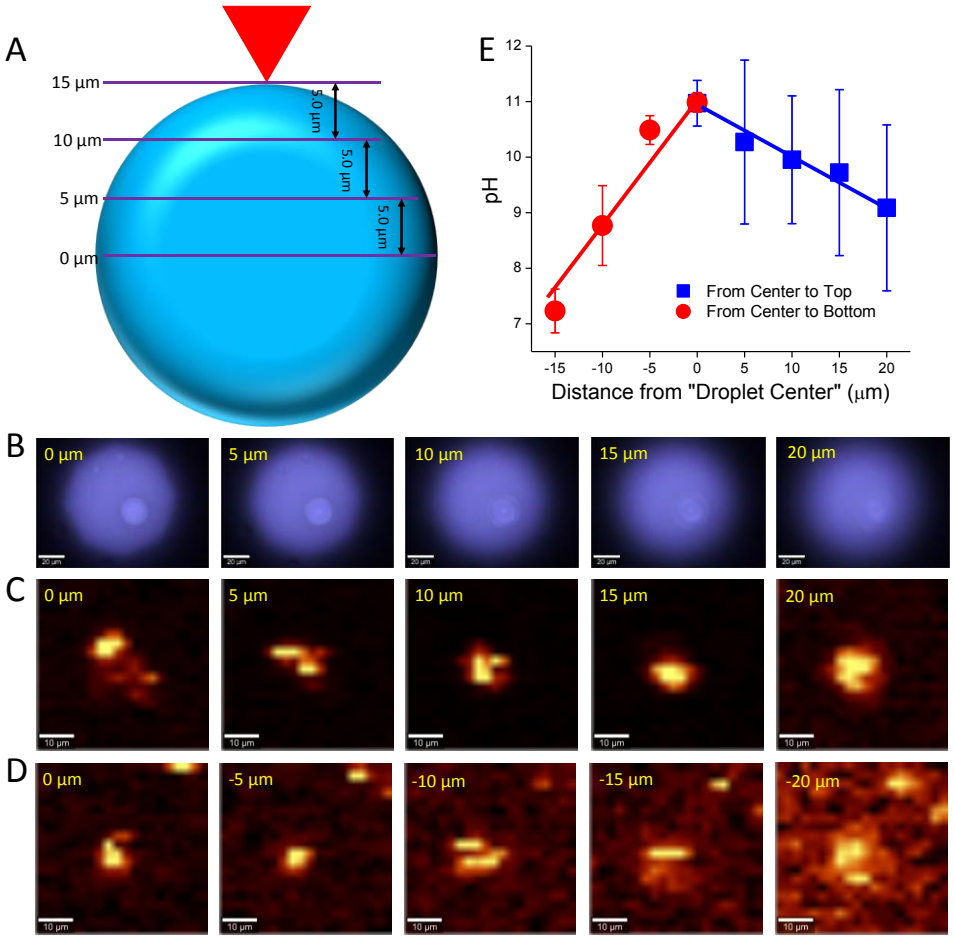

Figure 10.16 3D characterization of the pH inside aerosol droplets. A) Schematic of the 3D scan of the droplet. B) Optical images of droplets containing nanoprobes collected by focusing the light beam at different Z above the middle (0 µm); C) SERS maps of droplets containing nanoprobes collected by focusing the laser beam at different Z above the middle (0 µm); D) SERS maps of droplets containing nanoprobes collected by focusing the laser beam at different Z below the middle (0 µm); E) Variation of pH values at the center of each Raman map as a function of Z.

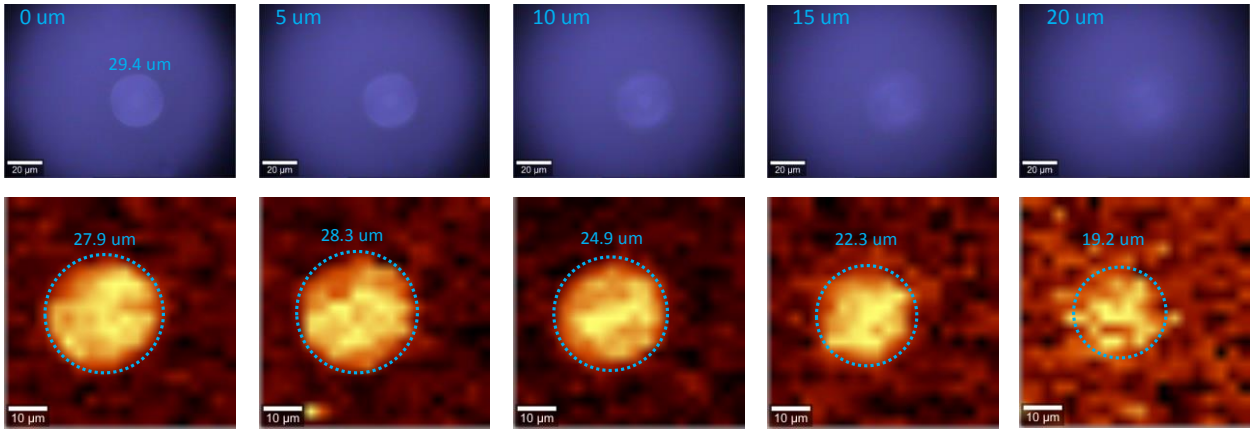

Figure 10.17 Variation of optical images and SERS maps (tracking 998 cm^{-1}) collected from the droplet generated from 1M PB solution as a function of Z.

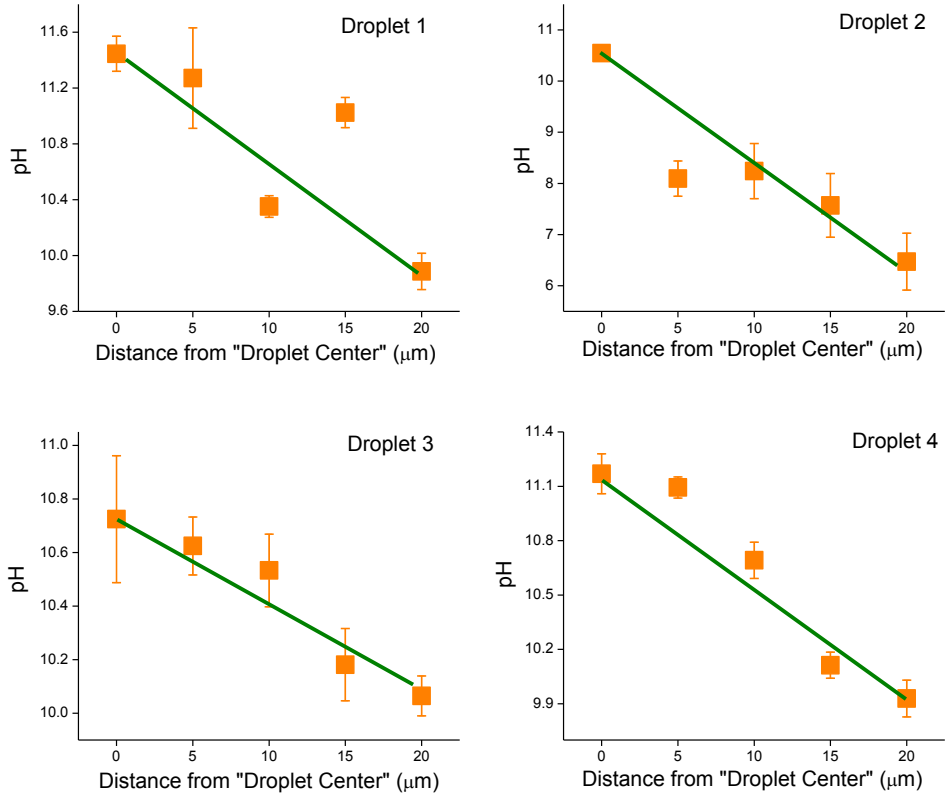

Figure 10.18 Variation of pH at the centroid of Raman maps as the objective is moved upward (Each data point is the average of four pixels within a 5 × 5 μm^2 area at the droplet center with the error bars reflecting the standard deviation of the four pixels).

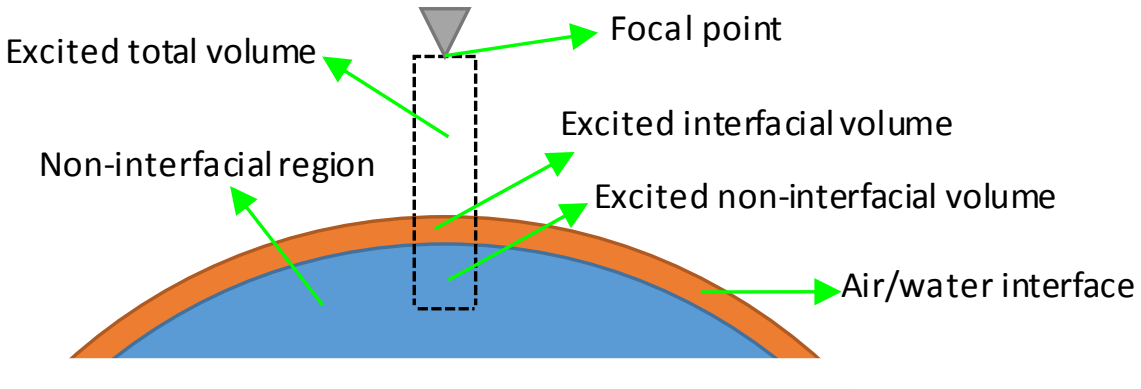

Figure 10.19 Schematic for the laser excited interfacial/non-interfacial volume when the focal point is above the top of the droplet.

To further support our conclusion, the objective was moved downward from 0 μm and Raman scans were conducted at each *Z*. As shown in Figure 10.16D, the contribution of the PVDF substrate to the collected SERS signal gradually increased when the objective was moved towards the droplet bottom. This then results in deteriorating contrast between the SERS signal and the background signal. Meanwhile, the pH values at the center of each Raman map decreased as the objective moved downward (Figure 10.16E). The observed differences in the slopes and the pH values at the extremes possibly reflect interactions between the droplet and the hydrophobic substrate. Nonetheless, in each case, the pH at the core of the droplet is substantially different from that at the droplet edge. Because of the large diffusion coefficient of PO_4^{3-}, HPO_4^{2-}, $H_2PO_4^-$, Na^+, and K^+ ($0.824 - 1.957 \times 10^{-5}$ cm^2/s),[487] the observed pH gradient is unlikely to result from incomplete mixing of the salts in water; rather, the gradient is thermodynamically controlled by the air/water interface.

10.2.5 Confirmation of Alkaline Droplet pH via Alkaline-Catalyzed Reaction

To confirm the SERS results, we conducted experiments with a different pH indicator (4-ATP). It was recently reported that two 4-ATP molecules co-located within a SERS hot spot dimerize to form dimercaptoazobenzene (DMAB) under alkaline conditions (Figure 10.20A).[488, 489] We

therefore expected that 4-ATP dimerization would be detectable in droplets because of the highly basic pH zone within the droplet core. To test this hypothesis, droplets containing 4-ATP-based nanoprobes were scanned. As shown in Figure 10.20B, Raman bands at 1138, 1392, and 1432 cm^{-1} that reflect formation of a -N=N- linkage were detected in randomly selected droplets. Using the DMAB Raman band at 1432 cm^{-1}, we constructed a SERS map of one droplet and observed consistently strong DMAB signals (Figure 10.20C). In the control, no DMAB signals were observed within the SERS map of the bulk solution of the same composition as the droplets (Figure 10.20D).

The LSPR of AuNPs can release heat through Landau damping and dramatically elevate the temperature (up to 465 K) in the nanoscale vicinity of NPs.[490, 491] Halas et al. recently reported that plasmonic nanoparticles with high scattering cross section can localize solar heat within a small volume at the solution surface when the nanoparticle concentration reaches multiple scattering regime.[492] This phenomenon has recently been used to efficiently generate steam without the requirement to boil the entire solution.[490] To exclude the effect of localized heating on this dimerization reaction, bulk solution containing 4-ATP probes was heated in a boiling water bath for 15 min prior to Raman imaging. As shown in Figure 10.20E, no signal for DMAB was observed in this situation indicating it is the pH rather than the temperature that accelerates the dimerization reaction in droplets. These alkaline catalytic reactions occurring in aerosol droplets generated from neutral bulk solution further indicate that the aerosol droplets are indeed basic.

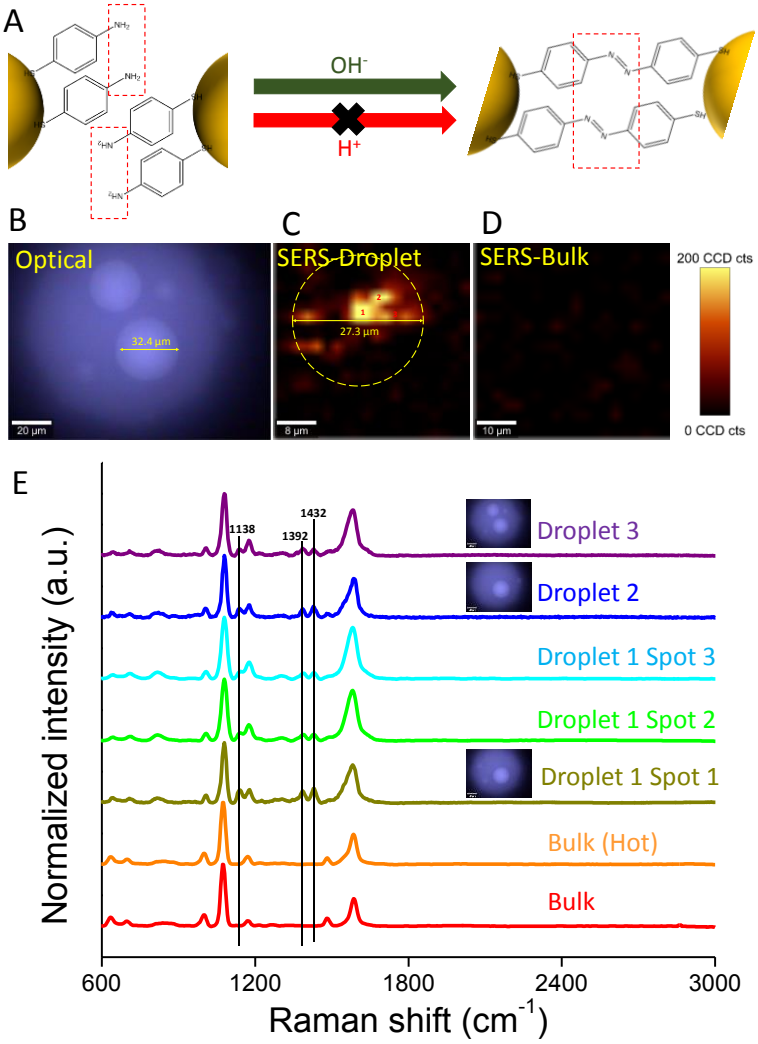

Figure 10.20 Basic-catalyzed reaction occurs in droplets generated from neutral bulk solution. A) Schematic for plasmon-catalyzed 4-ATP dimerization enhanced at alkaline conditions; B) Optical image and SERS map of a droplet containing 0.6 M PB solution + 4-ATP-based nanoprobes; C) SERS map of droplet containing 4-ATP-based probes constructed by tracking the DMAB band at 1432 cm^{-1}; D) SERS map of bulk solution containing the same composition as the droplet constructed by tracking the DMAB band at 1432 cm^{-1}; E) SERS spectra of 4-ATP in different spots within one droplet, different droplets, and bulk solutions at room or elevated temperature.

10.3 Discussion

Aqueous aerosols (droplets) are ubiquitous in the atmosphere and are acknowledged for their profound influence on many local-scale and global biogeochemical processes.[444, 451, 493, 494] In this study, we for the first time provide direct experimental evidence that the non-interfacial region of

aerosol droplets is more basic than the phosphate buffered bulk solution from which they were generated. We attribute this phenomenon to the preferential accumulation of protons within the interfacial region (Figure 10.8F). While the underlying physics and chemistry dictating this behavior are at best only partially understood, two possible explanations are that hydronium preferentially orients such that positively charged protons point towards 'bulk' water, with the electron rich oxygen groups pointing outwards towards the air. Such an orientation is consistent with the apparent negative surface charge of the interface. A second possibility is that localized disruption of the hydrogen-bond network in water stabilizes the Eigencation structure ($H_9O_4^+$) of water at the interface thus leading to enhanced H^+ stability.[465] In contrast to these studies, however, recent theoretical descriptions using the reactive and polarizable LEWIS model of water[495] suggest the air-water interface is enhanced in OH^-.[485, 486] The one overriding conclusion that can be reached from all of these, and many other,[496] conflicting studies is that the pH of the air-water interface is at present poorly understood. We hypothesize that these apparently divergent pH measurements at the air-water interface may be a result of variations in the water chemistry inside the tested aerosol droplets. Such a hypothesis calls for laboratory measurements of droplet pH using advanced *in situ* techniques.[497] Our ongoing studies seek to examine how aqueous and gas-phase chemistry affect the pH gradient inside droplets. We note that the size of droplets studied here is larger than many common aerosol particles due to the instrumental limitation required to observe and scan sub-micron particles. Single droplets of similar size, either levitated[498] or on surfaces[458, 499], have been extensively employed as model targets and have provided useful insights with respect to atmospheric chemistry. However, we must be cautious when extrapolating our conclusions to smaller size particles of different chemical composition.

It has been reported that the rates of many chemical reactions can be accelerated by up to several orders of magnitude in micrometer-sized droplets (microdroplets) generated by electrospray ionization (ESI).[500, 501] The reasons for such uncommon reaction rates are (although not unambiguously known) generally attributed to the unique air-water interfacial properties of the microdroplets such as high surface-to-volume ratio, altered pH, solvation, and reagent molecule orientation at interfacial region, microdroplet jet fission, and large electrostatic pressure.[502] The last two reasons are artifacts intrinsic to the ESI process. In this study, microdroplets were generated by an atomizer that excludes many of the above-mentioned artifacts. Nonetheless, our droplets still exhibit significantly accelerated reaction rates for an alkaline-catalyzed reaction. We argue that the pH gradient inside the microdroplet induced by air-water interface is the primary cause of this phenomenon.

In addition to the phosphate buffer system employed here, the methodology reported in this study has significant potential to be applied for a variety of more environmentally prevalent systems by altering the chemical composition of both the solution and the overlying gas-phase. The approach used in this effort introduces a novel way to probe the pH of individual droplets, and the results showing differences in pH between a bulk solution and micron-scale droplets have important implications not only for atmospheric chemistry, but also for biology and other fields where chemical reactions inside droplets drive processes and reactions.

10.4 Materials and Methods

10.4.1 Materials

4-Mercaptobenzoic acid (4-MBA), 4-aminothiophenol (4-ATP), sodium citrate tribasic dehydrate ($Na_3Citrate{\cdot}2H_2O$), gold chloride trihydrate ($HAuCl_4{\cdot}3H_2O$), polyvinylphenol (PVP, molecular

weight 10000) and 1 M phosphate buffer (PB, $C_T=[H_3PO_4]+[H_2PO_4^-]+[HPO_4^{2-}]+[PO_4^{3-}]=1M$) were purchased from Sigma-Aldrich. The range of buffer capacities (β) of 1M PB solution is 0.013-0.58 for the pH range 7.2 – 12.3, which is calculated based on Eq. 10.2 ($\alpha_0=[H_3PO_4]/C_T$, $\alpha_1=[H_2PO_4^-]/C_T$, $\alpha_2=[HPO_4^{2-}]/C_T$, $\alpha_3=[PO_4^{3-}]/C_T$). Thiolated poly(ethylene) glycol (HS-PEG, 5kDa) was purchased from Nanocs. AEROSIL®R202 (fumed silica treated with polydimethylsiloxane, average particle size: 14 nm) was purchased from Evonik Industries. Polyvinylidene fluoride (PVDF) membrane filters (0.22 μm pore size, 13 mm in diameter) and polytetrafluoroethylene (PTFE) membrane filters (0.1 μm pore size, 13 mm in diameter) were purchased from EMD Millipore.

$$\beta = 2.303([OH^-]+[H^+]+C_T\alpha_0\alpha_1+C_T\alpha_1\alpha_2+C_T\alpha_2\alpha_3) \qquad \text{Equation 10.2}$$

10.4.2 pH Nanoprobe

The synthesis of the SERS pH nanoprobes is described in our prior publication.[275] Briefly, 500 μL 4-MBA ethanol solution (100 μM) was added to 500 μL AuNP suspension (5×10^{10} NPs/mL). Following vortex mixing, the mixture was kept in room temperature for 120 min and subsequently, 100 μL HS-PEG solution (500 μM) was added into the mixture. The mixture was washed by DI water for three times by centrifugation. 4-ATP-coated AuNPs were synthesized by adding 10 μL 4-ATP in ethanol (1 mM) into 500 μL AuNP suspension followed by 1 min vortex mixing. PVP-coated nanoprobes were synthesized as the following procedure: 500 μL of AuNP suspension and 500 μL of 100 μM 4-MBA ethanol solution are mixed together in a centrifuge tube and vortex for 1 min. After 30 min reaction at room temperature, 100 μL of 500 mM PVP aqueous solution was added. After 1 h reaction at room temperature, the mixture was washed by centrifugation with the same condition as PEG-coated probes.[275]

10.4.3 Generation and Collection of Aerosol Droplets

The method to generate and collect aerosol droplets is illustrated in Figure 10.1A. In these experiments, 2 mL of probe suspension was added to 3 mL of 1 M PB solution followed by gently mixing. Aerosol droplets were generated by aerosolizing this suspension with a commercial atomizer (TSI 3076, TSI Inc.) that was contained in a custom chamber designed to maintain RH near 100% (Figure 10.21). Aerosolized droplets were collected on a superhydrophobic filter placed ~1 cm away from the atomizer outlet. The superhydrophobic filter was produced by drop coating 100 µL of AEROSIL in acetone suspension (4 g/L) onto a PVDF filter that was then air dried. Once the aerosolized droplets were collected, the superhydrophobic filter was sealed in a flow cell that is connected to an automatic humidity controller (Figure 10.22). Humid air with a relative humidity (RH) of 97±0.5% is generated by the humidity controller and flows through the flow cell to maintain a nearly saturated RH inside the cell. The flow cell was then placed on the sample stage of the Raman spectrometer for analysis.

Figure 10.21 Photo of the commercial atomizer contained in a homemade humidity chamber.

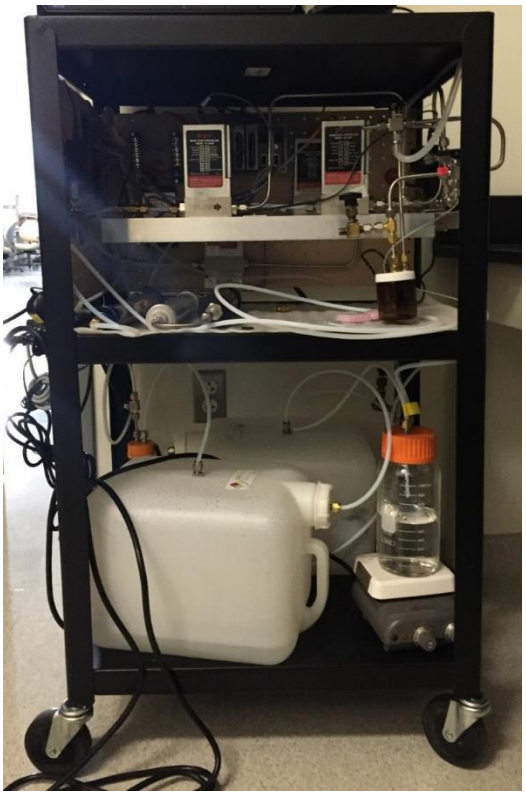

Figure 10.22 The photo of the homemade humidity controller.

10.4.4 Instrumentation

Single aerosol droplets were scanned by a confocal Raman microscope using a 50× objective (WITec Alpha 500R) and a 785 nm laser. Laser spot size limits the spatial resolution of SERS measurement. In this study, the lateral size of the laser spot is 0.68 μm, the axial size of the laser spot is 3.2 μm, and the excitation volume is 1.5 μm^3. Raman scanning is enabled by a motorized scanning table with a lateral (*X*-*Y*) travel range of 150 × 100 mm and depth (*Z*) travel range of 30 mm with a minimum step size of 0.01 μm. Each collected SERS map consists of 20 × 20 pixels and corresponds to a square area slightly larger than the droplet size. Each pixel represents a single Raman spectrum collected with an integration time of 0.1 s. Bulk solution (0.6 mL) is sealed in a quartz cell (Starna Cells Inc.). The laser is focused at 200 μm below the cell lid and Raman scan is performed with the same parameters as those for the droplets.

Chapter 11 Perspectives

As described in this dissertation, we have made significant progress in improving the sensitivity (AuNP/BC substrate), reproducibility ("hot spot"-normalized SERS), and applicability (pH-triggered approach) of SERS for environmental analysis. In addition, we have shown the possibility to use SERS to detect the pH in confined aqueous environments, e.g. aerosol droplets. These results collectively show that SERS is highly promising for aqueous pollutant detection due to its intrinsically high sensitivity. However, two main challenges still need to overcome before its real practical application:

1) **Affinity between pollutant and plasmonic nanoparticle**. The limiting factor for pollutant SERS detection is usually not the sensitivity of the SERS substrates, but the affinity (or lack thereof) between the pollutant and nanoparticle surface. In this effort, I have developed a pH-triggered approach to improve the electrostatic attraction between organic amines and cit-AuNP surface thus achieving SERS quantitation. However, for the other types of environmental pollutants, it is still necessary to find a facile way to "put" the pollutant onto the nanoparticle surface, especially within "hot spots". Proper functionalization of the nanoparticle surface according to the chemical structure of the pollutant is one feasible way to achieve this goal.
2) **Reproducibility**. The novel "hot spot"-normalized SERS developed herein has largely solved this problem. However, the fundamental aspects of this technique require more research. First, why are maps tracking the intensity of the band at 0 cm^{-1} complementary with that tracking the intensity of the band at 126 cm^{-1} (ASE)? How does the SERS background influence the normalization results? How is the "hot spot" density quantitatively correlated with ASE band intensity? To answer these questions, experiments

with highly uniform substrates are required. Single particle (cluster) SERS experiments will also be helpful.

SERS is a promising tool for studying aerosol and droplet chemistry. In my opinion, the following aspects are worth additonal research:

1) **Development of nanoprobes for different purposes**. For example, hydrophobic nanoprobes may be interesting for detecting the pH directly at the air/water interface of the aerosol droplets. To study specific atmospheric reactions occurring in aerosols, nanoprobes with specificity to a particular reactant/product (e.g., hydroxyl radicals) are required.
2) **Influence of chemical composition on pH gradient in aerosol droplets**. The partitioning of different inorganic ions (e.g. PO_4^{3-}, NH_4^+) at the air/water interface may influence the partitioning of protons and thus the pH gradient inside the droplet. Therefore, scanning droplets with various chemical compositions is needed and the mechanism for the changing pH gradient identified herein should be investigated in detail.
3) **Influence of atmospheric compositions on droplet pH**. Changing atmospheric compositions, such as the concentration of SO_2, CO_2, and NH_3 may exert significant influence on pH or other reactions inside aerosol droplets. Therefore, scanning of the droplets with different chemical compositions should be collected when different reactive gases (SO_2, CO_2, and NH_3) flow through the cell where the droplets are located. Information about the kinetics of varying pH or reaction pathways may be acquired. To improve the quantitation performance, "hot spot" normalized SERS will probably need to be used.

Reference

1. Dai, A., Increasing drought under global warming in observations and models. *Nature Climate Change* **2013,** *3*, (1), 52-58.

2. Barlow, M., *Blue covenant: the global water crisis and the coming battle for the right to water*. McClelland & Stewart: 2009.

3. Vörösmarty, C. J.; Green, P.; Salisbury, J.; Lammers, R. B., Global water resources: vulnerability from climate change and population growth. *science* **2000,** *289*, (5477), 284-288.

4. Wauchope, R., The pesticide content of surface water draining from agricultural fields—a review. *Journal of environmental quality* **1978,** *7*, (4), 459-472.

5. Stackelberg, P. E.; Furlong, E. T.; Meyer, M. T.; Zaugg, S. D.; Henderson, A. K.; Reissman, D. B., Persistence of pharmaceutical compounds and other organic wastewater contaminants in a conventional drinking-water-treatment plant. *Science of the total environment* **2004,** *329*, (1), 99-113.

6. Kolpin, D. W.; Furlong, E. T.; Meyer, M. T.; Thurman, E. M.; Zaugg, S. D.; Barber, L. B.; Buxton, H. T., Pharmaceuticals, hormones, and other organic wastewater contaminants in US streams, 1999− 2000: A national reconnaissance. *Environmental science & technology* **2002,** *36*, (6), 1202-1211.

7. Bellinger, D. C., Lead contamination in Flint—an abject failure to protect public health. *New England Journal of Medicine* **2016,** *374*, (12), 1101-1103.

8. Hanna-Attisha, M.; LaChance, J.; Sadler, R. C.; Champney Schnepp, A., Elevated blood lead levels in children associated with the Flint drinking water crisis: a spatial analysis of risk and public health response. *American journal of public health* **2016,** *106*, (2), 283-290.

9. Hansen, K. M.; Spiliotopoulou, A.; Chhetri, R. K.; Casas, M. E.; Bester, K.; Andersen, H. R., Ozonation for source treatment of pharmaceuticals in hospital wastewater–Ozone lifetime and required ozone dose. *Chemical Engineering Journal* **2016,** *290*, 507-514.

10. Beristain-Montiel, E.; Villalobos-Pietrini, R.; Arias-Loaiza, G.; Gómez-Arroyo, S.; Amador-Muñoz, O., An innovative ultrasound assisted extraction micro-scale cell combined with gas chromatography/mass spectrometry in negative chemical ionization to determine persistent organic pollutants in air particulate matter. *Journal of Chromatography A* **2016,** *1477*, 100-107.

11. Colthup, N., *Introduction to infrared and Raman spectroscopy*. Elsevier: 2012.

12. Baker, A., Fluorescence properties of some farm wastes: implications for water quality monitoring. *Water Research* **2002,** *36*, (1), 189-195.

13. Eisenthal, K., Liquid interfaces probed by second-harmonic and sum-frequency spectroscopy. *Chemical Reviews* **1996,** *96*, (4), 1343-1360.

14. Michel, K.; Bureau, B.; Boussard-Plédel, C.; Jouan, T.; Adam, J.; Staubmann, K.; Baumann, T., Monitoring of pollutant in waste water by infrared spectroscopy using chalcogenide glass optical fibers. *Sensors and Actuators B: Chemical* **2004,** *101*, (1), 252-259.

15. Henderson, R. K.; Baker, A.; Murphy, K.; Hambly, A.; Stuetz, R.; Khan, S., Fluorescence as a potential monitoring tool for recycled water systems: a review. *Water research* **2009,** *43*, (4), 863-881.

16. Li, D.-W.; Zhai, W.-L.; Li, Y.-T.; Long, Y.-T., Recent progress in surface enhanced Raman spectroscopy for the detection of environmental pollutants. *Microchimica Acta* **2014,** *181*, (1-2), 23-43.

17. Kneipp, K.; Kneipp, H.; Itzkan, I.; Dasari, R. R.; Feld, M. S., Ultrasensitive chemical analysis by Raman spectroscopy. *Chemical reviews* **1999,** *99*, (10), 2957-2976.

18. Jarvis, R. M.; Goodacre, R., Discrimination of bacteria using surface-enhanced Raman spectroscopy. *Anal. Chem.* **2004,** *76*, (1), 40-47.

19. Jeanmaire, D. L.; Van Duyne, R. P., Surface Raman spectroelectrochemistry: Part I. Heterocyclic, aromatic, and aliphatic amines adsorbed on the anodized silver electrode. *Journal of Electroanalytical Chemistry and Interfacial Electrochemistry* **1977,** *84*, (1), 1-20.

20. Fleischmann, M.; Hendra, P. J.; McQuillan, A. J., Raman spectra of pyridine adsorbed at a silver electrode. *Chemical Physics Letters* **1974,** *26*, (2), 163-166.

21. Schlücker, S., Surface-Enhanced raman spectroscopy: Concepts and chemical applications. *Angew. Chem. Int. Ed.* **2014,** *53*, (19), 4756-4795.

22. Haynes, C. L.; McFarland, A. D.; Duyne, R. P. V., Surface-enhanced Raman spectroscopy. In ACS Publications: 2005.

23. Kneipp, K.; Kneipp, H.; Kneipp, J., Surface-enhanced Raman scattering in local optical fields of silver and gold nanoaggregates from single-molecule Raman spectroscopy to ultrasensitive probing in live cells. *Accounts of chemical research* **2006,** *39*, (7), 443-450.

24. Kneipp, K.; Wang, Y.; Kneipp, H.; Perelman, L. T.; Itzkan, I.; Dasari, R. R.; Feld, M. S., Single molecule detection using surface-enhanced Raman scattering (SERS). *Phys. Rev. Lett.* **1997,** *78*, (9), 1667.

25. Nie, S.; Emory, S. R., Probing single molecules and single nanoparticles by surface-enhanced Raman scattering. *science* **1997,** *275*, (5303), 1102-1106.

26. Wei, H.; Abtahi, S. M. H.; Vikesland, P. J., Plasmonic colorimetric and SERS sensors for environmental analysis. *Environmental Science: Nano* **2015,** *2*, (2), 120-135.

27. Orendorff, C. J.; Gole, A.; Sau, T. K.; Murphy, C. J., Surface-enhanced Raman spectroscopy of self-assembled monolayers: sandwich architecture and nanoparticle shape dependence. *Anal. Chem.* **2005,** *77*, (10), 3261-3266.

28. Yu, Q.; Guan, P.; Qin, D.; Golden, G.; Wallace, P. M., Inverted size-dependence of surface-enhanced Raman scattering on gold nanohole and nanodisk arrays. *Nano letters* **2008,** *8*, (7), 1923-1928.

29. Wei, H.; Vikesland, P. J., pH-triggered molecular alignment for reproducible SERS detection via an AuNP/nanocellulose platform. *Scientific reports* **2015,** *5*, srep18131.

30. Contreras-Cáceres, R.; Abalde-Cela, S.; Guardia-Girós, P.; Fernández-Barbero, A.; Pérez-Juste, J.; Alvarez-Puebla, R. A.; Liz-Marzán, L. M., Multifunctional microgel magnetic/optical traps for SERS ultradetection. *Langmuir* **2011,** *27*, (8), 4520-4525.

31. Alvarez-Puebla, R. A.; Liz-Marzan, L. M., Traps and cages for universal SERS detection. *Chemical Society Reviews* **2012,** *41*, (1), 43-51.

32. Oh, Y. J.; Jeong, K. H., Glass Nanopillar Arrays with Nanogap-Rich Silver Nanoislands for Highly Intense Surface Enhanced Raman Scattering. *Advanced Materials* **2012,** *24*, (17), 2234-2237.

33. Cho, W. J.; Kim, Y.; Kim, J. K., Ultrahigh-density array of silver nanoclusters for SERS substrate with high sensitivity and excellent reproducibility. *ACS nano* **2011,** *6*, (1), 249-255.

34. Tripp, R. A.; Dluhy, R. A.; Zhao, Y., Novel nanostructures for SERS biosensing. *Nano Today* **2008,** *3*, (3), 31-37.

35. Subaihi, A.; Xu, Y.; Muhamadali, H.; Mutter, S.; Blanch, E. W.; Ellis, D. I.; Goodacre, R., Towards improved quantitative analysis using surface-enhanced Raman scattering incorporating internal isotope labelling. *Analytical Methods* **2017**.

36. Shen, W.; Lin, X.; Jiang, C.; Li, C.; Lin, H.; Huang, J.; Wang, S.; Liu, G.; Yan, X.; Zhong, Q., Reliable quantitative SERS analysis facilitated by core–shell nanoparticles with embedded internal standards. *Angew. Chem. Int. Ed.* **2015,** *54*, (25), 7308-7312.

37. Zhang, D.; Xie, Y.; Deb, S. K.; Davison, V. J.; Ben-Amotz, D., Isotope edited internal standard method for quantitative surface-enhanced Raman spectroscopy. *Anal. Chem.* **2005,** *77*, (11), 3563-3569.

38. Manuel, J., Crisis and emergency risk communication: lessons from the Elk River spill. *Environmental health perspectives* **2014,** *122*, (8), A214.

39. Fitzpatrick, C., US: Toledo without water as blue-green algae bloom surrounds water intake. **2014**.

40. Mac Kenzie, W. R.; Hoxie, N. J.; Proctor, M. E.; Gradus, M. S.; Blair, K. A.; Peterson, D. E.; Kazmierczak, J. J.; Addiss, D. G.; Fox, K. R.; Rose, J. B., A massive outbreak in Milwaukee of Cryptosporidium infection transmitted through the public water supply. *New England journal of medicine* **1994,** *331*, (3), 161-167.

41. Widerström, M.; Schönning, C.; Lilja, M.; Lebbad, M.; Ljung, T.; Allestam, G.; Ferm, M.; Björkholm, B.; Hansen, A.; Hiltula, J., Large Outbreak of Cryptosporidium hominis Infection Transmitted through the Public Water Supply, Sweden. *Emerging infectious diseases* **2014,** *20*, (4), 581.

42. van Alphen, L. B.; Dorléans, F.; Schultz, A. C.; Fonager, J.; Ethelberg, S.; Dalgaard, C.; Adelhardt, M.; Engberg, J. H.; Fischer, T. K.; Lassen, S. G., The Application of New Molecular Methods in the Investigation of a Waterborne Outbreak of Norovirus in Denmark, 2012. *PloS one* **2014,** *9*, (9), e105053.

43. Abbott, A.; Pearson, H., Fear of human pandemic grows as bird flu sweeps through Asia. *Nature* **2004,** *427*, (6974), 472-473.

44. Karasek, F.; Hutzinger, O., Dioxin danger from garbage incineration. *Analytical chemistry* **1986,** *58*, (6), 633A-642A.

45. Haes, A. J.; Haynes, C. L.; McFarland, A. D.; Schatz, G. C.; Van Duyne, R. P.; Zou, S., Plasmonic materials for surface-enhanced sensing and spectroscopy. *Mrs Bulletin* **2005,** *30*, (05), 368-375.

46. Haes, A. J.; Van Duyne, R. P., A unified view of propagating and localized surface plasmon resonance biosensors. *Analytical and Bioanalytical Chemistry* **2004,** *379*, (7-8), 920-930.

47. Link, S.; El-Sayed, M. A., Spectral properties and relaxation dynamics of surface plasmon electronic oscillations in gold and silver nanodots and nanorods. *The Journal of Physical Chemistry B* **1999,** *103*, (40), 8410-8426.

48. Sepúlveda, B.; Angelomé, P. C.; Lechuga, L. M.; Liz-Marzán, L. M., LSPR-based nanobiosensors. *Nano Today* **2009,** *4*, (3), 244-251.

49. Mock, J.; Barbic, M.; Smith, D.; Schultz, D.; Schultz, S., Shape effects in plasmon resonance of individual colloidal silver nanoparticles. *The Journal of Chemical Physics* **2002,** *116*, (15), 6755-6759.

50. Haynes, C. L.; Van Duyne, R. P., Nanosphere lithography: a versatile nanofabrication tool for studies of size-dependent nanoparticle optics. *The Journal of Physical Chemistry B* **2001,** *105*, (24), 5599-5611.

51. Daniel, W. L.; Han, M. S.; Lee, J.-S.; Mirkin, C. A., Colorimetric nitrite and nitrate detection with gold nanoparticle probes and kinetic end points. *J. Am. Chem. Soc.* **2009,** *131*, (18), 6362-6363.

52. Xia, F.; Zuo, X.; Yang, R.; Xiao, Y.; Kang, D.; Vallée-Bélisle, A.; Gong, X.; Yuen, J. D.; Hsu, B. B.; Heeger, A. J., Colorimetric detection of DNA, small molecules, proteins, and ions using unmodified gold nanoparticles and conjugated polyelectrolytes. *Proceedings of the National Academy of Sciences* **2010,** *107*, (24), 10837-10841.

53. Du, J.; Zhu, B.; Chen, X., Urine for Plasmonic Nanoparticle-Based Colorimetric Detection of Mercury Ion. *Small* **2013,** *9*, (24), 4104-4111.

54. Schatz, G. C.; Young, M. A.; Van Duyne, R. P., Electromagnetic mechanism of SERS. In *Surface-enhanced Raman scattering*, Springer: 2006; pp 19-45.

55. Haynes, C. L.; McFarland, A. D.; Duyne, R. P. V., Surface-enhanced Raman spectroscopy. *Analytical Chemistry* **2005,** *77*, (17), 338 A-346 A.

56. Liu, H.; Zhang, L.; Lang, X.; Yamaguchi, Y.; Iwasaki, H.; Inouye, Y.; Xue, Q.; Chen, M., Single molecule detection from a large-scale SERS-active Au79Ag21 substrate. *Scientific reports* **2011,** *1*.

57. Kneipp, J.; Kneipp, H.; Kneipp, K., SERS—a single-molecule and nanoscale tool for bioanalytics. *Chemical Society Reviews* **2008,** *37*, (5), 1052-1060.

58. Podstawka, E.; Ozaki, Y.; Proniewicz, L. M., Part III: Surface-enhanced Raman scattering of amino acids and their homodipeptide monolayers deposited onto colloidal gold surface. *Applied spectroscopy* **2005,** *59*, (12), 1516-1526.

59. Costa, J. C.; Ando, R. A.; Camargo, P. H.; Corio, P., Understanding the effect of adsorption geometry over substrate selectivity in the surface-enhanced Raman scattering spectra of simazine and atrazine. *The Journal of Physical Chemistry C* **2011,** *115*, (10), 4184-4190.

60. Abu Hatab, N. A.; Oran, J. M.; Sepaniak, M. J., Surface-enhanced Raman spectroscopy substrates created via electron beam lithography and nanotransfer printing. *Acs Nano* **2008,** *2*, (2), 377-385.

61. Tan, R.; Agarwal, A.; Balasubramanian, N.; Kwong, D.; Jiang, Y.; Widjaja, E.; Garland, M., 3D arrays of SERS substrate for ultrasensitive molecular detection. *Sensors and Actuators A: Physical* **2007,** *139*, (1), 36-41.

62. Campion, A.; Kambhampati, P., Surface-enhanced Raman scattering. *Chem. Soc. Rev.* **1998,** *27*, (4), 241-250.

63. Porter, M. D.; Lipert, R. J.; Siperko, L. M.; Wang, G.; Narayanan, R., SERS as a bioassay platform: fundamentals, design, and applications. *Chemical Society Reviews* **2008,** *37*, (5), 1001-1011.

64. Wang, Y.; Yan, B.; Chen, L., SERS tags: novel optical nanoprobes for bioanalysis. *Chemical reviews* **2012,** *113*, (3), 1391-1428.

65. Vendrell, M.; Maiti, K. K.; Dhaliwal, K.; Chang, Y.-T., Surface-enhanced Raman scattering in cancer detection and imaging. *Trends in biotechnology* **2013,** *31*, (4), 249-257.

66. Luo, S.-C.; Sivashanmugan, K.; Liao, J.-D.; Yao, C.-K.; Peng, H.-C., Nanofabricated SERS-active substrates for single-molecule to virus detection< i> in vitro</i>: A review. *Biosensors and Bioelectronics* **2014,** *61*, 232-240.

67. Halvorson, R. A.; Vikesland, P. J., Surface-enhanced Raman spectroscopy (SERS) for environmental analyses. *Environmental science & technology* **2010,** *44*, (20), 7749-7755.

68. Sharma, B.; Frontiera, R. R.; Henry, A.-I.; Ringe, E.; Van Duyne, R. P., SERS: materials, applications, and the future. *Materials today* **2012,** *15*, (1), 16-25.

69. Liu, D.; Wang, Z.; Jiang, X., Gold nanoparticles for the colorimetric and fluorescent detection of ions and small organic molecules. *Nanoscale* **2011,** *3*, (4), 1421-1433.

70. Zhao, W.; Brook, M. A.; Li, Y., Design of Gold Nanoparticle-Based Colorimetric Biosensing Assays. *ChemBioChem* **2008,** *9*, (15), 2363-2371.

71. Vilela, D.; González, M. C.; Escarpa, A., Sensing colorimetric approaches based on gold and silver nanoparticles aggregation: chemical creativity behind the assay. A review. *Anal. Chim. Acta* **2012,** *751*, 24-43.

72. Su, S.; Wu, W.; Gao, J.; Lu, J.; Fan, C., Nanomaterials-based sensors for applications in environmental monitoring. *Journal of Materials Chemistry* **2012,** *22*, (35), 18101-18110.

73. Alvarez-Puebla, R.; Liz-Marzan, L., Environmental applications of plasmon assisted Raman scattering. *Energy & Environmental Science* **2010,** *3*, (8), 1011-1017.

74. Masciangioli, T.; Zhang, W.-X., Peer Reviewed: Environmental technologies at the nanoscale. *Environmental Science & Technology* **2003,** *37*, (5), 102A-108A.

75. Wang, C.; Yu, C., Detection of chemical pollutants in water using gold nanoparticles as sensors: a review. *Rev. Anal. Chem* **2013,** *32*, (1), 1-14.

76. Wang, L.; Ma, W.; Xu, L.; Chen, W.; Zhu, Y.; Xu, C.; Kotov, N. A., Nanoparticle-based environmental sensors. *Materials Science and Engineering: R: Reports* **2010,** *70*, (3), 265-274.

77. Vikesland, P. J.; Wigginton, K. R., Nanomaterial enabled biosensors for pathogen monitoring-a review. *Environmental science & technology* **2010,** *44*, (10), 3656-3669.

78. Szunerits, S.; Boukherroub, R., Sensing using localised surface plasmon resonance sensors. *Chemical Communications* **2012,** *48*, (72), 8999-9010.

79. Anker, J. N.; Hall, W. P.; Lyandres, O.; Shah, N. C.; Zhao, J.; Van Duyne, R. P., Biosensing with plasmonic nanosensors. *Nature materials* **2008,** *7*, (6), 442-453.

80. Homola, J., Surface plasmon resonance sensors for detection of chemical and biological species. *Chemical reviews* **2008,** *108*, (2), 462-493.

81. Alvarez-Puebla, R. A.; Liz-Marzán, L. M., SERS detection of small inorganic molecules and ions. *Angewandte Chemie International Edition* **2012,** *51*, (45), 11214-11223.

82. Sun, Y.; Xia, Y., Gold and silver nanoparticles: a class of chromophores with colors tunable in the range from 400 to 750 nm. *Analyst* **2003,** *128*, (6), 686-691.

83. Mulvaney, P., Surface plasmon spectroscopy of nanosized metal particles. *Langmuir* **1996,** *12*, (3), 788-800.

84. Zielińska, A.; Skwarek, E.; Zaleska, A.; Gazda, M.; Hupka, J., Preparation of silver nanoparticles with controlled particle size. *Procedia Chemistry* **2009,** *1*, (2), 1560-1566.

85. Link, S.; El-Sayed, M. A., Optical properties and ultrafast dynamics of metallic nanocrystals. *Annual review of physical chemistry* **2003,** *54*, (1), 331-366.

86. Orendorff, C. J.; Sau, T. K.; Murphy, C. J., Shape-Dependent Plasmon-Resonant Gold Nanoparticles. *Small* **2006,** *2*, (5), 636-639.

87. Nehl, C. L.; Hafner, J. H., Shape-dependent plasmon resonances of gold nanoparticles. *J. Mater. Chem.* **2008,** *18*, (21), 2415-2419.

88. Zhong, L.; Zhou, X.; Bao, S.; Shi, Y.; Wang, Y.; Hong, S.; Huang, Y.; Wang, X.; Xie, Z.; Zhang, Q., Rational design and SERS properties of side-by-side, end-to-end and end-to-side assemblies of Au nanorods. *Journal of Materials Chemistry* **2011,** *21*, (38), 14448-14455.

89. Blakey, I.; Merican, Z.; Thurecht, K. J., A method for controlling the aggregation of gold nanoparticles: tuning of optical and spectroscopic properties. *Langmuir* **2013,** *29*, (26), 8266-8274.

90. Willets, K. A.; Van Duyne, R. P., Localized surface plasmon resonance spectroscopy and sensing. *Annu. Rev. Phys. Chem.* **2007,** *58*, 267-297.

91. Storhoff, J. J.; Elghanian, R.; Mucic, R. C.; Mirkin, C. A.; Letsinger, R. L., One-pot colorimetric differentiation of polynucleotides with single base imperfections using gold nanoparticle probes. *Journal of the American Chemical Society* **1998,** *120*, (9), 1959-1964.

92. Huang, C.-C.; Chang, H.-T., Parameters for selective colorimetric sensing of mercury (II) in aqueous solutions using mercaptopropionic acid-modified gold nanoparticles. *Chemical Communications* **2007**, (12), 1215-1217.

93. Liu, J.; Lu, Y., Fast colorimetric sensing of adenosine and cocaine based on a general sensor design involving aptamers and nanoparticles. *Angew. Chem.* **2006,** *118*, (1), 96-100.

94. Mrozek, I.; Otto, A., Quantitative separation of the "classical" electromagnetic and the "chemical" contribution to surface enhanced Raman scattering. *Journal of Electron Spectroscopy and Related Phenomena* **1990,** *54*, 895-911.

95. Compagnini, G.; Galati, C.; Pignataro, S., Distance dependence of surface enhanced Raman scattering probed by alkanethiol self-assembled monolayers. *Phys. Chem. Chem. Phys.* **1999,** *1*, (9), 2351-2353.

96. Su, K.-H.; Wei, Q.-H.; Zhang, X.; Mock, J.; Smith, D. R.; Schultz, S., Interparticle coupling effects on plasmon resonances of nanogold particles. *Nano Letters* **2003,** *3*, (8), 1087-1090.

97. Qian, X.; Zhou, X.; Nie, S., Surface-enhanced Raman nanoparticle beacons based on bioconjugated gold nanocrystals and long range plasmonic coupling. *Journal of the American Chemical Society* **2008,** *130*, (45), 14934-14935.

98. Qin, L.; Zou, S.; Xue, C.; Atkinson, A.; Schatz, G. C.; Mirkin, C. A., Designing, fabricating, and imaging Raman hot spots. *Proceedings of the National Academy of Sciences* **2006,** *103*, (36), 13300-13303.

99. Im, H.; Bantz, K. C.; Lindquist, N. C.; Haynes, C. L.; Oh, S.-H., Vertically oriented sub-10-nm plasmonic nanogap arrays. *Nano letters* **2010,** *10*, (6), 2231-2236.

100. Wang, H.; Levin, C. S.; Halas, N. J., Nanosphere arrays with controlled sub-10-nm gaps as surface-enhanced Raman spectroscopy substrates. *Journal of the American Chemical Society* **2005,** *127*, (43), 14992-14993.

101. Wustholz, K. L.; Henry, A.-I.; McMahon, J. M.; Freeman, R. G.; Valley, N.; Piotti, M. E.; Natan, M. J.; Schatz, G. C.; Duyne, R. P. V., Structure− Activity Relationships in Gold Nanoparticle Dimers and Trimers for Surface-Enhanced Raman Spectroscopy. *Journal of the American Chemical Society* **2010,** *132*, (31), 10903-10910.

102. Fabris, L.; Indrasekara, A. S. D.; Meyers, S.; Shubeita, S.; Feldman, L. C.; Gustafsson, T., Gold Nanostar Substrates for SERS-based Chemical Sensing in the Femtomolar Regime. *Nanoscale* **2014**.

103. Potara, M.; Gabudean, A.-M.; Astilean, S., Solution-phase, dual LSPR-SERS plasmonic sensors of high sensitivity and stability based on chitosan-coated anisotropic silver nanoparticles. *Journal of Materials Chemistry* **2011,** *21*, (11), 3625-3633.

104. McLintock, A.; Cunha-Matos, C. A.; Zagnoni, M.; Millington, O. R.; Wark, A. W., Universal Surface-Enhanced Raman Tags: Individual Nanorods for Measurements from the Visible to the Infrared (514–1064 nm). *ACS nano* **2014,** *8*, (8), 8600-8609.

105. Braun, G.; Pavel, I.; Morrill, A. R.; Seferos, D. S.; Bazan, G. C.; Reich, N. O.; Moskovits, M., Chemically patterned microspheres for controlled nanoparticle assembly in the construction of SERS hot spots. *Journal of the American Chemical Society* **2007,** *129*, (25), 7760-7761.

106. Kleinman, S. L.; Frontiera, R. R.; Henry, A.-I.; Dieringer, J. A.; Van Duyne, R. P., Creating, characterizing, and controlling chemistry with SERS hot spots. *Physical Chemistry Chemical Physics* **2013,** *15*, (1), 21-36.

107. Shiohara, A.; Wang, Y.; Liz-Marzán, L. M., Recent approaches toward creation of hot spots for SERS detection. *Journal of Photochemistry and Photobiology C: Photochemistry Reviews* **2014**.

108. Kim, N. H.; Lee, S. J.; Moskovits, M., Reversible Tuning of SERS Hot Spots with Aptamers. *Advanced Materials* **2011,** *23*, (36), 4152-4156.

109. Alvarez-Puebla, R. A.; Arceo, E.; Goulet, P. J.; Garrido, J. J.; Aroca, R. F., Role of nanoparticle surface charge in surface-enhanced Raman scattering. *The Journal of Physical Chemistry B* **2005,** *109*, (9), 3787-3792.

110. Lawson, L. S.; Chan, J. W.; Huser, T., A highly sensitive nanoscale pH-sensor using Au nanoparticles linked by a multifunctional Raman-active reporter molecule. *Nanoscale* **2014**.

111. Kong, K. V.; Dinish, U.; Lau, W. K. O.; Olivo, M., Sensitive SERS-pH sensing in biological media using metal carbonyl functionalized planar substrates. *Biosensors and Bioelectronics* **2014,** *54*, 135-140.

112. Ji, W.; Spegazzini, N.; Kitahama, Y.; Chen, Y.; Zhao, B.; Ozaki, Y., pH-Response Mechanism of p-Aminobenzenethiol on Ag Nanoparticles Revealed By Two-Dimensional Correlation Surface-Enhanced Raman Scattering Spectroscopy. *The Journal of Physical Chemistry Letters* **2012,** *3*, (21), 3204-3209.

113. Hill, W.; Wehling, B., Potential-and pH-dependent surface-enhanced Raman scattering of p-mercapto aniline on silver and gold substrates. *The Journal of Physical Chemistry* **1993,** *97*, (37), 9451-9455.

114. Alvarez-Puebla, R.; Cui, B.; Bravo-Vasquez, J.-P.; Veres, T.; Fenniri, H., Nanoimprinted SERS-active substrates with tunable surface plasmon resonances. *The Journal of Physical Chemistry C* **2007,** *111*, (18), 6720-6723.

115. Sarkar, U. K., A pH-dependent SERS study of thiophene-2-carboxylic acid adsorbed on Ag-sols. *Chemical physics letters* **2003,** *374*, (3), 341-347.

116. Yuan, H.; Fales, A. M.; Khoury, C. G.; Liu, J.; Vo-Dinh, T., Spectral characterization and intracellular detection of Surface-Enhanced Raman Scattering (SERS)-encoded plasmonic gold nanostars. *Journal of Raman Spectroscopy* **2013,** *44*, (2), 234-239.

117. Lim, D.-K.; Kim, I.-J.; Nam, J.-M., DNA-embedded Au/Ag core–shell nanoparticles. *Chemical Communications* **2008**, (42), 5312-5314.

118. Murphy, C. J.; Sau, T. K.; Gole, A. M.; Orendorff, C. J.; Gao, J.; Gou, L.; Hunyadi, S. E.; Li, T., Anisotropic metal nanoparticles: synthesis, assembly, and optical applications. *The Journal of Physical Chemistry B* **2005,** *109*, (29), 13857-13870.

119. Sherry, L. J.; Jin, R.; Mirkin, C. A.; Schatz, G. C.; Van Duyne, R. P., Localized surface plasmon resonance spectroscopy of single silver triangular nanoprisms. *Nano letters* **2006,** *6*, (9), 2060-2065.

120. Millstone, J. E.; Park, S.; Shuford, K. L.; Qin, L.; Schatz, G. C.; Mirkin, C. A., Observation of a quadrupole plasmon mode for a colloidal solution of gold nanoprisms. *Journal of the American Chemical Society* **2005,** *127*, (15), 5312-5313.

121. Rodríguez-Lorenzo, L.; Alvarez-Puebla, R. A.; Pastoriza-Santos, I.; Mazzucco, S.; Stéphan, O.; Kociak, M.; Liz-Marzán, L. M.; García de Abajo, F. J., Zeptomol detection through controlled ultrasensitive surface-enhanced Raman scattering. *Journal of the American Chemical Society* **2009,** *131*, (13), 4616-4618.

122. Orendorff, C. J.; Gearheart, L.; Jana, N. R.; Murphy, C. J., Aspect ratio dependence on surface enhanced Raman scattering using silver and gold nanorod substrates. *Physical Chemistry Chemical Physics* **2006,** *8*, (1), 165-170.

123. Bell, S. E.; McCourt, M. R., SERS enhancement by aggregated Au colloids: effect of particle size. *Physical Chemistry Chemical Physics* **2009,** *11*, (34), 7455-7462.

124. Iliescu, T.; Baia, M.; Kiefer, W., FT-Raman, surface-enhanced Raman spectroscopy and theoretical investigations of diclofenac sodium. *Chemical physics* **2004,** *298*, (1), 167-174.

125. Lin, H. Y.; Huang, C. H.; Hsieh, W. H.; Liu, L. H.; Lin, Y. C.; Chu, C. C.; Wang, S. T.; Kuo, I.; Chau, L. K.; Yang, C. Y., On-line SERS Detection of Single Bacterium Using Novel SERS Nanoprobes and A Microfluidic Dielectrophoresis Device. *Small* **2014,** *10*, (22), 4700-4710.

126. Mirkin, C. A.; Letsinger, R. L.; Mucic, R. C.; Storhoff, J. J., A DNA-based method for rationally assembling nanoparticles into macroscopic materials. *Nature* **1996,** *382*, (6592), 607-609.

127. Reynolds, R. A.; Mirkin, C. A.; Letsinger, R. L., Homogeneous, nanoparticle-based quantitative colorimetric detection of oligonucleotides. *Journal of the American Chemical Society* **2000,** *122*, (15), 3795-3796.

128. Thompson, D. G.; Enright, A.; Faulds, K.; Smith, W. E.; Graham, D., Ultrasensitive DNA detection using oligonucleotide-silver nanoparticle conjugates. *Analytical chemistry* **2008,** *80*, (8), 2805-2810.

129. Liu, L.; Li, S.; Liu, L.; Deng, D.; Xia, N., Simple, sensitive and selective detection of dopamine using dithiobis (succinimidylpropionate)-modified gold nanoparticles as colorimetric probes. *Analyst* **2012,** *137*, (16), 3794-3799.

130. Huizenga, D. E.; Szostak, J. W., A DNA aptamer that binds adenosine and ATP. *Biochemistry* **1995,** *34*, (2), 656-665.

131. Liu, J.; Lu, Y., Preparation of aptamer-linked gold nanoparticle purple aggregates for colorimetric sensing of analytes. *Nature Protocols* **2006,** *1*, (1), 246-252.

132. Zhu, Z.; Wu, C.; Liu, H.; Zou, Y.; Zhang, X.; Kang, H.; Yang, C. J.; Tan, W., An Aptamer Cross-Linked Hydrogel as a Colorimetric Platform for Visual Detection. *Angewandte Chemie* **2010,** *122*, (6), 1070-1074.

133. Sugunan, A.; Thanachayanont, C.; Dutta, J.; Hilborn, J., Heavy-metal ion sensors using chitosan-capped gold nanoparticles. *Science and Technology of Advanced Materials* **2005,** *6*, (3), 335-340.

134. Liu, J.; Lu, Y., A colorimetric lead biosensor using DNAzyme-directed assembly of gold nanoparticles. *Journal of the American Chemical Society* **2003,** *125*, (22), 6642-6643.

135. Lin, C.-Y.; Yu, C.-J.; Lin, Y.-H.; Tseng, W.-L., Colorimetric sensing of silver (I) and mercury (II) ions based on an assembly of Tween 20-stabilized gold nanoparticles. *Analytical chemistry* **2010,** *82*, (16), 6830-6837.

136. Üzer, A. e.; Can, Z.; Akın, I. l.; Erçağ, E.; Apak, R. a., 4-Aminothiophenol Functionalized Gold Nanoparticle-Based Colorimetric Sensor for the Determination of Nitramine Energetic Materials. *Analytical chemistry* **2013,** *86*, (1), 351-356.

137. Li, F.-M.; Liu, J.-M.; Wang, X.-X.; Lin, L.-P.; Cai, W.-L.; Lin, X.; Zeng, Y.-N.; Li, Z.-M.; Lin, S.-Q., Non-aggregation based label free colorimetric sensor for the detection of Cr (VI) based on selective etching of gold nanorods. *Sensors and Actuators B: Chemical* **2011,** *155*, (2), 817-822.

138. Zhang, Z.; Chen, Z.; Qu, C.; Chen, L., Highly Sensitive Visual Detection of Copper Ions Based on the Shape-Dependent LSPR Spectroscopy of Gold Nanorods. *Langmuir* **2014,** *30*, (12), 3625-3630.

139. Wang, G.; Chen, Z.; Wang, W.; Yan, B.; Chen, L., Chemical redox-regulated mesoporous silica-coated gold nanorods for colorimetric probing of Hg2+ and S 2−. *Analyst* **2011,** *136*, (1), 174-178.

140. Mazumdar, D.; Liu, J.; Lu, G.; Zhou, J.; Lu, Y., Easy-to-use dipstick tests for detection of lead in paints using non-cross-linked gold nanoparticle–DNAzyme conjugates. *Chem. Commun.* **2010,** *46*, (9), 1416-1418.

141. Zhao, W.; Ali, M. M.; Aguirre, S. D.; Brook, M. A.; Li, Y., Paper-based bioassays using gold nanoparticle colorimetric probes. *Analytical chemistry* **2008,** *80*, (22), 8431-8437.

142. Tseng, S.-C.; Yu, C.-C.; Wan, D.; Chen, H.-L.; Wang, L. A.; Wu, M.-C.; Su, W.-F.; Han, H.-C.; Chen, L.-C., Eco-friendly plasmonic sensors: using the photothermal effect to prepare metal nanoparticle-containing test papers for highly sensitive colorimetric detection. *Analytical chemistry* **2012,** *84*, (11), 5140-5145.

143. Ratnarathorn, N.; Chailapakul, O.; Henry, C. S.; Dungchai, W., Simple silver nanoparticle colorimetric sensing for copper by paper-based devices. *Talanta* **2012,** *99*, 552-557.

144. Fleischmann, M.; Hendra, P.; McQuillan, A., Raman spectra of pyridine adsorbed at a silver electrode. *Chemical Physics Letters* **1974,** *26*, (2), 163-166.

145. Vo-Dinh, T.; Hiromoto, M.; Begun, G.; Moody, R., Surface-enhanced Raman spectrometry for trace organic analysis. *Analytical Chemistry* **1984,** *56*, (9), 1667-1670.

146. Carrabba, M. M.; Edmonds, R. B.; Rauh, R. D., Feasibility studies for the detection of organic surface and subsurface water contaminants by surface-enhanced Raman spectroscopy on silver electrodes. *Analytical chemistry* **1987,** *59*, (21), 2559-2563.

147. Lim, D.-K.; Jeon, K.-S.; Hwang, J.-H.; Kim, H.; Kwon, S.; Suh, Y. D.; Nam, J.-M., Highly uniform and reproducible surface-enhanced Raman scattering from DNA-tailorable nanoparticles with 1-nm interior gap. *Nature nanotechnology* **2011,** *6*, (7), 452-460.

148. Lim, D.-K.; Jeon, K.-S.; Kim, H. M.; Nam, J.-M.; Suh, Y. D., Nanogap-engineerable Raman-active nanodumbbells for single-molecule detection. *Nature materials* **2009,** *9*, (1), 60-67.

149. Yang, J.; Palla, M.; Bosco, F. G.; Rindzevicius, T.; Alstrøm, T. S.; Schmidt, M. S.; Boisen, A.; Ju, J.; Lin, Q., Surface-Enhanced Raman Spectroscopy Based Quantitative Bioassay on Aptamer-Functionalized Nanopillars Using Large-Area Raman Mapping. *ACS nano* **2013,** *7*, (6), 5350-5359.

150. Leng, W.; Vikesland, P. J., MGITC Facilitated Formation of AuNP Multimers. *Langmuir* **2014**.

151. Taylor, R. W.; Coulston, R. J.; Biedermann, F.; Mahajan, S.; Baumberg, J. J.; Scherman, O. A., In Situ SERS Monitoring of Photochemistry within a Nanojunction Reactor. *Nano letters* **2013,** *13*, (12), 5985-5990.

152. Basu, S.; Pande, S.; Jana, S.; Bolisetty, S.; Pal, T., Controlled interparticle spacing for surface-modified gold nanoparticle aggregates. *Langmuir* **2008,** *24*, (10), 5562-5568.

153. Taylor, R. W.; Lee, T.-C.; Scherman, O. A.; Esteban, R.; Aizpurua, J.; Huang, F. M.; Baumberg, J. J.; Mahajan, S., Precise subnanometer plasmonic junctions for SERS within gold nanoparticle assemblies using cucurbit [n] uril “glue”. *ACS nano* **2011,** *5*, (5), 3878-3887.

154. Zhang, L.; Lang, X.; Hirata, A.; Chen, M., Wrinkled nanoporous gold films with ultrahigh surface-enhanced Raman scattering enhancement. *ACS nano* **2011,** *5*, (6), 4407-4413.

155. Tao, A.; Kim, F.; Hess, C.; Goldberger, J.; He, R.; Sun, Y.; Xia, Y.; Yang, P., Langmuir-Blodgett silver nanowire monolayers for molecular sensing using surface-enhanced Raman spectroscopy. *Nano Letters* **2003,** *3*, (9), 1229-1233.

156. Reilly, T. H.; Corbman, J. D.; Rowlen, K. L., Vapor deposition method for sensitivity studies on engineered surface-enhanced Raman scattering-active substrates. *Analytical chemistry* **2007,** *79*, (13), 5078-5081.

157. Jin, Y., Engineering plasmonic gold nanostructures and metamaterials for biosensing and nanomedicine. *Advanced Materials* **2012,** *24*, (38), 5153-5165.

158. Wang, P.; Liang, O.; Zhang, W.; Schroeder, T.; Xie, Y. H., Ultra-Sensitive Graphene-Plasmonic Hybrid Platform for Label-Free Detection. *Advanced Materials* **2013,** *25*, (35), 4918-4924.

159. Zhang, R.; Xu, B.-B.; Liu, X.-Q.; Zhang, Y.-L.; Xu, Y.; Chen, Q.-D.; Sun, H.-B., Highly efficient SERS test strips. *Chemical Communications* **2012,** *48*, (47), 5913-5915.

160. Lee, C. H.; Tian, L.; Singamaneni, S., Paper-based SERS swab for rapid trace detection on real-world surfaces. *ACS applied materials & interfaces* **2010,** *2*, (12), 3429-3435.

161. Zhang, W.; Li, B.; Chen, L.; Wang, Y.; Gao, D.; Ma, X.; Wu, A., Brushing, a simple way to fabricate SERS active paper substrates. *Analytical Methods* **2014,** *6*, (7), 2066-2071.

162. Ngo, Y. H.; Li, D.; Simon, G. P.; Garnier, G., Gold nanoparticle–paper as a three-dimensional surface enhanced raman scattering substrate. *Langmuir* **2012,** *28*, (23), 8782-8790.

163. Polavarapu, L.; Liz-Marzán, L. M., Towards low-cost flexible substrates for nanoplasmonic sensing. *Physical Chemistry Chemical Physics* **2013,** *15*, (15), 5288-5300.

164. Abbas, A.; Brimer, A.; Slocik, J. M.; Tian, L.; Naik, R. R.; Singamaneni, S., Multifunctional analytical platform on a paper strip: separation, preconcentration, and subattomolar detection. *Analytical chemistry* **2013,** *85*, (8), 3977-3983.

165. Zhang, L.; Gong, X.; Bao, Y.; Zhao, Y.; Xi, M.; Jiang, C.; Fong, H., Electrospun nanofibrous membranes surface-decorated with silver nanoparticles as flexible and active/sensitive substrates for surface-enhanced Raman scattering. *Langmuir* **2012,** *28*, (40), 14433-14440.

166. He, D.; Hu, B.; Yao, Q.-F.; Wang, K.; Yu, S.-H., Large-scale synthesis of flexible free-standing SERS substrates with high sensitivity: electrospun PVA nanofibers embedded with controlled alignment of silver nanoparticles. *ACS nano* **2009,** *3*, (12), 3993-4002.

167. Ko, H.; Chang, S.; Tsukruk, V. V., Porous substrates for label-free molecular level detection of nonresonant organic molecules. *Acs Nano* **2008,** *3*, (1), 181-188.

168. Aldeanueva-Potel, P.; Faoucher, E.; Alvarez-Puebla, R. n. A.; Liz-Marzán, L. M.; Brust, M., Recyclable molecular trapping and SERS detection in silver-loaded agarose gels with dynamic hot spots. *Analytical chemistry* **2009,** *81*, (22), 9233-9238.

169. Zhou, X.; Zhou, F.; Liu, H.; Yang, L.; Liu, J., Assembly of polymer–gold nanostructures with high reproducibility into a monolayer film SERS substrate with 5 nm gaps for pesticide trace detection. *Analyst* **2013,** *138*, (19), 5832-5838.

170. Saute, B.; Narayanan, R., Solution-based direct readout surface enhanced Raman spectroscopic (SERS) detection of ultra-low levels of thiram with dogbone shaped gold nanoparticles. *Analyst* **2011,** *136*, (3), 527-532.

171. Abalde-Cela, S.; Ho, S.; Rodríguez-González, B.; Correa-Duarte, M. A.; Álvarez-Puebla, R. A.; Liz-Marzán, L. M.; Kotov, N. A., Loading of exponentially grown LBL films with silver

nanoparticles and their application to generalized SERS detection. *Angewandte Chemie* **2009,** *121*, (29), 5430-5433.

172. Saute, B.; Premasiri, R.; Ziegler, L.; Narayanan, R., Gold nanorods as surface enhanced Raman spectroscopy substrates for sensitive and selective detection of ultra-low levels of dithiocarbamate pesticides. *Analyst* **2012,** *137*, (21), 5082-5087.

173. Dasary, S. S.; Singh, A. K.; Senapati, D.; Yu, H.; Ray, P. C., Gold nanoparticle based label-free SERS probe for ultrasensitive and selective detection of trinitrotoluene. *Journal of the American Chemical Society* **2009,** *131*, (38), 13806-13812.

174. Álvarez-Puebla, R. A.; Contreras-Cáceres, R.; Pastoriza-Santos, I.; Pérez-Juste, J.; Liz-Marzán, L. M., Au@ pNIPAM Colloids as Molecular Traps for Surface-Enhanced, Spectroscopic, Ultra-Sensitive Analysis. *Angewandte Chemie International Edition* **2009,** *48*, (1), 138-143.

175. Guerrini, L.; Garcia-Ramos, J. V.; Domingo, C.; Sanchez-Cortes, S., Nanosensors based on viologen functionalized silver nanoparticles: few molecules surface-enhanced raman spectroscopy detection of polycyclic aromatic hydrocarbons in interparticle hot spots. *Analytical chemistry* **2009,** *81*, (4), 1418-1425.

176. Guerrini, L.; Garcia-Ramos, J. V.; Domingo, C.; Sanchez-Cortes, S., Sensing polycyclic aromatic hydrocarbons with dithiocarbamate-functionalized Ag nanoparticles by surface-enhanced Raman scattering. *Analytical chemistry* **2009,** *81*, (3), 953-960.

177. Leyton, P.; Domingo, C.; Sanchez-Cortes, S.; Campos-Vallette, M.; Garcia-Ramos, J., Surface enhanced vibrational (IR and Raman) spectroscopy in the design of chemosensors based on ester functionalized p-tert-butylcalix [4] arene hosts. *Langmuir* **2005,** *21*, (25), 11814-11820.

178. Guerrini, L.; Garcia-Ramos, J. V.; Domingo, C.; Sanchez-Cortes, S., Functionalization of Ag nanoparticles with dithiocarbamate calix [4] arene as an effective supramolecular host for the

surface-enhanced Raman scattering detection of polycyclic aromatic hydrocarbons. *Langmuir* **2006,** *22*, (26), 10924-10926.

179. Kolomijeca, A.; Kwon, Y.; Sowoidnich, K.; Prien, R.; Schulz-Bull, D.; Kronfeldt, H., High sensitive Raman sensor for continuous in-situ detection of PAHs. *Proceedings of the Twenty-first* **2011**, 859-862.

180. Schmidt, H.; Bich Ha, N.; Pfannkuche, J.; Amann, H.; Kronfeldt, H.-D.; Kowalewska, G., Detection of PAHs in seawater using surface-enhanced Raman scattering (SERS). *Marine pollution bulletin* **2004,** *49*, (3), 229-234.

181. Pfannkuche, J.; Lubecki, L.; Schmidt, H.; Kowalewska, G.; Kronfeldt, H.-D., The use of surface-enhanced Raman scattering (SERS) for detection of PAHs in the Gulf of Gdańsk (Baltic Sea). *Marine pollution bulletin* **2012,** *64*, (3), 614-626.

182. Rubira, R. J.; Camacho, S. A.; Aoki, P. H.; Maximino, M. D.; Alessio, P.; Martin, C. S.; Oliveira Jr, O. N.; Fatore, F. M.; Paulovich, F. V.; Constantino, C. J., Detection of trace levels of atrazine using surface-enhanced Raman scattering and information visualization. *Colloid and Polymer Science* **2014**, 1-10.

183. Zheng, J.; Pang, S.; Labuza, T. P.; He, L., Semi-quantification of surface-enhanced Raman scattering using a handheld Raman spectrometer: a feasibility study. *Analyst* **2013,** *138*, (23), 7075-7078.

184. XuanáQuang, L.; HunáSeong, G.; JunáDo, K., A portable surface-enhanced Raman scattering sensor integrated with a lab-on-a-chip for field analysis. *Lab on a Chip* **2008,** *8*, (12), 2214-2219.

185. Rule, K. L.; Vikesland, P. J., Surface-enhanced resonance Raman spectroscopy for the rapid detection of Cryptosporidium parvum and Giardia lamblia. *Environmental science & technology* **2009,** *43*, (4), 1147-1152.

186. Maiti, K. K.; Dinish, U.; Fu, C. Y.; Lee, J.-J.; Soh, K.-S.; Yun, S.-W.; Bhuvaneswari, R.; Olivo, M.; Chang, Y.-T., Development of biocompatible SERS nanotag with increased stability by chemisorption of reporter molecule for< i> in vivo</i> cancer detection. *Biosensors and Bioelectronics* **2010,** *26*, (2), 398-403.

187. Guven, B.; Basaran-Akgul, N.; Temur, E.; Tamer, U.; Boyacı, İ. H., SERS-based sandwich immunoassay using antibody coated magnetic nanoparticles for Escherichia coli enumeration. *Analyst* **2011,** *136*, (4), 740-748.

188. Deng, S.; Xu, W.; Wang, J.; Ling, X.; Wu, J.; Xie, L.; Kong, J.; Dresselhaus, M. S.; Zhang, J., Direct Measurement of the Raman Enhancement Factor of R6G on Graphene under Resonant Excitation. **2014**.

189. Lin, D.; Qin, T.; Wang, Y.; Sun, X.; Chen, L., Graphene Oxide Wrapped SERS Tags: Multifunctional Platforms toward Optical Labeling, Photothermal Ablation of Bacteria, and the Monitoring of Killing Effect. *ACS applied materials & interfaces* **2014,** *6*, (2), 1320-1329.

190. Wei, H.; Rodriguez, K.; Renneckar, S.; Leng, W.; Vikesland, P. J., Preparation and evaluation of nanocellulose–gold nanoparticle nanocomposites for SERS applications. *Analyst* **2015,** *140*, (16), 5640-5649.

191. Klemm, D.; Kramer, F.; Moritz, S.; Lindström, T.; Ankerfors, M.; Gray, D.; Dorris, A., Nanocelluloses: A New Family of Nature-Based Materials. *Angewandte Chemie International Edition* **2011,** *50*, (24), 5438-5466.

192. Hu, L.; Zheng, G.; Yao, J.; Liu, N.; Weil, B.; Eskilsson, M.; Karabulut, E.; Ruan, Z.; Fan, S.; Bloking, J. T., Transparent and conductive paper from nanocellulose fibers. *Energy & Environmental Science* **2013,** *6*, (2), 513-518.

193. Siqueira, G.; Bras, J.; Dufresne, A., Cellulose whiskers versus microfibrils: influence of the nature of the nanoparticle and its surface functionalization on the thermal and mechanical properties of nanocomposites. *Biomacromolecules* **2008,** *10*, (2), 425-432.

194. Iguchi, M.; Yamanaka, S.; Budhiono, A., Bacterial cellulose—a masterpiece of nature's arts. *Journal of Materials Science* **2000,** *35*, (2), 261-270.

195. Svensson, A.; Nicklasson, E.; Harrah, T.; Panilaitis, B.; Kaplan, D.; Brittberg, M.; Gatenholm, P., Bacterial cellulose as a potential scaffold for tissue engineering of cartilage. *Biomaterials* **2005,** *26*, (4), 419-431.

196. Klemm, D.; Schumann, D.; Udhardt, U.; Marsch, S., Bacterial synthesized cellulose—artificial blood vessels for microsurgery. *Progress in Polymer Science* **2001,** *26*, (9), 1561-1603.

197. Zhou, P.; Wang, H.; Yang, J.; Tang, J.; Sun, D.; Tang, W., Bacteria cellulose nanofibers supported palladium (0) nanocomposite and its catalysis evaluation in Heck reaction. *Industrial & Engineering Chemistry Research* **2012,** *51*, (16), 5743-5748.

198. de Santa Maria, L. C.; Santos, A. L.; Oliveira, P. C.; Barud, H. S.; Messaddeq, Y.; Ribeiro, S. J., Synthesis and characterization of silver nanoparticles impregnated into bacterial cellulose. *Materials Letters* **2009,** *63*, (9), 797-799.

199. Wei, H.; Rodriguez, K.; Renneckar, S.; Vikesland, P. J., Environmental science and engineering applications of nanocellulose-based nanocomposites. *Environmental Science: Nano* **2014**.

200. Yang, J.; Sun, D.; Li, J.; Yang, X.; Yu, J.; Hao, Q.; Liu, W.; Liu, J.; Zou, Z.; Gu, J., < i> In situ</i> deposition of platinum nanoparticles on bacterial cellulose membranes and evaluation of PEM fuel cell performance. *Electrochimica Acta* **2009,** *54*, (26), 6300-6305.

201. Maneerung, T.; Tokura, S.; Rujiravanit, R., Impregnation of silver nanoparticles into bacterial cellulose for antimicrobial wound dressing. *Carbohydrate polymers* **2008,** *72*, (1), 43-51.

202. Park, M.; Chang, H.; Jeong, D. H.; Hyun, J., Spatial deformation of nanocellulose hydrogel enhances SERS. *BioChip Journal* **2013,** *7*, (3), 234-241.

203. Michaels, A. M.; Nirmal, M.; Brus, L., Surface enhanced Raman spectroscopy of individual rhodamine 6G molecules on large Ag nanocrystals. *J. Am. Chem. Soc.* **1999,** *121*, (43), 9932-9939.

204. Liu, J.-W.; Wang, J.-L.; Huang, W.-R.; Yu, L.; Ren, X.-F.; Wen, W.-C.; Yu, S.-H., Ordering Ag nanowire arrays by a glass capillary: A portable, reusable and durable SERS substrate. *Scientific reports* **2012,** *2*.

205. Abell, J.; Driskell, J.; Dluhy, R.; Tripp, R.; Zhao, Y.-P., Fabrication and characterization of a multiwell array SERS chip with biological applications. *Biosensors and Bioelectronics* **2009,** *24*, (12), 3663-3670.

206. Parolo, C.; Merkoçi, A., Paper-based nanobiosensors for diagnostics. *Chemical Society Reviews* **2013,** *42*, (2), 450-457.

207. Polavarapu, L.; Porta, A. L.; Novikov, S. M.; Coronado-Puchau, M.; Liz-Marzán, L. M., Pen-on-Paper Approach Toward the Design of Universal Surface Enhanced Raman Scattering Substrates. *Small* **2014**.

208. Abe, K.; Suzuki, K.; Citterio, D., Inkjet-printed microfluidic multianalyte chemical sensing paper. *Analytical chemistry* **2008,** *80*, (18), 6928-6934.

209. Zhang, C.-L.; Lv, K.-P.; Huang, H.-T.; Cong, H.-P.; Yu, S.-H., Co-assembly of Au nanorods with Ag nanowires within polymer nanofiber matrix for enhanced SERS property by electrospinning. *Nanoscale* **2012,** *4*, (17), 5348-5355.

210. Zhang, C. L.; Lv, K. P.; Cong, H. P.; Yu, S. H., Controlled Assemblies of Gold Nanorods in PVA Nanofiber Matrix as Flexible Free-Standing SERS Substrates by Electrospinning. *Small* **2012,** *8*, (5), 648-653.

211. Zhang, C.-L.; Yu, S.-H., Nanoparticles meet electrospinning: recent advances and future prospects. *Chemical Society Reviews* **2014,** *43*, (13), 4423-4448.

212. Marques, P. A.; Nogueira, H. I.; Pinto, R. J.; Neto, C. P.; Trindade, T., Silver-bacterial cellulosic sponges as active SERS substrates. *Journal of Raman Spectroscopy* **2008,** *39*, (4), 439-443.

213. Leng, W.; Vikesland, P. J., Nanoclustered Gold Honeycombs for Surface-Enhanced Raman Scattering. *Analytical chemistry* **2013,** *85*, (3), 1342-1349.

214. Freus, G., Controlled nucleation for the regulation of the particle size in monodisperse gold solutions. *Nature (Phys Sci)* **1973,** *241*, 20-22.

215. Brown, K. R.; Walter, D. G.; Natan, M. J., Seeding of colloidal Au nanoparticle solutions. 2. Improved control of particle size and shape. *Chemistry of Materials* **2000,** *12*, (2), 306-313.

216. Wu, X.; Lu, C.; Zhou, Z.; Yuan, G.; Xiong, R.; Zhang, X., Green synthesis and formation mechanism of cellulose nanocrystal-supported gold nanoparticles with enhanced catalytic performance. *Environmental Science: Nano* **2014,** *1*, (1), 71-79.

217. Ji, X.; Song, X.; Li, J.; Bai, Y.; Yang, W.; Peng, X., Size control of gold nanocrystals in citrate reduction: the third role of citrate. *Journal of the American Chemical Society* **2007,** *129*, (45), 13939-13948.

218. Zou, X.; Ying, E.; Dong, S., Seed-mediated synthesis of branched gold nanoparticles with the assistance of citrate and their surface-enhanced Raman scattering properties. *Nanotechnology* **2006,** *17*, (18), 4758.

219. Lee, K.-Y.; Quero, F.; Blaker, J. J.; Hill, C. A.; Eichhorn, S. J.; Bismarck, A., Surface only modification of bacterial cellulose nanofibres with organic acids. *Cellulose* **2011,** *18*, (3), 595-605.

220. Brewer, S. H.; Glomm, W. R.; Johnson, M. C.; Knag, M. K.; Franzen, S., Probing BSA binding to citrate-coated gold nanoparticles and surfaces. *Langmuir* **2005,** *21*, (20), 9303-9307.

221. Deckert-Gaudig, T.; Deckert, V., Ultraflat Transparent Gold Nanoplates—Ideal Substrates for Tip-Enhanced Raman Scattering Experiments. *Small* **2009,** *5*, (4), 432-436.

222. Sun, Y.; Wiederrecht, G. P., Surfactantless synthesis of silver nanoplates and their application in SERS. *Small* **2007,** *3*, (11), 1964-1975.

223. Xie, J.; Lee, J. Y.; Wang, D. I.; Ting, Y. P., Identification of Active Biomolecules in the High-Yield Synthesis of Single-Crystalline Gold Nanoplates in Algal Solutions. *Small* **2007,** *3*, (4), 672-682.

224. Shao, Y.; Jin, Y.; Dong, S., Synthesis of gold nanoplates by aspartate reduction of gold chloride. *Chem. Commun.* **2004**, (9), 1104-1105.

225. Wang, D.; Imae, T., Watching the transformation from Au nanoparticles to microplates. *Chemistry Letters* **2006,** *35*, (10), 1152-1153.

226. Ibano, D.; Yokota, Y.; Tominaga, T., Preparation of gold nanoplates protected by an anionic phospholipid. *Chemistry Letters* **2003,** *32*, (7), 574-575.

227. Gonzaga, F.; D'Souza, R.; Brook, M. A., Oriented crystallization of ultra-thin (2 nm) gold nanoplatelets inside a reactive hydrophobic polymeric matrix. *Soft Matter* **2011,** *7*, (2), 722-729.

228. Gierlinger, N.; Keplinger, T.; Harrington, M., Imaging of plant cell walls by confocal Raman microscopy. *Nature protocols* **2012,** *7*, (9), 1694-1708.

229. Li, Q.; Renneckar, S., Supramolecular structure characterization of molecularly thin cellulose I nanoparticles. *Biomacromolecules* **2011,** *12*, (3), 650-659.

230. Krug, J. T.; Wang, G. D.; Emory, S. R.; Nie, S., Efficient Raman enhancement and intermittent light emission observed in single gold nanocrystals. *Journal of the American Chemical Society* **1999,** *121*, (39), 9208-9214.

231. Malinsky, M. D.; Kelly, K. L.; Schatz, G. C.; Van Duyne, R. P., Chain length dependence and sensing capabilities of the localized surface plasmon resonance of silver nanoparticles chemically modified with alkanethiol self-assembled monolayers. *Journal of the American Chemical Society* **2001,** *123*, (7), 1471-1482.

232. Takai, M.; Tsuta, Y.; Hayashi, J.; Watanabe, S., Biosynthesis of cellulose by Acetobacter xylinum. III. X-ray studies of preferential orientation of the crystallites in a bacterial cellulose membrane. *Polymer Journal* **1975,** *7*, (2), 157-164.

233. Wei, H.; Leng, W.; Song, J.; Willner, M. R.; Marr, L. C.; Zhou, W.; Vikesland, P. J., Improved Quantitative SERS Enabled by Surface Plasmon Enhanced Elastic Light Scattering. *Anal. Chem.*

234. De Angelis, F.; Gentile, F.; Mecarini, F.; Das, G.; Moretti, M.; Candeloro, P.; Coluccio, M.; Cojoc, G.; Accardo, A.; Liberale, C., Breaking the Diffusion Limit with Super-Hydrophobic Delivery of Molecules to Plasmonic Nanofocusing SERS Structures. *Nature Photonics* **2011,** *5*, (11), 682-687.

235. Liu, H.; Yang, Z.; Meng, L.; Sun, Y.; Wang, J.; Yang, L.; Liu, J.; Tian, Z., Three-Dimensional and Time-Ordered Surface-Enhanced Raman Scattering Hotspot Matrix. *Journal of the American Chemical Society* **2014,** *136*, (14), 5332-5341.

236. Wei, H.; Vikesland, P. J., pH-Triggered Molecular Alignment for Reproducible SERS Detection via an AuNP/Nanocellulose Platform. *Sci. Rep.* **2015,** *5*.

237. Alabi, O.; Edilbi, A.; Brolly, C.; Muirhead, D.; Parnell, J.; Stacey, R.; Bowden, S., Asphaltene Detection using Surface Enhanced Raman Scattering (SERS). *Chemical Communications* **2015,** *51*, (33), 7152-7155.

238. Li, J. F.; Huang, Y. F.; Ding, Y.; Yang, Z. L.; Li, S. B.; Zhou, X. S.; Fan, F. R.; Zhang, W.; Zhou, Z. Y.; Ren, B., Shell-Isolated Nanoparticle-Enhanced Raman Spectroscopy. *nature* **2010,** *464*, (7287), 392-395.

239. Alvarez-Puebla, R. A.; Agarwal, A.; Manna, P.; Khanal, B. P.; Aldeanueva-Potel, P.; Carbó-Argibay, E.; Pazos-Pérez, N.; Vigderman, L.; Zubarev, E. R.; Kotov, N. A., Gold Nanorods 3D-Supercrystals as Surface Enhanced Raman Scattering Spectroscopy Substrates for the Rapid Detection of Scrambled Prions. *Proceedings of the National Academy of Sciences* **2011,** *108*, (20), 8157-8161.

240. Guttler, B.; Zakel, S.; Wundrack, S.; Stosch, R., Isotope-Dilution Surface-Enhanced Raman Spectroscopy: Metrologically Traceable Reference Measurements at the Highest Precision Level and Their Application in Clinical Chemistry. In *Handbook of Enhanced Spectroscopy*, Pan Stanford: 2015; pp 307-328.

241. Chen, H.-Y.; Lin, M.-H.; Wang, C.-Y.; Chang, Y.-M.; Gwo, S., Large-Scale Hot Spot Engineering for Quantitative SERS at the Single-Molecule Scale. *Journal of the American Chemical Society* **2015,** *137*, (42), 13698-13705.

242. Shen, W.; Lin, X.; Jiang, C.; Li, C.; Lin, H.; Huang, J.; Wang, S.; Liu, G.; Yan, X.; Zhong, Q., Reliable Quantitative SERS Analysis Facilitated by Core–Shell Nanoparticles with Embedded Internal Standards. *Angewandte Chemie* **2015,** *127*, (25), 7416-7420.

243. Itoh, N.; Bell, S. E., High Dilution Surface-Enhanced Raman Spectroscopy for Rapid Determination of Nicotine in E-Liquids for Electronic Cigarettes. *Analyst* **2017,** *142*, (6), 994-998.

244. Bell, S. E.; Sirimuthu, N. M., Quantitative Surface-Enhanced Raman Spectroscopy. *Chemical Society Reviews* **2008,** *37*, (5), 1012-1024.

245. Blackie, E. J.; Ru, E. C. L.; Etchegoin, P. G., Single-Molecule Surface-Enhanced Raman Spectroscopy of Nonresonant Molecules. *Journal of the American Chemical Society* **2009,** *131*, (40), 14466-14472.

246. Qian, X.; Peng, X.-H.; Ansari, D. O.; Yin-Goen, Q.; Chen, G. Z.; Shin, D. M.; Yang, L.; Young, A. N.; Wang, M. D.; Nie, S., In Vivo Tumor Targeting and Spectroscopic Detection with Surface-Enhanced Raman Nanoparticle Tags. *Nature biotechnology* **2008,** *26*, (1), 83.

247. Zavaleta, C. L.; Smith, B. R.; Walton, I.; Doering, W.; Davis, G.; Shojaei, B.; Natan, M. J.; Gambhir, S. S., Multiplexed Imaging of Surface Enhanced Raman Scattering Nanotags in Living Mice Using Noninvasive Raman Spectroscopy. *Proceedings of the National Academy of Sciences* **2009,** *106*, (32), 13511-13516.

248. Camden, J. P.; Dieringer, J. A.; Zhao, J.; Van Duyne, R. P., Controlled Plasmonic Nanostructures for Surface-Enhanced Spectroscopy and Sensing. *Accounts of chemical research* **2008,** *41*, (12), 1653-1661.

249. Alonso-González, P.; Albella, P.; Schnell, M.; Chen, J.; Huth, F.; García-Etxarri, A.; Casanova, F.; Golmar, F.; Arzubiaga, L.; Hueso, L., Resolving the Electromagnetic Mechanism of Surface-Enhanced Light Scattering at Single Hot Spots. *Nature communications* **2012,** *3*, 684.

250. Novotny, L.; Hecht, B., *Principles of Nano-Optics*. Cambridge university press: 2012.

251. Efrima, S.; Metiu, H., Classical Theory of Light Scattering by an Adsorbed Molecule. I. Theory. *The Journal of Chemical Physics* **1979,** *70*, (4), 1602-1613.

252. Wall, K. F.; Chang, R. K., I_2-Vapor Notch Filter with Optical Multichannel Detection of Low-Frequency-Shift Inelastic Scattering from Surface-Enhanced Raman-Scattering Active Electrodes. *Optics letters* **1986,** *11*, (8), 493-495.

253. Lumdee, C.; Yun, B.; Kik, P. G., Gap-Plasmon Enhanced Gold Nanoparticle Photoluminescence. *Acs Photonics* **2014,** *1*, (11), 1224-1230.

254. Maruyama, Y.; Futamata, M., Elastic Scattering and Emission Correlated with Single-Molecule SERS. *Journal of Raman Spectroscopy* **2005,** *36*, (6-7), 581-592.

255. Lin, K.-Q.; Yi, J.; Zhong, J.-H.; Hu, S.; Liu, B.-J.; Liu, J.-Y.; Zong, C.; Lei, Z.-C.; Wang, X.; Aizpurua, J., Plasmonic photoluminescence for recovering native chemical information from surface-enhanced Raman scattering. *Nature Communications* **2017,** *8*.

256. Galloway, C.; Etchegoin, P.; Le Ru, E., Ultrafast Nonradiative Decay Rates on Metallic Surfaces by Comparing Surface-Enhanced Raman and Fluorescence Signals of Single Molecules. *Physical review letters* **2009,** *103*, (6), 063003.

257. Chung, T. S.; Zhang, S.; Wang, K. Y.; Su, J.; Ling, M. M., Forward osmosis processes: yesterday, today and tomorrow. *Desalination* **2012,** *287*, 78-81.

258. Buchanan, S.; Le Ru, E.; Etchegoin, P., Plasmon-Dispersion Corrections and Constraints for Surface Selection Rules of Single Molecule SERS Spectra. *Physical Chemistry Chemical Physics* **2009,** *11*, (34), 7406-7411.

259. Le Ru, E.; Etchegoin, P.; Grand, J.; Felidj, N.; Aubard, J.; Levi, G., Mechanisms of Spectral Profile Modification in Surface-Enhanced Fluorescence. *The Journal of Physical Chemistry C* **2007,** *111*, (44), 16076-16079.

260. Shahbazyan, T. V., Theory of Plasmon-Enhanced Metal Photoluminescence. *Nano letters* **2012,** *13*, (1), 194-198.

261. Mahajan, S.; Cole, R. M.; Speed, J. D.; Pelfrey, S. H.; Russell, A. E.; Bartlett, P. N.; Barnett, S. M.; Baumberg, J. J., Understanding the Surface-Enhanced Raman Spectroscopy "Background". *The Journal of Physical Chemistry C* **2009,** *114*, (16), 7242-7250.

262. Jiang, J.; Bosnick, K.; Maillard, M.; Brus, L., Single Molecule Raman Spectroscopy at the Junctions of Large Ag Nanocrystals. In ACS Publications: 2003.

263. Eilers, P. H., Parametric Time Warping. *Analytical chemistry* **2004,** *76*, (2), 404-411.

264. Guan, Z.; Gao, N.; Jiang, X.-F.; Yuan, P.; Han, F.; Xu, Q.-H., Huge Enhancement in Two-Photon Photoluminescence of Au Nanoparticle Clusters Revealed by Single-Particle Spectroscopy. *Journal of the American Chemical Society* **2013,** *135*, (19), 7272-7277.

265. Bouhelier, A.; Bachelot, R.; Lerondel, G.; Kostcheev, S.; Royer, P.; Wiederrecht, G., Surface Plasmon Characteristics of Tunable Photoluminescence in Single Gold Nanorods. *Physical review letters* **2005,** *95*, (26), 267405.

266. Campion, A.; Kambhampati, P., Surface-Enhanced Raman Scattering. *Chem. Soc. Rev.* **1998,** *27*, (4), 241-250.

267. Boyd, G.; Yu, Z.; Shen, Y., Photoinduced Luminescence from the Noble Metals and its Enhancement on Roughened Surfaces. *Physical Review B* **1986,** *33*, (12), 7923.

268. Huang, J.-A.; Zhao, Y.-Q.; Zhang, X.-J.; He, L.-F.; Wong, T.-L.; Chui, Y.-S.; Zhang, W.-J.; Lee, S.-T., Ordered Ag/Si Nanowires Array: Wide-Range Surface-Enhanced Raman Spectroscopy for Reproducible Biomolecule Detection. *Nano letters* **2013,** *13*, (11), 5039-5045.

269. Lin, D.; Wu, Z.; Li, S.; Zhao, W.; Ma, C.; Wang, J.; Jiang, Z.; Zhong, Z.; Zheng, Y.; Yang, X., Large-Area Au-Nanoparticle-Functionalized Si Nanorod Arrays for Spatially Uniform Surface-Enhanced Raman Spectroscopy. *ACS nano* **2017**.

270. Yan, B.; Thubagere, A.; Premasiri, W. R.; Ziegler, L. D.; Dal Negro, L.; Reinhard, B. M., Engineered SERS Substrates with Multiscale Signal Enhancement: Nanoparticle Cluster Arrays. *Acs Nano* **2009,** *3*, (5), 1190-1202.

271. Schmidt, M. S.; Hübner, J.; Boisen, A., Large Area Fabrication of Leaning Silicon Nanopillars for Surface Enhanced Raman Spectroscopy. *Advanced Materials* **2012,** *24*, (10).

272. Chirumamilla, M.; Toma, A.; Gopalakrishnan, A.; Das, G.; Zaccaria, R. P.; Krahne, R.; Rondanina, E.; Leoncini, M.; Liberale, C.; De Angelis, F., 3D Nanostar Dimers with a Sub-10-nm Gap for Single-/Few-Molecule Surface-Enhanced Raman Scattering. *Advanced Materials* **2014,** *26*, (15), 2353-2358.

273. Li, A.; Baird, Z.; Bag, S.; Sarkar, D.; Prabhath, A.; Pradeep, T.; Cooks, R. G., Using Ambient Ion Beams to Write Nanostructured Patterns for Surface Enhanced Raman Spectroscopy. *Angewandte Chemie International Edition* **2014,** *53*, (46), 12528-12531.

274. Schwarzenbach, R. P.; Gschwend, P. M.; Imboden, D. M., *Environmental organic chemistry*. John Wiley & Sons: 2005.

275. Wei, H.; Willner, M. R.; Marr, L. C.; Vikesland, P. J., Highly Stable SERS pH Nanoprobes Produced by Co-Solvent Controlled AuNP Aggregation. *Analyst* **2016**.

276. Zhang, Y.; Li, X.; Xue, B.; Kong, X.; Liu, X.; Tu, L.; Chang, Y., A Facile and General Route to Synthesize Silica-Coated SERS Tags with the Enhanced Signal Intensity. *Scientific reports* **2015,** *5*.

277. Wackerbarth, H.; Salb, C.; Gundrum, L.; Niederkrüger, M.; Christou, K.; Beushausen, V.; Viöl, W., Detection of Explosives Based on Surface-Enhanced Raman Spectroscopy. *Applied optics* **2010,** *49*, (23), 4362-4366.

278. Wei, H.; McCarthy, A.; Song, J.; Zhou, W.; Vikesland, P. J., Quantitative SERS by hot spot normalization–surface enhanced Rayleigh band intensity as an alternative evaluation parameter for SERS substrate performance. *Faraday Discussions* **2017**.

279. Xu, L.; Lei, Z.; Li, J.; Zong, C.; Yang, C. J.; Ren, B., Label-free surface-enhanced Raman spectroscopy detection of DNA with single-base sensitivity. *Journal of the American Chemical Society* **2015,** *137*, (15), 5149-5154.

280. Huang, J.; Zhao, Y.; Zhang, X.; He, L.; Wong, T.; Chui, Y.; Zhang, W.; Lee, S., Ordered Ag/Si nanowires array: wide-range surface-enhanced Raman spectroscopy for reproducible biomolecule detection. *Nano Letters* **2013,** *13*, (11), 5039-5045.

281. Camargo, P. H.; Au, L.; Rycenga, M.; Li, W.; Xia, Y., Measuring the SERS enhancement factors of dimers with different structures constructed from silver nanocubes. *Chemical physics letters* **2010,** *484*, (4), 304-308.

282. Sivanesan, A.; Adamkiewicz, W.; Kalaivani, G.; Kamińska, A.; Waluk, J.; Hołyst, R.; Izake, E. L., Towards improved precision in the quantification of surface-enhanced Raman scattering (SERS) enhancement factors: a renewed approach. *Analyst* **2014,** *140*, (2), 489-496.

283. Dawson, P.; Duenas, J.; Boyle, M.; Doherty, M.; Bell, S.; Kern, A.; Martin, O.; Teh, A.-S.; Teo, K.; Milne, W., Combined antenna and localized plasmon resonance in Raman scattering

from random arrays of silver-coated, vertically aligned multiwalled carbon nanotubes. *Nano letters* **2011,** *11*, (2), 365-371.

284. Li, J.; Chen, C.; Jans, H.; Xu, X.; Verellen, N.; Vos, I.; Okumura, Y.; Moshchalkov, V. V.; Lagae, L.; Van Dorpe, P., 300 mm Wafer-level, ultra-dense arrays of Au-capped nanopillars with sub-10 nm gaps as reliable SERS substrates. *Nanoscale* **2014,** *6*, (21), 12391-12396.

285. Haidar, I.; Lévi, G.; Mouton, L.; Aubard, J.; Grand, J.; Lau-Truong, S.; Neuville, D. R.; Félidj, N.; Boubekeur-Lecaque, L., Highly stable silica-coated gold nanorods dimers for solution-based SERS. *Physical Chemistry Chemical Physics* **2016,** *18*, (47), 32272-32280.

286. Le Ru, E.; Blackie, E.; Meyer, M.; Etchegoin, P. G., Surface enhanced Raman scattering enhancement factors: a comprehensive study. *The Journal of Physical Chemistry C* **2007,** *111*, (37), 13794-13803.

287. Gui, J. Y.; Stern, D. A.; Frank, D. G.; Lu, F.; Zapien, D. C.; Hubbard, A. T., Adsorption and surface structural chemistry of thiophenol, benzyl mercaptan, and alkyl mercaptans. Comparative studies at silver (111) and platinum (111) electrodes by means of Auger spectroscopy, electron energy loss spectroscopy, low energy electron diffraction and electrochemistry. *Langmuir* **1991,** *7*, (5), 955-963.

288. Fang, Y.; Seong, N.-H.; Dlott, D. D., Measurement of the distribution of site enhancements in surface-enhanced Raman scattering. *Science* **2008,** *321*, (5887), 388-392.

289. Hu, M.; Ou, F. S.; Wu, W.; Naumov, I.; Li, X.; Bratkovsky, A. M.; Williams, R. S.; Li, Z., Gold nanofingers for molecule trapping and detection. *Journal of the American Chemical Society* **2010,** *132*, (37), 12820-12822.

290. Fraire, J. C.; Sueldo Ocello, V. N.; Allende, L. G.; Veglia, A. V.; Coronado, E. A., Toward the Design of Highly Stable Small Colloidal SERS Substrates with Supramolecular Host–Guest

Interactions for Ultrasensitive Detection. *The Journal of Physical Chemistry C* **2015,** *119*, (16), 8876-8888.

291. Kasera, S.; Biedermann, F.; Baumberg, J. J.; Scherman, O. A.; Mahajan, S., Quantitative SERS using the sequestration of small molecules inside precise plasmonic nanoconstructs. *Nano letters* **2012,** *12*, (11), 5924-5928.

292. Kleinman, S. L.; Frontiera, R. R.; Henry, A. I.; Dieringer, J. A.; Van Duyne, R. P., Creating, characterizing, and controlling chemistry with SERS hot spots. *Physical Chemistry Chemical Physics* **2013,** *15*, (1), 21-36.

293. Stranahan, S. M.; Willets, K. A., Super-resolution optical imaging of single-molecule SERS hot spots. *Nano letters* **2010,** *10*, (9), 3777-3784.

294. Shiohara, A.; Wang, Y.; Liz-Marzan, L. M., Recent approaches toward creation of hot spots for SERS detection. *Journal of Photochemistry and Photobiology C: Photochemistry Reviews* **2014,** *21*, 2-25.

295. Le Ru, E.; Etchegoin, P., Rigorous justification of the| E| 4 enhancement factor in surface enhanced Raman spectroscopy. *chemical Physics letters* **2006,** *423*, (1), 63-66.

296. Xu, H.; Aizpurua, J.; Käll, M.; Apell, P., Electromagnetic contributions to single-molecule sensitivity in surface-enhanced Raman scattering. *Physical Review E* **2000,** *62*, (3), 4318.

297. Maitani, M. M.; Ohlberg, D. A.; Li, Z.; Allara, D. L.; Stewart, D. R.; Williams, R. S., Study of SERS chemical enhancement factors using buffer layer assisted growth of metal nanoparticles on self-assembled monolayers. *Journal of the American Chemical Society* **2009,** *131*, (18), 6310-6311.

298. Niu, C.; Zou, B.; Wang, Y.; Cheng, L.; Zheng, H.; Zhou, S., Highly Sensitive and Reproducible SERS Performance from Uniform Film Assembled by Magnetic Noble Metal Composite Microspheres. *Langmuir* **2016,** *32*, (3), 858-863.

299. Zheng, Y.; Thai, T.; Reineck, P.; Qiu, L.; Guo, Y.; Bach, U., DNA-Directed Self-Assembly of Core-Satellite Plasmonic Nanostructures: A Highly Sensitive and Reproducible Near-IR SERS Sensor. *Advanced Functional Materials* **2013,** *23*, (12), 1519-1526.

300. Zhang, C.; Jiang, S. Z.; Yang, C.; Li, C. H.; Huo, Y. Y.; Liu, X. Y.; Liu, A. H.; Wei, Q.; Gao, S. S.; Gao, X. G., Gold@ silver bimetal nanoparticles/pyramidal silicon 3D substrate with high reproducibility for high-performance SERS. *Scientific Reports* **2016,** *6*, 26243.

301. Wei, H.; Vikesland, P. J., pH-Triggered Molecular Alignment for Reproducible SERS Detection via an AuNP/Nanocellulose Platform. *Scientific reports* **2014,** *5*, 18131-18131.

302. Wei, H.; Willner, M. R.; Marr, L. C.; Vikesland, P. J., Highly stable SERS pH nanoprobes produced by co-solvent controlled AuNP aggregation. *Analyst* **2016,** *141*, (17), 5159-5169.

303. Lin, D.; Wu, Z.; Li, S.; Zhao, W.; Ma, C.; Wang, J.; Jiang, Z.; Zhong, Z.; Zheng, Y.; Yang, X., Large-Area Au-Nanoparticle-Functionalized Si Nanorod Arrays for Spatially Uniform Surface-Enhanced Raman Spectroscopy. *ACS Nano* **2017,** *11*, (2), 1478-1487.

304. Sperling, R. A.; Gil, P. R.; Zhang, F.; Zanella, M.; Parak, W. J., Biological applications of gold nanoparticles. *Chemical Society Reviews* **2008,** *37*, (9), 1896-1908.

305. Stratakis, M.; Garcia, H., Catalysis by supported gold nanoparticles: beyond aerobic oxidative processes. *Chemical Reviews* **2012,** *112*, (8), 4469-4506.

306. Vance, M. E.; Kuiken, T.; Vejerano, E. P.; McGinnis, S. P.; Hochella Jr, M. F.; Rejeski, D.; Hull, M. S., Nanotechnology in the real world: Redeveloping the nanomaterial consumer products inventory. *Beilstein journal of nanotechnology* **2015,** *6*, 1769.

307. Li, Y. F.; Chen, C., Fate and Toxicity of Metallic and Metal-Containing Nanoparticles for Biomedical Applications. *Small* **2011,** *7*, (21), 2965-2980.

308. Murphy, C. J.; Vartanian, A. M.; Geiger, F. M.; Hamers, R. J.; Pedersen, J.; Cui, Q.; Haynes, C. L.; Carlson, E. E.; Hernandez, R.; Klaper, R. D., Biological responses to engineered nanomaterials: needs for the next decade. *ACS central science* **2015,** *1*, (3), 117-123.

309. Smith, B. M.; Pike, D. J.; Kelly, M. O.; Nason, J. A., Quantification of heteroaggregation between citrate-stabilized gold nanoparticles and hematite colloids. *Environmental science & technology* **2015,** *49*, (21), 12789-12797.

310. Stankus, D. P.; Lohse, S. E.; Hutchison, J. E.; Nason, J. A., Interactions between natural organic matter and gold nanoparticles stabilized with different organic capping agents. *Environmental science & technology* **2010,** *45*, (8), 3238-3244.

311. Louie, S. M.; Spielman-Sun, E. R.; Small, M. J.; Tilton, R. D.; Lowry, G. V., Correlation of the physicochemical properties of natural organic matter samples from different sources to their effects on gold nanoparticle aggregation in monovalent electrolyte. *Environmental science & technology* **2015,** *49*, (4), 2188-2198.

312. Louie, S. M.; Tilton, R. D.; Lowry, G. V., Effects of molecular weight distribution and chemical properties of natural organic matter on gold nanoparticle aggregation. *Environmental science & technology* **2013,** *47*, (9), 4245-4254.

313. Afrooz, A. N.; Khan, I. A.; Hussain, S. M.; Saleh, N. B., Mechanistic heteroaggregation of gold nanoparticles in a wide range of solution chemistry. *Environ. Sci. Technol* **2013,** *47*, (4), 1853-1860.

314. Judy, J. D.; Unrine, J. M.; Rao, W.; Wirick, S.; Bertsch, P. M., Bioavailability of gold nanomaterials to plants: importance of particle size and surface coating. *Environmental science & technology* **2012,** *46*, (15), 8467-8474.

315. Saei, A. A.; Yazdani, M.; Lohse, S. E.; Bakhtiary, Z.; Serpooshan, V.; Ghavami, M.; Asadian, M.; Mashaghi, S.; Dreaden, E. C.; Mashaghi, A., Nanoparticle Surface Functionality Dictates Cellular and Systemic Toxicity. *Chemistry of Materials* **2017,** *29*, (16), 6578-6595.

316. Zhu, M.; Nie, G.; Meng, H.; Xia, T.; Nel, A.; Zhao, Y., Physicochemical properties determine nanomaterial cellular uptake, transport, and fate. *Accounts of chemical research* **2012,** *46*, (3), 622-631.

317. Oh, E.; Delehanty, J. B.; Sapsford, K. E.; Susumu, K.; Goswami, R.; Blanco-Canosa, J. B.; Dawson, P. E.; Granek, J.; Shoff, M.; Zhang, Q., Cellular uptake and fate of PEGylated gold nanoparticles is dependent on both cell-penetration peptides and particle size. *Acs Nano* **2011,** *5*, (8), 6434-6448.

318. Zhu, Z.-J.; Wang, H.; Yan, B.; Zheng, H.; Jiang, Y.; Miranda, O. R.; Rotello, V. M.; Xing, B.; Vachet, R. W., Effect of surface charge on the uptake and distribution of gold nanoparticles in four plant species. *Environmental science & technology* **2012,** *46*, (22), 12391-12398.

319. Torelli, M. D.; Putans, R. A.; Tan, Y.; Lohse, S. E.; Murphy, C. J.; Hamers, R. J., Quantitative determination of ligand densities on nanomaterials by X-ray photoelectron spectroscopy. *ACS applied materials & interfaces* **2015,** *7*, (3), 1720-1725.

320. Dinkel, R.; Braunschweig, B. r.; Peukert, W., Fast and slow ligand exchange at the surface of colloidal gold nanoparticles. *The Journal of Physical Chemistry C* **2016,** *120*, (3), 1673-1682.

321. Marbella, L. E.; Millstone, J. E., NMR techniques for noble metal nanoparticles. *Chemistry of Materials* **2015,** *27*, (8), 2721-2739.

322. Halvorson, R. A.; Vikesland, P. J., Surface-enhanced Raman spectroscopy (SERS) for environmental analyses. In ACS Publications: 2010.

323. Craig, D.; McAughtrie, S.; Simpson, J.; McCraw, C.; Faulds, K.; Graham, D., Confocal SERS mapping of glycan expression for the identification of cancerous cells. *Analytical chemistry* **2014,** *86*, (10), 4775-4782.

324. Villarreal, E.; Li, G. G.; Zhang, Q.; Fu, X.; Wang, H., Nanoscale Surface Curvature Effects on Ligand-Nanoparticle Interactions: a Plasmon-Enhanced Spectroscopic Study of Thiolated Ligand Adsorption, Desorption, and Exchange on Gold Nanoparticles. *Nano Letters* **2017**.

325. DeVetter, B. M.; Mukherjee, P.; Murphy, C. J.; Bhargava, R., Measuring binding kinetics of aromatic thiolated molecules with nanoparticles via surface-enhanced Raman spectroscopy. *Nanoscale* **2015,** *7*, (19), 8766-8775.

326. Kent, R. D.; Oser, J. G.; Vikesland, P. J., Controlled evaluation of silver nanoparticle sulfidation in a full-scale wastewater treatment plant. *Environmental science & technology* **2014,** *48*, (15), 8564-8572.

327. Kent, R. D.; Vikesland, P. J., Controlled evaluation of silver nanoparticle dissolution using atomic force microscopy. *Environmental science & technology* **2012,** *46*, (13), 6977-6984.

328. Sekine, R.; Khaksar, M.; Brunetti, G.; Donner, E.; Scheckel, K. G.; Lombi, E.; Vasilev, K., Surface immobilization of engineered nanomaterials for in situ study of their environmental transformations and fate. *Environmental science & technology* **2013,** *47*, (16), 9308-9316.

329. Pazos-Perez, N.; Wagner, C. S.; Romo-Herrera, J. M.; Liz-Marzán, L. M.; García de Abajo, F. J.; Wittemann, A.; Fery, A.; Alvarez-Puebla, R. A., Organized plasmonic clusters with high coordination number and extraordinary enhancement in surface-enhanced raman scattering (sers). *Angewandte Chemie International Edition* **2012,** *51*, (51), 12688-12693.

330. Park, J.-W.; Shumaker-Parry, J. S., Strong resistance of citrate anions on metal nanoparticles to desorption under thiol functionalization. *ACS nano* **2015,** *9*, (2), 1665-1682.

331. Park, J.-W.; Shumaker-Parry, J. S., Structural study of citrate layers on gold nanoparticles: role of intermolecular interactions in stabilizing nanoparticles. *Journal of the American Chemical Society* **2014,** *136*, (5), 1907-1921.

332. Perera, G. S.; Athukorale, S.; Perez, F.; Pittman, C. U.; Zhang, D., Facile displacement of citrate residues from gold nanoparticle surfaces. *Journal of Colloid and Interface Science* **2017**.

333. Mabuchi, M.; Takenaka, T.; Fujiyoshi, Y.; Uyeda, N., Surface enhanced Raman scattering of citrate ions adsorbed on gold sol particles. *Surface Science* **1982,** *119*, (2-3), 150-158.

334. Al-Johani, H.; Abou-Hamad, E.; Jedidi, A.; Widdifield, C. M.; Viger-Gravel, J.; Sangaru, S. S.; Gajan, D.; Anjum, D. H.; Ould-Chikh, S.; Hedhili, M. N., The structure and binding mode of citrate in the stabilization of gold nanoparticles. *Nature Chemistry* **2017**.

335. Uehara, T.; de Aguiar, H.; Bergamaski, K.; Miranda, P. B., Adsorption of alkylthiol self-assembled monolayers on gold and the effect of substrate roughness: a comparative study using scanning tunneling microscopy, cyclic voltammetry, second-harmonic generation, and sum-frequency generation. *The Journal of Physical Chemistry C* **2014,** *118*, (35), 20374-20382.

336. Sun, M.; Xu, H., A novel application of plasmonics: plasmon-driven surface-catalyzed reactions. *Small* **2012,** *8*, (18), 2777-2786.

337. Xi, W.; Shrestha, B. K.; Haes, A. J., Promoting Intra-and Intermolecular Interactions in Surface-enhanced Raman Scattering (SERS). *Analytical Chemistry* **2017**.

338. Wojciechowski, P. M.; Michalska, D., Theoretical Raman and infrared spectra, and vibrational assignment for para-halogenoanilines: DFT study. *Spectrochimica Acta Part A: Molecular and Biomolecular Spectroscopy* **2007,** *68*, (3), 948-955.

339. Kennedy, B.; Spaeth, S.; Dickey, M.; Carron, K., Determination of the distance dependence and experimental effects for modified SERS substrates based on self-assembled monolayers formed using alkanethiols. *The Journal of Physical Chemistry B* **1999,** *103*, (18), 3640-3646.

340. Chan, M. Y.; Leng, W.; Vikesland, P. J., Surface-Enhanced Raman Spectroscopy Characterization of Salt-Induced Aggregation of Gold Nanoparticles. *ChemPhysChem* **2018,** *19*, (1), 24-28.

341. Kaushal, S. S.; Groffman, P. M.; Likens, G. E.; Belt, K. T.; Stack, W. P.; Kelly, V. R.; Band, L. E.; Fisher, G. T., Increased salinization of fresh water in the northeastern United States. *Proceedings of the National Academy of Sciences of the United States of America* **2005,** *102*, (38), 13517-13520.

342. Guerrini, L.; Krpetić, Ž.; van Lierop, D.; Alvarez-Puebla, R. A.; Graham, D., Direct Surface-Enhanced Raman Scattering Analysis of DNA Duplexes. *Angewandte Chemie* **2015,** *127*, (4), 1160-1164.

343. Bell, S.; Dick, S., Quantitative Surface-enhanced Raman Spectroscopy of Single Bases in Oligodeoxynucleotides. *Faraday Discussions* **2017**.

344. Barhoumi, A.; Halas, N. J., Label-free detection of DNA hybridization using surface enhanced Raman spectroscopy. *Journal of the American Chemical Society* **2010,** *132*, (37), 12792-12793.

345. Kim, A.; Barcelo, S. J.; Williams, R. S.; Li, Z., Melamine sensing in milk products by using surface enhanced Raman scattering. *Analytical chemistry* **2012,** *84*, (21), 9303-9309.

346. Levak, M.; Burić, P.; Dutour Sikirić, M.; Domazet Jurašin, D.; Mikac, N.; Bacic, N.; Drexel, R.; Meier, F.; Jaksic, Z.; Lyons, D. M., Effect of Protein Corona on Silver Nanoparticle

Stabilization and Ion Release Kinetics in Artificial Seawater. *Environmental science & technology* **2017,** *51*, (3), 1259-1266.

347. Walkey, C. D.; Olsen, J. B.; Song, F.; Liu, R.; Guo, H.; Olsen, D. W. H.; Cohen, Y.; Emili, A.; Chan, W. C., Protein corona fingerprinting predicts the cellular interaction of gold and silver nanoparticles. *ACS nano* **2014,** *8*, (3), 2439-2455.

348. Pallem, V. L.; Stretz, H. A.; Wells, M. J., Evaluating aggregation of gold nanoparticles and humic substances using fluorescence spectroscopy. *Environmental science & technology* **2009,** *43*, (19), 7531-7535.

349. Guo, H.; Zhang, Z.; Xing, B.; Mukherjee, A.; Musante, C.; White, J. C.; He, L., Analysis of silver nanoparticles in antimicrobial products using surface-enhanced Raman spectroscopy (SERS). *Environmental science & technology* **2015,** *49*, (7), 4317-4324.

350. Hou, R.; Zhang, Z.; Pang, S.; Yang, T.; Clark, J. M.; He, L., Alteration of the nonsystemic behavior of the pesticide ferbam on tea leaves by engineered gold nanoparticles. *Environmental science & technology* **2016,** *50*, (12), 6216-6223.

351. Metch, J. W.; Ma, Y.; Pruden, A.; Vikesland, P. J., Enhanced disinfection by-product formation due to nanoparticles in wastewater treatment plant effluents. *Environmental Science: Water Research & Technology* **2015,** *1*, (6), 823-831.

352. Wegman, R.; De Korte, G., Aromatic amines in surface waters of the Netherlands. *Water Research* **1981,** *15*, (3), 391-394.

353. Ning, X.-A.; Liang, J.-Y.; Li, R.-J.; Hong, Z.; Wang, Y.-J.; Chang, K.-L.; Zhang, Y.-P.; Yang, Z.-Y., Aromatic amine contents, component distributions and risk assessment in sludge from 10 textile-dyeing plants. *Chemosphere* **2015,** *134*, 367-373.

354. Muz, M.; Dann, J. P.; Jäger, F.; Brack, W.; Krauss, M., Identification of Mutagenic Aromatic Amines in River Samples with Industrial Wastewater Impact. *Environmental Science & Technology* **2017,** *51*, (8), 4681-4688.

355. Muz, M.; Krauss, M.; Kutsarova, S.; Schulze, T.; Brack, W., Mutagenicity in Surface Waters: Synergistic Effects of Carboline Alkaloids and Aromatic Amines. *Environmental science & technology* **2017,** *51*, (3), 1830-1839.

356. Park, J.-W.; Dec, J.; Kim, J.-E.; Bollag, J.-M., Effect of humic constituents on the transformation of chlorinated phenols and anilines in the presence of oxidoreductive enzymes or birnessite. *Environmental Science & Technology* **1999,** *33*, (12), 2028-2034.

357. Salter-Blanc, A. J.; Bylaska, E. J.; Lyon, M. A.; Ness, S. C.; Tratnyek, P. G., Structure–activity relationships for rates of aromatic amine oxidation by manganese dioxide. *Environmental science & technology* **2016,** *50*, (10), 5094-5102.

358. Li, H.; Lee, L. S.; Jafvert, C. T.; Graveel, J. G., Effect of substitution on irreversible binding and transformation of aromatic amines with soils in aqueous systems. *Environmental science & technology* **2000,** *34*, (17), 3674-3680.

359. Samaraweera, M.; Jolin, W.; Vasudevan, D.; MacKay, A. A.; Gascón, J. A., Atomistic prediction of sorption free energies of cationic aromatic amines on montmorillonite: a linear interaction energy method. *Environmental Science & Technology Letters* **2014,** *1*, (6), 284-289.

360. Xiao, F.; Pignatello, J. J., π+–π Interactions between (Hetero) aromatic amine cations and the graphitic surfaces of pyrogenic carbonaceous materials. *Environmental science & technology* **2015,** *49*, (2), 906-914.

361. Ghosh, P.; Han, G.; De, M.; Kim, C. K.; Rotello, V. M., Gold nanoparticles in delivery applications. *Advanced drug delivery reviews* **2008,** *60*, (11), 1307-1315.

362. Daniel, M.-C.; Astruc, D., Gold nanoparticles: assembly, supramolecular chemistry, quantum-size-related properties, and applications toward biology, catalysis, and nanotechnology. *Chemical reviews* **2004,** *104*, (1), 293-346.

363. Murphy, C. J.; Gole, A. M.; Stone, J. W.; Sisco, P. N.; Alkilany, A. M.; Goldsmith, E. C.; Baxter, S. C., Gold nanoparticles in biology: beyond toxicity to cellular imaging. *Accounts of chemical research* **2008,** *41*, (12), 1721-1730.

364. Surette, M.; Nason, J., Effects of surface coating character and interactions with natural organic matter on the colloidal stability of gold nanoparticles. *Environmental Science: Nano* **2016,** *3*, (5), 1144-1152.

365. Valley, N.; Greeneltch, N.; Van Duyne, R. P.; Schatz, G. C., A look at the origin and magnitude of the chemical contribution to the enhancement mechanism of surface-enhanced Raman spectroscopy (SERS): Theory and experiment. *The Journal of Physical Chemistry Letters* **2013,** *4*, (16), 2599-2604.

366. Wang, X.; Li, M.; Meng, L.; Lin, K.; Feng, J.; Huang, T.; Yang, Z.; Ren, B., Probing the location of hot spots by surface-enhanced Raman spectroscopy: toward uniform substrates. *ACS nano* **2013,** *8*, (1), 528-536.

367. Dinish, U.; Yaw, F. C.; Agarwal, A.; Olivo, M., Development of highly reproducible nanogap SERS substrates: comparative performance analysis and its application for glucose sensing. *Biosensors and Bioelectronics* **2011,** *26*, (5), 1987-1992.

368. Gschwend, P. M., *Environmental organic chemistry*. John Wiley & Sons: 2016.

369. Haes, A. J.; Zou, S.; Schatz, G. C.; Van Duyne, R. P., Nanoscale optical biosensor: short range distance dependence of the localized surface plasmon resonance of noble metal nanoparticles. *The Journal of Physical Chemistry B* **2004,** *108*, (22), 6961-6968.

370. Masango, S. S.; Hackler, R. A.; Large, N.; Henry, A.-I.; McAnally, M. O.; Schatz, G. C.; Stair, P. C.; Van Duyne, R. P., High-resolution distance dependence study of surface-enhanced raman scattering enabled by atomic layer deposition. *Nano letters* **2016,** *16*, (7), 4251-4259.

371. Kahl, M.; Voges, E.; Kostrewa, S.; Viets, C.; Hill, W., Periodically structured metallic substrates for SERS. *Sensors and Actuators B: Chemical* **1998,** *51*, (1), 285-291.

372. Ho, C. C.; Zhao, K.; Lee, T. Y., Quasi-3D gold nanoring cavity arrays with high-density hot-spots for SERS applications via nanosphere lithography. *Nanoscale* **2014,** *6*, (15), 8606-8611.

373. Gong, J.; Lipomi, D. J.; Deng, J.; Nie, Z.; Chen, X.; Randall, N. X.; Nair, R.; Whitesides, G. M., Micro-and nanopatterning of inorganic and polymeric substrates by indentation lithography. *Nano letters* **2010,** *10*, (7), 2702-2708.

374. Nergiz, S. Z.; Gandra, N.; Farrell, M. E.; Tian, L.; Pellegrino, P. M.; Singamaneni, S., Biomimetic SERS substrate: peptide recognition elements for highly selective chemical detection in chemically complex media. *Journal of Materials Chemistry A* **2013,** *1*, (22), 6543-6549.

375. Alvarez-Puebla, R. A.; Aroca, R. F., Synthesis of silver nanoparticles with controllable surface charge and their application to surface-enhanced Raman scattering. *Analytical chemistry* **2009,** *81*, (6), 2280-2285.

376. Ye, Q.; Fang, J.; Sun, L., Surface-enhanced Raman scattering from functionalized self-assembled monolayers. 2. Distance dependence of enhanced Raman scattering from an azobenzene terminal group. *The Journal of Physical Chemistry B* **1997,** *101*, (41), 8221-8224.

377. Carpenter, A. W.; de-Lannoy, C. F.; Wiesner, M. R., Cellulose Nanomaterials in Water Treatment Technologies. *Environmental science & technology* **2015**.

378. Wei, H.; Rodriguez, K.; Renneckar, S.; Vikesland, P. J., Environmental science and engineering applications of nanocellulose-based nanocomposites. *Environ. Sci. Nano* **2014,** *1*, (4), 302-316.

379. Wang, P.; Keller, A. A., Sorption and desorption of atrazine and diuron onto water dispersible soil primary size fractions. *water research* **2009,** *43*, (5), 1448-1456.

380. Hildebrandt, A.; Guillamón, M.; Lacorte, S.; Tauler, R.; Barceló, D., Impact of pesticides used in agriculture and vineyards to surface and groundwater quality (North Spain). *Water research* **2008,** *42*, (13), 3315-3326.

381. Tixier, C.; Singer, H. P.; Oellers, S.; Müller, S. R., Occurrence and fate of carbamazepine, clofibric acid, diclofenac, ibuprofen, ketoprofen, and naproxen in surface waters. *Environmental science & technology* **2003,** *37*, (6), 1061-1068.

382. Wei, H.; Deng, S.; Huang, Q.; Nie, Y.; Wang, B.; Huang, J.; Yu, G., Regenerable granular carbon nanotubes/alumina hybrid adsorbents for diclofenac sodium and carbamazepine removal from aqueous solution. *Water research* **2013,** *47*, (12), 4139-4147.

383. Solomon, K. R.; Baker, D. B.; Richards, R. P.; Dixon, K. R.; Klaine, S. J.; La Point, T. W.; Kendall, R. J.; Weisskopf, C. P.; Giddings, J. M.; Giesy, J. P., Ecological risk assessment of atrazine in North American surface waters. *Environmental Toxicology and Chemistry* **1996,** *15*, (1), 31-76.

384. Scheytt, T.; Mersmann, P.; Lindstädt, R.; Heberer, T., 1-Octanol/water partition coefficients of 5 pharmaceuticals from human medical care: carbamazepine, clofibric acid, diclofenac, ibuprofen, and propyphenazone. *Water, Air, and Soil Pollution* **2005,** *165*, (1-4), 3-11.

385. Qian, X.; Emory, S. R.; Nie, S., Anchoring molecular chromophores to colloidal gold nanocrystals: surface-enhanced Raman evidence for strong electronic coupling and irreversible structural locking. *Journal of the American Chemical Society* **2012,** *134*, (4), 2000-2003.

386. Leng, W.; Vikesland, P. J., MGITC Facilitated Formation of AuNP Multimers. *Langmuir* **2014,** *30*, (28), 8342-8349.

387. Osawa, M.; Matsuda, N.; Yoshii, K.; Uchida, I., Charge transfer resonance Raman process in surface-enhanced Raman scattering from p-aminothiophenol adsorbed on silver: Herzberg-Teller contribution. *The Journal of Physical Chemistry* **1994,** *98*, (48), 12702-12707.

388. Otto, A.; Mrozek, I.; Grabhorn, H.; Akemann, W., Surface-enhanced Raman scattering. *Journal of Physics: Condensed Matter* **1992,** *4*, (5), 1143.

389. Carrillo-Carrión, C.; Simonet, B. M.; Valcárcel, M.; Lendl, B., Determination of pesticides by capillary chromatography and SERS detection using a novel Silver-Quantum dots "sponge" nanocomposite. *Journal of Chromatography A* **2012,** *1225*, 55-61.

390. Song, X.; Li, H.; Al-Qadiri, H. M.; Lin, M., Detection of herbicides in drinking water by surface-enhanced Raman spectroscopy coupled with gold nanostructures. *Journal of Food Measurement and Characterization* **2013,** *7*, (3), 107-113.

391. Rubira, R. J.; Camacho, S. A.; Aoki, P. H.; Maximino, M. D.; Alessio, P.; Martin, C. S.; Oliveira Jr, O. N.; Fatore, F. M.; Paulovich, F. V.; Constantino, C. J., Detection of trace levels of atrazine using surface-enhanced Raman scattering and information visualization. *Colloid Polym. Sci.* **2014,** *292*, (11), 2811-2820.

392. Bonora, S.; Benassi, E.; Maris, A.; Tugnoli, V.; Ottani, S.; Di Foggia, M., Raman and SERS study on atrazine, prometryn and simetryn triazine herbicides. *Journal of Molecular Structure* **2013,** *1040*, 139-148.

393. Xu, J.; Turner, J. W.; Idso, M.; Biryukov, S. V.; Rognstad, L.; Gong, H.; Trainer, V. L.; Wells, M. L.; Strom, M. S.; Yu, Q., In situ strain-level detection and identification of Vibrio parahaemolyticus using surface-enhanced Raman spectroscopy. *Analytical chemistry* **2013,** *85*, (5), 2630-2637.

394. Rezaee, M.; Assadi, Y.; Hosseini, M.-R. M.; Aghaee, E.; Ahmadi, F.; Berijani, S., Determination of organic compounds in water using dispersive liquid–liquid microextraction. *Journal of Chromatography A* **2006,** *1116*, (1), 1-9.

395. EPA method 523. *http://water.epa.gov/scitech/drinkingwater/labcert/upload/epa815r11002.pdf*.

396. Severyukhina, A. N.; Parakhonskiy, B. V.; Prikhozhdenko, E. S.; Gorin, D. A.; Sukhorukov, G. B.; Möhwald, H.; Yashchenok, A. M., Nanoplasmonic chitosan nanofibers as effective SERS substrate for detection of small molecules. *ACS applied materials & interfaces* **2015,** *7*, (28), 15466-15473.

397. Zhu, H.; Du, M.; Zhang, M.; Wang, P.; Bao, S.; Zou, M.; Fu, Y.; Yao, J., Self-assembly of various Au nanocrystals on functionalized water-stable PVA/PEI nanofibers: a highly efficient surface-enhanced Raman scattering substrates with high density of “hot” spots. *Biosensors and Bioelectronics* **2014,** *54*, 91-101.

398. Zhang, C. L.; Lv, K. P.; Cong, H. P.; Yu, S. H., Controlled asemblies of gold nanorods in PVA nanofiber matrix as flexible free-standing SERS substrates by electrospinning. *Small* **2012,** *8*, (5), 648-653.

399. Martín, A.; Wang, J.; Iacopino, D., Flexible SERS active substrates from ordered vertical Au nanorod arrays. *RSC Advances* **2014,** *4*, (38), 20038-20043.

400. Yao, S.; Zhou, C.; Chen, D., A highly porous PVA dried gel with gold nanoparticles embedded in the network as a stable and ultrasensitive SERS substrate. *Chemical Communications* **2013,** *49*, (57), 6409-6411.

401. Shin, K.; Ryu, K.; Lee, H.; Kim, K.; Chung, H.; Sohn, D., Au nanoparticle-encapsulated hydrogel substrates for robust and reproducible SERS measurement. *Analyst* **2013,** *138*, (3), 932-938.

402. Lee, C. H.; Hankus, M. E.; Tian, L.; Pellegrino, P. M.; Singamaneni, S., Highly sensitive surface enhanced Raman scattering substrates based on filter paper loaded with plasmonic nanostructures. *Analytical chemistry* **2011,** *83*, (23), 8953-8958.

403. Matsuoka, M.; Tsuchida, T.; Matsushita, K.; Adachi, O.; Yoshinaga, F., A synthetic medium for bacterial cellulose production by Acetobacter xylinum subsp. sucrofermentans. *Bioscience, biotechnology, and biochemistry* **1996,** *60*, (4), 575-579.

404. Costa, J. C. S.; Ando, R. A.; Sant'Ana, A. C.; Rossi, L. M.; Santos, P. S.; Temperini, M. L. A.; Corio, P., High performance gold nanorods and silver nanocubes in surface-enhanced Raman spectroscopy of pesticides. *Physical Chemistry Chemical Physics* **2009,** *11*, (34), 7491-7498.

405. Hu, S.; Smith, K. M.; Spiro, T. G., Assignment of protoheme resonance Raman spectrum by heme labeling in myoglobin. *Journal of the American Chemical Society* **1996,** *118*, (50), 12638-12646.

406. Diem, M.; Polavarapu, P. L.; Oboodi, M.; Nafie, L. A., Vibrational circular dichroism in amino acids and peptides. 4. vibrational analysis, assignments, and solution-phase Raman spectra of deuterated isotopomers of alanine. *Journal of the American Chemical Society* **1982,** *104*, (12), 3329-3336.

407. Palings, I.; Pardoen, J. A.; Van den Berg, E.; Winkel, C.; Lugtenburg, J.; Mathies, R. A., Assignment of fingerprint vibrations in the resonance Raman spectra of rhodopsin, isorhodopsin, and bathorhodopsin: implications for chromophore structure and environment. *Biochemistry* **1987,** *26*, (9), 2544-2556.

408. Chinsky, L.; Turpin, P.; Duquesne, M.; Brahms, J., Nucleic acid derivatives studied by preresonance and resonance Raman spectroscopy in the ultraviolet region. *Biopolymers* **1978,** *17*, (5), 1347-1359.

409. Wei, H.; Vikesland, P. J., pH-Triggered Molecular Alignment for Reproducible SERS Detection via an AuNP/Nanocellulose Platform. *Sci. Rep.* **2015,** *5*, 18131.

410. Halvorson, R. A.; Vikesland, P. J., Surface-Enhanced Raman Spectroscopy (SERS) for Environmental Analyses. *Environ. Sci. Tech.* **2010,** *44*, (20), 7749-7755.

411. Wei, H.; Abtahi, S. M. H.; Vikesland, P. J., Plasmonic Colorimetric and SERS Sensors for Environmental Analysis. *Environ. Sci. Nano* **2015,** *2*, (2), 120-135.

412. Rule, K. L.; Vikesland, P. J., Surface-Enhanced Resonance Raman Spectroscopy for the Rapid Detection of Cryptosporidium Parvum and Giardia Lamblia. *Environ. Sci. Tech.* **2009,** *43*, (4), 1147-1152.

413. Braun, G.; Pavel, I.; Morrill, A. R.; Seferos, D. S.; Bazan, G. C.; Reich, N. O.; Moskovits, M., Chemically Patterned Microspheres for Controlled Nanoparticle Assembly in the Construction of SERS Hot Spots. *J Am Chem Soc* **2007,** *129*, (25), 7760-7761.

414. Kleinman, S. L.; Frontiera, R. R.; Henry, A. I.; Dieringer, J. A.; Van Duyne, R. P., Creating, Characterizing, and Controlling Chemistry with SERS Hot Spots. *Phys Chem Chem Phys* **2013,** *15*, (1), 21-36.

415. Lawson, L. S.; Chan, J. W.; Huser, T., A Highly Sensitive Nanoscale pH-Sensor Using Au Nanoparticles Linked by a Multifunctional Raman-Active Reporter Molecule. *Nanoscale* **2014,** *6*, (14), 7971-7980.

416. Braun, G. B.; Lee, S. J.; Laurence, T.; Fera, N.; Fabris, L.; Bazan, G. C.; Moskovits, M.; Reich, N. O., Generalized Approach to SERS-Active Nanomaterials via Controlled Nanoparticle Linking, Polymer Encapsulation, and Small-Molecule Infusion. *J. Phys. Chem. C* **2009,** *113*, (31), 13622-13629.

417. Romo-Herrera, J. M.; Alvarez-Puebla, R. A.; Liz-Marzán, L. M., Controlled Assembly of Plasmonic Colloidal Nanoparticle Clusters. *Nanoscale* **2011,** *3*, (4), 1304-1315.

418. Lim, D.-K.; Jeon, K.-S.; Hwang, J.-H.; Kim, H.; Kwon, S.; Suh, Y. D.; Nam, J.-M., Highly Uniform and Reproducible Surface-Enhanced Raman Scattering from DNA-Tailorable Nanoparticles with 1-nm Interior Gap. *Nat. Nanotechnol.* **2011,** *6*, (7), 452-460.

419. Taylor, R. W.; Lee, T. C.; Scherman, O. A.; Esteban, R.; Aizpurua, J.; Huang, F. M.; Baumberg, J. J.; Mahajan, S., Precise Subnanometer Plasmonic Junctions for SERS within Gold Nanoparticle Assemblies using Cucurbit [n] uril "Glue". *ACS Nano* **2011,** *5*, (5), 3878-3887.

420. Pallaoro, A.; Braun, G. B.; Reich, N.; Moskovits, M., Mapping local pH in live cells using encapsulated fluorescent SERS nanotags. *Small* **2010,** *6*, (5), 618-622.

421. Wang, Z.; Bonoiu, A.; Samoc, M.; Cui, Y.; Prasad, P. N., Biological pH Sensing Based on Surface Enhanced Raman Scattering through a 2-Aminothiophenol-Silver Probe. *Biosensors and Bioelectronics* **2008,** *23*, (6), 886-891.

422. Talley, C. E.; Jusinski, L.; Hollars, C. W.; Lane, S. M.; Huser, T., Intracellular pH Sensors Based on Surface-Enhanced Raman Scattering. *Anal. Chem.* **2004,** *76*, (23), 7064-7068.

423. Bishnoi, S. W.; Rozell, C. J.; Levin, C. S.; Gheith, M. K.; Johnson, B. R.; Johnson, D. H.; Halas, N. J., All-optical nanoscale pH meter. *Nano Lett.* **2006,** *6*, (8), 1687-1692.

424. Piotrowski, P.; Wrzosek, B.; Królikowska, A.; Bukowska, J., A SERS-Based pH Sensor Utilizing 3-Amino-5-Mercapto-1, 2, 4-Triazole Functionalized Ag Nanoparticles. *Analyst* **2014,** *139*, (5), 1101-1111.

425. Zheng, X. S.; Hu, P.; Cui, Y.; Zong, C.; Feng, J. M.; Wang, X.; Ren, B., BSA-Coated Nanoparticles for Improved SERS-Based Intracellular pH Sensing. *Anal. Chem.* **2014,** *86*, (24), 12250-12257.

426. Zong, S.; Wang, Z.; Yang, J.; Cui, Y., Intracellular pH Sensing Using p-Aminothiophenol Functionalized Gold Nanorods with Low Cytotoxicity. *Analytical chemistry* **2011,** *83*, (11), 4178-4183.

427. Liu, Y.; Yuan, H.; Fales, A. M.; Vo-Dinh, T., pH-sensing nanostar probe using surface-enhanced Raman scattering (SERS): theoretical and experimental studies. *J. Raman Spectrosc.* **2013,** *44*, (7), 980-986.

428. Gühlke, M.; Heiner, Z.; Kneipp, J., Combined Near-Infrared Excited SEHRS and SERS Spectra of pH Sensors Using Silver Nanostructures. *Physical Chemistry Chemical Physics* **2015,** *17*, (39), 26093-26100.

429. Jaworska, A.; Jamieson, L. E.; Malek, K.; Campbell, C. J.; Choo, J.; Chlopicki, S.; Baranska, M., SERS-Based Monitoring of the Intracellular pH in Endothelial Cells: the Influence of the Extracellular Environment and Tumour Necrosis Factor-α. *Analyst* **2015,** *140*, (7), 2321-2329.

430. Jamieson, L.; Jaworska, A.; Jiang, J.; Baranska, M.; Harrison, D.; Campbell, C., Simultaneous Intracellular Redox Potential and pH Measurements in Live Cells Using SERS Nanosensors. *Analyst* **2015,** *140*, (7), 2330-2335.

431. Wang, F.; Widejko, R. G.; Yang, Z.; Nguyen, K. T.; Chen, H.; Fernando, L. P.; Christensen, K. A.; Anker, J. N., Surface-Enhanced Raman Scattering Detection of pH with Silica-Encapsulated 4-Mercaptobenzoic Acid-Functionalized Silver Nanoparticles. *Analytical chemistry* **2012,** *84*, (18), 8013-8019.

432. Liao, J.; Zhang, Y.; Yu, W.; Xu, L.; Ge, C.; Liu, J.; Gu, N., Linear Aggregation of Gold Nanoparticles in Ethanol. *Colloids Surf. A Physicochem. Eng. Asp.* **2003,** *223*, (1), 177-183.

433. Darby, B. L.; Le Ru, E. C., Competition between Molecular Adsorption and Diffusion: Dramatic Consequences for SERS in Colloidal Solutions. *Journal of the American Chemical Society* **2014,** *136*, (31), 10965-10973.

434. Eilers, P. H., and Hans FM Boelens *Baseline Correction with Asymmetric Least Squares Smoothing*; 2005.

435. Leng, W.; Pati, P.; Vikesland, P. J., Room Temperature Seed Mediated Growth of Gold Nanoparticles: Mechanistic Investigations and Life Cycle Assesment. *Environ. Sci. Nano* **2015,** *2*, (5), 440-453.

436. Ge, Z.; Wu, L.; Zhang, F.; He, Z., Energy extraction from a large-scale microbial fuel cell system treating municipal wastewater. *Journal of Power Sources* **2015,** *297*, 260-264.

437. Jokerst, J. V.; Lobovkina, T.; Zare, R. N.; Gambhir, S. S., Nanoparticle PEGylation for Imaging and Therapy. *Nanomedicine* **2011,** *6*, (4), 715-728.

438. Leopold, M. C.; Black, J. A.; Bowden, E. F., Influence of Gold Topography on Carboxylic Acid Terminated Self-Assembled Monolayers. *Langmuir* **2002,** *18*, (4), 978-980.

439. Ma, C.; Harris, J. M., Surface-Enhanced Raman Spectroscopy Investigation of the Potential-Dependent Acid− Base Chemistry of Silver-Immobilized 2-Mercaptobenzoic Acid. *Langmuir* **2011,** *27*, (7), 3527-3533.

440. Gregas, M. K.; Scaffidi, J. P.; Lauly, B.; Vo-Dinh, T., Surface-Enhanced Raman Scattering Detection and Tracking of Nanoprobes: Enhanced Uptake and Nuclear Targeting in Single Cells. *Appl. Spectrosc.* **2010,** *64*, (8), 858-866.

441. Chithrani, B. D.; Ghazani, A. A.; Chan, W. C. W., Determining the Size and Shape Dependence of Gold Nanoparticle Uptake into Mammalian Cells. *Nano Lett.* **2006,** *6*, (4), 662-668.

442. Chou, L. Y. T.; Ming, K.; Chan, W. C. W., Strategies for the Intracellular Delivery of Nanoparticles. *Chem. Soc. Rev.* **2011,** *40*, (1), 233-245.

443. ATCC, PC-3 (ATCC® CRL-1435™). In.

444. Stevens, B.; Feingold, G., Untangling aerosol effects on clouds and precipitation in a buffered system. *Nature* **2009,** *461*, (7264), 607-613.

445. Ariya, P. A.; Amyot, M.; Dastoor, A.; Deeds, D.; Feinberg, A.; Kos, G.; Poulain, A.; Ryjkov, A.; Semeniuk, K.; Subir, M., Mercury physicochemical and biogeochemical transformation in the atmosphere and at atmospheric interfaces: a review and future directions. *Chem. Rev.* **2015,** *115*, (10), 3760-3802.

446. Von Schneidemesser, E.; Monks, P. S.; Allan, J. D.; Bruhwiler, L.; Forster, P.; Fowler, D.; Lauer, A.; Morgan, W. T.; Paasonen, P.; Righi, M., Chemistry and the linkages between air quality and climate change. *Chem. Rev.* **2015,** *115*, (10), 3856-3897.

447. Lohmann, U.; Feichter, J., Global indirect aerosol effects: a review. *Atmos. Chem. Phys.* **2005,** *5*, (3), 715-737.

448. Christensen, M. W.; Neubauer, D.; Poulsen, C. A.; Thomas, G. E.; McGarragh, G. R.; Povey, A. C.; Proud, S. R.; Grainger, R. G., Unveiling aerosol–cloud interactions–Part 1: Cloud contamination in satellite products enhances the aerosol indirect forcing estimate. *Atmos. Chem. Phys.* **2017,** *17*, (21), 13151-13164.

449. Ault, A. P.; Zhao, D.; Ebben, C. J.; Tauber, M. J.; Geiger, F. M.; Prather, K. A.; Grassian, V. H., Raman microspectroscopy and vibrational sum frequency generation spectroscopy as probes of the bulk and surface compositions of size-resolved sea spray aerosol particles. *Phys. Chem. Chem. Phys.* **2013,** *15*, (17), 6206-6214.

450. Herrmann, H.; Schaefer, T.; Tilgner, A.; Styler, S. A.; Weller, C.; Teich, M.; Otto, T., Tropospheric aqueous-phase chemistry: kinetics, mechanisms, and its coupling to a changing gas phase. *Chem. Rev.* **2015,** *115*, (10), 4259-4334.

451. Pöschl, U.; Shiraiwa, M., Multiphase chemistry at the atmosphere–biosphere interface influencing climate and public health in the Anthropocene. *Chem. Rev.* **2015,** *115*, (10), 4440-4475.

452. Lin, Y. H.; Zhang, Z.; Docherty, K. S.; Zhang, H.; Budisulistiorini, S. H.; Rubitschun, C. L.; Shaw, S. L.; Knipping, E. M.; Edgerton, E. S.; Kleindienst, T. E., Isoprene epoxydiols as precursors to secondary organic aerosol formation: acid-catalyzed reactive uptake studies with authentic compounds. *Environ. Sci. Technol.* **2011,** *46*, (1), 250-258.

453. Li, Y. J.; Cheong, G. Y.; Lau, A. P.; Chan, C. K., Acid-catalyzed condensed-phase reactions of limonene and terpineol and their impacts on gas-to-particle partitioning in the formation of organic aerosols. *Environ. Sci. Technol.* **2010,** *44*, (14), 5483-5489.

454. Zhang, H.; Zhang, Z.; Cui, T.; Lin, Y.-H.; Bhathela, N. A.; Ortega, J.; Worton, D. R.; Goldstein, A. H.; Guenther, A.; Jimenez, J. L., Secondary organic aerosol formation via 2-methyl-

3-buten-2-ol photooxidation: evidence of acid-catalyzed reactive uptake of epoxides. *Environ. Sci. Technol. Lett.* **2014,** *1*, (4), 242-247.

455. Weber, R. J.; Guo, H.; Russell, A. G.; Nenes, A., High aerosol acidity despite declining atmospheric sulfate concentrations over the past 15 years. *Nat. Geosci.* **2016,** *9*, (4), 282-285.

456. Guo, H.; Xu, L.; Bougiatioti, A.; Cerully, K. M.; Capps, S. L.; Hite Jr, J.; Carlton, A.; Lee, S.; Bergin, M.; Ng, N., Fine-particle water and pH in the southeastern United States. *Atmos. Chem. Phys* **2015,** *15*, (9), 5211-5228.

457. Dallemagne, M. A.; Huang, X. Y.; Eddingsaas, N. C., Variation in pH of model secondary organic aerosol during liquid–liquid phase separation. *J. Phys. Chem. A* **2016,** *120*, (18), 2868-2876.

458. Losey, D. J.; Parker, R. G.; Freedman, M. A., pH dependence of liquid-liquid phase separation in organic aerosol. *J. Phys. Chem. Lett.* **2016,** *7*, (19), 3861-3865.

459. Boyer, H. C.; Dutcher, C. S., Atmospheric aqueous aerosol surface tensions: isotherm-based modeling and biphasic microfluidic measurements. *J. Phys. Chem. A* **2017,** *121*, (25), 4733-4742.

460. Boyer, H. C.; Bzdek, B. R.; Reid, J. P.; Dutcher, C. S., Statistical thermodynamic model for surface tension of organic and inorganic aqueous mixtures. *J. Phys. Chem. A* **2016,** *121*, (1), 198-205.

461. Ault, A. P.; Axson, J. L., Atmospheric aerosol chemistry: spectroscopic and microscopic advances. *Anal. Chem.* **2016,** *89*, (1), 430-452.

462. Agmon, N.; Bakker, H. J.; Campen, R. K.; Henchman, R. H.; Pohl, P.; Roke, S.; Thamer, M.; Hassanali, A., Protons and hydroxide ions in aqueous systems. *Chem. Rev.* **2016,** *116*, (13), 7642-7672.

463. Saykally, R. J., Air/water interface: Two sides of the acid-base story. *Nat. Chem.* **2013,** *5*, (2), 82-84.

464. Duignan, T. T.; Parsons, D. F.; Ninham, B. W., Hydronium and hydroxide at the air-water interface with a continuum solvent model. *Chem. Phys. Lett.* **2015,** *635*, 1-12.

465. Tse, Y. L. S.; Chen, C.; Lindberg, G. E.; Kumar, R.; Voth, G. A., Propensity of hydrated excess protons and hydroxide anions for the air–water interface. *J. Am. Chem. Soc.* **2015,** *137*, (39), 12610-12616.

466. Vácha, R.; Horinek, D.; Berkowitz, M. L.; Jungwirth, P., Hydronium and hydroxide at the interface between water and hydrophobic media. *Phys. Chem. Chem. Phys.* **2008,** *10*, (32), 4975-4980.

467. Shi, G.; Xu, J.; Peng, X.; Xiao, Z.; Chen, K.; Tian, Y.; Guan, X.; Feng, Y.; Yu, H.; Nenes, A., pH of aerosols in a polluted atmosphere: source contributions to highly acidic aerosol. *Environ. Sci. Technol.* **2017,** *51*, (8), 4289-4296.

468. Murphy, J. G.; Gregoire, P.; Tevlin, A.; Wentworth, G.; Ellis, R.; Markovic, M.; VandenBoer, T., Observational constraints on particle acidity using measurements and modelling of particles and gases. *Faraday Discuss.* **2017,** *200*, 379-395.

469. Nguyen, T. K. V.; Zhang, Q.; Jimenez, J. L.; Pike, M.; Carlton, A. G., Liquid water: ubiquitous contributor to aerosol mass. *Environ. Sci. Technol. Lett.* **2016,** *3*, (7), 257-263.

470. Rindelaub, J. D.; Craig, R. L.; Nandy, L.; Bondy, A. L.; Dutcher, C. S.; Shepson, P. B.; Ault, A. P., Direct measurement of pH in individual particles via Raman microspectroscopy and variation in acidity with relative humidity. *J. Phys. Chem. A* **2016,** *120*, (6), 911-917.

471. Craig, R. L.; Nandy, L.; Axson, J. L.; Dutcher, C. S.; Ault, A. P., Spectroscopic determination of aerosol pH from acid–base equilibria in inorganic, organic, and mixed systems. *J. Phys. Chem. A* **2017,** *121*, (30), 5690-5699.

472. Craig, R. L.; Bondy, A. L.; Ault, A. P., Surface enhanced Raman spectroscopy enables observations of previously undetectable secondary organic aerosol components at the individual particle level. *Anal. Chem.* **2015,** *87*, (15), 7510-7514.

473. Fu, Y.; Kuppe, C.; Valev, V. K.; Fu, H.; Zhang, L.; Chen, J., Surface-enhanced Raman spectroscopy: a facile and rapid method for the chemical component study of individual atmospheric aerosol. *Environ. Sci. Technol.* **2017,** *51*, (11), 6260-6267.

474. Etchegoin, P. G.; Le Ru, E., A perspective on single molecule SERS: current status and future challenges. *Phys. Chem. Chem. Phys.* **2008,** *10*, (40), 6079-6089.

475. Le Ru, E. C.; Meyer, M.; Etchegoin, P. G., Proof of single-molecule sensitivity in surface enhanced Raman scattering (SERS) by means of a two-analyte technique. *J. Phys. Chem. B* **2006,** *110*, (4), 1944-1948.

476. Kneipp, J.; Kneipp, H.; Wittig, B.; Kneipp, K., One-and two-photon excited optical pH probing for cells using surface-enhanced Raman and hyper-Raman nanosensors. *Nano Lett.* **2007,** *7*, (9), 2819-2823.

477. Wei, H.; Willner, M. R.; Marr, L. C.; Vikesland, P. J., Highly stable SERS pH nanoprobes produced by co-solvent controlled AuNP aggregation. *Analyst* **2016,** *141*, 5159-5169.

478. Myriokefalitakis, S.; Nenes, A.; Baker, A. R.; Mihalopoulos, N.; Kanakidou, M., Bioavailable atmospheric phosphorous supply to the global ocean: a 3-D global modeling study. *Biogeosciences* **2016,** *13*, (24), 6519.

479. Anderson, L.; Faul, K.; Paytan, A., Phosphorus associations in aerosols: what can they tell us about P bioavailability? *Mar. Chem.* **2010,** *120*, (1), 44-56.

480. Longo, A. F.; Ingall, E. D.; Diaz, J. M.; Oakes, M.; King, L. E.; Nenes, A.; Mihalopoulos, N.; Violaki, K.; Avila, A.; Benitez-Nelson, C. R., P-NEXFS analysis of aerosol phosphorus delivered to the Mediterranean Sea. *Geophys. Res. Lett.* **2014,** *41*, (11), 4043-4049.

481. Abràmoff, M. D.; Magalhães, P. J.; Ram, S. J., Image processing with ImageJ. *Biophotonics Intern.* **2004,** *11*, (7), 36-42.

482. Mandair, G. S.; Morris, M. D., Contributions of Raman spectroscopy to the understanding of bone strength. *Bonekey Rep.* **2015,** *4*.

483. Michota, A.; Bukowska, J., Surface-enhanced Raman scattering (SERS) of 4-mercaptobenzoic acid on silver and gold substrates. *J. Raman Spectrosc.* **2003,** *34*, (1), 21-25.

484. Guo, X.; Yin, Y.; Tan, Z.; Zhang, Z.; Chen, Y.; Liu, J., Significant enrichment of engineered nanoparticles in water surface microlayer. *Environ. Sci. Technol. Lett.* **2016,** *3*, (10), 381-385.

485. Enami, S.; Hoffmann, M. R.; Colussi, A. J., Proton availability at the air/water interface. *J. Phys. Chem. Lett.* **2010,** *1*, (10), 1599-1604.

486. Mishra, H.; Enami, S.; Nielsen, R. J.; Stewart, L. A.; Hoffmann, M. R.; Goddard, W. A.; Colussi, A. J., Brønsted basicity of the air–water interface. *Proc. Natl. Acad. Sci.* **2012,** *109*, (46), 18679-18683.

487. Haynes, W. M., *CRC handbook of chemistry and physics*. CRC press: 2014.

488. Gabudean, A.; Biro, D.; Astilean, S., Localized surface plasmon resonance (LSPR) and surface-enhanced Raman scattering (SERS) studies of 4-aminothiophenol adsorption on gold nanorods. *J. Mol. Struct.* **2011,** *993*, (1), 420-424.

489. Sun, M.; Huang, Y.; Xia, L.; Chen, X.; Xu, H., The pH-controlled plasmon-assisted surface photocatalysis reaction of 4-aminothiophenol to p, p′-dimercaptoazobenzene on Au, Ag, and Cu colloids. *J. Phys. Chem. C* **2011,** *115*, (19), 9629-9636.

490. Neumann, O.; Urban, A. S.; Day, J.; Lal, S.; Nordlander, P.; Halas, N. J., Solar vapor generation enabled by nanoparticles. *Acs Nano* **2012,** *7*, (1), 42-49.

491. Fang, Z.; Zhen, Y.-R.; Neumann, O.; Polman, A.; García de Abajo, F. J.; Nordlander, P.; Halas, N. J., Evolution of light-induced vapor generation at a liquid-immersed metallic nanoparticle. *Nano Lett.* **2013,** *13*, (4), 1736-1742.

492. Hogan, N. J.; Urban, A. S.; Ayala-Orozco, C.; Pimpinelli, A.; Nordlander, P.; Halas, N. J., Nanoparticles heat through light localization. *Nano Lett.* **2014,** *14*, (8), 4640-4645.

493. Seinfeld, J. H.; Pandis, S. N., *Atmospheric chemistry and physics: from air pollution to climate change*. John Wiley & Sons: 2016.

494. Milton, D. K.; Fabian, M. P.; Cowling, B. J.; Grantham, M. L.; McDevitt, J. J., Influenza virus aerosols in human exhaled breath: particle size, culturability, and effect of surgical masks. *PLoS Pathog.* **2013,** *9*, (3), e1003205.

495. Bai, C.; Herzfeld, J., Surface propensities of the self-ions of water. *ACS Cent. Sci.* **2016,** *2*, (4), 225-231.

496. Bjornehohn, E.; Hansen, M. H.; Hodgson, A.; Liu, L. M.; Limmer, D. T.; Michaelides, A.; Pedevilla, P.; Rossmeisl, J.; Shen, H.; Tocci, G.; Tyrode, E.; Walz, M. M.; Werner, J.; Bluhm, H., Water at Interfaces. *Chem. Rev.* **2016,** *116*, (13), 7698-7726.

497. Marsh, A.; Rovelli, G.; Song, Y.-C.; Pereira, K. L.; Willoughby, R. E.; Bzdek, B. R.; Hamilton, J.; Orr-Ewing, A.; Topping, D. O.; Reid, J. P., Accurate representations of the

physicochemical properties of atmospheric aerosols: when are laboratory measurements of value? *Faraday Discuss.* **2017,** *200*, 639-661.

498. Krieger, U. K.; Marcolli, C.; Reid, J. P., Exploring the complexity of aerosol particle properties and processes using single particle techniques. *Chem. Soc. Rev.* **2012,** *41*, (19), 6631-6662.

499. You, Y.; Renbaum-Wolff, L.; Carreras-Sospedra, M.; Hanna, S. J.; Hiranuma, N.; Kamal, S.; Smith, M. L.; Zhang, X.; Weber, R. J.; Shilling, J. E., Images reveal that atmospheric particles can undergo liquid–liquid phase separations. *Proc. Natl. Acad. Sci.* **2012,** *109*, (33), 13188-13193.

500. Müller, T.; Badu-Tawiah, A.; Cooks, R. G., Accelerated carbon-carbon bond-forming reactions in preparative electrospray. *Angew. Chem. Int. Ed.* **2012,** *51*, (47), 11832-11835.

501. Bain, R. M.; Pulliam, C. J.; Cooks, R. G., Accelerated Hantzsch electrospray synthesis with temporal control of reaction intermediates. *Chem. Sci.* **2015,** *6*, (1), 397-401.

502. Banerjee, S.; Gnanamani, E.; Yan, X.; Zare, R. N., Can all bulk-phase reactions be accelerated in microdroplets? *Analyst* **2017,** *142*, 1399-1402.